UNIVERSITÀ DEGLI STUDI DI PALERMO
Dottorato in Scienze della Terra e del Mare
Dipartimento di Scienze della Terra e del Mare
GEO 07

Petrology and geochemistry of peri-Mediterranean carbonatite magmatism: case studies from Fuerteventura (Canary Islands) and Mt. Vulture volcano (southern Italy)

IL DOTTORE
Gabriele Carnevale

Gabriele Carnevale

IL COORDINATORE
Prof. Alessandro Aiuppa

IL TUTOR
Prof. Silvio G. Rotolo

Silvio Rotolo

IL CO-TUTOR
Dott. Antonio Caracausi

Antonio Caracausi

CICLO XXXV -
2019/2023

INDEX

Abstract

Carbonatites are rare magmatic rocks of great scientific and economic importance, and carbonatite magmatism is mainly associated with intraplate continental tectonic settings, with some rare occurrences in oceanic contexts. Despite their importance, many aspects of carbonatite petrogenesis and evolution processes remain still poorly constrained.

In order to further constrain the mantle source and the storage system of carbonatite magmas, Fuerteventura (Canary Islands) was taken as a representative case study of oceanic carbonatites, while Mt. Vulture (southern Italy) was taken as a representative case study of intra-continental carbonatites, with a two-fold aim: to understand (i) the role of the carbonatite primary melts in metasomatizing the mantle source in different geodynamic settings with possible implications in terms of volcanic hazard, and (ii) the role of the infiltrating fluids in the transport and concentration of Rare Earth Elements (REEs) with the processes involved in the carbonatite-related hydrothermal mineralization.

The first noble gases study on intrusive oceanic Ca-carbonatites from Fuerteventura reflects a sub-continental lithospheric mantle (SCLM) signature in their petrogenesis, corroborating that, also in the rare context of oceanic lithosphere, a contribute of a sub-continental lithosphere is needed. As regards the REEs characterization, detailed petrographic and micro-thermometric studies on the same carbonatites show how REEs can be mobilised locally by low-temperature hydrothermal fluids with a process known as autometasomatism (for intrusive carbonatites). At sub-solidus temperatures (T > 600 °C) and the brine-melt stage (600 ≤ T ≤ 400 °C), where REEs are sufficiently concentrated in the residual brine-melt to form REE-minerals, the infiltrating fluids play an important role in the transport and concentration of REEs, as testified by the presence of REEs-rich filled microfractures in accessory minerals.

As regards the Mt. Vulture case study, a suite of several pelletal lapilli (enclosing ultramafic mantle xenoliths), mantle xenoliths and loose olivine and clinopyroxene xenocrysts, brought to the surface by the last melilitite-carbonatite explosive volcano activity, was characterized. The melilitite-carbonatite matrix and carbonatite-rich layers within the matrix in the ash-rich tuff deposits, show whole rock compositions comparable with those of the average values of extrusive carbonatites, suggesting a possible contribution of a carbonatite melt in the trace elements enrichment processes. Furthermore, petrographic evidences of wehrlitization processes reflects the direct evidence of carbonatite metasomatism beneath the Mt. Vulture. Detailed petrographic, micro-thermometric, and geothermometric studies provide insights into the P-T history of the mineral-melt-fluid interaction processes in the mantle and within the Mt. Vulture magma storage system, identifying evidences of wehrlitization processes and two different magma ponding stages at the local crust-mantle boundary and at a shallower crustal level. Calculations on magma dynamics show how the ascent rates of carbonatite magmas can be comparable with kimberlite magmas, with the important role of a pure CO_2 gas phase as principal propellent in an upward moving elutriated gas-dominated medium. High calculated oxygen fugacity supports the geochemical evidence that Mt. Vulture xenoliths would have formed by interaction with an oxidized CO_2-rich metasomatic fluid, according to the presence of pure CO_2 fluid inclusions within the mantle xenoliths-forming minerals.

List of figures

respectively. ol = olivine; opx = orthopyroxene; cpx = clinopyroxene (emerald green Cr-diopside); spl = spinel.

Fig. 5.4: Mantle xenoliths hand specimens and related parallel polars (PPL) photomicrographs of (a) fine-grained wehrlite, (b) medium-grained ol-clinopyroxenite, and (c) medium-grained wehrlite, respectively. ol = olivine; opx = orthopyroxene; cpx = clinopyroxene (emerald green Cr-diopside); spl = spinel.

Fig. 5.5: Mg# vs. NiO wt.% in (a) olivine, and Mg# vs. Cr_2O_3 wt.% in (b) orthopyroxene and (c) clinopyroxene in mantle xenoliths from Mt. Vulture. Mt. Vulture xenoliths are from our previous study (Carnevale et al., 2022, C22) and from Jones et al. (2000). Hyblean Plateau xenoliths are from Correale et al. (2012) and Scribano et al. (2009). lhz = lherzolite, whr = wehrlite, dun = dunite.

Fig. 5.6: (**a**) Multi-element and (**b**) REE abundance diagram normalized to chondrite (McDonough and Sun, 1995), showing patterns of the external portion of lapilli and the carbonatite layer. Patterns of Fuerteventura oceanic carbonatites (Carnevale et al., 2021) and sedimentary calcrete-carbonate fraction (Innocenzi et al., 2021) are also shown for comparison. Average extrusive carbonatites from Stoppa (2003).

Fig. 5.7: Photomicrographs (parallel polars) of fluid inclusions and their textures enclosed by (a) olivine, (b) orthopyroxene, (c) clinopyroxene in a lherzolite xenolith, and (d) clinopyroxene in wehrlite xenolith from Mt. Vulture.

Fig. 5.8: Frequency distribution of densities of fluid inclusions hosted by olivine, orthopyroxene and clinopyroxene in lherzolite (lhz) and wehrlite (whr) xenoliths from Mt. Vulture. N = number of measures.

Fig. 5.9: Mt. Vulture mantle xenoliths in the pressure-temperature region of interest along the carbonate-bearing lherzolite solidus in the system CMAS-CO_2 (a) (Dalton and Presnall, 1998). Temperature-lines of the lower and higher temperature from the applied geothermometers are depicted ($TBM_{opx\text{-}cpx}$ = Bertrand and Mercier, 1985; $TBK_{opx\text{-}cpx}$ = Brey and Köhler, 1990) with the plagioclase-out boundary at 8-9 kbar and the spinel-garnet phase transition boundary at 15-20 kbar (Borghini et al., 2010; Su et al., 2010). Hyblean mantle xenoliths are also depicted for comparison (Correale et al., 2012; Scribano et al., 2009). Mt. Vulture within the geodynamic context of the Ionian subduction (b). Red arrows show the asthenospheric mantle flow along the vertical slab windows (D'Orazio et al., 2007).

Fig. 5.10: Olivine (a,b,c) and spinel (d,e) Mössbauer spectra with an X-ray beam focused on an area of 8x3 μm^2. Spectra were fitted through a full transmission integral with a

List of tables

Chapter 1: Introduction

1.1 Aim of this work

Carbonatites are rare magmatic rocks but of great importance for several reasons, among which: (i) scientific importance, given their petrogenesis that involves modified carbonated mantle, liquid immiscibility, geodynamic setting; (ii) economic relevance, given that they are considered the main natural hosts of critical metals for key economic sectors in heavily industrialized countries, due to their great abundance in Rare Earth Elements (REEs) and trace elements (such as Nb, Hf, U, Th, etc), essential in many high-tech applications; (iii) environmental, due their strict ties with CO_2 uptake and exsolution. Despite their importance, many aspects of carbonatites petrogenesis and evolution processes remain still poorly constrained.

One of the principal purposes of the scientific community is to refine the existing models for carbonatite magma petrogenesis, because they provide meaningful information on the deep geochemical cycle of carbon and mantle metasomatism. Then, it is fundamental to understand not only the genesis of carbonatite magmatism investigating its source, but also any possible post-genetic process during the evolutionary history of carbonatite melt.

This work adopts a multidisciplinary approach (with different analytical methods) to define petrology and isotope geochemistry of carbonatites in different geodynamic settings. The goal is to characterize the source of carbonatite magmatism and identify any post-genetic processes such as crustal contamination, mixing processes, isotopic exchanges, hydrothermal mineralization, that were able to modify the primary signature and the origin composition of carbonatite melts. Fuerteventura (Canary Islands) was taken representative of oceanic carbonatites, while Mt. Vulture (southern Italy) was taken representative of intra-continental carbonatites, within the particular geodynamic context of Apennine subduction zone. The comparison of oceanic carbonatites with intra-continental ones was aimed to provide information on the mantle source and the relationship of carbonatite magmatism with the various geodynamic settings, trying to understand why oceanic carbonatites are so rare if compared with continental counterpart. Principal inferences regard also the role of the carbonatite melts in metasomatizing the mantle source, and also on the importance of post-magmatic processes in which the infiltrating fluids play an important role in the transport and concentration of REEs.

To achieve these objectives, for each case study, a detailed minero-petrographic and minero-chemical characterization was firstly carried out. In particular, a detailed micro-thermometric study was performed in Fuerteventura carbonatites to understand the processes involved in carbonatite-related hydrothermal mineralization and formation condition (temperature, pressure and composition of fluid inclusions), and in Mt. Vulture products to provide important information about the melilitite-carbonatite magma ascent path and its mantle source, describing the volcano plumbing system and the way in which these very particular magmas are transported to the surface, with considerations about carbonatite mantle metasomatism and possible implications in terms of volcanic hazard. Subsequently, a characterization of noble gases (He, Ne and Ar), together with literature data of stable isotopes ($\delta^{13}C$ and $\delta^{18}O$), and Sr-Nd-Pb systematics, applied on studied carbonatite products (or closely related to them), was implemented. A preliminary study on iron isotope compositions of Fuerteventura carbonatites in order to record differentiation processes (e.g., liquid immiscibility) was also performed. Moreover, to reconstruct the redox conditions of the last eruption of Vulture volcano fed by a melilitite-carbonatite magma (Monticchio Lakes Syntheme) and further characterize the mantle source beneath Vulture area, the iron partitioning between spinel and liquid was investigated. All analytical techniques, methods, and sampling details are described in the Chapter 3.

1.2 Thesis organization

The research presented here is divided into seven Chapters.

The first three chapters, in which theoretical background, sampling details and analytical techniques are presented. Particularly: ***Chapter 1*** contains a brief introduction to the goal of this research (*Sub-Chapter 1.1*) and the thesis organization (*Sub-Chapter 1.2*); in ***Chapter 2*** an overview of the carbonatite classification (*Sub-Chapter 2.1*), a petrological (*Sub-Chapter 2.2*) and geochemical (*Sub-Chapter 2.3*) background, and the relationship between the carbonatite magmatism and its geodynamics (*Sub-Chapter 2.4*) is presented; ***Chapter 3*** includes the description of sampling (*Sub-Chapter 3.1*) and analytical methods (*Sub-Chapter 3.2*), particularly the Scanning Electron Microscopy (*Sub-Sub-Chapter 3.2.1*), X-ray diffraction (*Sub-Sub-Chapter 3.2.2*), Laser Ablation Inductively Coupled Plasma Mass Spectrometry (*Sub-Sub-Chapter 3.2.3*), Microthermometry for fluid inclusions (*Sub-Sub-Chapter 3.2.4*), Noble gases (*Sub-Sub-Chapter 3.2.5*), Mössbauer spectroscopy and Micro-transmittance Fourier transform infrared spectroscopy (*Sub-Sub-Chapter 3.2.6*).

Then, other three chapters in which the case studies of Fuerteventura and Mt. Vulture are treated separately with a final comparation between oceanic and intra-continental carbonatites. Particularly, the case study of Fuerteventura oceanic carbonatite (***Chapter 4***) is divided into three sub-chapters: *Sub-Chapter 4.1* shows new insights about carbonatite genesis from our review of geochemical characteristics in oceanic carbonatites with the first noble gas analysis in Fuerteventura and the implication on the mantle source. *Sub-Chapter 4.2* shows preliminary results of iron isotopes. *Sub-Chapter 4.3* shows the importance of post-magmatic processes in the transport and enrichment of REEs in carbonatites, and includes the micro-thermometric analysis of fluid inclusions. The case study of Mt. Vulture (***Chapter 5***) is divided into two sub-chapters: *Sub-Chapter 5.1* describes the petrography (*Sub-Sub-Chapter 5.1.1*), mineral and whole rock chemistry (*Sub-Sub-Chapter 5.1.2*), micro-thermometry of fluid inclusions (*Sub-Sub-Chapter 5.1.3*), geothermobarometry (*Sub-Sub-Chapter 5.1.4*), oxybarometry and redox conditions (*Sub-Sub-Chapter 5.1.5*), and the noble gases isotope geochemistry (*Sub-Sub-Chapter 5.1.6*) of the studied products; *Sub-Chapter 5.2* shows new inferences on carbonatite magma dynamics with implications in volcanic hazards and the role of the gas expansion during magma ascent (*Sub-Sub-Chapter 5.2.1*). A final comparation between oceanic and intra-continental carbonatites with possible future perspectives is presented in ***Chapter 6***.

Finally, the conclusive remarks are summarized in ***Chapter 7***.

Parts of this thesis (*Sub-Chapters 4.1*, *4.3*, and 5.2) are published in 4 papers, and two (*Sub-Sub-Chapter 5.1.5 and 5.2.1*) are in preparation, proving the high potential of the covered topics:

Carnevale, G., Arroyo Rey, X., Correale, A., Rotolo, S.G. (2020). Hydrothermal processes with REE enrichment in Fuerteventura carbonatites: evidences in accessory minerals. *Geogaceta*, *69*, 23-26.

Carnevale, G., Caracausi, A., Correale, A., Italiano, L., Rotolo, S.G. (2021). An Overview of the Geochemical Characteristics of Oceanic Carbonatites: New Insights from Fuerteventura Carbonatites (Canary Islands). *Minerals*, *11* (2), 203.

Carnevale, G., Zanon, V., Casillas, R., Ahijado, A. (2022). Microthermometry of fluid inclusions in calcite from Fuerteventura carbonatites: composition and formation conditions. *Geogaceta*, *72*, 31-34.

Carnevale, G., Caracausi, A., Paternoster, M., Rotolo, S.G., Zanon, V. (2022). New Inferences on Magma Dynamics in Melilitite-Carbonatite Volcanoes: The Case Study of Mt. Vulture (Southern Italy). *Geophysical Research Letters*, *49*, e2022GL099075.

Chapter 2: Carbonatite magmas

2.1 Classification

Since the pioneering work of Streckeisen (1980), a carbonatite rock is defined as an igneous, intrusive or effusive rock, which contains more than 50% of carbonate minerals. More specifically, according to a more recent definition (Le Maitre, 2002) and to the classification proposed by IUGS (International Union of Geological Sciences), a carbonatite rock is defined as an igneous, intrusive or effusive rock, which contains more than 50% modal of primary carbonate minerals (i.e. magmatic origin) and less than 20 wt.% of SiO_2. Thus, a classification ternary diagram with the wt.% of CaO, MgO and $FeO+Fe_2O_3+MnO$ is identified (**Fig. 2.1**), and three different types of carbonatites are recognized:

(i) *Ca-carbonatite* (composed of Ca-rich carbonate minerals as calcite)
(ii) *Mg-carbonatite* (composed of Mg-rich carbonate minerals as dolomite and magnesite)
(iii) *Fe-carbonatite* (composed of Fe-rich carbonate minerals as siderite and ankerite)

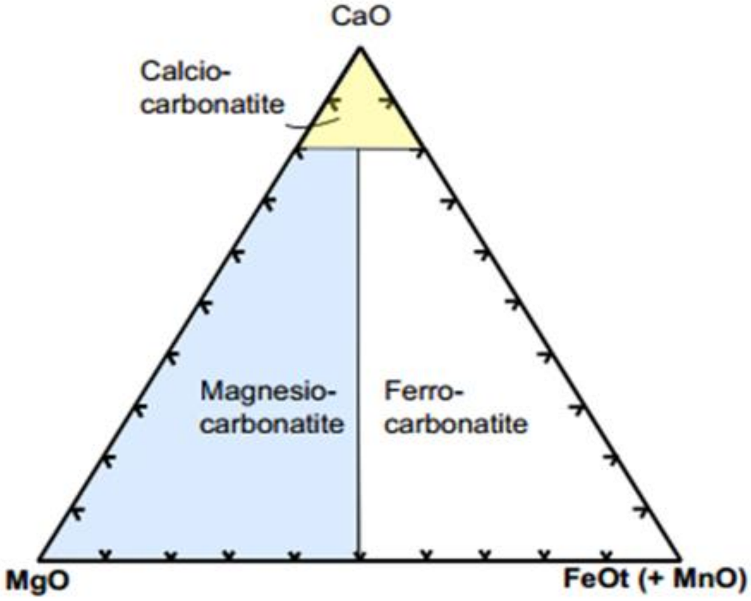

Fig. 2.1: Carbonatite classification diagram from Jones et al. (2013) (redrawn after Woolley and Kempe, 1989).

In addition to the identified three carbonatite types, there are other two recognized types: (iv) *silico-carbonatite*, when the amount of silicate phases reaches up to 50% of the rock volume, and (v) *natrocarbonatite*, composed of Na-, K- and Ca-rich carbonate minerals as nyerereite and gregoryite. Currently, the only rocks with natrocarbonatitic affinity were produced by the effusive activity of the Oldoinyo Lengai volcano, in Tanzania (*i.e.*, the only active carbonatite volcano on Earth).

A mineralogical-genetic classification of carbonatites was proposed by Mitchell (2005). His paper points to pitfalls of the IUGS classification, subdividing carbonatites into “primary carbonatites” and "carbothermal residua". Woolley and Kjarsgaard (2008) have taken into consideration the suggestions proposed by Mitchell (2005), but instead of using "primary carbonatites" and "carbothermal residua" they adopted the terms "magmatic" and "carbo-hydrothermal", as carbonatite which precipitated at sub-solidus temperatures from a mixed CO_2–H_2O fluid that can be either CO_2-rich (*i.e.*, carbothermal), or H_2O-rich (*i.e.*, hydrothermal). This classification is in line with number of recent studies highlighting the role of fluids in formation of carbonatite-related REE deposits, such as at Bayan Obo Fe-REE-Nb deposit, Inner Mongolia (Smith et al. 2015), and with studies that provide evidences on transport of REE by hydrothermal fluids and their deposition, such as at Fuerteventura, Canary Islands (Carnevale et al., 2020) (see Sub-Chapter 4.3 of this work for detailed information). Incorrect classification can lead to misdirected exploration programs and incorrect evaluation of potential ore deposits. For this reason, Mitchell and Gittings (2022) recently propose a new approach in classifying the carbonatite-like rocks, using a quaternary SiO_2-MgO-CaO-(FeO + Fe_2O_3 + MnO) diagram as an alternative scheme of representing bulk compositional variation.

Carbonate melts are ionic liquids consisting of carbonate CO_3^{2-} molecular anions and metal cations that interact principally due to coulombic interactions and they are therefore very different from silicate melts, which on the contrary have network structures characterized by polymerization. The low concentration of cations such as Si, Al and Fe^{3+} ("network forming cations"), related to a high concentration of cations such as Ca, K, Na, Fe^{2+}, and Mg ("network modifying cations"), translate in a low polymerized carbonatite liquid, presenting peculiar physicochemical properties. Indeed, one of the main physical characteristics of carbonatite magmas is their very low viscosity. *In situ* experiments using falling spheres method coupled to synchrotron X-ray facilities and calculations for pressures up to 6.2 GPa, show viscosities of carbonatite melts in the order of 10^{-3} – 10^{-2} Pa s (Kono et al., 2014; Stagno et al., 2018). At the same time, very low eruption temperatures were measured, as is the case of the only active carbonatite volcano Oldoinyo Lengai, with eruption temperatures of about 590 °C (Norton and Pinkerton, 1997).

Almost the 74% of known carbonatite occurrences are associated with alkaline-rich-silica undersaturated rocks (Woolley and Kjarsgaard, 2008), such as *nepheline-sienites*, *sienites*, *ijolites-melteigites-urtites*, and *clinopyroxenites*. Indeed, carbonatite occurrences are often described as part of alkaline-carbonatite complexes, spatially tied to one or more intrusive rocks. Most of these alkaline-carbonatite complexes are surrounded by country rock affected by intrusion-related fenitization metasomatism, defined as a solid-state process by which the chemical composition of a rock is altered in a pervasive manner involving the introduction and/or removal of chemical components as a result of the interaction of the rock with fluids, leading to the formation of fenites (**Fig. 2.2**) (Zharikov et al. 2007; Kamenetsky et al., 2021). Within fenites and their associated intrusive rocks, other forms of localized metasomatic processes are also observed, such as auto-metasomatism in the peripheral parts of intrusions or contact metasomatism at the intrusion country rock interface, as is the case of Fuerteventura alkaline-carbonatite complex (Casillas et al., 2011; Carnevale et al., 2020).

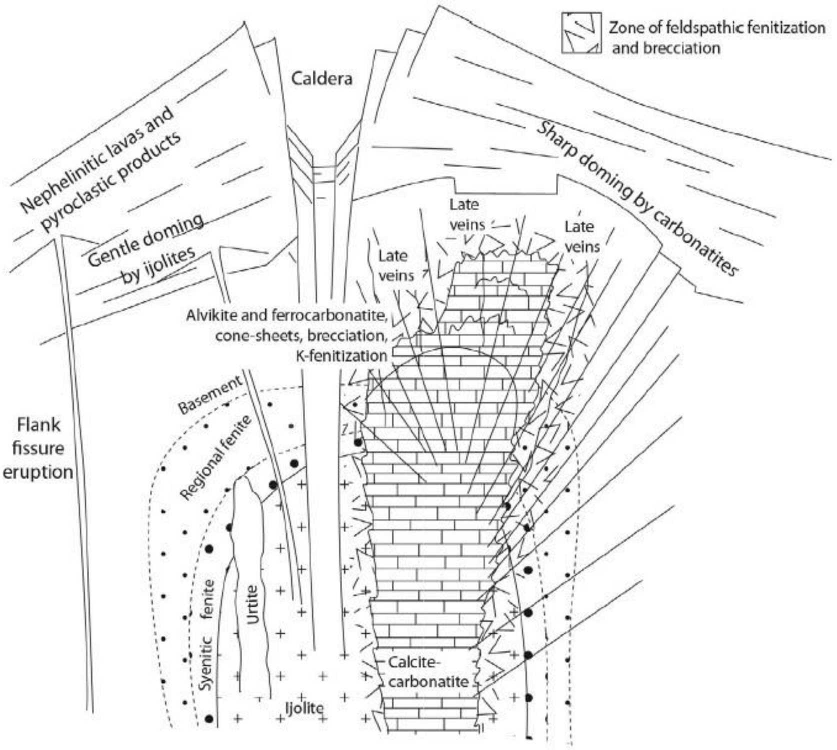

Fig. 2.2: Model of fenitization and brecciation associated with alkaline and carbonatitic magmas (from Elliott et al., 2018).

2.2 Petrological background

Carbonatite petrogenesis is still a debated topic and there are currently three main hypotheses explaining the origin of carbonatite melts, all being related to the formation of a primary carbonate melt derived from a carbonated mantle:

(1) **immisciblity** and **separation** from a CO_2-rich alkaline silicate melt (Brooker, 1998; Brooker and Kjarsgaard, 2011),

(2) **low-degree partial melting** of a carbonated mantle source (Wyllie and Huang, 1975; Wallace and Green, 1988; Wyllie and Lee, 1998),

(3) **late-stage** result of a **fractional crystallization** of a carbonated alkaline silicate melt (Lee and Wyllie, 1994; Veksler et al., 1998). Then, the mantle must coexist with a C-bearing phase, that under certain conditions of pressure, temperature, and fO_2, speciate either as fluid phase (CO_2) or solid phase (graphite, diamond, carbonates), at low P and medium-high oxidizing conditions and at higher P and increasingly high fO_2, respectively.

Normally, two different reference systems for carbonatite petrogenesis are considered, an ultramafic system (*i.e.*, peridotite) and a mafic system (*i.e.*, eclogite), both able to generate carbonatite melts.

2.2.1 Peridotite melting

It has been experimentally demonstrated that at pressures > 2 GPa (≈ 60 km depth) in presence of CO_2 volatile phase, CO_2 reacts with mantle minerals such as olivine, clinopyroxene and orthopyroxene, forming dolomite, substituted by magnesite in the sub-solidus region at pressure > 2.7 GPa (**Fig. 2.3**) (Dalton and Presnall, 1998a; Gudfinnsson and Presnall, 2005). Once carbon-bearing fluids react with mantle-wedge peridotites, a sort of COH-rich plume will form, containing low-density phases such as carbonates and carbonatitic melt. Their low density compared with the dry host peridotite can promote the upwelling of the metasomatized mantle, representing a carrier of carbon and a source of CO_2 from the slab to the upper mantle. Thus, together with COH fluids, carbonatitic melt represent the reservoir of volatiles in the mantle wedge (Tumiati et al., 2013). Hammouda and Keshav (2015) reported high-pressure experiments demonstrating that a relatively hot environment could favour both the survival of carbonate melt at shallow mantle depth and the emplacement of carbonatites at or near the surface.

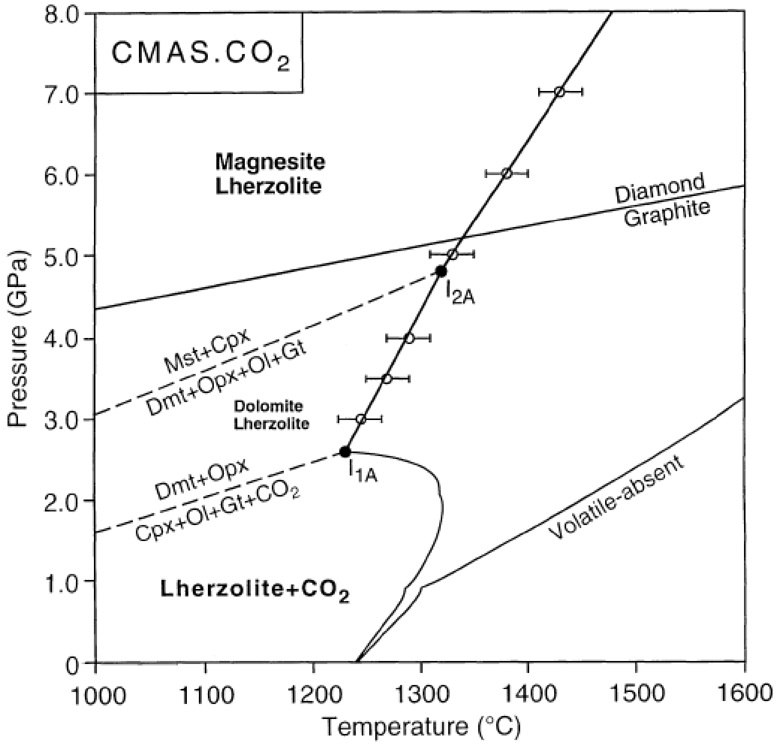

Fig. 2.3: P-T diagram with solidus curve for model carbonated lherzolite in the system CaO-MgO-Al_2O_3-SiO_2-CO_2 (from Dalton and Presnall, 1998a). Note the piercing point (invariant

in the CMAS-CO_2 system) at 2.2 GPa, where sub-solidus dolomite-in reaction intersects the carbonated solidus.

Carbonatite petrogenesis is also related to kimberlite- and melilitite-type melts. Indeed, a *continuum* between carbonatite and silicate melts has been experimentally documented by Dalton and Presnall (1998b), who showed the transition from carbonatite to kimberlite at 6 GPa, and by Moore and Wood (1998), who documented the transition from carbonatite to melilitite-type melts on the 3 GPa isobar. Hammouda and Keshav (2015), show that the transition from carbonatite to kimberlite (at $P > 4$ GPa) or melilitite (for $P < 4$ GPa) is a matter of degree of melting (**Fig. 2.4**). Therefore, the *continuum* of silica-undersaturated melts can result from melting of the same source if temperature and pressure are varied, where carbonatites can be formed by very low partial melting degrees of the order of 0.1%, whereas kimberlites and melilitites require melting degree around 1%. The carbonatitic melt reacts with orthopyroxene (*i.e.* the mantle mineral with the highest silica activity, $aSiO_2$) whose assimilation drives the melt towards more silicic compositions (**Fig. 2.5**), until reaching a kimberlitic melt composition ($SiO_2 > 18$ wt%), producing a massive exsolution of a CO_2-rich volatile phase that reduces magma density, increases buoyancy, and supports rapid and accelerating ascent (Russel et al., 2012). A detailed analysis of the role of the gas expansion in carbonatite magma ascent is described in the sub-sub-chapter 5.3.1. It is clear, therefore, that carbonatites can have multiple processes involved in their petrogenesis and complex evolutionary histories during their ascent to the surface (Yaxley et al., 2021).

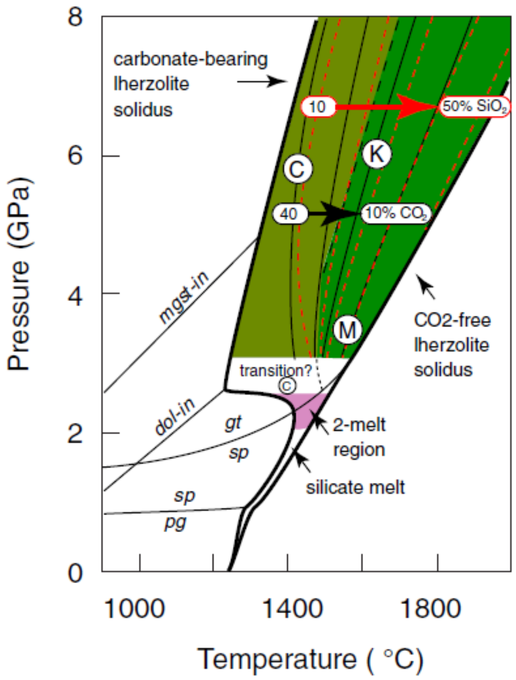

Fig. 2.4: P-T diagram with carbonatite–kimberlite transition during melting of model lherzolite + CO_2 (in the system CMAS–CO_2, after Dalton and Presnall, 1998a).

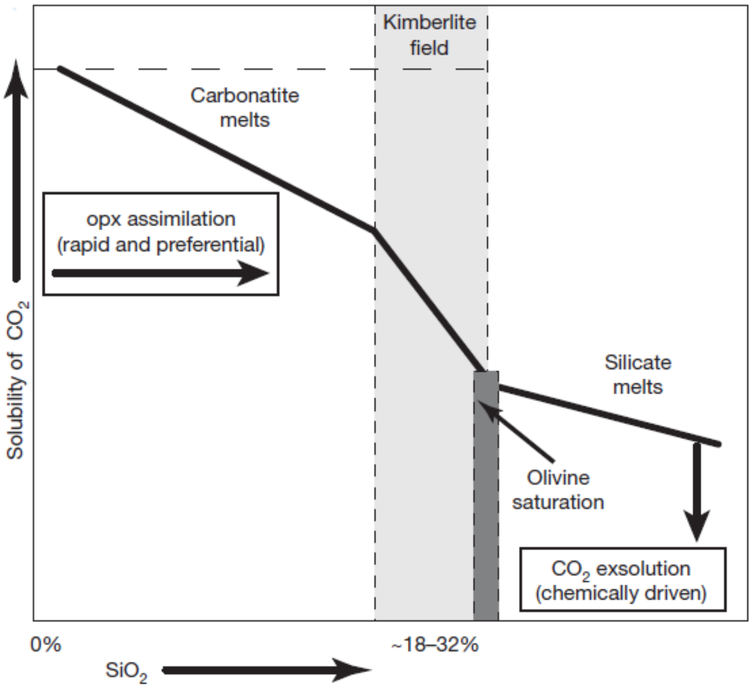

Fig. 2.5: Schematic model showing opx assimilation and the transition from carbonatitic melts to more silicic melts (from Russell et al., 2012).

2.2.2 Eclogite melting

For crustally emplaced carbonatites, carbonated eclogite as source it was proposed (Yaxley and Brey, 2004; Dasgupta et al., 2004). Indeed, calcio-dolomitic carbonatite liquids are likely to form from carbonated eclogites at upper mantle pressure–temperature conditions, providing ambient oxygen fugacity for carbonate stability (Yaxley and Brey, 2004). Moreover, subduction is likely to introduce carbonated eclogite to significant mantle depths (more than 300 km), where carbonated eclogite might expels a carbonatitic melt that can be captured into surrounding peridotite (Dasgupta et al., 2004), owing to the much higher solidus of carbonated peridotite (**Fig. 2.6**). Hypotheses invoking or supporting a possible derivation of carbonatites from the Earth’s crust (Ferrero et al. 2016), or from the mantle with some crustal contribution (Song et al. 2017), have also been proposed, emphasizing the importance of assimilation of sedimentary carbonates in carbonatite petrogenesis.

Recent studies also suggest the presence of a global carbonatite-rich layer under the oceanic lithosphere that is fed by subduction processes, and this layer can be the source of mechanical weakening of the lithosphere–asthenosphere boundary under the oceans, underlying the importance of carbonatite-rich melt, thought to be a possible candidate toward causing the seismically detected low velocity zone (LVZ) located at approximate depths of 70–150 km in the suboceanic mantle (Gaillard et al., 2008; Hammouda et al., 2015, 2020).

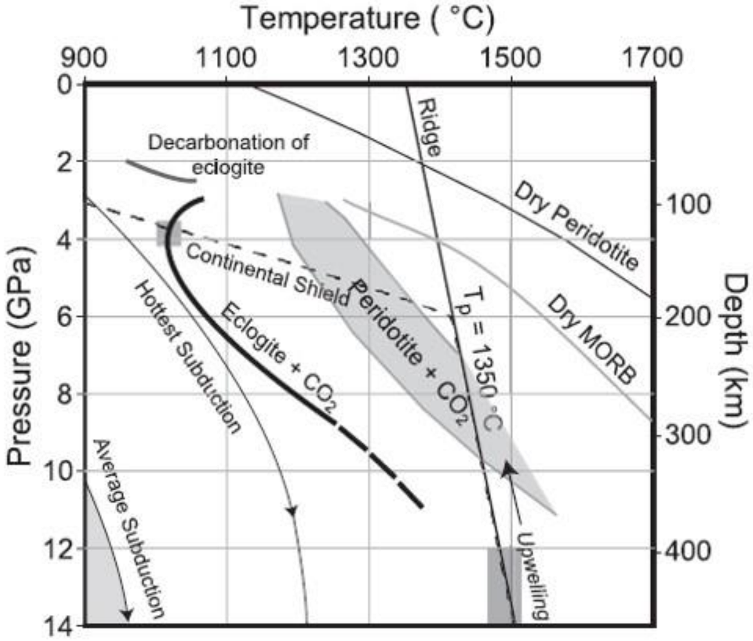

Fig. 2.6: A comparation between the carbonated eclogite solidus and the carbonated peridotite solidus (Dasgupta et al., 2004). Dry peridotite and MORB are also depicted for comparison (Dasgupta et al., 2004 and references therein).

2.3 Geochemical background

The extreme variability of rock-forming minerals in carbonatites (especially accessory and exotic minerals), together with several processes occurring in the route to the surface or in the source region, make the interpretation of chemical analyses of carbonatite rocks quite difficult. This is particularly verified with major and trace elements concentration in carbonatite rocks. The abundance of major oxides CaO, MgO and FeO in bulk rock compositions, not only depends on the carbonate minerals that characterized the carbonatite (calcite, dolomite, ankerite), but also essentially on the forsterite, pyroxene, mica-group minerals, apatite and magnetite content. On the contrary, Fe_2O_3, TiO_2 and P_2O_5 whole rock content is almost completely controlled by the presence of oxides and apatite (the most common accessory mineral in carbonatites).

Carbonatites contain very high concentration of incompatible trace elements, such as Ba, Sr, REEs, Th, U, Nb and in many cases this pattern is used to distinguish between carbonatite rocks and sedimentary carbonates (*e.g.*, Innocenzi et al., 2021), that have very low concentrations if compared with carbonatite concentrations (average concentrations Rb = 14 ppm; Sr = 7272 ppm; REE = 3731 ppm) (Chakhmouradian 2006). This enriched concentration in incompatible elements is often coupled with negative anomalies of Zr, Hf, and Ti, and this is typical of carbonatite in the garnet-peridotite stability field (Dasgupta et al., 2009). Most carbonatites show wide ranges of fractionation patterns, with $(La/Sm)_N$ = 4-100, and $(Gd/Yb)_N$ = 2-50 (Jones et al., 2013), although they generally depict steep patterns (*e.g.*, Carnevale et al., 2021). Normally, during the igneous fractionation stage (T >

600 °C), the principal early crystallising minerals are olivine, clinopyroxene, and magnetite, all of which exclude REEs from their crystal structures. Once the melts become carbonate-saturated and voluminous carbonatite cumulates form, the REEs are strongly enriched in the liquid owing to their incompatibility in calcite (Anenburg et al., 2021). Subsequently, during the brine-melt stage ($600 \leq T \leq 400$ °C), REEs are sufficiently concentrated in the residual brine-melt to form REE-minerals, such as monazite and alkali REE carbonates from the burbankite groups (Zaitsev et al., 2002). Finally, during the late-stage evolution of carbonatite system (hydrothermal stage), alkalis are removed and the original minerals are replaced by an assemblage of less-soluble REE-bastnäsite or monazite (Giebel et al., 2017). Low-temperature fluids, therefore, do not directly precipitate REE minerals but re-crystallise existing, highly soluble, alkali–REE-carbonates into less soluble, often calcic, phases. Thus, the main REE enrichment occurs during the brine-melt stage, but REEs can be mobilised on the local scale by low-temperature hydrothermal fluids with a process known as autometasomatism, resulting in further redistribution and concentration of the REEs (**Fig. 2.7**) (see Sub-Chapter 4.1 for further details about the role of hydrothermal fluids in REEs remobilization).

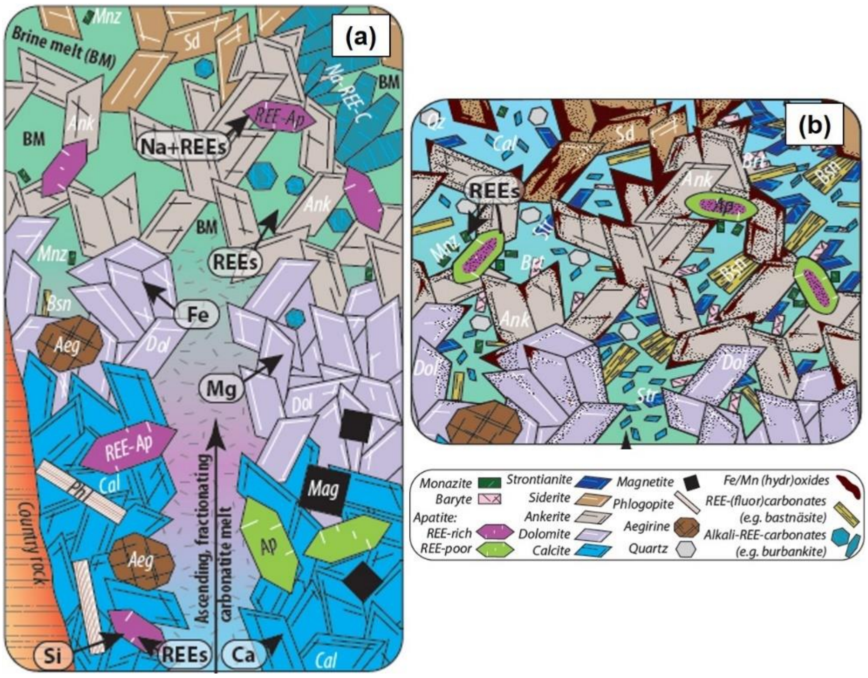

Fig. 2.7: Mineral fractionation and brine-melt formation (carbonatite melt progressively evolves to brine-melt composition) (a). Hydrothermal alteration where low-T fluid reacts with carbonatite rock and partial remobilization of REEs into REE minerals (b) (Anenburg et al., 2021).

Another important geochemical tool principally used to address the question from where the carbonatite magmas are derived (lithosphere or asthenosphere), is the isotope dataset. Normally, stable C and O isotopes are used to reconstruct the original magmatic fingerprint of the primary carbonatite. The C and O isotopic compositions of the carbonatite compositional field, the so-called "primary igneous carbonatite" box, range between 6% and 10% for δ^{18}O (SMOW) and between -4% and -8% for δ^{13}C (PDB) (Taylor et al., 1967; Sheppard and Dawson, 1973; Hoefs, 1987). Works on Oldoinyo Lengai (the only worldwide active volcano that erupts Na-carbonatitic magma) volcanic fresh products allowed to narrow the range of the C and O isotopic signature of primary igneous carbonatites (**Fig. 2.8**), and, although particular as natrocarbonatites, the range can be considered representative of undegassed and uncontaminated mantle compositions, with δ^{13}C values ranging from -5% to -7%, and δ^{18}O values ranging from 5.5% to 7% (Keller and Hoefs, 1995).

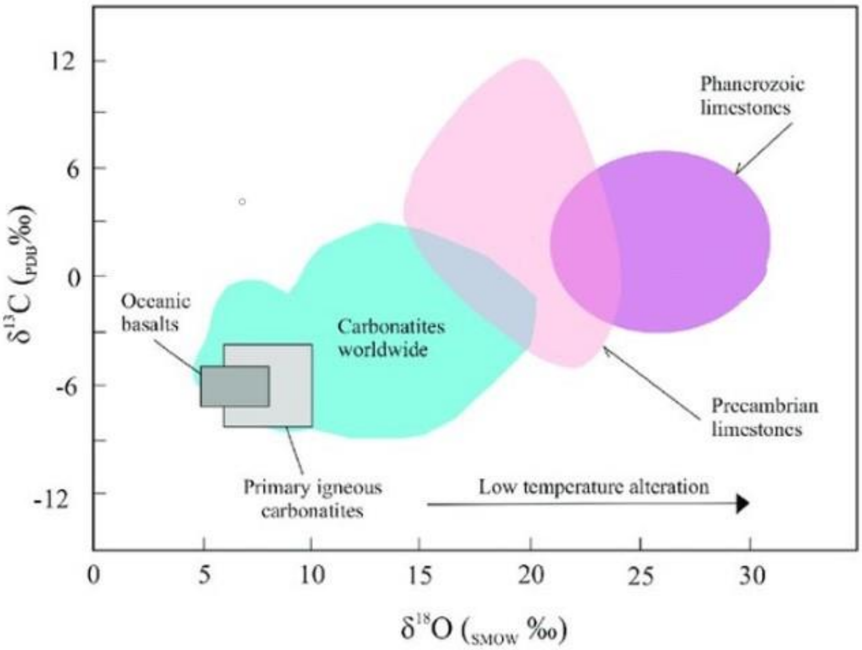

Fig. 2.8: Primary igneous carbonatites (***PIC***) and oceanic basalts (Deines, 1989; Keller and Hoefs,1995) fields with carbonatites from worldwide sources and limestones (Bell and Simonetti, 2010).

The Sr-Nd-Pb isotopic systematics have also been widely used to characterize the sources of carbonatites and the contribution of the different mantle end members involved in carbonatites petrogenesis (**Fig. 2.9**). Early Sr-Nd-Pb isotope studies pointed out the similarity between carbonatites and ocean island basalts (OIBs), suggesting that the majority of carbonatites were derived from relatively undepleted mantle sources dominated by high-μ isotopic component ($\mu = {}^{238}U/{}^{204}Pb$) and enriched mantle components (Bell and Tilton 2001, 2002). Generally, carbonatites are characterized by relatively radiogenic Nd and Hf and a non-radiogenic Sr isotope composition, and this is related to a depleted or slightly enriched mantle source (Bell and Simonetti, 2010; Jones et al., 2013). The isotopically enriched components have been variably interpreted as representing metasomatized continental mantle lithosphere or recycling of different sedimentary material located either within the convecting upper mantle or within the rising lower mantle plumes (Hoernle et al., 2002; Bell and Simonetti, 2010). As concerning the rare occurrences of carbonatite magmatism in oceanic environments, the presence of a delaminated sub-continental lithospheric mantle domain beneath the southern Cape Verde Islands was proposed, considering Cape Verde carbonatites derived from the melting of such a SCLM domain (Bonadiman et al., 2005; Martins et al., 2010). In the same way, the involvement of a SCLM in Fuerteventura carbonatites petrogenesis was also presented (Carnevale et al., 2021), although some geochemical differences between the two oceanic occurrences exist (see Sub-Chapter 4.1 for further details).

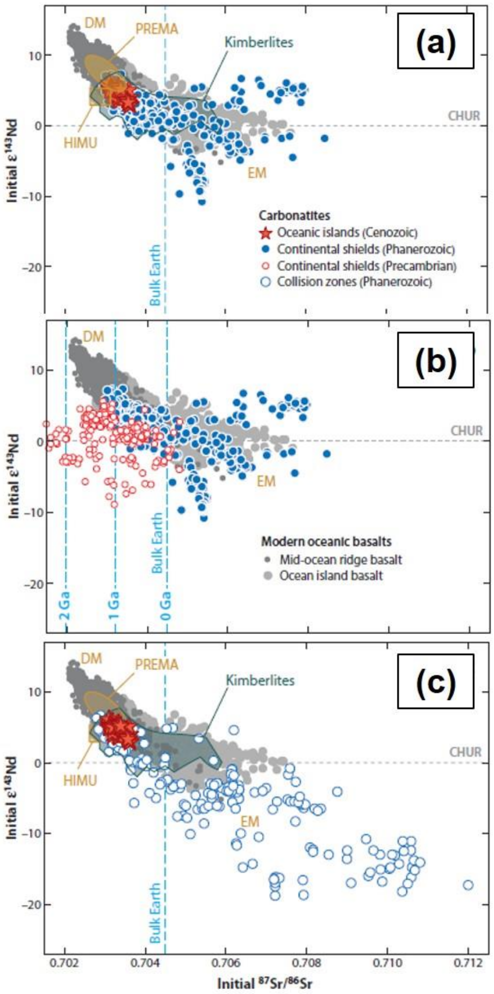

Fig. 2.9: Variations of Sr and Nd isotopic compositions for global carbonatites with focus on carbonatites from modern oceanic islands and Phanerozoic carbonatites from continental shield settings (a), on Phanerozoic and Precambrian carbonatites from continental shield settings (b), and on Phanerozoic carbonatites from continental collision zone settings (c) (Yaxley et al., 2022).

To further constrain the origin of carbonatites, the evolution of their mantle source, and the possible involvement of recycled sedimentary material, recent non-traditional isotope systems such as $^{44}Ca/^{42}Ca$ (Amsellem et al., 2020; Sun et al., 2021), $\delta^{11}B$ (Hulett et al., 2016), and $\delta^{34}S$ (Hutchinson et al., 2019), are increasingly explored (**Fig. 2.10**). Moreover, noble gases isotopes are also used in order to constrain the source of carbonatites, from the pioneering work of Sasada et al. (1997), up to the recent application on oceanic carbonatite magmatism (*e.g.*, Mata et al., 2010; Carnevale et al., 2021; Day and Hilton, 2020; Day, 2022).

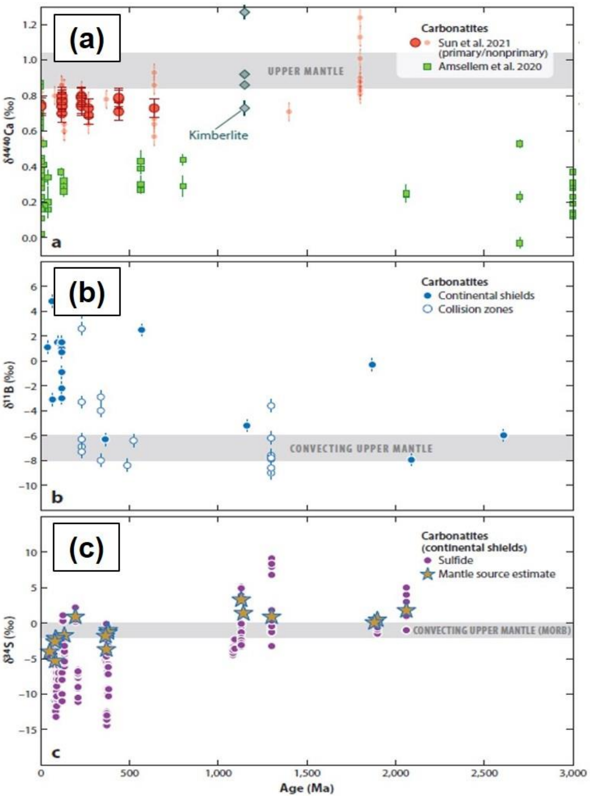

Fig. 2.10: Ca (a), B (b), and S (c) isotope compositions for a 3 Ga time span for carbonatites of different settings and age (Yaxley et al., 2022).

2.4 Carbonatite magmatism and geodynamic setting

Carbonatite magmatism is essentially related to intraplate continental tectonic settings characterized by significant extension and even rifting (Woolley and Kjarsgaard, 2008; Jones et al., 2013; Yaxley et al., 2022). However, carbonatites occur in a variety of tectonic settings (**Fig. 2.11**), such as stable intraplate areas (not associated with rifting), lithospheric highs, unconventional areas such as subduction zones (e.g., D'Orazio et al., 2007; Li et al., 2018; Lustrino et al., 2019, 2020), obduction zones (*e.g.*, Nasir et al., 2010) or rare oceanic contexts (*e.g.*, Doucelance et al., 2010; Mata et al., 2010; Schmidt and Weidendorfer, 2018; Carnevale et al., 2021). Thus, their occurrence is widely present in all continent (**Fig. 2.12**).

The oldest known carbonatite occurrence is the Mesoarchean 3.01 Ga Tupertalik (Greenland) carbonatite (Bizzarro et al., 2002), and currently the only active carbonatite volcano is Oldoinyo Lengai (Tanzania), characterized by a natrocarbonatitic affinity (*e.g.*, Berkesi et al., 2020). Thus, the emplacement of carbonatites is largely continuous from 3 Ga to the present, but the presence of carbonatite magmatism normally increases in number with time, with a major concentration of occurrences in post-Precambrian age with respect to Precambrian age (**Fig. 2.13**). This aspect may partially reflect also the preservation of the geological record through time, but recent studies point out how preservation is not the unique factor influencing the emplacement of carbonatites through time, and other factors such as the origin, the abundance and the cycle of carbon within the mantle, must be considered to explain the temporal variation of carbonatites. Indeed, the continued modification of the carbon budget of the mantle depends on the carbon subducted into the mantle and the carbon degassed from volcanoes, and the impact of the carbonatite magmatism on the global carbon cycle is beginning to be recognized. Carbonatite petrogenesis therefore require (i) very specific physico-chemical conditions within the asthenospheric and/or lithospheric modified mantle source in order to generate their low-degree melts (as resumed in the previous Sub-Chapter 2.2 and 2.3), and also (ii) favorable tectonic settings, facilitating their genesis and transport to the surface.

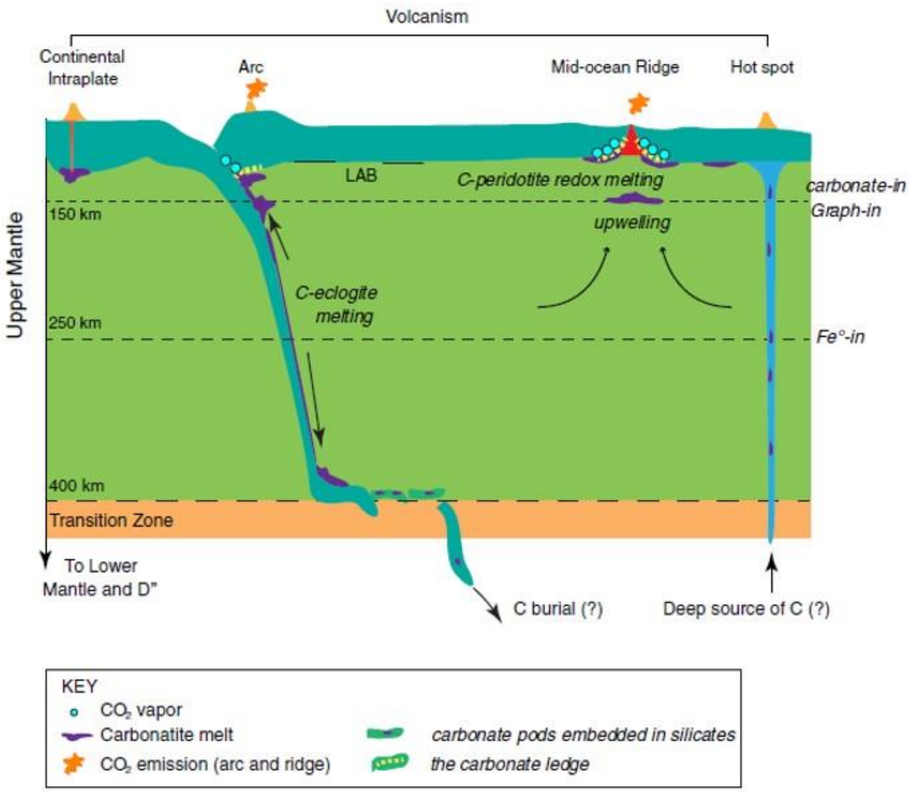

Fig. 2.11: Conceptual representation of the carbon geodynamical cycle and carbonatite genesis in different geodynamic settings (Hammouda and Keshav, 2015).

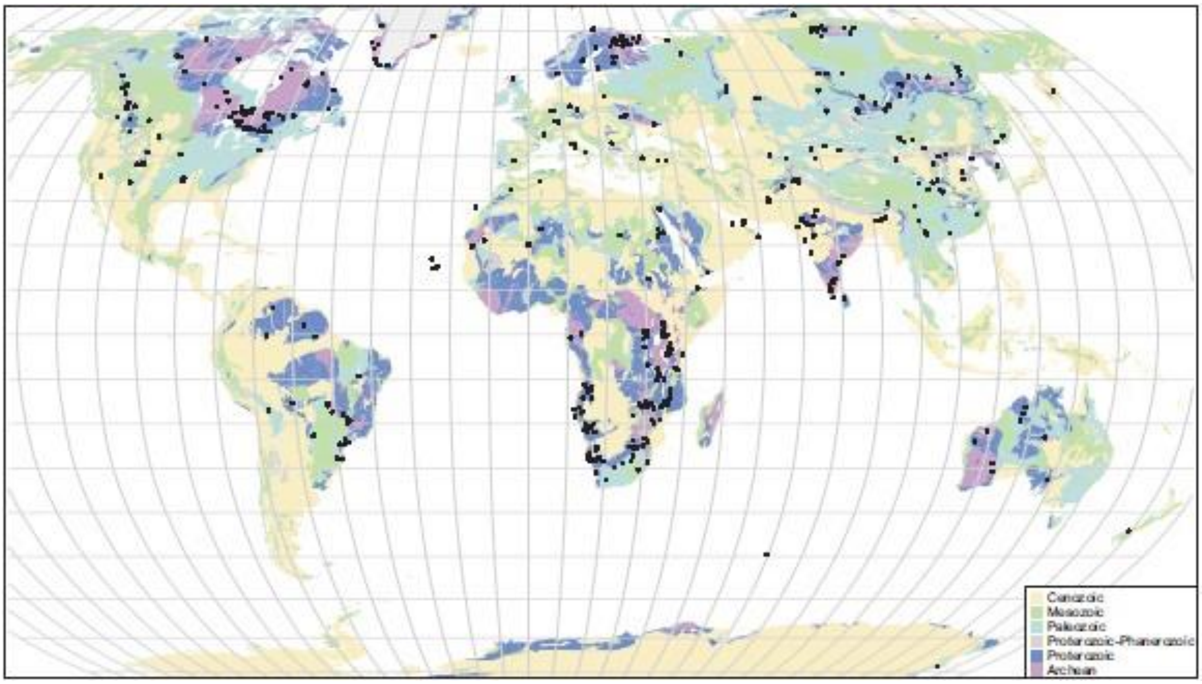

Fig. 2.12: Global distribution of carbonatites (Wooley and Kjarsgaard, 2008).

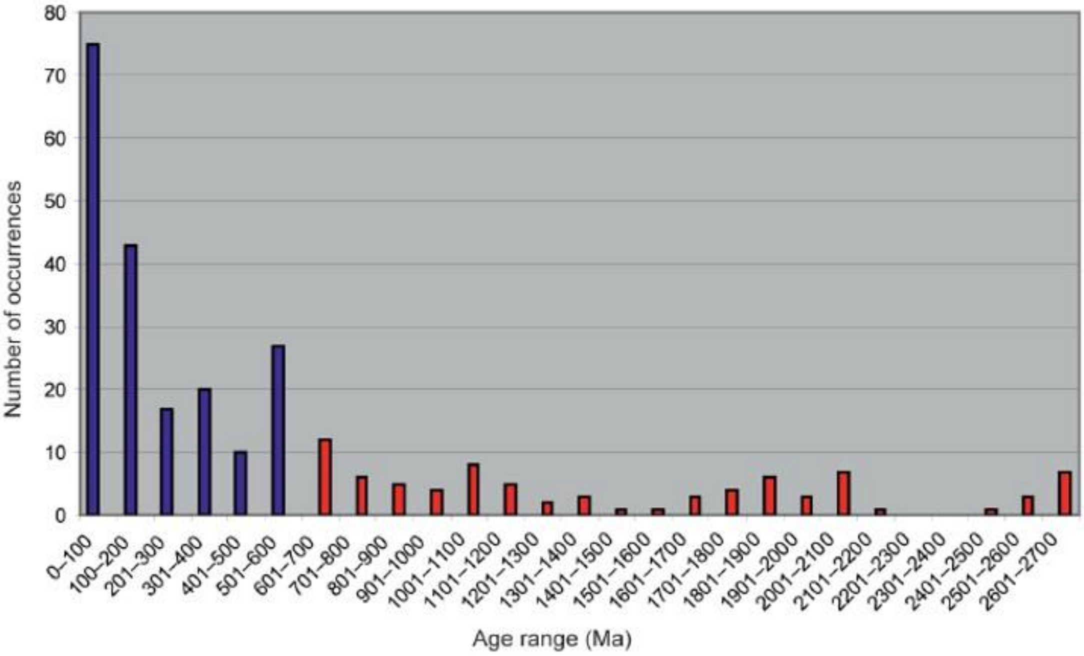

Fig. 2.13: Frequency of carbonatite eruptions plotted against age (Woolley and Bailey, 2012).

Chapter 3: Sampling sites and analytical methods

3.1 Sampling sites

The studied areas are essentially two (**Fig. 3.1**):

(1) the central-western sector of Fuerteventura Island (eastern part of Canary Archipelago),

(2) the area of Mt. Vulture volcano (southern Italy).

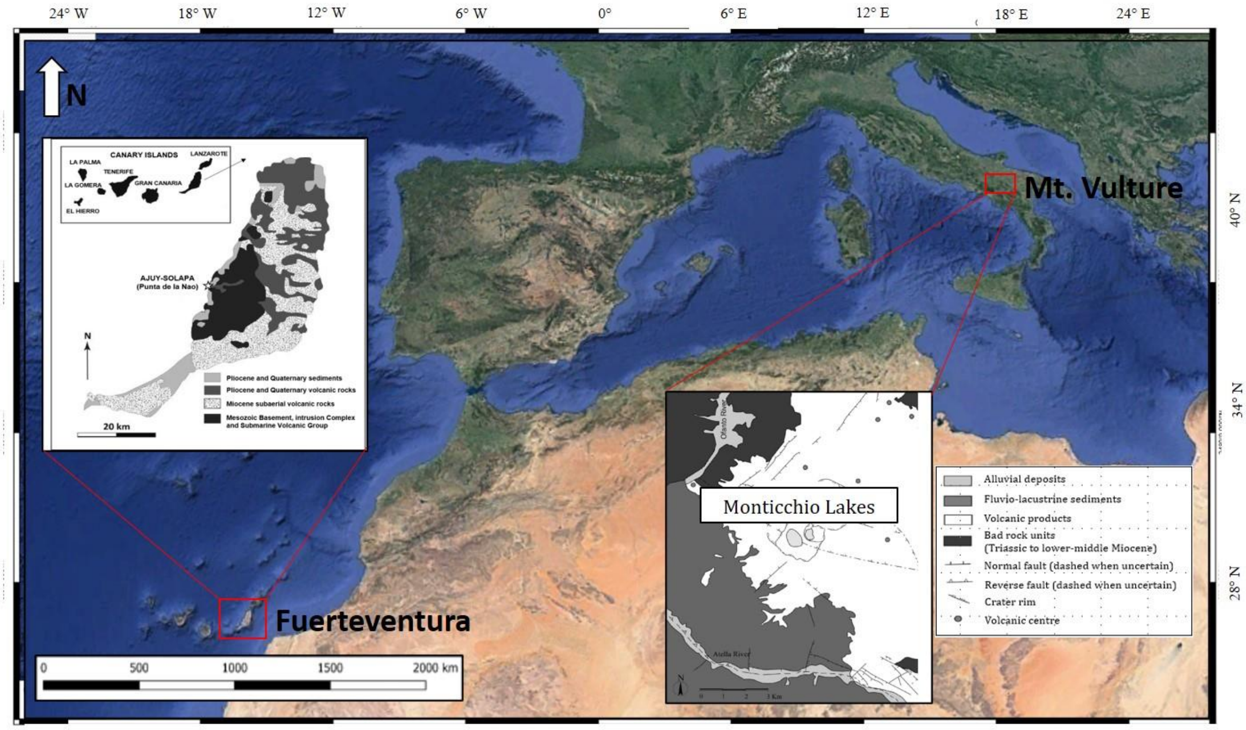

Fig. 3.1: Geographic location of the two studied areas.

(1) Although there are other exposures of the alkaline-carbonatite complex in **Fuerteventura** (*e.g.*, the north-western Montaña Blanca-Esquinzo sector), one of the main outcrops is in the central-western part of the island, along the coast (Ajuy-Solapa). The choice to sample carbonatite rocks from the Ajuy-Solapa (particularly from Punta de la Nao sector) is not only because it is one of the best-preserved outcrops, but also because carbonatite outcrops in Punta de La Nao escaped the thermal metamorphism overprint caused by the intrusion of a gabbroid-pyroxenitic series (Pájara Pluton), preserving the original igneous assemblage and textures. Thus, accordingly, in order to focus the study on well preserved carbonatite rocks, all samples studied here were collected from Punta de La Nao area (see Chapter 4 for geographic details of the outcrop). Fuerteventura carbonatites are intrusive Ca-carbonatites and they are always associated to undersaturated rocks such as *clinopyroxenites*, *melteijites-ijolites*, *nepheline-sienites* and *sienites*. The outcrops from which the studied samples were collected are shown in **Fig. 3.2**.

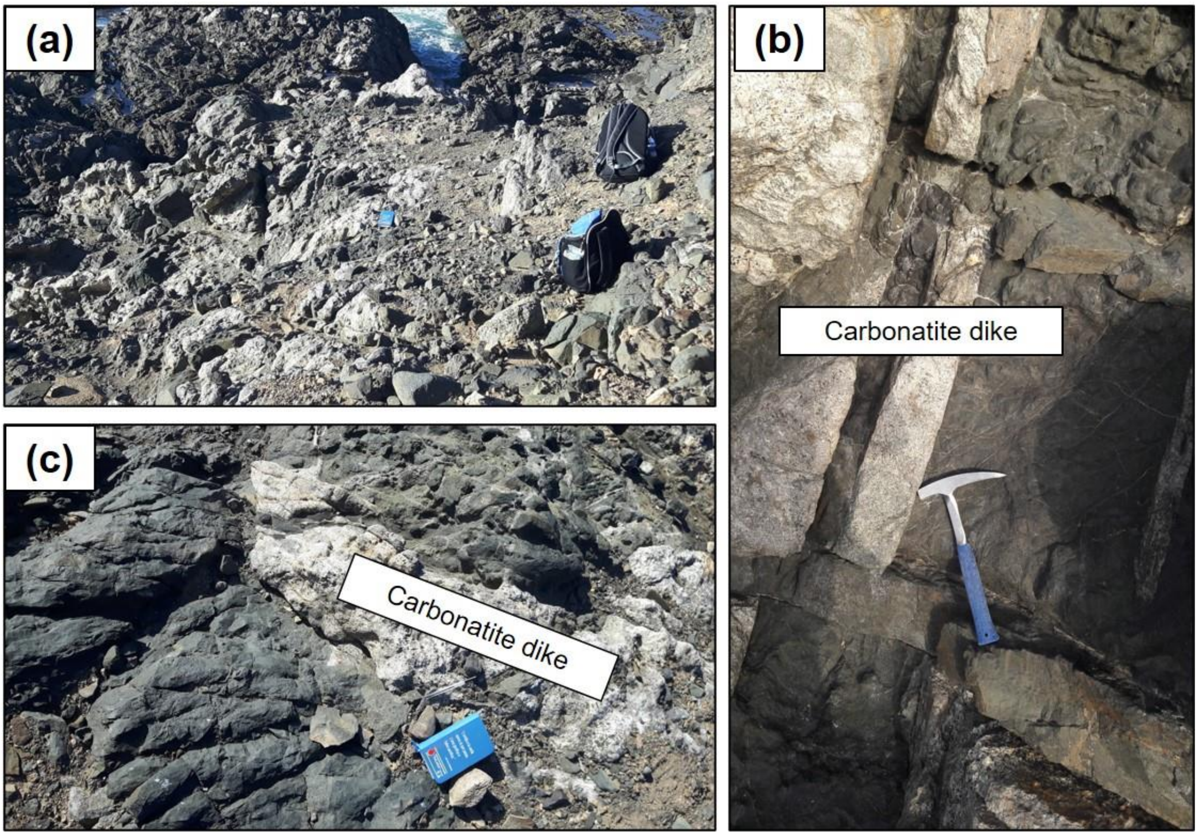

Fig. 3.2: Punta de la Nao outcrop (a) and details of Ca-carbonatite dikes (b and c) from Fuerteventura, Canary Islands.

(2) As regards the second investigated area of **Mt. Vulture** volcano, the outcrops from which the studied samples were collected are located in the Monticchio Lakes sector (Lago Piccolo and Lago Grande). The carbonatite magmatism from Mt. Vulture is essentially associated to the last eruptive activity of the volcano, and it is very different if compared with intrusive Fuerteventura carbonatite magmatism. Indeed, the carbonatitic affinity is mainly related to the presence of ash-rich tuff deposits with a melilitite-carbonatite matrix. In this case, the studied samples were collected from the melilitite-carbonatite matrix and from carbonatite-rich layers within the matrix. Furthermore, a robust amount of pelletal lapilli (enclosing mantle xenoliths), mantle xenoliths and loose (disaggregated) mafic xenocrysts from the melilitite-carbonatite matrix were also sampled in different sites (see Chapter 5 for detailed petrographic and chemical characterization of the samples). Part of the outcrops from which the melilitite-carbonatite matrix and carbonatite-rich layer with pelletal lapilli, mantle

xenoliths and loose mafic xenocrysts were collected are shown in **Fig. 3.3**. Details of studied samples and related GPS coordinates are described in **Table 1**.

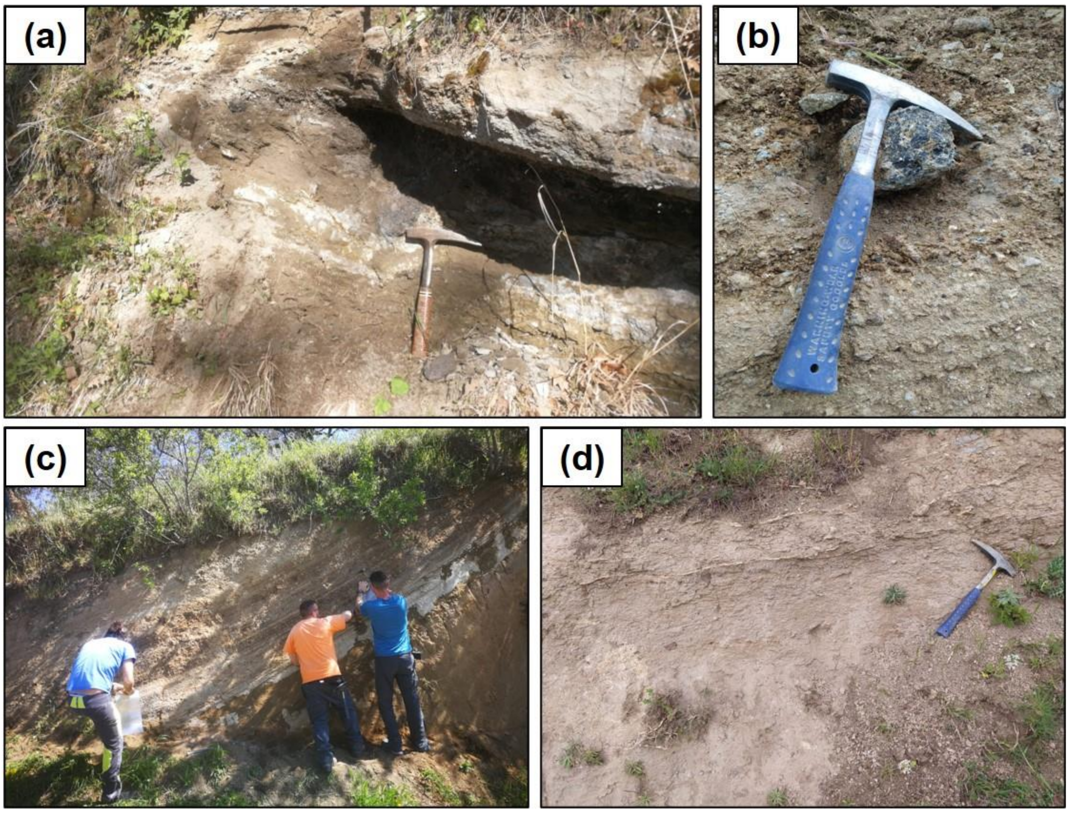

Fig. 3.3: Ash-rich tuff deposit (a) and detail of a mantle xenolith (b). Sampling of loose material (c). Detail of ash-rich tuff deposit with carbonatite-rich layers (d). All sampling site belong to the Monticchio Lakes Syntheme (140 ka).

Table 1. Sites of studied samples with geographic coordinates.

Site	**Sample**	**Latitude**	**Longitude**
Fuerteventura (Canary Islands)			
Ajuy-Solapa	carbonatite dikes	28°23'12.04" N	14°09'44.11" W
Ajuy-Solapa	clinopyroxenite host	28°23'12.10" N	14°09'44.23" W
Ajuy-Solapa	carbonatite dikes	28°23'30.28" N	14°09'41.42" W
Mt. Vulture (southern Italy)			
Monticchio (Lago Piccolo)	pelletal lapilli	40°55'12.83" N	15°36'37.80" E
Monticchio (Lago Piccolo)	mantle xenoliths	40°55'12.83" N	15°36'37.80" E
Monticchio (Lago Grande)	carbonatite-rich layer	40°57'16.84" N	15°34'57.32" E
Monticchio (Masseria Cuscito)	mantle xenoliths	40°57'16.85" N	15°34'53.60" E

3.2 Analytical methods

3.2.1 Scanning Electron Microscopy (SEM-EDS) and Electron Microprobe Analyses (EMPA)

All mineral chemical composition of studied sample was determined by different SEM-EDS equipment. Samples from Fuerteventura were analysed by a JEOL JSM-820 scanning electron microprobe operating at 20 kV accelerating voltage and in the range of 0.1-10nA beam current, at the Universidad Complutense de Madrid. Samples from Mt. Vulture were analysed by a (i) CAMECA SX100 electron microprobe, at the Observatoire des Sciences de l'Univers (UPMC-INSU) (Paris, France), operating at 15 kV accelerating voltage and a 20nA beam current, and by a (ii) JEOL JXA-8200 electron microprobe at the Istituto di Geofisica e Vulcanologia (INGV, Rome), operating at 15 kV accelerating voltage and a 7nA beam current with a beam spot size of 1 µm. Natural standards were used for calibration.

3.2.2 X-Ray Diffraction (XRD)

The X-ray diffraction technique was essentially used to study the presence of hydrothermal mineral association within Fuerteventura carbonatites, in order to detect possible fluid/rock interaction between the carbonatite rock and hydrothermal fluids (meteoric/sea water or fluids from autometasomatism processes). The analyses were made by a BRUKER D8 Advance at the Universidad Complutense de Madrid, equipped with an X-ray source with a high stability copper anode, and an energy dispersion SOL-X detector with a large active area for X-ray diffraction, and operating between 2 and 35° 2θ (0.02°/s), and analysing the fraction < 0.5 µm and < 2 µm (with the standard procedure of the oriented clay mineral mounts).

3.2.3 Laser Ablation Inductively Coupled Plasma Mass Spectrometry (LA-ICP-MS)

Trace elements composition of the minerals and rocks from Fuerteventura carbonatites was analysed at the Istituto di Geofisica e Vulcanologia (INGV, Palermo) using a GeoLasPro 193nm ArFExcimer laser ablation (LA) system, connected to an Agilent 7500ce quadrupole ICP–MS. The analyses were performed with a constant laser repetition rate of 10 Hz, a fluency of 14-15 J/cm^2, a He flux of about 0.8 L/min in the ablation cell and a 32-44µm spot. Glass reference material NIST612 was used as external standard for all the clinopyroxene and apatite minerals whereas for calcite minerals was used the Microanalytical Carbonate Standard MACS3.

3.2.4 Microthermometry

Fluid Inclusions (in both Fuerteventura and Mt. Vulture samples) were studied in doubly-polished wafers and single mineral grains by a LINKAM THMSG 600 microscopic heating/cooling stage hosted at the Instituto de Vulcanologia e Avaliação de Riscos (IVAR, Ponta Delgada, Portugal).

Loose xenocrysts samples were embedded in epoxy resin and doubly polished to a thickness of 100-80 µm. The stage was cooled with liquid nitrogen and calibrated using a single standard crystal of quartz with pure H_2O and CO_2 inclusions. In order to minimize the effect of metastable transformations during cooling, very common in fluid inclusions, melting and homogenization temperatures were determined during heating at the minimum rate (1 °C/min). For CO_2-rich inclusions of Mt. Vulture samples (H_2O:CO_2 ratio = 1:10), densities were firstly calculated on the basis of the equation provided in Sterner and Bodnar (1991) and finally corrected according to Hansteen and Klügel (2008), while isochore trajectories/curves were calculated using the software "Fluids" (Bakker, 2003).

3.2.5 Noble gases (He, Ne, Ar)

Noble gases isotopic analyses were carried out at Istituto Nazionale di Geofisica e Vulcanologia (INGV, Palermo). Samples have been cleaned in acetone and millipore water by using an ultrasonic bath, and the portion of the selected sample material has been loaded into a stainless-steel crusher baked for 48-72 h at 120 °C in order to achieve ultra-high-vacuum conditions (10^{-9} mbar). Fluid inclusions from minerals were released by a single-step crushing performed at 250 bar (in-vacuum). Noble gases were separated from the other volatiles by using a "cold finger" immersed in liquid nitrogen (T= -196 °C) that allows freezing H_2O and CO_2 and successively were further cleaned in an ultra-high vacuum (10^{-9}-10^{-10} mbar) purification line, and all the species of the gas mixture, except noble gases, were removed using four getters. Helium (^{3}He and ^{4}He) and neon (^{20}Ne) isotopes were measured separately by two different split-flight-tube mass spectrometers (Helix SFT-Thermo). The analytical uncertainty of He isotopic ratio is $\leq$ 6%, while that of $^{20}Ne/^{22}Ne$ is < 0.17%. The Ne isotope ratios are corrected for isobaric interferences at m/z values of 20 ($^{40}Ar^{2+}$) and 22 ($^{44}CO_2^{2+}$). Argon isotopes (^{36}Ar, ^{38}Ar and ^{40}Ar) were analysed by a multi-collector mass spectrometer (GVI Argus), with an analytical uncertainty < 0.14%. The uncertainty in the determinations of He, Ne, and Ar elemental contents was less than 0.1%.

3.2.6 Mössbauer spectroscopy and Micro-transmittance Fourier transform infrared (FTIR) spectroscopy

Mössbauer spectroscopy analyses were performed at the European Synchrotron Radiation Facility (ESRF, Grenoble, France) by Stagno V. and Marras G. in the framework of a common research project. Single crystals of 20-30 µm each of Vulture mantle xenoliths were measured using in situ SMS technique (Mikhailenko et al., 2020), recently implemented with an X-ray beam focused on an area of 8x3 μm^2. Spectra were fitted through a full transmission integral with a normalized Lorentzian-squared source lines shape using MossA software package (Prescher et al., 2012).

FTIR measurements on the olivine host were performed at the SISSI beamline of the ELETTRA synchrotron (Trieste). This beamline is equipped with a FTIR spectrometer coupled to collimated infrared radiation produced by the synchrotron light. This kind of set-up provides a high spatial resolution, aperture of 20 µm and excellent signal/noise ratio, impossible to be developed with a laboratory FTIR spectrometer, allowing transects and grids to detect OH- bands absorption through minerals. The data were collected using a Vertex 70V Bruker interferometer coupled with a conventional Globar infrared source, a Hyperion IR microscope and a mercury cadmium telluride (MCT) detector to focus and resolve the areas of interest in the full spectral range. Spectra collected in transmission mode with a resolution of 2 cm^{-1} and an aperture of 40 µm. A total of 4 spectra were acquired. Signal was averaged three times for 128 scans (128 seconds) on each measurement spot. Air spectra were collected as a reference.

Chapter 4: Oceanic carbonatites: the case study of Fuerteventura (Canary Islands)

Here is presented a recently published paper (Carnevale et al., 2021) dealing with the geochemical characteristics of the oceanic carbonatites with inferences on their mantle source. Preliminary study on iron isotope compositions of carbonatite rocks is also introduced. Moreover, an abstract of two other published paper dealing with the characterization of the importance of post-magmatic processes in which the infiltrating fluids play an important role in the transport and concentration of REEs, with the formation conditions of these fluids is presented.

4.1 An Overview of the Geochemical Characteristics of Oceanic Carbonatites: New Insights from Fuerteventura Carbonatites (Canary Islands) (paper published in *Minerals*)

Authors: Gabriele Carnevale [1], Antonio Caracausi [2], Alessandra Correale [2], Laura Italiano [1] and Silvio G. Rotolo [1,2]

[1] Dipartimento di Scienze della Terra e del Mare (DiSTeM), Università degli Studi di Palermo, Via Archirafi, 22, 90123, Palermo, Italy; laura.italiano29@gmail.com (L.I.); silvio.rotolo@unipa.it (S.G.R.)

[2] Istituto Nazionale di Geofisica e Vulcanologia (INGV), Via Ugo la Malfa, 153, 90146, Palermo, Italy; antonio.caracausi@ingv.it (A.Ca.); alessandra.correale@ingv.it (A.Co.)

Abstract: The occurrence of carbonatites in oceanic settings is very rare if compared with their continental counterpart, having been reported only in Cape Verde and Canary Islands. This paper provides an overview of the main geochemical characteristics of oceanic carbonatites, around which many still debates exist regarding their petrogenesis. We present new data on trace elements in minerals and whole-rock, together with the first noble gases isotopic study (He, Ne, Ar) in apatite, calcite and clinopyroxene from Fuerteventura carbonatites (Canary Islands). Trace elements show a similar trend with Cape Verde carbonatites, almost tracing the same patterns on multi-element and REE abundance diagrams. ^{3}He/^{4}He isotopic ratios of Fuerteventura carbonatites reflect a shallow (sub-continental lithospheric mantle, SCLM) He signature in their petrogenesis, and they clearly differ from Cape Verde carbonatites, in which fluids from a deep and low degassed mantle with a primitive plume-derived He signature are involved in their petrogenesis.

Introduction

Carbonatites are rare carbonate-rich rocks of igneous origin, with more than 50 % modal carbonates (Le Maitre et al., 2002). Alkaline-carbonatite complexes are considered one of the main sources of critical metals for key economic sectors in heavily industrialised countries, and their occurrence is almost exclusive in continental region (Wolley and Kjarsgaard, 2008), while in oceanic settings carbonatites are very rare and they are limited to only two occurrences in the western side of Atlantic Ocean just in front of the African coasts: at Cape Verde Archipelago and Fuerteventura Island (Canary Archipelago).

Carbonatite petrogenesis is still a debated topic and three petrogenetic processes have been variably proposed, all being related to the formation of a primary carbonate melt derived from a carbonated mantle (Jones et al., 2013): (1) low-degree partial melting of a carbonated mantle source (Wallace and Green, 1988; Wyllie and Huang, 1975; Wyllie and Lee, 1998); (2) immiscible separation from a CO_2-rich alkaline silicate melt (Brooker, 1998; Brooker and Kjarsgaard, 2011), and (3) late stage result of a fractional crystallization of a carbonated alkaline silicate melt (Lee and Wyllie, 1994; Veksler et al., 1998; Wyllie and Lee, 1998).

The nature of the mantle that sourced the oceanic carbonatites (shallow convective mantle vs. a deep-seated mantle reservoir, plume-type) is still a debated issue. More in details a shallow origin for oceanic carbonatites was suggested for some oceanic carbonatites (Doucelance et al., 2010), with the plume contribution limited to be a thermal input, a trigger for low-degree partial melting at the base of oceanic lithosphere. A thickened and metasomatized oceanic lithosphere is needed (Doucelance et al., 2014), and a relatively hot environment could favour both the survival of carbonate melt at shallow mantle depths and the emplacement of carbonatites at or near the surface (Hammouda et al., 2014), at the same time becoming more calcic with respect to primary dolomitic melts (Dalton and Wood, 1993; Hammouda et al., 2014). In addition, the role of the carbonated eclogite for deep global cycling of carbon and potential source for carbonatites is also recognized (Dasgupta et al., 2004; Hammouda, 2003; Yaxley and Brey, 2004). Other models proposed for the petrogenesis of oceanic carbonatites involve either the contribution of marine carbonates recycled via subduction (Doucelance et al., 2014, 2010; Hoernle et al., 2002) or contribution of primordial carbon (de Ignacio et al., 2012, 2006; Mata et al., 2010).

An increasing number of multi-isotopic studies (C-O-Sr-Nd-Pb) tackled the petrogenesis of oceanic carbonatites and the characterization of their mantle source (de Ignacio et al., 2012, 2006; Doucelance et al., 2014, 2010; Hoernle et al., 2002; Hoernle and Tilton, 1991; Mourão et al., 2012), and more recently, additional constraints were placed by the noble gases isotopes (Mata et al., 2010). Indeed, their properties (such as large mass range, high volatility and chemical inertia) make noble gases geochemical tracers of primary importance (Allègre, 1987; Porcelli and Wasserburg, 1995; Zindler and Hart, 1986) to investigate mantle heterogeneity and degassing and mantle-crust interaction processes occurring in the volcanic plumbing systems (e.g. crustal assimilation). Despite their important role and potential significance for deciphering carbonatite genesis, there are no previous studies of noble gases isotopes on Fuerteventura carbonatites. On the contrary, noble gases isotopes on Cape Verde carbonatites are widely studied (Mata et al., 2010), also because carbonatite outcrops are present in at least 6 of the 10 Cape Verde Islands (S. Vicente, S. Nicolau, Maio, Santiago, Fogo and Brava), while on Canary Islands carbonatites occur only on Fuerteventura (the easternmost island of the Canary Archipelago). Mata et al. (2010) recognized the presence of fluids from a deep and low degassed mantle (He isotopic ratios higher than the typical MORB mantle values of 8 ± 1 Ra) on Cape Verde carbonatites (Mata et al., 2010), supporting a deep-rooted mantle plume in the region as inferred by geophysical investigations (Montelli et al., 2006; Zhao, 2007), however it is not necessarily so as helium mantle signature can be easily survived during contribution of hydrothermal fluids that can introduce surface-related noble gases, nitro-gen and also CO_2. These evidences support the presence of a no recycled carbon in the genesis of the Cape Verde carbonatites.

The aim of this paper is firstly to summarize the geological, petrological and geochemical background of the two oceanic carbonatite complexes (Fuerteventura and Cape Verde) in order to discuss analogies and differences. We also integrate the literature data (trace elements and C-O-Sr-Nd-Pb-He-Ne-Ar isotopes) with new geochemical data from Fuerteventura, which include major and trace elements determinations on whole-rock samples and minerals and also the first noble gases (He, Ne, Ar) isotopic analysis on Fuerteventura carbonatites. Data are discussed all together in order to add some new constraints on the origin of Fuerteventura carbonatites and further characterize their mantle source. We also briefly discuss the possible future research directions to better address the petrogenesis of carbonatites in such rare and particular geodynamic settings.

Geological and geochemical background

Regional geology

Fuerteventura (Canary Islands)

The volcanism of the Canary Archipelago is located 100 km off the northwestern African continental margin (Figure 1a). The age of the oceanic crust beneath Canary Islands is constrained by the 175 Ma S1 magnetic anomaly separating the easternmost Canary Islands and northwest Africa and the 156 Ma M25 magnetic anomaly separating the westernmost islands of La Palma and Hierro (Hoernle, 1998; Klitgord and Schouten, 1986; Roeser, 1982; Roest et al., 1992). The Moho depth decreases from west to east (i.e. towards Africa), varying in depth from approximately 12 km beneath

El Hierro and La Palma to 20-30 km beneath Lanzarote and Fuerteventura (Martinez-Arevalo et al., 2013). Therefore, Fuerteventura is located on a transitional oceanic to continental crust.

Among all the Canary Islands, Fuerteventura is the only one where the various phases of submarine formation, transitional phases and subaerial growth are better recognized (Ancochea et al., 1996; Balogh et al., 1999; Coello et al., 1992; Fernández et al., 2006; Fúster et al., 1968; Gutiérrez et al., 2006; Le Bas et al., 1986; Muñoz et al., 2005; Steiner et al., 1998; Stillman et al., 1975). This volcanic island consists essentially of Mesozoic sediments, Oligocene submarine volcanic complexes, late Oligocene transitional volcanic complexes, Miocene subaerial basaltic and trachytic lava flows, ultramafic, mafic to felsic intrusive rocks and carbonatitic dyke swarms (Ancochea et al., 1996; Gutiérrez, 2000; Gutiérrez et al., 2006). These intrusives and carbonatitic dyke swarms, with the submarine, transitional and earliest subaerial complexes and their associated plutonic bodies, form a lithostratigraphic unit known as the Basal Complex.

Carbonatites and closely associated alkaline-rich-silica undersaturated rocks (clinopyroxenites, melteijites-ijolites, nepheline-sienites and sienites) form a typical alkaline-carbonatitic association, outcropping in the central western part of the island, in an almost continuous NE-SW direction parallel to the coast. This association represents the first Magmatic Episode during upper Oligocene (≈25 Ma) (Muñoz et al., 2005), subsequent to the Submarine and early Transitional Volcanic Episodes. The main exposures of the alkaline-carbonatitic association are the northwestern Montaña Blanca-Esquinzo sector and the central-western Ajuy-Solapa sector (Figure 1b). The Early Miocene intrusion of a gabbroid-pyroxenitic series (Pájara Pluton) after the emplacement of the alkaline-carbonatitic complex, produced bands of thermal metamorphism on host rocks up to 1 km of lateral extension (Hobson et al., 1998), thus the original igneous mineral assemblage within the contact zone was variably overprinted and substituted with a metamorphic association composed of wollastonite, monticellite, diopside, vesuvianite, garnet, calcite, perovskite, alabandite, pyrrhotite and Nb-Zr-Ca silicates (e.g. cuspidine-niocalite-baghdadite series) (Casillas et al., 2011). Nevertheless, carbonatite outcrops in Punta de La Nao (Ajuy-Solapa sector) escaped this thermal overprint and preserve their original igneous assemblage and textures (Carnevale et al., 2020). Accordingly, in order to focus the study on well preserved carbonatite rocks, all samples studied here were collected from Punta de La Nao area (Figure 1b).

After the Miocene subaerial volcanic activity, a period of quiescence occurred until Pliocene, where a renewed volcanic activity produced some basaltic volcanoes in the northern part of the island (Coello et al., 1992). During Plio-Quaternary, alluvial and aeolian complexes were also generated (Zazo et al., 2002).

Cape Verde Archipelago

The Cape Verde Archipelago is located 500 km off the Senegalese coast (Figure 1a). The lithospheric crust beneath the islands is constrained by 140 Ma M16 and 120 Ma M0 magnetic anomalies (Williams et al., 1990). In the same way as Canary Archipelago, crustal thickness beneath Cape Verde Islands is also anomalously high (up to 22 km), and this is mainly due to magmatic transfer from upper mantle to shallow (i.e. crustal) accumulation levels (Lodge and Helffrich, 2006), although between the islands of the archipelago the crustal thickness decreases considerably to ca 7 km (Pim et al., 2008). Plume activity beneath Cape Verde Archipelago is supported by tomographic studies, which show the evidence of a P-wave negative anomaly down to about 1000 km, that includes Azores and Canary plumes apparently reaching the core-mantle boundary (Montelli et al., 2006).

The archipelago is composed of ten major islands, which can be divided into two groups: (i) northern Islands (S. Antão, S. Vicente, S. Luzia, S. Nicolau, Sal and Boavista) and (ii) southern Islands (Brava, Fogo, Santiago and Maio).

The lack of a simple age progression of volcanism at Cape Verde Archipelago reflects that the archipelago is located close to the rotation pole of the slowly drifting African Plate (Holm et al., 2008). The oldest exposed magmatic rocks related to Cape Verde hot spot volcanism occur at Sal Island, that preserves a magmatic history ranging from 25.6 Ma to 0.6 Ma (Torres et al., 2010), although a 40Ar-39Ar study limits the volcanic evolution for Sal Island from around 15 Ma to 1.1 Ma (Holm et al., 2008). Indeed, several age determinations studies on Cape Verde Islands suggest that most of the volcanic activity took place from 16 Ma until the present (Ancochea et al., 2010; Holm et al., 2008; Huertas et al., 2006; Mitchell et al., 1983; Plesner et al., 2003), such as the volcanic activity on S. Vicente (6.6 Ma to 0.3 Ma), on S. Antão (7.5 Ma to 0.1 Ma), on Maio (12 Ma – 7 Ma) or on Fogo (Quaternary to the present). Currently, at least three islands of the Cape Verde Archipelago are considered volcanically active (S. Antão, Brava and Fogo), with the latest historical eruptions occurred on Fogo Island, with the 1995 and 2014 events (Mata et al., 2017).

Cape Verde magmatism is strongly alkaline, as testified by the occurrence of nephelinitic and melilititic rocks in several islands, and all volcanic rocks are silica-undersaturated, with basanites, tephrites and nephelinites representing the most dominant compositions (Duprat et al., 2007; Holm et al., 2006). Carbonatites occur in 6 out of 10 islands (S. Vicente, S. Nicolau, Maio, Santiago, Fogo and Brava) (Figure 1c) and they are grouped into two main types: (i) Ca-carbonatites (the most dominant type) and (ii) Mg-carbonatites. S. Vicente presents the largest exposed carbonatites which occur either as intrusive or extrusive type (de Ignacio et al., 2012), similarly to Brava Island (Mourão et al., 2010). Carbonatites on Fogo Islands occur in the basement and they are all coarse-grained Ca-carbonatites (sövite), while on Santiago and Maio are present also Mg-carbonatites (Hoernle et al., 2002). Carbonatites on the Secos islets near Brava Island and on S. Nicolau Island were also described (Kogarko, 1993).

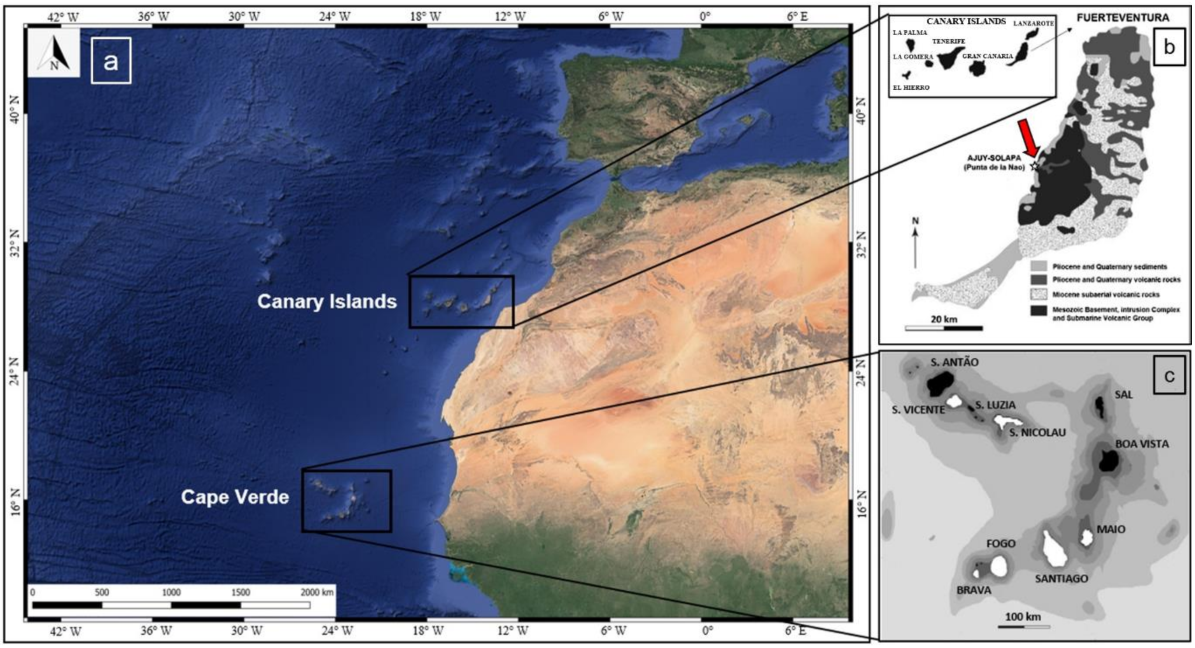

Figure 1. (a) Canary Islands and Cape Verde Archipelago in their geographic contest. (b) Simplified geology map of Fuerteventura showing the location of carbonatite studied samples (red arrow) (modified from Sagan et al., 2020) and (c) detail of Cape Verde Archipelago, where the islands in which carbonatites are present are shown in white (modified from Mata et al., 2010).

Geochemistry

Despite that both Fuerteventura and Cape Verde oceanic carbonatites are characterized by a large variability in minor and trace elements compositions, they show broadly similar trace element characteristics (Hoernle et al., 2002). Indeed, it has been recognized in both the carbonatitic complexes a depletion in Rb, K, Hf, Zr and Ti, coupled to an enrichment in Ba, Th, U, Sr, Y, LREE and MREE, especially if compared with OIB, and although elements such as Th, U, Nb and Ta normally show differences in their relative abundances, interpreted as due to the pyrochlore fractionation/accumulation (Hoernle et al., 2002).

Hoernle et al. (2002) proposed that calcio-carbonatites from Fuerteventura, similar to the calcio-carbonatites from Cape Verde, result from melting of secondary Ca-carbonate belonging to recycled 1.6 Ga oceanic crust (Hoernle et al., 2002). Furthermore, coupling Ce and Nd isotopic data, Doucelance et al. (2014) suggested the recycling of marine carbonates in the source region of Cape Verde oceanic carbonatites (Doucelance et al., 2014). In the same way, a recent study on Ca isotopes of carbonatites (tracers of subducted sedimentary material) confirms the recycled marine carbonates contribution on Fuerteventura and Cape Verde carbonatites petrogenesis (Amsellem et al., 2020).

Although there are several models that underline the importance of recycling of marine carbonates and oceanic crust on carbonatites origin, other hypothesis involving a primary deep-seated signature (de Ignacio et al., 2006; Mata et al., 2010) suggest a role of primordial carbon on the origin of the oceanic carbonatites source.

As regards the Cape Verde carbonatites there is not a unique viewpoint: if De Ignacio et al. (2012) suggest that Ca-carbonatites from São Vicente (Northern Cape Verde Islands) represent fractionated melts from a parental nephelinitic magma (Hoernle et al., 2002), similarly, models in which the carbonatites result from liquid immiscibility were also proposed for Brava, one of the southern Cape Verde Islands (Mata et al., 2010). Although in some cases (*e.g.*, Fogo and Santiago islands) isotopic compositions (Sr-Nd-Pb) of carbonatites significantly differ from those of their associated alkaline silicate rocks, the close association of carbonatites with evolved alkaline silica-undersaturated magmas suggests a common origin. Indeed, a recent study proposes that both oceanic carbonatites (Cape Verde and Fuerteventura carbonatites) occur where primitive silicate melts have the lowest silica and highest alkalis contents, driving the liquid line of descent into the silicate-carbonatite miscibility gap (Schmidt and Weidendorfer, 2018).

With respect to the continental carbonatites, Fuerteventura oceanic carbonatites present a much narrower spread in the ^{143}Nd/^{144}Nd vs ^{87}Sr/^{86}Sr diagram (de Ignacio et al., 2006; Hoernle et al., 2002). Regarding Pb isotopic compositions, carbonatites instead plot in a relatively large range and ^{207}Pb/^{204}Pb initial ratios plot below the trend of Northern Hemisphere Reference Line (NHRL) (Hart, 1984), as normal for oceanic carbonatites (^{207}Pb/^{204}Pb initial ratios of Cape Verde carbonatites also plot below the NHRL) and OIB (Hoernle et al., 2002; Thirlwall, 1997).

Given a close similarity in isotopic compositions between Cape Verde and Fuerteventura oceanic carbonatites with Tamazert continental carbonatites (Morocco, ca 970 km north-east wards from Fuerteventura), a common source for these latter was also proposed (Bouabdellah et al., 2010), emphasizing the invoked eastward deflection of Canary mantle plume head through a subcontinental lithospheric corridor from the eastern Atlantic to the Middle Atlas mountain chain and the western Mediterranean (Duggen et al., 2009).

Lastly, Mata et al. (2010) reported the first noble gases results obtained for Cape Verde carbonatites and some of the analysed calcite and apatite minerals present high ^{3}He/^{4}He ratios (R/Ra up to 15.5 and 9.76 respectively), suggesting a contribution of He from a deep and more primitive mantle (plume-type) for Cape Verde carbonatites (Mata et al., 2010).

Analytical methods

Noble gases isotopic ratios (He, Ne, Ar) were determined on calcite, apatite and clinopyroxene mineral separates from Fuerteventura carbonatites. Clinopyroxenes from a clinopyroxenite adjacent to Fuerteventura carbonatites were also analysed. Calcites were concentrated using a Frantz isodynamic separator. Apatite and clinopyroxene were concentrated using magnetic methods and magnetic heavy liquid separation (sodium polytungstate) and finally refined by handpicking.

Noble gases isotopic analyses were carried out at Istituto Nazionale di Geofisica e Vulcanologia (INGV-Palermo) following the preparation and analytical protocols described in Rizzo et al. (2018, 2019) (Rizzo et al., 2019, 2018). Phenocrysts have been cleaned in acetone and millipore water by using an ultrasonic bath, and the portion of the selected sample material has been loaded into a stainless-steel crusher baked for 48-72 h at 120 °C in order to achieve ultra-high-vacuum conditions (10^{-9} mbar). Fluid inclusions from minerals were released by an in-vacuum single-step crushing and the external pressure applied to the minerals by the hydraulic press was 250 bar. According to the literature (e.g. (Hilton et al., 2002, 1993)) this procedure is the most conservative for minimizing the contribution of cosmogenic ^{3}He and radiogenic ^{4}He possibly grown and/or trapped in the crystal lattice. Noble gases were separated from the other volatiles by using a "cold finger" immersed in liquid nitrogen (T= -196 °C) that allows freezing H_2O and CO_2 and successively were further cleaned in an ultra-high vacuum (10^{-9}-10^{-10} mbar) purification line, and all the species of the gas mixture, except noble gases, were removed using four getters. Helium (^{3}He and ^{4}He) and neon (^{20}Ne) isotopes were measured separately by two different split-flight-tube mass spectrometers (Helix SFT-Thermo). The analytical uncertainty of He isotopic ratio is ≤ 4%, while that for ^{20}Ne/^{22}Ne and ^{21}Ne/^{22}Ne are < 2% and < 4% respectively. The Ne isotope ratios are corrected for isobaric interferences at m/z values of 20 ($^{40}Ar^{2+}$) and 22 ($^{44}CO_2^{2+}$). Corrections are generally carried out by measuring ^{20}Ne, ^{21}Ne, ^{22}Ne, ^{40}Ar and $^{44}CO_2$ during the same analyses, and considering the previously determined $^{40}Ar^{2+}/^{40}Ar^{+}$ and $^{44}CO_2^{2+}/CO_2^{+}$ ratios in static conditions on the same Helix-SFT mass spectrometers used to perform Ne measurements. Argon isotopes (^{36}Ar, ^{38}Ar and ^{40}Ar) were analysed by a multi-collector mass spectrometer (GVI Argus), with an analytical uncertainty < 1%. The uncertainty in the determinations of He, Ne, and Ar elemental contents was less than 5%. More details about the sample preparation and analytical procedures are available in Rizzo et al. (2018, 2019).

Whole-rock analyses of Fuerteventura carbonatites were performed at ALS Geochemistry Laboratory.

Trace elements composition of the minerals and rocks from Fuerteventura carbonatites was analysed at the INGV laboratory-Palermo using a GeoLasPro 193nm ArFExcimer laser ablation (LA) system, connected to an Agilent 7500ce quadrupole ICP–MS. The analyses were performed with a constant laser repetition rate of 10 Hz, a fluency of 14-15 J/cm^{2}, a He flux of about 0.8 L/min in the ablation cell and a 32-44µm spot. Glass reference material NIST612 was used as external standard for all the clinopyroxene and apatite minerals whereas for calcite minerals was used the Microanalytical Carbonate Standard MACS3. ^{43}Ca, estimated by ESEM measures, was used as internal standard for all samples. The analytical accuracy was calculated by repeated analyses of the USGS basaltic reference glass BCR-2G for the clinopyroxene and apatite minerals and of the glass reference material NIST612 for calcite minerals. It resulted to be ≤15% for most of the elements. The analytical precision was estimated by repeated analyses of the reference material NIST612 and the MACS3 carbonate standard and resulted to be ≤20% for most of the elements.

Results

Petrography

Based on petrographic characteristics, Fuerteventura carbonatites are grouped into two main types: (i) calcio-carbonatites (the most dominant type) and (ii) silico-carbonatites, when the amount of silicate phases reach up to 50% of the rock volume. Fuerteventura carbonatites are medium- (microsövite) to coarse-grained (sövite) (Figure 2a) and they are composed of calcite, with variable amounts of clinopyroxene (aegirine-augite), feldspar, biotite, Fe- and Ti-oxides and accessory minerals such as apatite, pyrochlore, titanite, barite and zircon.

Calcite occurs as euhedral to sub-euhedral grains with typical rhombohedral cleavage (Figure 2b). Tabular calcite phenocrysts are common, forming aggregates with 120° grain boundaries angle (Figure 2c). Occasionally (*e.g.*, at Punta de la Nao area) also occur as elongated calcite crystals arranged in a spinifex-like texture. The occurrence at Punta de la Nao of both tabular calcite and typical spinifex textures reflect the magmatic origin of non-recrystallized carbonatite.

Apatite is largely the most abundant accessory phase typically in rounded grains or elongated prisms with typical igneous tapered pill-like shape. Furthermore, apatite is commonly enclosed either by calcite or other silicate phases, in poikilitic textures, suggesting that apatite is the liquidus phase. Other common accessory minerals are pyrochlore, that occurs as small zoned microphenocrysts, and zircon, less abundant than apatite and pyrochlore, but it occurs larger than these latter (up to 1-2 mm) (Figure 2d).

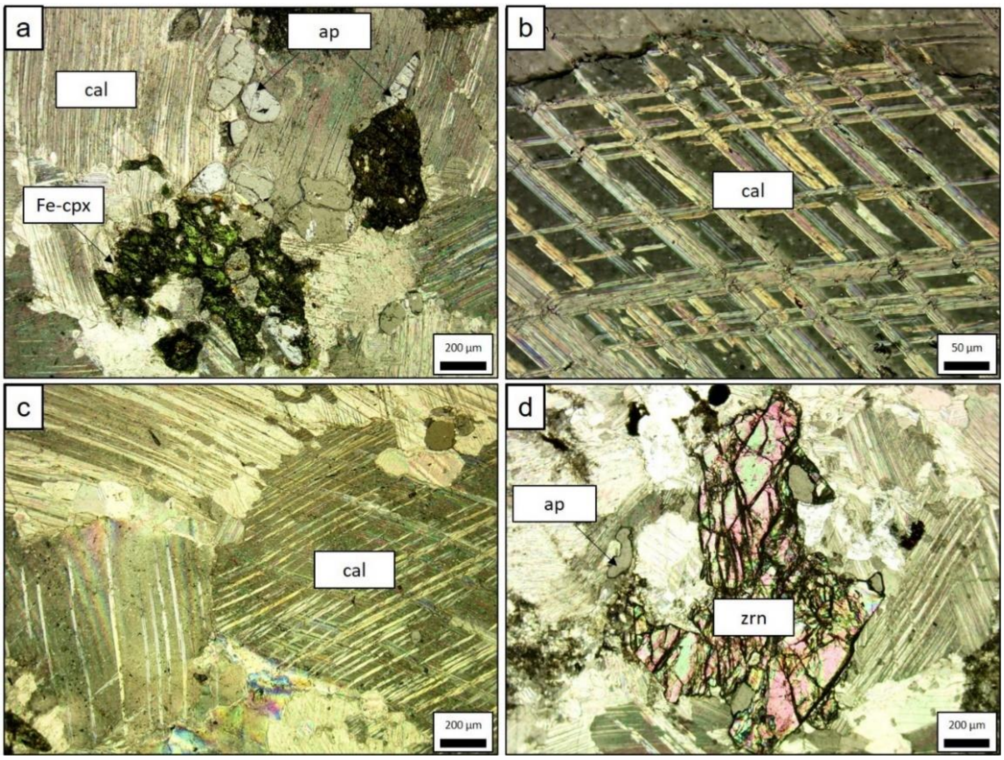

Figure 2. Microscopic aspects of Fuerteventura carbonatite textures (crossed polars). (a) Coarse-grained carbonatite (sövite) with Fe-clinopyroxene (dark green), calcite and associated euhedral rounded apatite (light grey, top centre). (b) Detail on different grain-size of calcite with typical rhombohedral cleavage. (c) Calcite aggregates with 120° grain boundaries angle on coarse-grained carbonatite. (d) Zircon crystal in a medium-grained carbonatite (microsövite).

Major and trace elements

Major and trace elements compositions of Fuerteventura carbonatites (whole-rock) are reported in Table 1. In Table 2 is reported trace elements content in calcite and apatite from Fuerteventura carbonatites, while in Table 3 are reported trace elements in clinopyroxenes from Fuerteventura carbonatites and clinopyroxenite.

Whole-rock analyses on Fuerteventura carbonatites show very small variations of MgO (1.2-1.3 wt.%), Fe_2O_3 t (3.9-4.0 wt.%), Na_2O (1.5-1.6 wt.%), P_2O_5 (2.2-3.0 wt.%) and loss on ignition LOI (29.8-30.4 wt.%), while CaO (41.9-43.8 wt.%), SiO_2 (11.5-12.8wt.%) and Al_2O_3 (1.9-3.3 wt.%) show slightly more appreciable variations (Table 1).

Concentrations measured for calcites are similar to those determined for carbonatites, mostly on Ba (up to 989 ppm), La (up to 624 ppm) and Ce (up to 1116 ppm) content, while Sr concentrations on calcites (up to 26330 ppm) are higher than Sr concentrations on whole-rock sample (up to 15900 ppm). Apatites show higher concentrations of REE (∑REE up to 16690 ppm) if compared to carbonatites (∑REE up to 2637 ppm), especially on La (up to 3270 ppm), Ce (up to 7620 ppm), Pr (up to 914 ppm) and Nd (up to 3603 ppm) content (Table 2). In the same way, clinopyroxenes from carbonatites show also different concentrations than whole-rock samples, with REE concentrations (∑REE up to 177 ppm) lower than carbonatites. Moreover, if compared with clinopyroxenes from Fuerteventura clinopyroxenite, clinopyroxenes from carbonatites present some differences on trace elements concentrations, especially on Sc, V, Cr, Co and Ni abundances (Table 3). Th is normally more abundant than U for whole-rock samples, with Th/U ratios ranging from 5.9 to 8.9. It is the same for apatite and calcite minerals, with Th/U ratios ranging from 5 to 17 on calcite and from 8 to 10 on apatite. On the contrary, clinopyroxene present U concentrations higher than Th concentrations, with Th/U ratios up to 0.5.

Table 1. Major and trace elements compositions of Fuerteventura whole-rock carbonatites.

Occurrence	**Fuerteventura**	
Sample	**FUE1-03**	**FUE1-04**
SiO_2 (wt.%)	11.55	12.8
TiO_2	0.13	0.45
Al_2O_3	1.9	3.33
$Fe_2O_{3\,t}$	4.04	3.9
MnO	0.31	0.32
MgO	1.29	1.19
CaO	43.8	41.9
Na_2O	1.5	1.66
K_2O	0.34	0.37
P_2O_5	3.01	2.23
LOI	30.4	29.8
Total	98.27	97.95
Sr (ppm)	15900	14300
Y	142.5	129.5
Rb	10.4	15.1
Ba	659	428
La	589	487
Ce	1205	1025
Pr	140	122
Nd	487	419
Sm	71.6	62.3
Eu	21.6	18.2
Gd	53.7	46.8
Tb	6.6	5.6
Dy	32.4	28.8
Ho	5.3	4.9
Er	13.1	10.9
Tm	1.4	1.3
Yb	9.1	8.05
Lu	1.3	1.1
Hf	3.7	8.4
Zr	424	755
Pb	8	10
Th	33.2	21.8
U	3.7	3.7
Nb	63.7	378
∑REE	2637.1	2241.0
Th/U	8.9	5.9
$(La/Yb)_N$	46.4	43.4
Eu/Eu *	1.02	0.99

Sr/Sr *	23.37	22.75

Note. $Eu^* = Eu_N/(Sm_N \times Gd_N)^{1/2}$; $Sr^* = (Ce_N + Nd_N)^{1/2}$.

Table 2. Representative trace elements compositions of calcite and apatite on Fuerteventura carbonatites.

Occurrence	**Fuerteventura**		
Mineral	**Calcite**		
Sample	**FUE1-03**	**FUE1-04**	**FUE3-01**
Mn (ppm)	1545.56	1422.88	2225.86
Sr	25643.40	25341.66	26331.39
Y	116.59	121.32	124.79
Rb	0.07	0.07	0.93
Ba	721.41	989.64	607.97
La	607.83	624.27	453.81
Ce	1092.91	1116.05	896.40
Pr	104.27	105.67	81.12
Nd	355.19	361.49	288.65
Sm	50.47	51.06	42.99
Eu	14.45	14.84	12.30
Gd	39.12	40.06	41.11
Tb	4.46	4.55	4.43
Dy	23.09	23.70	23.66
Ho	4.16	4.27	4.25
Er	10.39	10.70	10.73
Tm	1.26	1.31	1.38
Yb	7.29	7.62	8.29
Lu	1.02	1.06	1.15
Hf	0.01	0.01	0.02
Zr	0.03	0.04	0.78
Pb	5.77	5.31	6.03
Th	0.04	0.07	8.62
U	<0.1	<0.1	1.45
Nb	0.01	0.02	2.12
∑REE	2315.90	2366.64	1870.28
Th/U	10.03	16.60	5.94
$(La/Yb)_N$	59.86	58.79	39.27
Eu/Eu *	0.96	0.97	0.88
Sr/Sr *	41	40.11	46.55
δCe	0.98	0.97	1.06
δEu	0.96	0.97	0.88
δY	0.95	0.97	0.99

Note. See the main text for δCe, δEu and δY calculation.

Table 2. Continued.

Occurrence	**Fuerteventura**	
Mineral	**Apatite**	
Sample	**FUE1-03**	**FUE1-04**
Mn (ppm)	353.28	427.57
Sr	14243.53	14520.67
Y	770.19	776.35
Rb	0.13	0.15
Ba	23.78	27.38
La	3166.94	3269.77
Ce	7619.98	7598.89
Pr	904.29	914.20
Nd	3517.07	3603.46
Sm	494.68	498.70
Eu	132.34	131.24
Gd	443.72	396.08
Tb	42.72	40.93
Dy	200.23	198.20
Ho	29.35	29.96
Er	63.53	63.55
Tm	6.77	6.72
Yb	33.92	34.17
Lu	3.83	3.74
Hf	0.10	0.06
Zr	17.61	13.35
Pb	2.23	2.27
Th	347.35	333.71
U	39.72	34.36
Nb	7.68	5.96
∑REE	16659.36	16789.61
Th/U	8.74	9.71
$(La/Yb)_N$	63.41	65.01
Eu/Eu *	0.85	0.87
Sr/Sr *	8.13	8.25
δCe	1.08	1.05
δEu	0.84	0.86
δY	0.82	0.82

Table 3. Representative trace elements compositions of clinopyroxene on Fuerteventura carbonatites and clinopyroxenite.

Rock type	**Carbonatite**		**Clinopyroxenite**	
Mineral	**Clinopyroxene**			
Sample	**FUE3-01**	**FUE3-01[1]**	**FUE4-03**	**FUE4-03[1]**
Sc (ppm)	4.35	3.32	62.05	65.68
V	62.04	53.54	327.90	275.10
Cr	14.68	13.78	248.88	859.38
Co	9.46	7.89	44.34	46.15
Ni	12.59	10.89	214.97	300.33
Zn	106.20	89.90	35.68	31.84
Sr	271.97	245.87	134.06	87.66
Y	18.07	15.06	18.76	10.34
Zr	134.15	124.23	128.87	52.43
Nb	6.75	5.25	0.69	0.41
Rb	16.36	15.87	0.26	0.27
Ba	28.22	26.46	0.13	0.05
La	60.29	71.21	6.93	2.95
Ce	49.46	50.98	26.19	12.27
Pr	9.27	5.87	4.71	2.29
Nd	25.58	20.98	28.30	13.58
Sm	7.94	8.97	7.87	4.09
Eu	2.03	2.07	2.20	1.28
Gd	6.53	7.11	7.87	3.80
Tb	0.68	0.87	0.85	0.50
Dy	3.58	4.01	4.81	2.81
Ho	0.66	0.77	0.77	0.49
Er	1.65	1.75	1.61	0.95
Tm	0.21	0.32	0.20	0.13
Yb	1.44	1.56	1.06	0.61
Lu	0.21	0.32	0.14	0.08
Hf	2.13	2.15	6.31	2.57
Ta	0.79	0.87	0.16	0.06
Pb	7.27	7.35	0.07	0.12
Th	1.21	0.89	0.06	0.04
U	4.36	1.90	0.02	<0.01
∑REE	169.52	176.79	93.52	45.83
Th/U	0.27	0.46	3	4.44

Note. [1] second analysis of the same sample.

Noble gas (He, Ne, Ar) isotopes

In this study, we measured the He, Ne and Ar isotopic compositions in minerals of calcite, clinopyroxene and apatite in Fuerteventura carbonatites and clinopyroxene in a clinopyroxenite. Furthermore, in order to better understand the significance of ^{3}He/^{4}He ratios on calcite, apatite and clinopyroxene separates from Fuerteventura carbonatites and from clinopyroxenite, it was calculated also the radiogenic ^{4}He* in situ produced by Th and U decay (Table 4). Noble gases concentrations and isotopic ratios of mineral separates from Fuerteventura carbonatites and Fuerteventura clinopyroxenite are shown in Table 5.

Calcite is characterized by ^{4}He concentrations in a restricted range of 5.7 x 10^{-7} to 15.2 x 10^{-7} ccSTP/g, in contrast we measured high ^{4}He in the apatite that are from 51.6 x 10^{-7} to 22.1 x 10^{-6} ccSTP/g (Table 5). So high concentrations of ^{4}He in the apatite are associated to very low signature of the ^{3}He/^{4}He ratios in the same minerals that are from 3 x 10^{-9} to 8 x 10^{-8} and they correspond to R/Ra from 0.003Ra to 0.08Ra (Table 5). We analysed only one sample of clinopyroxene in carbonatite and one in the clinopyroxenite and the 4He concentrations are 4.96 x 10^{-7} ccSTP/g and 0.83 x 10^{-7} ccSTP/g, respectively (Table 5). The He isotopic ratios in clinopyroxene from carbonatite (R/Ra = 2.23) are lower than calcite (R/Ra = 3.86), while clinopyroxene from clinopyroxenite show the highest He isotopic ratios (6.66Ra). The ^{4}He/^{20}Ne in all the analysed samples are at least three order of magnitude higher than the same ratio in atmosphere (^{4}He/^{20}Ne = 0.318 (Ozima and Podosek, 2002)) and it indicates that He air component of He is negligible in all the samples.

^{20}Ne/^{22}Ne and ^{21}Ne/^{22}Ne ratios from calcite (up to 10.02 and 0.0302 respectively) and apatite (up to 10.12 and 0.0297 respectively) are a little higher than the air ratio (Table 5). Clinopyroxenes from carbonatites present ^{20}Ne/^{22}Ne and ^{21}Ne/^{22}Ne ratios of 10.02 and 0.0301, while clinopyroxenes from clinopyroxenite show ^{20}Ne/^{22}Ne and ^{21}Ne/^{22}Ne ratios of 9.95 and 0.0295, in both cases a little higher than air ratio (Table 5).

The ^{40}Ar/^{36}Ar isotopic ratios (Table 5) are always higher than atmospheric value of 298.6 +/- 0.3 (Lee et al., 2006) for all mineral separates: calcite ^{40}Ar/^{36}Ar ranges from 614 to 2068, apatite vary from 409 to 690, clinopyroxene in carbonatite and clinopyroxenite are 650 and 431 respectively. Thus, considering the low K content of calcite and apatite minerals, the ^{40}Ar/^{36}Ar isotopic ratios, similarly to ^{4}He/^{20}Ne isotopic ratios, suggest a low atmospheric contamination, corroborating the choice of these minerals to investigate the noble gases isotopic signature in carbonatites.

Table 4. Th and U concentrations and related ^{4}He* production on mineral separates from Fuerteventura carbonatites and clinopyroxenite.

	Th (ppm)	**U (ppm)**	**Age (Ma)**	**^{4}He*(μccSTP/g)**
Carbonatite				
Apatite				
FUE1-03	347.3	39.7	25	7.3
FUE1-04	333.7	34.3	25	6.7
Calcite				
FUE1-03	0.04	0.004	25	< 0.001
FUE3-01	8.62	1.45	25	0.2
FUE3-01 duplicate	2.3	1.1	25	0.01
Clinopyroxene				
FUE3-01	1.2	4.4	25	0.3
Clinopyroxenite				
Clinopyroxene				
FUE4-03	0.06	0.02	22	0.002

Note. The equation ^{4}He* ≈ 2.8 x 10-8 (4.35 + Th/U) x (U) x (t) was used to calculate the ^{4}He* radiogenic (from Mata et al., 2010). [Th] and [U] in ppm, t in Ma.

Table 5. He concentrations (ccSTP/g) and He, Ne, Ar isotopic ratios on mineral separates from Fuerteventura carbonatites and clinopyroxenite.

	^{4}He (10^{-7})	**^{3}He (10^{-12})**	**R/Ra**	**1σ**	**^{4}He/^{20}Ne**	**^{20}Ne/^{22}Ne**	**1σ**	**^{21}Ne/^{22}Ne**	**1σ**	**^{40}Ar/^{36}Ar**	**1σ**
Carbonatite											
Apatite											
FUE1-03	221	0.08	0.003	*0.002*	45374.6	n.d.	*n.d.*	n.d.	*n.d.*	409.08	*0.19*
FUE1-04	51.6	0.50	0.08	*0.02*	8294.3	10.12	*0.04*	0.0297	*0.0007*	689.59	*0.18*
Calcite											
FUE1-03	15.2	7.09	3.35	*0.03*	641.1	10.01	*0.03*	0.0302	*0.0004*	2067.92	*1.34*
FUE3-01	8.55	4.57	3.84	*0.04*	500.1	10.02	*0.03*	0.0293	*0.0003*	614.42	*0.06*
FUE3-01 duplicate	5.77	3.10	3.86	*0.04*	388.8	9.90	*0.02*	0.0288	*0.0004*	713.82	*0.05*
Clinopyroxene											
FUE3-01	4.96	1.54	2.23	*0.04*	1582.6	10.02	*0.02*	0.0301	*0.0003*	650.52	*0.61*
Clinopyroxenite											
Clinopyroxene											
FUE4-03	0.83	0.76	6.66	*0.07*	1120.7	9.95	*0.04*	0.0295	*0.0006*	431.17	*0.06*
Air			**1.00**			**9.80**		**0.0290**		**298.6 +/- 0.3**	

Note. The atmospheric value for ^{20}Ne/^{22}Ne and ^{21}Ne/^{22}Ne is taken from Ozima and Podosek, (2002), while for ^{40}Ar/^{36}Ar is taken from Lee et al. (2006). n.d. = not determined.

Discussion

Major and trace elements

Major elements data of oceanic carbonatites show a large range in CaO and MgO, and this is due to the presence of two different groups, especially on Cape Verde Archipelago: (i) Ca-carbonatites with high CaO and low MgO content, and (ii) Mg-carbonatites with low CaO and high MgO content (Figure 2 in Hoernle et al. 2002). Although our new whole-rock analysis on Fuerteventura carbonatites shows slightly lower CaO content (41.9-43.8 wt.%) if compared with literature data (48.1-51.4 wt.%, Hoernle et al., 2002), they confirm that the studied samples are Ca-carbonatites with low MgO content (up to 1.29 wt.%). Our data on the major elements content of Fuerteventura carbonatites are comparable with literature data (Hoernle et al., 2002), with the exception of SiO2 content which results a little higher (11.5-12.8 wt.%) if compared with previous values (up to 5.85 wt.%, Hoernle et al., 2002), but this is probably due to a higher content of silicate phases in the analysed samples. In the same way, also Cape Verde carbonatites show significant variations, especially on CaO (48.82-54.76 wt.%), SiO_2 (0.27-5.81 wt.%), P_2O_5 (0.21-8.94 wt.%) and LOI (29.26-42.33 wt.%) (Table A1).

The interpretation of trace elements variations in carbonatites might be difficult, due to several processes occurring in the route to surface that could mask the pristine source and the primary processes (liquid immiscibility, crystal fractionation, occurrence of exotic accessory minerals high in incompatible elements), or also in the source region (*e.g.*, the lack of well constrained partition coefficients for trace elements between the peridotite or eclogite and carbonatite melts at high pressures, between 3 GPa and 5 GPa, where carbonated source melting is likely to take place (Hammouda and Keshav, 2015), in addition to other parameters that may control trace elements partitioning, volatile content and occurrence of a mixed volatile free-fluid phase, oxygen fugacity, etc.

The large variation in incompatible elements and trace elements of oceanic carbonatites reflects the presence of different mineral phases such as pyrochlore (high in High field strength elements, HFSE such as Ta, Nb, Zr, Ti and Hf and LREE), apatite (high in LREE, Sr, Th and U), zircon (HFSE-rich) and titanite (HFSE-rich). Negative anomalies of Zr, Hf and Ti are present, and this is typical of a carbonatite (or CO2-rich silicate melt metasomatized) in the garnet-peridotite stability field (Dasgupta et al., 2009). These negative anomalies are coupled to enrichment in REE and Sr, and this is one of the main characteristics of carbonatite rocks. As a consequence, mineral such as calcite and apatite result particularly enriched in Sr (Ahijado et al., 2005).

Representative multi-element (spider diagram) and REE patterns of both oceanic carbonatites are shown in Figure 3.

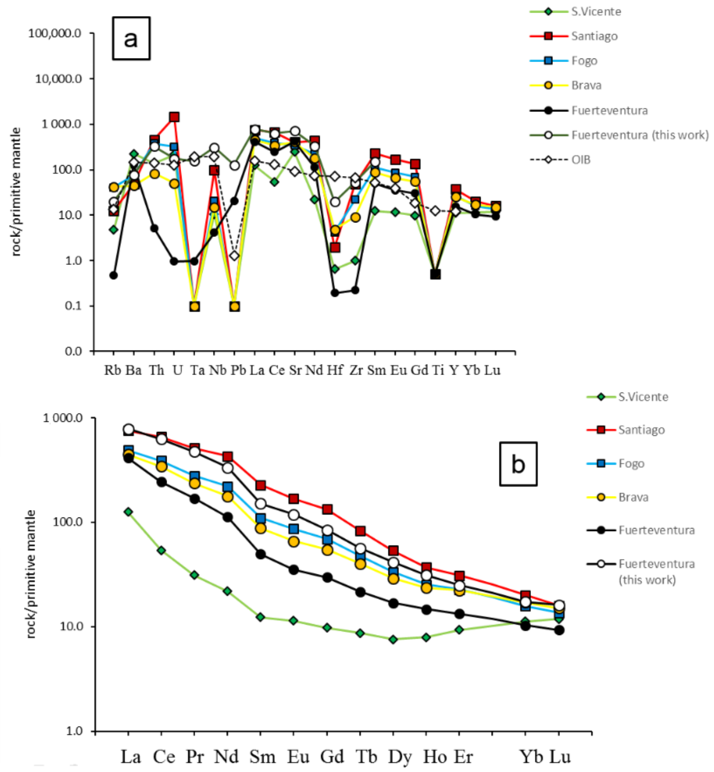

Figure 3. (a) Multi-element and (b) REE abundance diagram normalized to primitive mantle of McDonough and Sun (1995), showing patterns of Fuerteventura and Cape Verde carbonatites (from Hoernle et al., 2002). Ocean island basalt (OIB) from Sun and McDonough (1989).

Fuerteventura and Cape Verde oceanic carbonatites show large variations in the abundances of most trace elements. High field strength elements (HFSE), large ion lithophile elements (LILE), such as Rb, Ba, Pb and Sr, and REE, range from below to 600-700 times above primitive mantle values (Figure 3a). All samples show fractionated REE patterns with high LREE with respect to HREE (a common feature of both continental and oceanic carbonatites), with moderate steep patterns (La/Yb)N = 11-49 (Figure 3b). REE diagram shows also moderate negative Eu anomalies (Eu/Eu* = 0.99-0.88), with some exception for some Fuerteventura (Eu/Eu* = 1.02) and Cape Verde carbonatites (Eu/Eu* = 1.03-1.09), coupled with large Sr positive anomalies (Sr/Sr* = 9.6-28). Trace elements variation of apatite on oceanic carbonatites (Table A2), with respect to whole-rock samples, suggest that trace elements variability is mostly controlled by crystallization of apatite (and other main REE mineral reservoirs such as pyrochlore and monazite). It is worthy of note that calcite and apatite share broadly similar REE patterns (Figure 4), indicating that these two phases have a common origin and a genetic relationship in the magma from which they crystallized. On the contrary, clinopyroxene depict different REE patterns if compared with calcite and apatite (Figure 4).

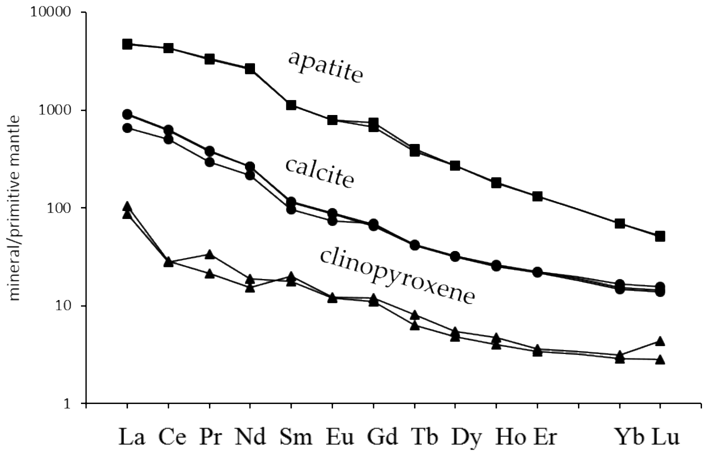

Figure 4. REE abundance diagram normalized to primitive mantle of McDonough and Sun (1995), showing patterns of apatite, calcite and clinopyroxene on Fuerteventura carbonatites.

A strong difference on Cr and Ni abundances on Fuerteventura samples between clinopyroxenes from carbonatite (Cr= 13-17 ppm, Ni= 8-13 ppm) and clinopyroxenes from clinopyroxenite (Cr= 248-860 ppm, Ni= 215-300 ppm), suggests that clinopyroxenes from clinopyroxenite crystallized from a primitive magma, while clinopyroxenes from carbonatite crystallized from an evolved magma. Indeed, Fuerteventura and Cape Verde oceanic carbonatites are both characterized by the presence of aegirine-augite, a clinopyroxene that crystallize from an evolved magma (Schmidt and Weidendorfer, 2018).

Trace elements data (this work) not only show a broadly similar trend in multi-element and REE abundance diagrams with previous Fuerteventura whole-rock carbonatites data (Hoernle et al., 2002), but also show a similar trend with Cape Verde carbonatites. Thus, both Fuerteventura and Cape Verde carbonatites depict the same trace elements characteristics, almost tracing the same patterns on multi-element and REE abundance diagrams.

Igneous vs. hydrothermal apatite

Very commonly the original mineral association of carbonatites is partially overprinted by late-stage metasomatic fluids (Chakhmouradian and Zaitsev, 2012), which precipitate phosphate minerals such as apatite-group, monazite or xenotime. Among these, apatite plays a dual role, being one of the earliest minerals on carbonatitic liquidus, but also a common late-stage metasomatic mineral.

The criteria we used to clarify apatite crystallization (near-liquidus or sub-solidus phase), were textural and chemical. We use a variety of chemical criteria typical of igneous carbonatites defined by Chakhmouradian et al. (2017), such as concentrations of Mn $\leq$ 1000 ppm and Sr $\geq$ 2000 ppm, $\delta Eu \approx 1$ with $\delta Eu = Eu_{cn}/[0.5 \times (Sm_{cn} + Gd_{cn})]$, $0.6 \leq \delta Y \leq 0.9$ with $\delta Y = Y_{cn}/[(0.25 \times Dy_{cn}) + (0.75 \times Ho_{cn})]$ and $\delta Ce > 1$ with $\delta Ce = Ce_{cn}/[0.5 \times (La_{cn} + Pr_{cn})]$. Figure 5a shows analysis of apatites from

Fuerteventura carbonatites plotted on δEu vs. δY diagram with different igneous and hydrothermal apatite fields. Almost all the analyses fall into the igneous apatite field, with δEu ranging from 0.82 to 0.91 and δY from 0.77 to 0.88 (see Table A3 for all plotted analyses), with some exception regarding only the δCe criterion (δCe < 1). Mn and Sr concentrations are also in agreement with igneous origin (i.e. Mn ≤ 1000 ppm, Sr ≥ 2000 ppm). Apatites from Cape Verde carbonatites are not plotted on δEu vs. δY diagram due to lack of data.

In extrusive or shallow intrusive carbonatites, apatite occurs as euhedral prismatic phenocrysts and/or groundmass crystals (Chakhmouradian et al., 2017). On the contrary, igneous apatite from plutonic carbonatites normally occurs with smooth contours and a tapered pill-like shape (Chakhmouradian et al., 2017), and apatite from Fuerteventura carbonatites presents this typical well faceted morphology (Figure 5b), confirming its igneous origin.

Overall, trace elements and REE on apatites from Fuerteventura carbonatites are consistent with an igneous origin with a low/null interaction with metasomatic fluids instead of hydrothermal, allowing the choice of using apatite as a tracer for primary carbonatitic magma.

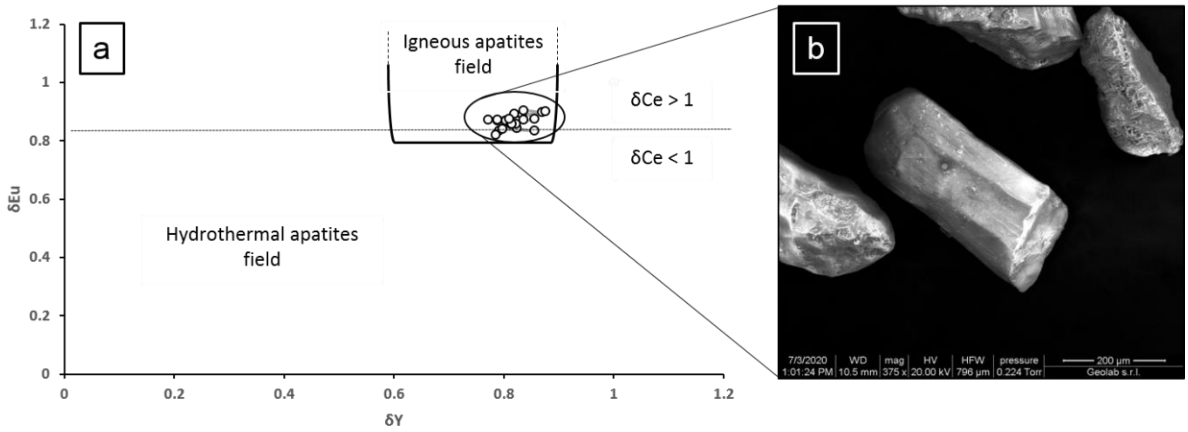

Figure 5. (a) Apatite minerals from Fuerteventura carbonatites plotted on δEu vs. δY diagram with different igneous and hydrothermal apatite fields using REE criteria (δEu, δY and δCe) of Chakhmouradian et al. (2017). (b) Secondary Electrons (SE) image of some plotted apatite minerals with typical igneous tapered pill-like shape; scale bar = 200µm.

Stable isotopes ($\delta^{13}C$ and $\delta^{18}O$)

Carbon and oxygen isotope compositions of carbonates on carbonatites provide important information about the origin of the carbonatitic magma and the isotopic composition of the mantle source. The C and O isotopic compositions of the carbonatite compositional field, the so-called "primary igneous carbonatite" box, range between 6% and 10% for $\delta^{18}O$ (SMOW) and between -4% and -8% for $\delta^{13}C$ (PDB) (Hoefs, 1987; Sheppard and Dawson, 1973; Taylor et al., 1967). Recent work on Oldoinyo Lengai (the only worldwide active volcano that erupts Na-carbonatitic magma) volcanic fresh products allowed to narrow the range of the C and O isotopic signature of primary igneous carbonatites, and, although particular as natrocarbonatites, the range can be considered representative of undegassed and uncontaminated mantle compositions, with δ^{13}C values ranging from -5% to -7% and δ^{18}O values ranging from 5.5% to 7% (Keller and Hoefs, 1995).

Compared with the mantle range for oxygen isotopes, the carbon isotope signature of the mantle is more difficult to constrain, due to the apparent under-estimation of high-temperature fractionation for carbon in the mantle (Mikhail et al., 2011), and also because the average concentration of the carbon in the mantle is still uncertain (Marty et al., 2013; Shirey et al., 2013; Wood et al., 2013). Thus, even though C and O isotope compositions give important information regarding carbonatite genesis, there are several secondary processes that may affect the primary mantle fingerprint, such as low-temperature alteration, high-temperature fractionation or crustal assimilation, causing post-emplacement changes in δ^{13}C and/or δ^{18}O values (Deines, 1989; Santos and Clayton, 1995), and making their interpretation particularly difficult.

Figure 6 shows oxygen and carbon isotope compositions for Fuerteventura and Cape Verde carbonatites, plotted within the mantle boxes of Taylor et al. (1967) and Keller and Hoefs (1995) (Keller and Hoefs, 1995; Taylor et al., 1967). δ^{13}C values of calcite on Fuerteventura carbonatites, are within the primary igneous carbonatite field as originally defined by Taylor et al. (1967) (Taylor et al., 1967), but also into the smaller box proposed by later authors (Keller and Hoefs, 1995), with δ^{13}C values ranging from -5% to -7% (Demény et al., 1998). Oxygen isotope compositions on Fuerteventura carbonatites vary in a slightly wider range if compared with carbon isotope compositions (δ^{18}O values ranging from 5.2 to 9.6%), and this is related to local fluid/rock interactions, as a result of low-temperature isotopic exchange between carbonatites and water-rich fluids where δ^{13}C is not affected (Demény et al., 1998).

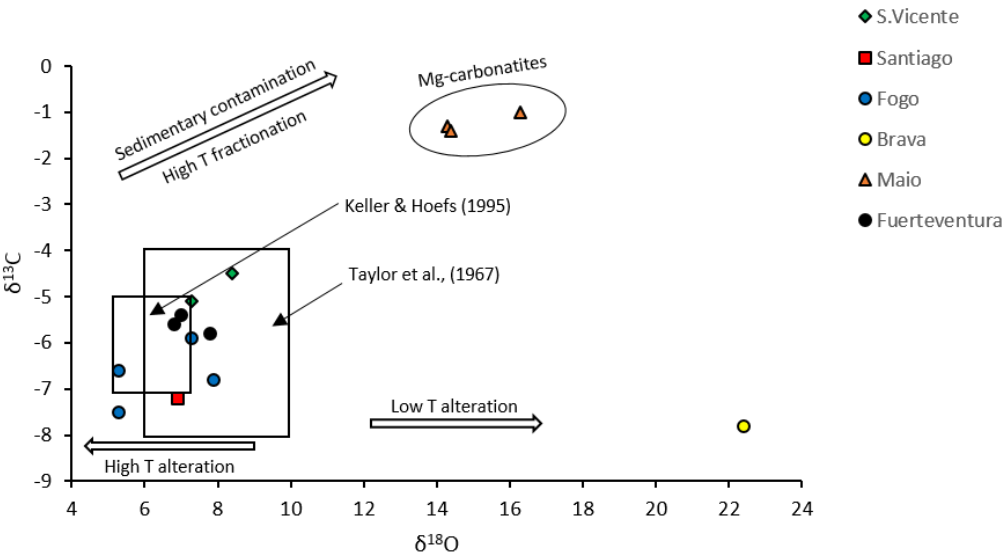

Figure 6. Stable isotope ($\delta^{13}C$ and $\delta^{18}O$) compositions (in % relative to PDB and SMOW, respectively) of Fuerteventura and Cape Verde carbonatites. White arrows indicate possible post-emplacement changes in $\delta^{13}C$ and/or $\delta^{18}O$ values caused by secondary processes. Data from Hoernle et al. (2002).

Typical mantle $\delta^{13}C$ values (-8% to -4.2%) were measured in Cape Verde carbonatites (Mata et al., 2010), suggesting a role of primordial carbon in their genesis. In contrast, $\delta^{13}C$ (-0.6% to -0.2%) and $\delta^{18}O$ (12.3% to 21%) values obtained on dolomite separates from Cape Verde Mg-rich carbonatites show clearly not typical mantle-derived values, suggesting the contribution of secondary processes on carbon and oxygen isotopic signature (Hoernle et al., 2002; Mata et al., 2010).

Overall, carbon and oxygen isotope compositions of both oceanic carbonatites (Fuerteventura and Cape Verde), share a common mantle-derived isotopic signature, with the exception of Mg-carbonatites from Cape Verde, in which secondary processes are more evident.

Sr-Nd-Pb isotopic systematics

Radiogenic Sr-Nd-Pb isotope systematics have been widely used to characterize the sources of the oceanic carbonatites and the contribution of the different end member involved in carbonatites genesis. De Ignacio et al. (2006) proposed a FOZO (defined as a source region deep-seated in the mantle by Hart et al. 1992 (Hart et al., 1992)) mixed with HIMU ("high μ", $\mu = {}^{238}U/{}^{204}Pb$ ratio) signature for alkali-carbonatitic association of Fuerteventura (de Ignacio et al., 2006). However, the involvement of a FOZO mantle component on carbonatites source is difficult to be exactly constrained. Indeed, many Sr-Nd isotopic ratios of carbonatites plot into the FOZO field (Hauri et al., 1994), and if we consider the more recent definitions of FOZO component (Jackson et al., 2007;

Stracke et al., 2005), most of those Ca-carbonatites plot outside of the box (Figure 9a in Doucelance et al., 2010).

Sr initial isotopic ratios (calculated for an age of 25 Ma, de Ignacio et al., 2006) of Fuerteventura carbonatites plot in a very restricted range (0.703202 ≤ (^{87}Sr/^{86}Sr)i ≤ 0.703244) and it is the same for Nd initial isotopic ratios (0.512840 ≤ (^{143}Nd/^{144}Nd)i ≤ 0.512877) (de Ignacio et al., 2006). The restricted range of Sr isotopic ratios of Fuerteventura carbonatites is clearly at odds with a large degree of assimilation of sedimentary carbonate proposed by Demény et al. (1998). If we assume 10% to 20% assimilation of sedimentary carbonate during differentiation processes in shallow magma chambers in alkaline-carbonatitic complex of Fuerteventura (Demény et al., 1998), Sr isotopic ratios would not plot in such a narrow range, as evidenced by De Ignacio et al. (2006).

Even though both Fuerteventura and Cape Verde oceanic carbonatites have similar isotopic compositions, Fuerteventura carbonatites show some differences with respect to the Cape Verde compositions. If we compare the previous Sr and Nd initial isotopic ratios of Fuerteventura with Cape Verde carbonatites, these latter show a slightly wider range. Indeed, (^{87}Sr/^{86}Sr)i ratio vary from 0.703120 (S. Vicente, northern Archipelago) to 0.703356 (Brava, southern Archipelago), and (^{143}Nd/^{144}Nd)i ratio vary from 0.512884 to 0.512911, for S. Vicente and Brava respectively (Doucelance et al., 2010). Regarding lead isotopic ratios, Fuerteventura display lower ^{206}Pb/^{204}Pb and ^{207}Pb/^{204}Pb, and slightly higher ^{208}Pb/^{204}Pb ratios if compared with the other oceanic carbonatites (de Ignacio et al., 2006), being in the range from 19.601 to 19.869 for ^{206}Pb/^{204}Pb ratio, from 15.593 to 15.602 for ^{207}Pb/^{204}Pb ratio and from 39.536 to 39.672 for ^{208}Pb/^{204}Pb (de Ignacio et al., 2006). Cape Verde carbonatites instead plot in a large range on the uranogenic Pb isotope diagram, varying from 19.646 to 20.338 for ^{206}Pb/^{204}Pb ratio and from 15.586 to 15.657 for ^{207}Pb/^{204}Pb ratio (Hoernle et al., 2002).

Although it is more evident considering Cape Verde basaltic rocks, the slightly wider range of Sr-Nd-Pb isotopes on Cape Verde carbonatites is probably due to the isotopic dichotomy of the Cape Verde Archipelago, involving a depleted end-member mostly evident in northern Islands (interpreted as the local oceanic lithosphere assimilated by ascending plume melts (Millet et al., 2008)) and an enriched end-member (compatible with old marine carbonates) with a EMI-like ("enriched mantle I") isotopic signature predominant in the southern Islands (Doucelance et al., 2010).

Figure 7 compares Sr-Pb and Nd-Pb ratios of Fuerteventura and Cape Verde carbonatites, and isotope diagrams show a more restricted range for Fuerteventura carbonatites compared to Cape Verde carbonatites. Interestingly, even though both oceanic carbonatites present slight isotopic differences, Fuerteventura and Cape Verde carbonatites project in the middle of the field defined by the three end-member mantle components: DMM, EM-I (especially the southern Cape Verde Islands), and HIMU, being similar to his Canary and Cape Verde mafic rocks (Figure 7a,b).

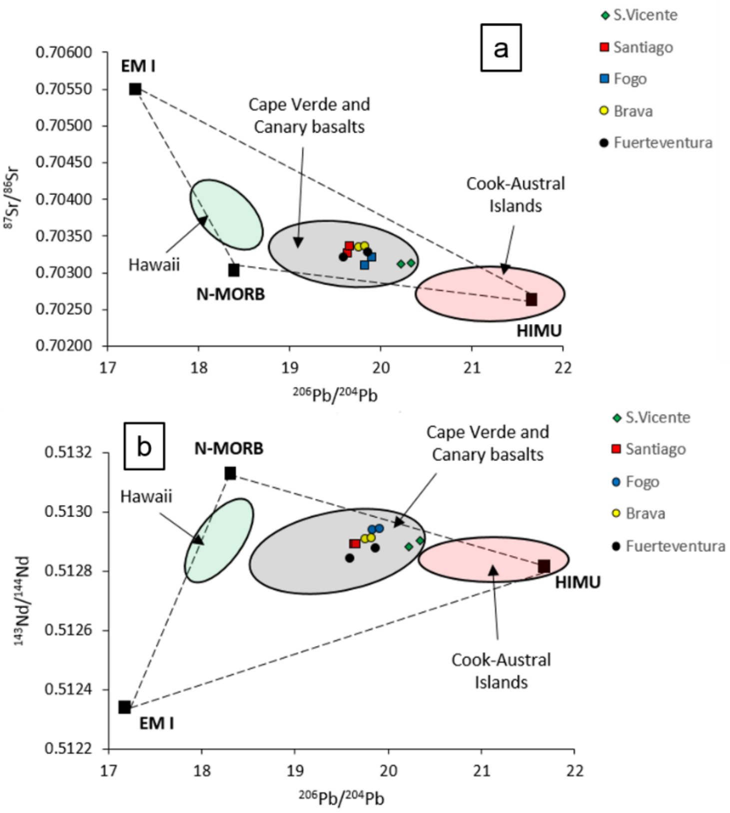

Figure 7. (a) $^{87}Sr/^{86}Sr$ vs. $^{206}Pb/^{204}Pb$ and (b) $^{143}Nd/^{144}Nd$ vs. $^{206}Pb/^{204}Pb$ initial ratios of Fuerteventura and Cape Verde carbonatites (data from De Ignacio et al., 2006 and Hoernle et al., 2002 respectively). Mantle components after Hart (1988). Also shown for comparison: (1) Canary and Cape Verde basalts (Doucelance et al., 2003; Gurenko et al., 2006); (2) Hawaii (Abouchami et al., 2000; Bryce et al., 2005; Harrison and Weis, 2018) and Cook-Austral Islands volcanic rocks (Stracke et al., 2005).

The Canary and Cape Verde basalts and carbonatites clearly differ from HIMU-OIB and OIB isotopic compositions represented by Cook-Austral Islands and Hawaii, suggesting a different geochemical footprint and just a slight contribution of a moderately radiogenic Pb isotope signature, comparable with isotopic compositions of the second group of OIB defined by Stracke et al. (2005) with $^{206}Pb/^{204}Pb = 19.5\text{-}20.5$. Overall, Canary (Fuerteventura) and Cape Verde carbonatites, regarding Sr-Nd-Pb isotopic compositions, appear to be generated from a binary mixing between DMM component and a second component resulting from a mixing involving an enriched mantle component (EM-I) and a moderately HIMU-like component, reflecting a similar trend on Sr-Pb and Nd-Pb diagrams. Previous studies of mantle source on Cape Verde magmas show the DMM component as dominant in the northern Cape Verde islands and in lesser amounts in sub-continental lithospheric mantle (SCLM) component relative to those of the southern Islands (Doucelance et al., 2003; Gerlach et al., 1988). Furthermore, the occurrence of a delaminated sub-continental lithospheric mantle domain beneath the southern Cape Verde Islands was also proposed (Bonadiman et al., 2005; Martins et al., 2010), considering Cape Verde carbonatites derived from melting of such SCLM domain. On the contrary, Mata et al. (2010), given the high $^3He/^4He$ ratios on calcite and apatite minerals of Cape Verde carbonatites (R/Ra up to 15.5), exclude the SCLM domain as their origin, considering the high $^3He/^4He$ ratios as evidence of a deep mantle contribution to the carbonatites genesis (Mata et al., 2010). The role of the primitive high He signature as a component on the Cape Verde carbonatites genesis and its relationship with the He signature of Fuerteventura carbonatites it will be discussed in detail in the Subsubsection 5.4.2.

Noble gases (He, Ne, Ar) isotopes

Radiogenic time-integrated $^4He^*$ production

Apatite sample from Fuerteventura carbonatites (FUE1-03 and FUE1-04) present a radiogenic $^4He^*$ content of approximately 7 x 10^{-6} ccSTP/g (Table 4), compared with a measured 4He content of few 10^{-7} ccSTP/g (221 and 51.6 for FUE1-03 and FUE1-04 respectively). Thus, although the low percentage of the radiogenic $^4He^*$, it is high enough to dominate the signal of the mantle derived He. The radiogenic $^4He^*$ production on apatite separates from Cape Verde carbonatites (Table A4), although they present lower Th and U content than Fuerteventura carbonatites (up to 133 ppm for Th and 15 ppm for U), is also high enough to influence the apatite He signal (Mata et al., 2010).

With respect to apatite, calcite contains significantly lower Th and U contents (up to 8.6 ppm and 1.4 ppm respectively) (Table 4) and therefore the radiogenic $^4He^*$ contribution to decrease the pristine He isotopic signature is lower than in apatite. Clinopyroxene from carbonatites and clinopyroxenite presents also low Th and U contents (Table 4). In the same way, calcite separates from Cape Verde carbonatites present low Th and U contents (up to 20.4 ppm and 2.7 ppm respectively), preserving their isotopic signature.

Overall, although the modal abundance of apatite of Fuerteventura and Cape Verde carbonatites and their magmatic origin, due to the high content of Th and U, they are not good indicators of the noble gas isotopic signature of their precursor magmas. On the contrary, calcite and clinopyroxene represent good tracers for magma source and its noble gas isotopic signature.

R/Ra: shallow vs. deep primitive He isotopic signature

Even though calcite $^3He/^4He$ ratios on Fuerteventura carbonatites (up to 3.86Ra) are a little higher than clinopyroxenes (≈ 2.23Ra) and higher than apatites (up to 0.08Ra), they present values significantly lower than typical MORB mantle values (R/Ra = 8 ± 1) (Allègre et al., 1995), while clinopyroxenes from clinopyroxenite show $^3He/^4He$ ratios (≈ 6.66Ra) slightly lower than typical

MORB mantle values and in the range of sub-continental lithospheric mantle values (SCLM, 6.1 Ra ± 0.9 (Gautheron and Moreira, 2002)). In contrast, calcite and apatite $^{3}He/^{4}He$ ratios on Cape Verde carbonatites present values higher than typical MORB mantle values, reaching values of 15.5Ra and 9.76Ra respectively (Table A5).

The lower R/Ra values on mineral separates from Fuerteventura carbonatites might be caused by "magma aging" (*i.e.* internal production of radiogenic $^{4}He^{*}$ from U and Th content that lower the original R/Ra ratio of the magmatic source). However, considering (i) ^{3}He and ^{4}He concentration, (ii) Th and U content measured on calcite and clinopyroxene separates and (iii) contribution of radiogenic $^{4}He^{*}$ (see Table 4 for radiogenic $^{4}He^{*}$ calculation), using a simple magma aging model, initial R/Ra ratios of calcite and clinopyroxene from carbonatite and clinopyroxene from clinopyroxenite are not significantly modified. Indeed, initial R/Ra ratios continue to present values lower than typical MORB mantle values (≈5.10Ra and ≈5.24Ra for calcite and clinopyroxene from carbonatite and ≈6.82Ra for clinopyroxene from clinopyroxenite), and they are in the range of SCLM. An age of 53.5 Ma would be required for Fuerteventura carbonatites to bring the initial R/Ra ratio of 8 on calcite, and this is not realistic as have ages close to 25 Ma (Muñoz et al., 2005). We therefore consider the He isotopic ratio from the calcite to be reflective of a sub-continental lithospheric mantle signature.

If plotted into R/Ra vs $^{4}He/^{20}Ne$ ratios diagram (Figure 8a), calcite samples from Fuerteventura carbonatites fall below the SCLM field, and they clearly differ from those of Cape Verde carbonatites that fall between MORB field and plume-type field.

The $^{20}Ne/^{22}Ne$ and $^{21}Ne/^{22}Ne$ ratios of calcite from Fuerteventura carbonatites are not distinguishable from the value of air and from the mass-dependent fractionation line (MDFL), while calcites from Cape Verde carbonatites seem to plot along the mixing line between air and the hypothetical pristine MORB value, with the exception of Fogo Island (Figure 8b). On the contrary, $^{20}Ne/^{22}Ne$ and $^{21}Ne/^{22}Ne$ ratios of apatite from Cape Verde carbonatites, in which the values are distinct from air ratios, plot clearly to the left of the MORB line (Figure 3 in Mata et al., 2010). Furthermore, Fuerteventura carbonatites show higher $^{40}Ar/^{36}Ar$ isotopic ratios than Cape Verde carbonatites (Figure 8c), suggesting a lower extent of atmospheric contamination.

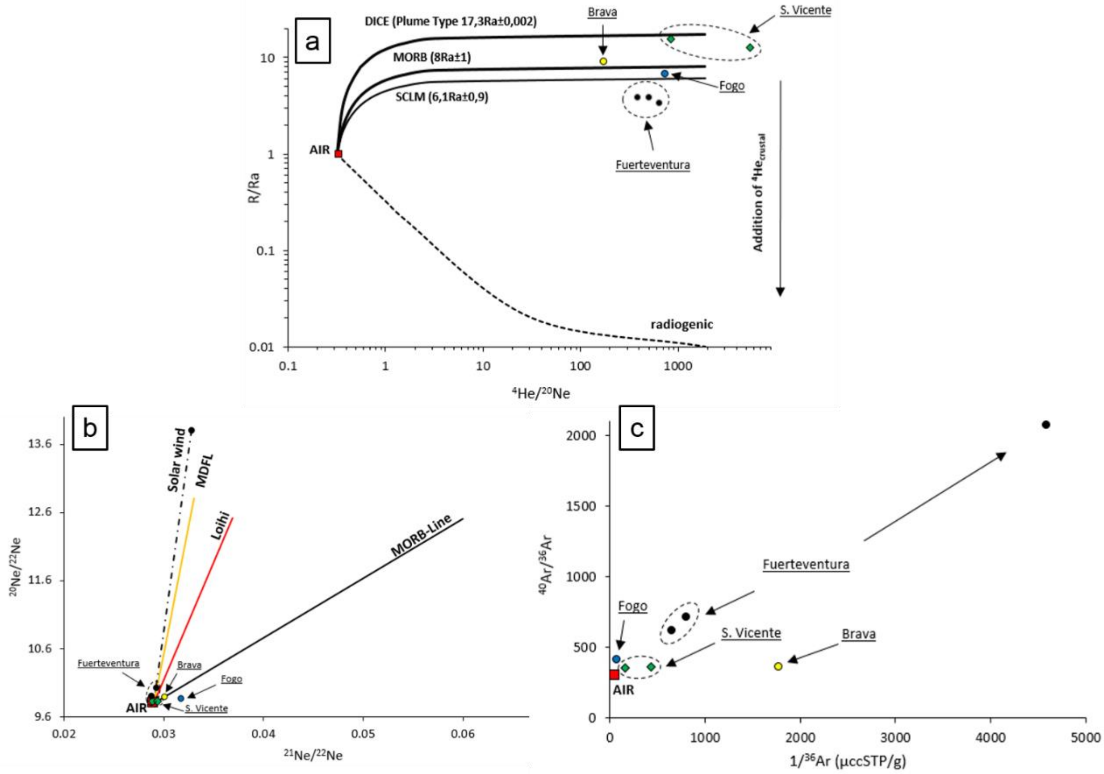

Figure 8. (a) R/Ra ratios vs $^4He/^{20}Ne$ ratios obtained by crushing calcite in Fuerteventura and Cape Verde carbonatites. (b) $^{20}Ne/^{22}Ne$ vs $^{21}Ne/^{22}Ne$ and (c) $^{40}Ar/^{36}Ar$ vs $1/^{36}Ar$ diagram from the same samples. Data from Cape Verde islands are from Mata et al. (2010). Mixing lines in $^{20}Ne/^{22}Ne$ vs $^{21}Ne/^{22}Ne$ diagram are from Broadley et al. (2020). The $^{20}Ne/^{22}Ne$ and $^{21}Ne/^{22}Ne$ air ratio is taken from Ozima and Podosek, (2002), while the $^{40}Ar/^{36}Ar$ air ratio is taken from Lee et al. (2006).

Figure 9 shows a summary of the proposed mantle components for Canary and Cape Verde primitive magmas and shows also a clear regional distribution and an isotopic dichotomy of $^3He/^4He$ ratios in both silicate rocks and Cape Verde carbonatites. Samples from the northern Cape Verde Islands (e.g. S. Antão, S. Vicente and S. Nicolau) present a relatively primitive He signature, indicating the involvement of the relatively primordial mantle component in these magmas, while samples from the southern Cape Verde Islands (e.g. Fogo and Santiago) present MORB-like values (Doucelance et al., 2003; Mata et al., 2010). This regional distribution appears to be slight on Canary Islands, with an apparent increase of R/Ra from eastern (oldest) to western (youngest) Islands, and all islands with the exception of Fuerteventura, present a MORB-like values (Figure 9). Interestingly, both Fuerteventura carbonatites and silicate rocks, present R/Ra values lower to slightly lower than typical MORB mantle values, and they are in the range of SCLM.

A recent study on helium isotope variations in geothermal fluids of the Canary Islands (Day and Hilton, 2020) shows the presence of distinct He reservoirs, with a moderately radiogenic lead rich mantle source for La Palma (western Canaries) and a more enriched mantle source with the possible involvement of a continental lithospheric mantle influence for Tenerife (central Canaries). These authors show how the differences of $^3He/^4He$ ratios between La Palma and Tenerife are not evident if we consider the values from mineral separates (La Palma = 9.7-6.6Ra; Tenerife = 8.6-6.6Ra), which show considerable overlap (Figure 1 in Day and Hilton, 2020). On the contrary, the analysis in fluids and gases from geothermal systems of the same islands (La Palma = 9.27-8.79Ra; Tenerife = 6.63-6.09Ra) allow to identify a heterogeneous mantle below the Canary Islands.

To sum up, $^3He/^4He$ ratios in both silicate rocks and carbonatites from the northern Cape Verde Islands range from MORB-like values towards the high $^3He/^4He$ values that indicate a relatively primordial mantle signature, while $^3He/^4He$ ratios from southern Cape Verde Islands and Canary Islands range from MORB-like values extending to lower values, revealing the involvement of refertilized SCLM component in their source (Day and Hilton, 2011; Doucelance et al., 2003; Gurenko et al., 2006). He isotopic signature of Fuerteventura carbonatites clearly differs from Cape Verde carbonatites, in which are probably involved deep mantle plume-derived melts.

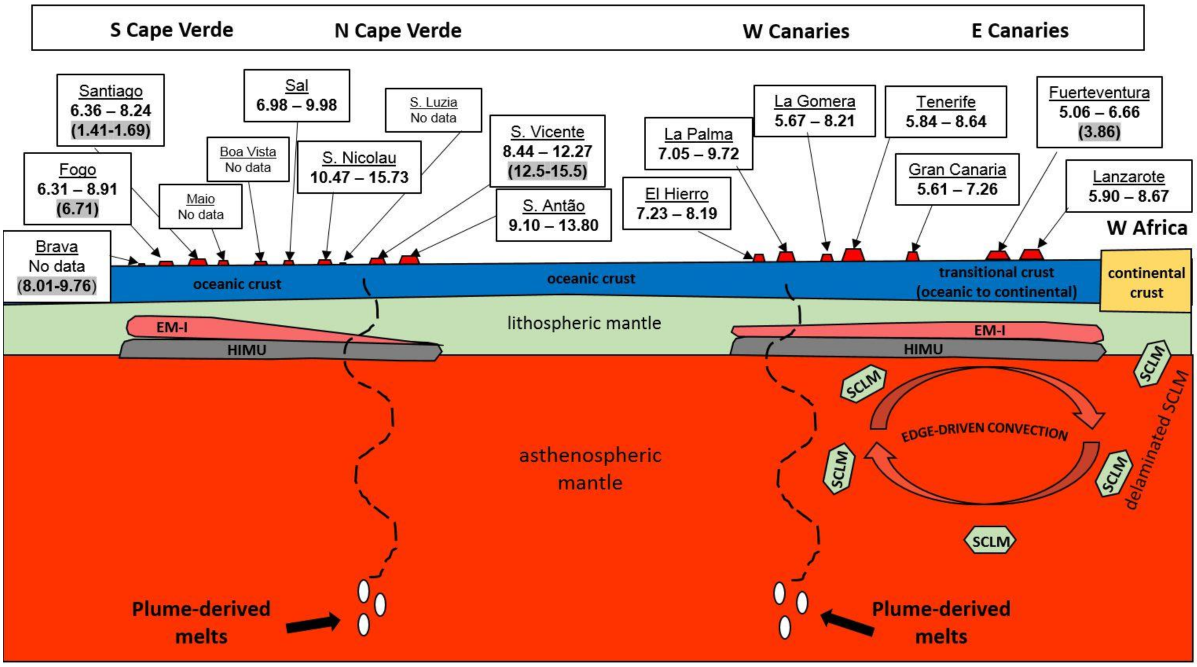

Figure 9. Hypothetical schematic profile view of the upper mantle/crust under Cape Verde and Canary Archipelago (not in scale) with the involvement of the proposed mantle components and the mechanism of physical detachment of the sub-continental lithospheric mantle (SCLM) caused by edge-driven convection during breakup of the Pangea Supercontinent and incorporated into the oceanic lithospheric mantle beneath at least some Canary Islands (Gurenko et al., 2010; Hoernle et al., 2002, 1991; Hoernle and Tilton, 1991). It is also shown a geographical distribution of the R/Ra range for each island of olivine (clinopyroxene in the case of Fuerteventura) from mafic/ultramafic rocks, and calcite from carbonatites (values in

grey field). Data of Canary Islands are from: (Gurenko et al., 2006) for Gran Canaria, Tenerife and La Gomera; (Day and Hilton, 2011) for La Palma and El Hierro; (Grachev, 2012) for Lanzarote. Data of Cape Verde Archipelago are from: (Christensen et al., 2001) for S. Antão; (Doucelance et al., 2003) for Fogo, Santiago, S. Vicente, S. Nicolau and Sal; (Mata et al., 2010) for Fogo, Santiago, S. Vicente and Brava (on carbonatites).

Conclusions

The comparison of our new data on trace elements in minerals and whole-rock and noble gases isotopes (He, Ne, Ar) of Fuerteventura carbonatites with literature data of Fuerteventura and Cape Verde oceanic carbonatites, allow to remark the following points:

- Even though Fuerteventura and Cape Verde oceanic carbonatites show some differences on trace elements compositions, due to the presence of different mineral phases, they depict almost the same patterns on multi-element and REE abundance diagrams.
- Carbon and oxygen isotope (δ^{13}C and δ^{18}O) compositions of Fuerteventura and Cape Verde carbonatites share a common isotopic signature, showing typical mantle-derived values and plotting into the so-called "primary igneous carbonatite" box.
- Although they present slight differences on Sr-Nd-Pb isotopic compositions, Fuerteventura and Cape Verde carbonatites seem to reflect contributions from three mantle components (DMM, EM-I and HIMU), particularly from a mixing between a MORB-like component and a second component resulting from an enriched mantle component and a moderately HIMU-like component, showing a similar trend on Sr-Pb and Nd-Pb diagrams.
- ^{3}He/^{4}He ratios of Fuerteventura carbonatites and adjacent clinopyroxenite are in the range of sub-continental lithospheric mantle (SCLM) and they are different if compared with He isotopic signature of Cape Verde carbonatites, in which a deep lower mantle contribution is present. Comparing major and trace elements and C-O-Sr-Nd-Pb-He-Ne-Ar isotopes of Fuerteventura and Cape Verde carbonatites, the only marked difference is represented by He isotopic signature, with a shallow (sub-continental lithospheric mantle, SCLM) He signature for Fuerteventura carbonatites, and a deep (lower mantle) He signature for Cape Verde carbonatites.

Future research on the importance of the heterogeneous metasomatism of the oceanic lithosphere (carbonatites occur only in few islands of Canary and Cape Verde Archipelagos) and a possible role of lithosphere thickness could be fundamental to understand why oceanic carbonatites are so rare and are not found in all HIMU-OIB-like archipelagos. As mantle reservoirs possibly sourcing carbonatites formation could be similar in some cases (plume-, MORB- or SCLM-), it would be reasonable to compare the mantle signature of noble gases in the studied oceanic carbonatites with intra-continental carbonatites. Furthermore, future research should be focused on obtaining stepwise crushing data for noble gases, in order to better characterize all the non-magmatic isotopic components contribution on large set of samples as well.

Appendix A

Table A1. Literature data of major and trace elements compositions of Fuerteventura and Cape Verde whole-rock carbonatites.

Occurrence	**Fuerteventura**		**Brava**		**Fogo**		**Santiago**		**S. Vicente**	
Sample	**68SC/73**	**F/75/65**	**Br-15**	**Br-23**	**F-211C**	**F-230B**	**S-309**	**S-311**	**SV-186**	**SV-188**
SiO$_2$ (wt.%)	5.85	0.92	3.04	0.27	4.62	5.81	4.12	0.84	0.80	0.56
TiO$_2$	0.34	0.02	0.21	0.00	0.29	0.09	0.47	0.08	0.03	0.03
Al$_2$O$_3$	3.24	0.35	0.52	0.10	1.02	1.44	0.35	0.11	0.18	0.08
Fe$_2$O$_{3\,t}$	6.20	0.36	3.93	2.16	3.54	1.87	4.67	2.64	1.20	1.10
MnO	0.24	0.26	0.27	0.36	0.18	0.22	0.26	0.31	0.10	0.22
MgO	0.96	0.11	0.45	0.12	1.05	0.57	1.89	0.38	0.58	0.67
CaO	48.10	51.40	49.75	53.87	49.51	49.35	48.82	53.92	54.76	54.59
Na$_2$O	1.16	0.35	0.31	0.08	0.21	0.61	0.31	0.16	0.11	0.11
K$_2$O	0.10	0.02	0.26	0.05	0.42	0.28	0.13	0.08	0.18	0.09
P$_2$O$_5$	1.51	1.36	5.63	0.21	3.30	2.11	8.94	2.39	3.27	0.56
LOI	31.50	42.60	34.20	42.33	35.93	36.78	29.26	39.56	39.39	42.00
Total	99.20	97.75	98.57	99.55	100.07	99.13	99.22	100.47	100.60	100.01
Sr (ppm)	8770	6900	8466	8622	7301	9222	8568	10000	5146	6423
Y	71.60	139	115	98.80	120	94.40	169	119	50.30	74.90
Rb	0.30	0.30	27	1	26	8	8	5	3	1
Ba	897	1070	314	1041	535	450	337	878	1582	7201
La	284	740	307	280	335	231	517	445	85.90	159
Ce	434	1380	608	502	689	394	1170	789	95.80	204
Pr	47	146	65.10	48.30	76.80	44.50	142	79.90	8.62	18.40
Nd	152	505	241	166	299	166	583	284	29.50	57.60
Sm	22.10	72.80	39.10	26.80	48.90	28.50	101	44.40	5.47	8.39
Eu	5.93	20.50	11.10	7.95	14.50	8.60	28.20	13.10	1.92	3.21
Gd	17.80	53.20	32.80	22.80	41.20	25.90	79.70	36.10	5.85	9.58
Tb	2.35	6.90	4.35	3.33	5.14	3.36	9	4.60	0.94	1.72
Dy	12.50	34.20	21.50	17.10	24.70	16.60	39.40	22.20	5.59	10.40
Ho	2.41	6.02	3.87	3.20	4.14	2.90	6.07	3.97	1.30	2.14
Er	6.40	14.80	10.70	9.22	10.90	7.85	14.90	10.70	4.47	6.68
Tm	0.84	1.81	1.48	1.36	1.40	1.08	1.85	1.47	0.79	1.14
Yb	5.09	10.80	8.41	9	7.80	6.09	9.92	8.76	5.54	7.83
Lu	0.69	1.39	1.12	1.28	1.01	0.78	1.18	1.14	0.88	1.18
Hf	0.06	0.08	1.50	0.20	1.30	1.60	0.60	0.50	0.20	0.30
Zr	2.30	2.30	103	4	24	223	539	33	11	7
Pb	1.46	10.10	n.d.	n.d.	n.d.	n.d.	n.d.	n.d.	n.d.	n.d.
Th	0.44	8.45	7.05	1.95	32.10	6.65	38.90	10.60	11.90	25.20
U	0.02	1.49	1.06	3.11	6.75	2.11	30.60	115	4.48	3.04
Nb	2.95	13	10.80	4.60	14.90	51.10	69.10	255	7.50	15.20
∑REE	993.11	2993.42	1355.53	1098.34	1559.49	937.16	2703.22	1744.34	252.57	491.27
Th/U	22	5.67	6.65	0.62	4.75	3.15	1.27	0.09	2.65	8.28
(La/Yb)$_N$	40.04	49.17	26.20	22.33	30.82	27.22	37.40	36.45	11.13	14.57
Eu/Eu *	0.88	0.96	0.92	0.96	0.96	0.95	0.93	0.97	1.03	1.09
Sr/Sr *	21.99	9.64	17.58	17.58	14.01	23.53	12.29	18.52	28.01	24.25

Note. In the sample references, Fuerteventura analysis are from Hoernle et al. (2002), Cape Verde analysis are from Doucelance et al. (2010). Eu* = EuN/(SmN x GdN)1/2 ; Sr* = (CeN + NdN)1/2. n.d. = not determined.

Table A2. Literature trace elements compositions of calcite and apatite on Cape Verde carbonatites.

Occurrence	**Brava**		**Fogo**		**S. Vicente**	
Mineral	**Calcite**					
Sample	**Br-15**	**Br-23**	**F-211C**	**F-230B**	**SV-186**	**SV-188**
Mn (ppm)	n.d.	n.d.	n.d.	n.d.	n.d.	n.d.
Sr	>1000	>1000	>1000	>1000	>1000	>1000
Y	92.50	83.70	99	81.50	24.20	101
Rb	1	0.80	0.80	1.10	0.90	1
Ba	467	613	596	554	603	2310
La	260	201	285	206	56.40	119
Ce	456	349	530	330	61.40	158
Pr	n.d.	n.d.	n.d.	n.d.	n.d.	n.d.
Nd	172	129	214	128	18.70	53.40
Sm	25.20	19.20	32.80	20.10	3.10	8.40
Eu	7.30	6.10	9.60	6.30	1.10	3.70
Gd	n.d.	n.d.	n.d.	n.d.	n.d.	n.d.
Tb	3.10	2.60	3.70	2.60	0.50	2.50
Dy	n.d.	n.d.	n.d.	n.d.	n.d.	n.d.
Ho	n.d.	n.d.	n.d.	n.d.	n.d.	n.d.
Er	n.d.	n.d.	n.d.	n.d.	n.d.	n.d.
Tm	n.d.	n.d.	n.d.	n.d.	n.d.	n.d.
Yb	8.20	8.70	7.40	5.90	2.60	9.50
Lu	1.10	1.20	1	0.80	0.40	1.30
Hf	<0.1	<0.1	<0.1	<0.1	<0.1	<0.1
Zr	0.80	0.60	0.50	1.10	12.70	8
Pb	n.d.	n.d.	n.d.	n.d.	n.d.	n.d.
Th	1.70	0.90	2.50	0.40	3.80	20.40
U	0.10	0.20	0.60	0.30	1.40	2.70
Nb	0.90	0.10	3	5.50	0.60	1.40
∑REE	n.d.	n.d.	n.d.	n.d.	n.d.	n.d.
Th/U	17	4.50	4.17	1.33	2.71	7.56
$(La/Yb)_N$	22.75	16.58	27.64	25.06	15.57	8.99
Eu/Eu *	n.d.	n.d.	n.d.	n.d.	n.d.	n.d.
Sr/Sr *	n.d.	n.d.	n.d.	n.d.	n.d.	n.d.
δCe	n.d.	n.d.	n.d.	n.d.	n.d.	n.d.
δEu	n.d.	n.d.	n.d.	n.d.	n.d.	n.d.
δY	n.d.	n.d.	n.d.	n.d.	n.d.	n.d.

Note. In the sample references, Cape Verde analysis are from Doucelance et al. (2010). n.d. = not determined.

Table A2. Continued.

Occurrence	**Brava**	**Fogo**		**Santiago**	
Mineral	**Apatite**				
Sample	**Br-15**	**F-211C**	**F-230B**	**S-309**	**S-311**
Mn (ppm)	n.d.	n.d.	n.d.	n.d.	n.d.
Sr	>1000	>1000	>1000	>1000	>1000
Y	228	402	317	285	223
Rb	1.70	0.50	8.50	0.50	1.20
Ba	671	397	137	376	881
La	834	1560	983	1120	1010
Ce	1930	3500	2000	2850	2310
Pr	n.d.	n.d.	n.d.	n.d.	n.d.
Nd	842	1700	967	1480	919
Sm	>100	>100	>100	>100	>100
Eu	37.10	79.60	52.80	69.50	43.90
Gd	n.d.	n.d.	n.d.	n.d.	n.d.
Tb	12.50	25.40	16.80	20	13.40
Dy	n.d.	n.d.	n.d.	n.d.	n.d.
Ho	n.d.	n.d.	n.d.	n.d.	n.d.
Er	n.d.	n.d.	n.d.	n.d.	n.d.
Tm	n.d.	n.d.	n.d.	n.d.	n.d.
Yb	13.40	20.90	15.50	14	11.30
Lu	1.50	2.20	1.60	1.70	1.20
Hf	0.30	0.30	0.20	0.20	0.10
Zr	7.50	18.10	13.40	8.70	13.20
Pb	n.d.	n.d.	n.d.	n.d.	n.d.
Th	39.50	133	44.20	55.80	30.20
U	3.40	13.90	11	7.60	1
Nb	1.20	20	9.90	3.30	4.60
∑REE	n.d.	n.d.	n.d.	n.d.	n.d.
Th/U	11.62	9.57	4.02	7.34	30.20
$(La/Yb)_N$	44.66	53.56	45.51	57.41	64.14
Eu/Eu *	n.d.	n.d.	n.d.	n.d.	n.d.
Sr/Sr *	n.d.	n.d.	n.d.	n.d.	n.d.
δCe	n.d.	n.d.	n.d.	n.d.	n.d.
δEu	n.d.	n.d.	n.d.	n.d.	n.d.
δY	n.d.	n.d.	n.d.	n.d.	n.d.

Note. In the sample references, Cape Verde analysis are from Doucelance et al. (2010). n.d. = not determined.

Table A3. δEu, δY and δCe of apatites from Fuerteventura carbonatites plotted on Figure 5.

Occurrence	**Fuerteventura**		
	δCe	δEu	δY
Apatite			
2_1CX02	1.09	0.84	0.79
2_1CX03	1.07	0.84	0.80
2_1CX04	1.09	0.83	0.85
2_1CX05	1.09	0.84	0.82
2_1CX06	1.09	0.89	0.83
2_1CX07	1.04	0.82	0.78
2_1CX08	1.06	0.87	0.80
2_1CX09	1.07	0.87	0.82
2_1CY02	1.05	0.87	0.84
2_1CY03	1.04	0.86	0.82
2_1CY04	1.07	0.86	0.81
2_1CY05	1.04	0.87	0.79
2_1CY06	1.05	0.87	0.79
2_1CY07	1.03	0.87	0.77
2_1CZ01	0.97	0.90	0.87
2_1CZ02	0.98	0.91	0.84
2_1CZ03	0.99	0.87	0.86
2_1CZ04	1.04	0.86	0.81
2_1CZ05	1.06	0.89	0.82
2_1CZ06	1.06	0.88	0.81
2_1CZ07	0.97	0.90	0.88

Note. See Subsubsection 5.1.1 in the text for δCe, δEu and δY calculation.

Table A4. Th and U concentrations and related ^{4}He* production on mineral separates from Cape Verde carbonatites.

	Th (ppm)	**U (ppm)**	**Age (Ma)**	**^{4}He*(μccSTP/g)**
Carbonatite				
Apatite				
Br-15	39.5	3.4	2	3.0
F-230B	44.2	11.0	4	10.3
S-309	55.8	7.6	9	22.4
Calcite				
Br-23	0.9	0.2	2	0.1
F-230B	0.4	0.3	4	0.2
SV-186	3.8	1.4	5.7	1.6
SV-188	20.4	2.7	5.7	5.1

Note. Analysis and ages from Mata et al. (2010). The equation ^{4}He* ≈ 2.8 x 10-8 (4.35 + Th/U) · (U) · (t) was used to calculate the ^{4}He* radiogenic (from Mata et al., 2010). [Th] and [U] in ppm, t in Ma.

Table A5. He concentrations (ccSTP/g) and He, Ne, Ar isotopic ratios on mineral separates from Cape Verde carbonatites.

	^{4}He (10^{-7})	**^{3}He (10^{-12})**	**R/Ra**	**1σ**	**^{4}He/^{20}Ne**	**^{20}Ne/^{22}Ne**	**1σ**	**^{21}Ne/^{22}Ne**	**1σ**	**^{40}Ar/^{36}Ar**	**1σ**
Carbonatite											
Apatite											
Br-15 step 1	0.69	0.93	9.76	0.51	1000.4	10.34	0.04	0.0314	0.0008	624	2
F-230B step 1	1.07	0.10	0.67	0.14	508.4	9.88	0.03	0.0293	0.0005	531	2
S-309 step 1	1.49	0.34	1.64	0.17	8017.5	9.73	0.11	0.0298	0.0015	736	9
Calcite											
Br-23	1.6	2.00	9.02	0.71	172	9.89	0.02	0.0301	0.0005	363	19
F-230B	1.1	1.02	6.71	0.43	738	9.86	0.05	0.0318	0.0011	414	21
SV-186 step 1	5.1	10.91	15.5	0.22	850	9.83	0.02	0.0289	0.0005	354	18
SV-188	8.3	14.45	12.6	0.20	5460	9.83	0.02	0.0294	0.0004	363	19
Air			**1.00**			**9.80**		**0.0290**		**298.6 +/- 0.3**	

Note. Analysis from Mata et al., (2010). The atmospheric value for ^{20}Ne/^{22}Ne and ^{21}Ne/^{22}Ne is taken from Ozima and Podosek (2002), while for ^{40}Ar/^{36}Ar is taken from Lee et al. (2006).

4.2 Application of Fe isotopes in oceanic carbonatites: preliminary results

During the last two decades the stable and radiogenic isotope studies of carbonatites has grown exponentially, and this also includes nontraditional stable isotope systems such as $^{7}Li/^{6}Li$ or $^{44}Ca/^{42}Ca$ (*e.g.*, Halama et al., 2008; Amsellam et al., 2020; Sun et al., 2021). This ever-growing isotope dataset is principally used to address the long-standing questions of the carbonatite magmas: if they are derived from lithospheric or asthenospheric mantle source, if they are related to a deeply sourced mantle plume in their origin, and if the carbonate assimilation plays an important role in their origin and evolution. Among nontraditional stable isotope systems, Fe isotopes have the particular sensitivity to trace processes commonly invoked in models for carbonatite genesis and evolution, including magmatic and fluid evolution, crystal fractionation and liquid immiscibility.

The first application of Fe isotopes in carbonatites, including whole rocks and mineral phases, was performed by Johnson et al. (2010). Data of Fe isotopes are reported in standard δ notation, in $\delta^{56}Fe$ and $\delta^{57}Fe$, where $\delta^{56}Fe = [(^{56}Fe/^{54}Fe)_{sample} / (^{56}Fe/^{54}Fe)_{standard} - 1] \times 10^{3}$ (equation (1) from Johnson et al., 2010). The $(^{56}Fe/^{54}Fe)_{standard}$ is referred to the average terrestrial igneous rocks (Beard et al., 2003). The authors show how carbonatites present the largest range in Fe isotope compositions among igneous rocks ($-1 < \delta^{56}Fe > +0.8\%$), in contrast to the relatively restricted range for mantle-derived basaltic magmas ($\delta^{56}Fe = 0.0 \pm 0.1\%$) (**Fig. 4.1**).

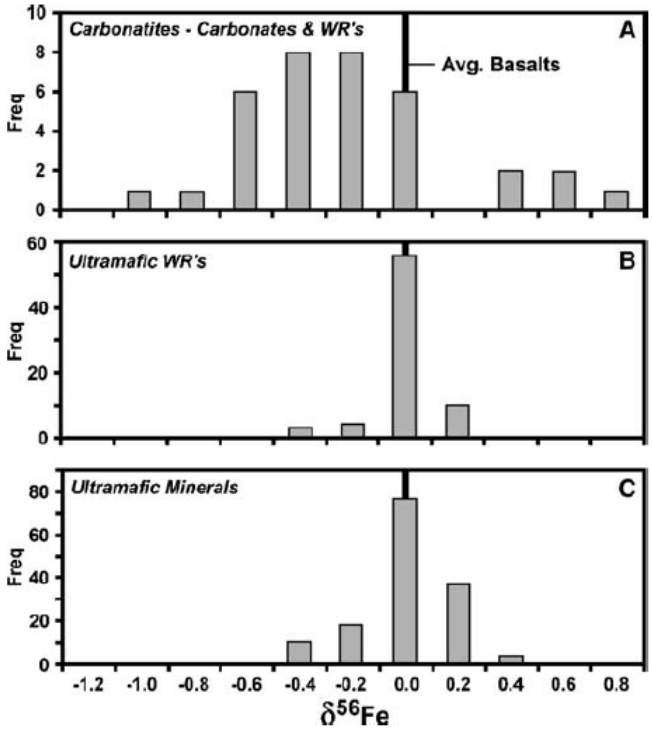

Fig. 4.1: Histograms of $\delta^{56}Fe$ values for carbonatites (a), whole rock samples for ultramafic rocks (b), and ultramafic minerals (c) (Johnson et al., 2010).

Interestingly, our results show a relatively restricted range of δ^{56}Fe in Fuerteventura oceanic carbonatites (whole rock analyses) (δ^{56}Fe between -0.15 and -0.02 ‰; δ^{57}Fe between -0.27 and -0.05 ‰) if compared with other carbonatite occurrences (**Fig. 4.2**). Ca-carbonate magmas in equilibrium with silicate mantle present δ^{56}Fe value of ≈ -0.3 ‰ (Johnson et al., 2010). However, more negative δ^{56}Fe values (< -0.3 ‰) are produced by several differentiation processes such as crystal fractionation or liquid immiscibility, while positive δ^{56}Fe values are related to the interaction between low-Fe carbonates and Fe^{3+} -rich fluids near igneous temperatures (Johnson et al., 2010). Although it is a preliminary study, Fe isotope data in Fuerteventura carbonatites reflect some differentiation process, mostly liquid immiscibility with the silicate melt counterpart, but further detailed analyses are needed to constrain the petrogenetic and differentiation processes.

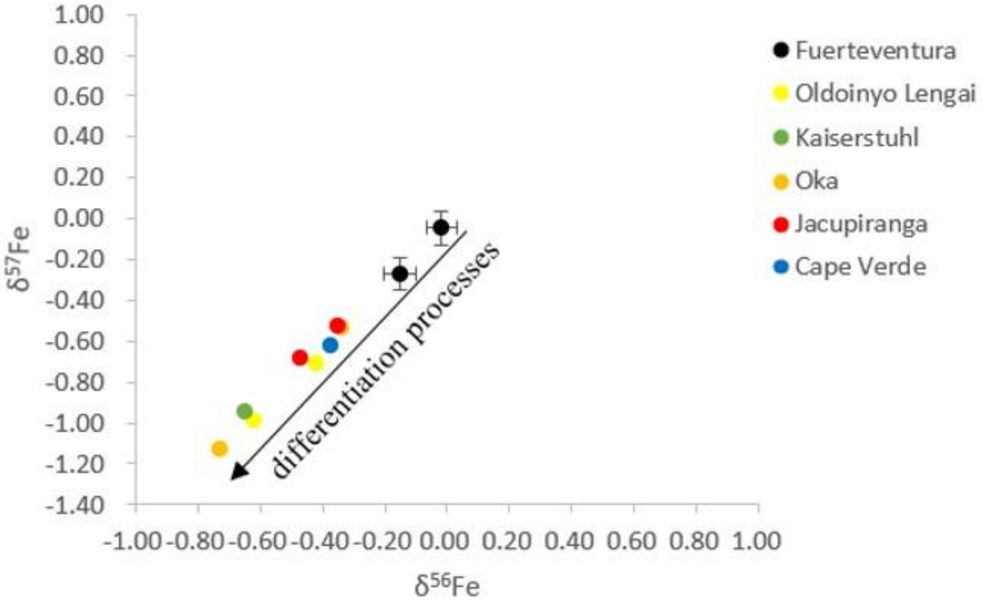

Fig. 4.2: δ^{56}Fe vs. δ^{56}Fe values for Fuerteventura carbonatites. Values from other carbonatite occurrences are depicted for comparison (from Johnson et al., 2010 and references therein). Intrusive carbonatites from Fuerteventura, Kaiserstuhl, Oka, and Jacupiranga, while effusive carbonatites from Oldoinyo Lengai and Cape Verde.

4.3 Hydrothermal fluids and formation conditions of REE enrichment in Fuerteventura carbonatites

Carbonatitic dykes that crop out in the central western part of Fuerteventura Basal Complex were affected by the Miocene intrusive event responsible for contact metamorphism and partial melting of part of the alkaline-carbonatitic complex (Casillas et al., 2011). Indeed, the original igneous mineralogy disappeared, and a metamorphic association composed of wollastonite, monticellite, diopside, vesuvianite, garnet, calcite, perovskite, alabandite, pyrrhotite and Nb–Zr–Ca silicates (cuspidine–niocalite–baghdadite series) was formed (Casillas et al., 2011), although this association is also related to late-magmatic stage of peralkaline and differentiated rocks (Sharygin et al., 1996).

The absence of metamorphic minerals typical of the contact zone, together with the presence of primary magmatic minerals such as apatite, biotite, and aegirine-augite, indicate that carbonatite outcrops in Punta de La Nao (Ajuy-Solapa sector) escaped this thermal overprint and preserve their original igneous assemblage and textures (Carnevale et al., 2020). Furthermore, the presence of monazite enriched in LREE (La, Ce, Nd) formation processes in microfractures that affect zircon crystals (**Fig. 4.3**), suggest carbonatite interactions with hydrothermal fluids and partial REE remobilization processes. Indeed, at sub-solidus temperatures (T > 600 °C) and the brine-melt stage ($600 \leq T \leq 400$ °C), where REEs are sufficiently concentrated in the residual brine-melt to form REE-minerals, the infiltrating fluids during the hydrothermal stage play an important role in the transport and concentration of REEs. The identification of chlorite (d_{001}=14 Å), vermiculite (d_{001}=16,6 Å) and interstratified illite-smectite (d_{001}=13 Å) as hydrothermal alteration minerals (**Fig. 4.4**), allows to frame the hydrothermal event in the metamorphic facies of zeolites, and the formation of these hydrothermal alteration minerals is due to a metasomatism process caused by the exsolution of a hydrothermal fluid phase from the magma that gave rise to carbonatite in the last moments of cooling (i.e. *autometasomatism*, a common process in intrusive carbonatites).

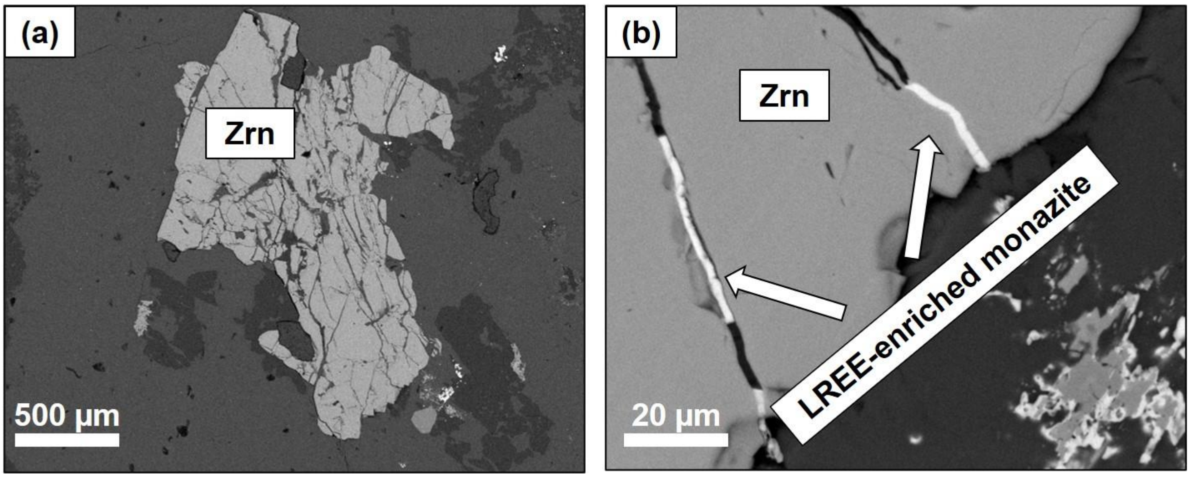

Fig. 4.3: Backscattered electron images (BSE) of (a) zircon (Zrn) crystal and (b) filled microfractures in zircon crystal with monazite enriched in LREE (La, Ce, Nd).

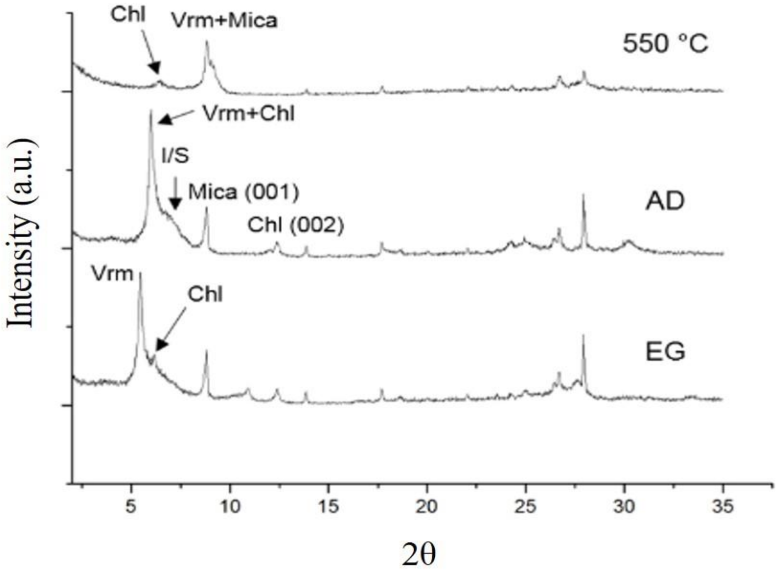

Fig. 4.4: Diffractograms of oriented aggregates of < 2µm fraction. Thermal treatment (550 °C), air-dried (AD) and ethylene glycol treatment (EG). Chl=chlorite, Mica=biotite-phlogopite, I/S=illite/smectite, Vrm=vermiculite.

In order to further constrain the formation conditions and characterize the late-stage hydrothermal fluids, the study of fluid inclusions (FIs) in carbonatite rocks is essential, and micro-thermometric studies represent the most straightforward method to obtain information about fluid temperature, pressure and composition (e.g., Walter et al., 2020; Carnevale et al., 2022). Fluid inclusions which are formed during the formation of the host mineral phase are considered primary in origin and they are generally trapped along the growth zone or tend to occur isolated. Fuerteventura carbonatites shows the presence of isolated FIs in host calcite minerals (**Fig. 4.5**), suggesting a primary origin, although additional criteria related to crystal growth would be useful to confirm their primary nature. The size of the inclusions is < 10 µm, and they mostly are in the range of 1-5 µm. Their shape is generally irregular, with negative-crystal forms and square shapes, according to the host calcite mineral. Few rounded isolated FIs in apatite are also present. Some FIs show textural characteristics of partial decrepitation, such as haloes of tiny fluid inclusions (diameter < 0.1 µm) surrounding the inclusion cavity, revealing that some events of partial density re-equilibration have occurred. Some intragranular trails (according with trail terminology described in Randive et al., 2014) confined within calcite grain-boundary and crystal interior are also found (**Fig. 4.6**).

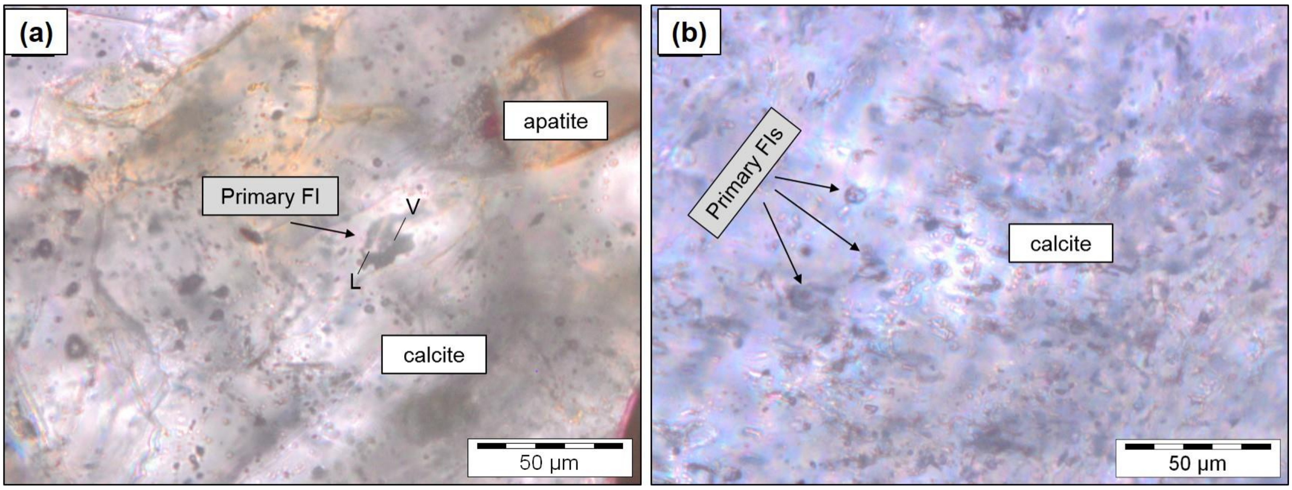

Fig. 4.5: Photomicrographs of fluid inclusions from Fuerteventura carbonatites. a) Primary fluid inclusions in calcite (L=liquid phase; V=vapour phase). b) Different primary fluid inclusions in calcite.

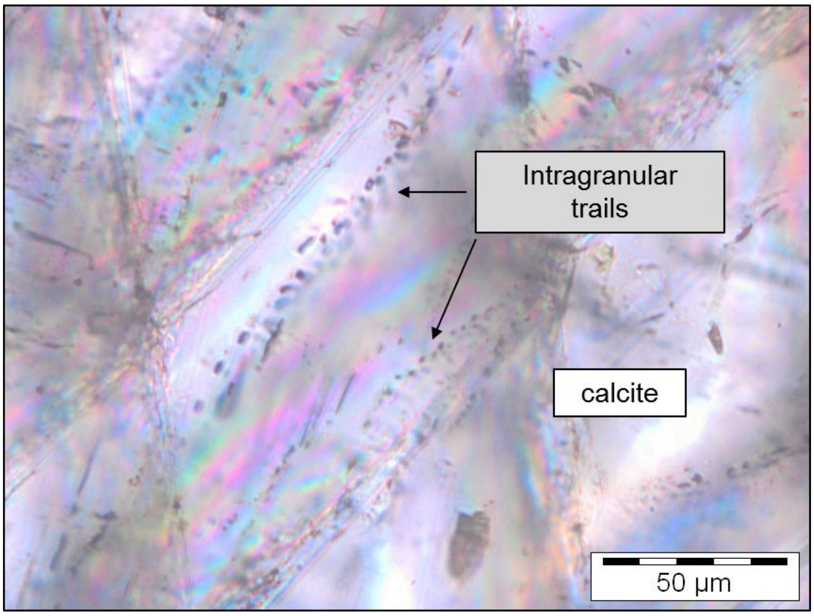

Fig. 4.6: Photomicrograph of intragranular fluid inclusions in calcite from Fuerteventura carbonatites.

Observing the temperatures of phase changes in FIs during heating/cooling analyses, it is possible to know the composition of the inclusions for the appropriate chemical system, because each chemical system has its own eutectic temperature (Te). However, some authors suggest to use the term "first melting temperature" (Tfm) or "apparent eutectic temperature" (Te*) instead of eutectic temperature, as this term is more observational rather than theoretical (Chi et al., 2021). Indeed, results of apparent eutectic temperatures should be considered as approximate rather than exact. Results show apparent eutectic temperatures ranging from -21.7 to -21.0 °C, although the small dimension of FIs did not allow the correct determination of Te* for almost all inclusions. Thus, the eutectic behavior and the narrow range of measured Te* suggest the well know binary NaCl-H_2O system (Te = -21.2 °C) as a characterizing chemical system in studied FIs. No CO_2 was detected (the eutectic temperature of pure CO_2 is -56.6 °C).

At room temperature the studied fluid inclusions were essentially two phases, liquid and vapour (L + V), commonly liquid rich, or rarely multiphase with the presence of daughter phases (probably hydrohalite, $NaCl \cdot 2H_2O$). With the Te* range and the chemical system, the final ice melting temperatures (Tim) during heating was also measured, in order to calculate the salinity (expressed as wt. % $NaCl_{eq}$) using the $NaCl$-H_2O phase diagram of the empirical expression given by Bodnar (1993). The final ice melting temperatures range between -3.2 and -2.1 °C, corresponding to salinities of 5.3 and 3.6 wt. % $NaCl_{eq}$, respectively.

All studied fluid inclusions homogenize to liquid phase (Th_L; L + V = L), with homogenization temperature ranging from 142.7 to 208.7 °C (corresponding to densities of 0.95 and 0.88 g/cm^3, respectively) and homogenization pressures ranging from 4.6 to 15.3 bars. A sketch showing the complete procedure of cooling and heating analyses of studied fluid inclusions in order to measure apparent eutectic temperature (Te*), final ice melting temperature (Tim) and homogenization temperature (Th), is presented (**Fig. 4.7**).

Normally, the homogenization temperature is less than the real trapping temperature, although if there is no evidence that fluid inclusions have re-equilibrated and they were trapped in an immiscible fluid system, then the homogenization temperature is equal to the real trapping temperature (Bodnar, 2003). In this case a pressure correction (the difference between homogenization temperature and estimated trapping temperature of the fluid inclusions) must be added to the measured homogenization temperatures to obtain the trapping temperatures. Indeed, our study shows no evidences of immiscible fluid system with the presence of some fluid inclusions with partial decrepitation. In order to estimate a pressure correction, it is necessary to determine the slope of the isochores along which the fluid inclusions were trapped. In **Figure 4.8** the results of the equation described in the fluid inclusion technique of Bodnar and Vityk (1994), with the relationship between trapping temperature and pressure, salinity (about 5 wt % $NaCl_{eq}$ in our case) and homogenization temperatures are reported. The slope of the iso-Th lines (≅ isochores) for $NaCl$-H_2O solutions with salinity of 5 wt. % and homogenization temperatures ranging from 50 to 700 °C, with an upper limit of 6 kbar are shown. To resume, micro-thermometric studies on Fuerteventura carbonatites shows the presence of low salinity (≅ 5 wt. % $NaCl_{eq}$) and low temperatures (< 300 °C) fluids trapped within primary calcite crystals, corroborating that processes of fluid/rock interaction occurred. Thus, REEs can be mobilised and concentrated on the local scale by low-temperature hydrothermal fluids with a process known as autometasomatism, accordingly with the more recent classification proposed by

Mitchell and Gittings (2022) using the term carbo-hydrothermalite, where a carbonatite can precipitate at sub-solidus temperatures from a mixed CO_2–H_2O fluid during late-stage processes.

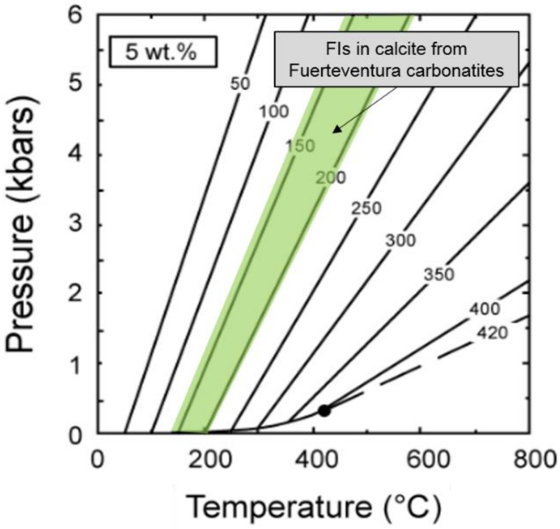

Fig. 4.7: Sketch showing the phase behaviour of an H_2O-NaCl fluid inclusion during a complete procedure of a micro-thermometric analysis. The fluid inclusion is first cooled and then heated in order to observe the phase changes. The sketch shows the example of a studied fluid inclusion.

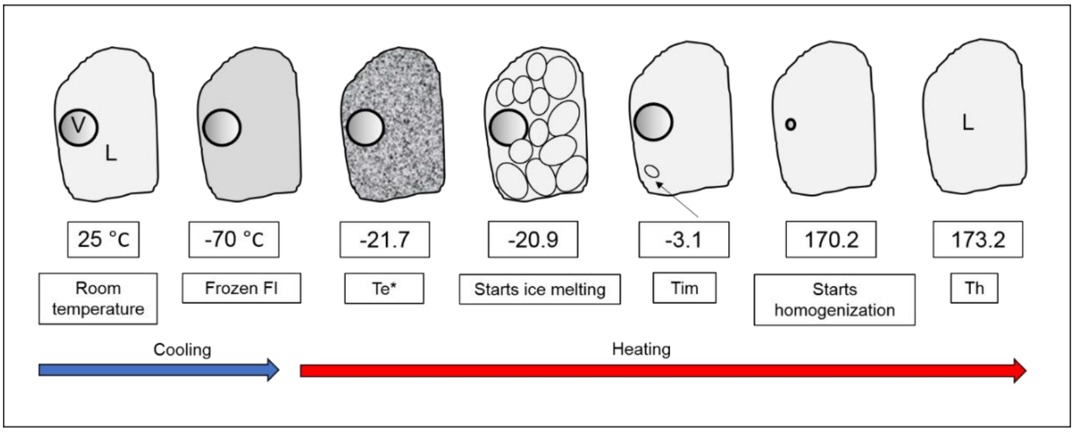

Fig. 4.8: Iso-Th curves for NaCl-H_2O inclusions having salinity of 5 wt.% NaCl. Th range of studied fluid inclusions depicted in green.

Chapter 5: Intra-continental carbonatites: the case study of Mt. Vulture (southern Italy)

Here is presented a recent published paper (Carnevale et al., 2022) dealing with the studied Mt. Vulture products, in order to provide important information about the melilitite-carbonatite magma ascent path and its mantle source, describing the volcano plumbing system and the way in which the particular melilitite-carbonatite magmas are transported to the surface, with possible implications in terms of volcanic hazard. Considerations about (i) the role of the carbonatite melts in metasomatizing the mantle source (with particular attention to *wehrlitization* process), (ii) the geothermobarometric and oxybarometric conditions, and (iii) the signature of noble gases isotopes are also implemented.

5.1 Mt. Vulture carbonatites and xenoliths: a look into the mantle

The carbonatite magmatism from Mt. Vulture is essentially associated to the last eruptive activity of the volcano (≈ 140 ka), and it is very different if compared with Fuerteventura carbonatite magmatism (i.e., intrusive oceanic Ca-carbonatites). The carbonatitic affinity is mainly related to the presence of ash-rich tuff deposits with a melilitite-carbonatite matrix and carbonatite-rich layers within the matrix. Thus, this work is focused not only on the nature of the carbonate-rich matrix, but also on the mantle processes that gave rise the carbonatitic affinity in the Mt. Vulture magmatism, with a particular focus on the role of the primary carbonatite melts in metasomatizing the mantle and how the melts react with the surrounding mantle ultramafic rocks. For this reason, in the following sub-sub-chapters, in addition to the direct study of the carbonate-rich layers within the ash-rich tuff deposits, a complete characterization of mantle xenoliths enclosed within the matrix is implemented, in order to constrain the mantle metasomatism processes beneath the Mt. Vulture and consequently beneath the general context of central-southern Italy.

5.1.1 Petrography

The presence of ash-rich tuff deposits with a melilitite-carbonatite matrix and carbonatite-rich layers within the matrix, reflects the direct evidence of carbonatite magmatism. Furthermore, a robust amount of pelletal lapilli (enclosing mantle xenoliths) and mantle xenoliths from the melilitite-carbonatite matrix, represents a great tool to understand the composition and possible modification of a mantle source influenced by carbonatite metasomatic fluids. Twenty-nine pelletal lapilli (LAP01-29) and six mantle xenoliths (SLP-xen01-04,06; SMC$_{(B)}$-xen01) were selected from different ash-rich tuff deposits. The ultramafic core of pelletal lapilli is essentially formed by olivine and clinopyroxene with rare occurrence of orthopyroxene, although in some samples olivine megacrysts are the only mineral phase. Thus, they can be classified as wehrlites, or dunites if the presence of clinopyroxene and orthopyroxene is very subordinate, if any. On the contrary, in mantle xenoliths the presence of orthopyroxene is more abundant, indeed one sample (SLP-xen01) can be classified as lherzolite, although the other samples are wehrlite (SLP-xen02,04,06), olivine-clinopyroxenite (SLP-xen03) and dunite (SMC$_{(B)}$-xen01). All studied samples are plotted onto the ultramafic classification ternary diagram (**Fig. 5.1**).

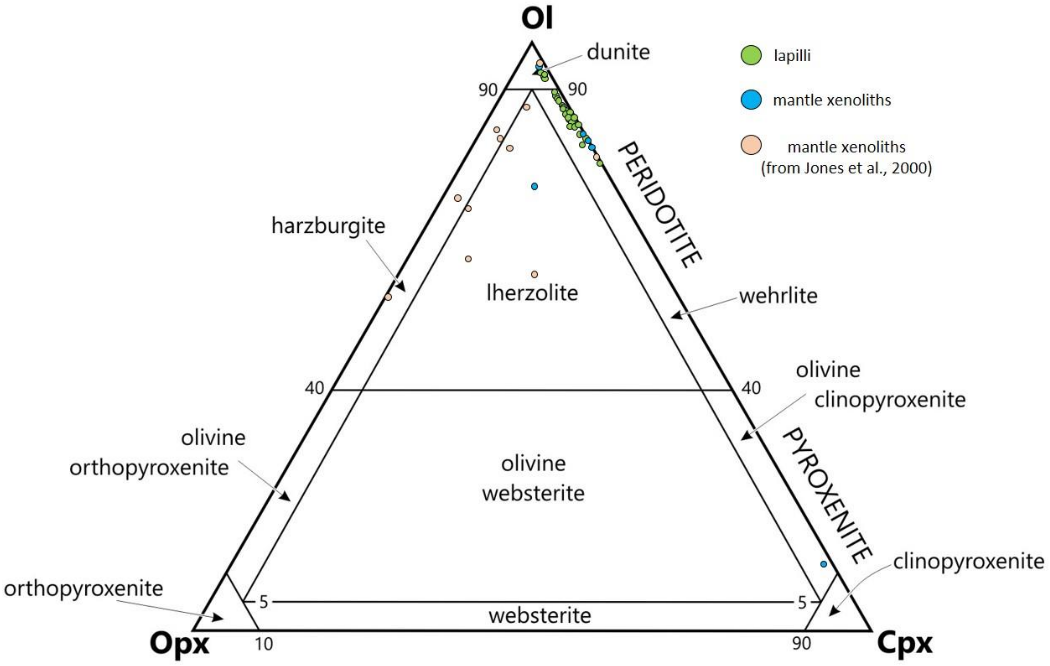

Fig. 5.1: Classification ternary diagram of studied Mt. Vulture lapilli and mantle xenoliths.

The ultramafic core of pelletal lapilli exhibit a fine- to medium-grained and idioblastic to sub-idioblastic equigranular texture, with a granoblastic to granoblastic-decussate metamorphic structure, where the interlocking and randomly oriented olivine and clinopyroxene grains are variably elongated (**Fig. 5.2**). Indeed, olivine usually shows undulose extinction and deformation structures as micro-faults. Inclusions of spinel in olivine micro-phenocrysts are also present. Clinopyroxene (distinctive emerald green coloured Cr-diopside) occurs as sub-hedral/anhedral with strongly curvilinear boundaries, with no deformation structures. The rim of pelletal lapilli is composed of fine-grained xenocrystic debris of olivine and clinopyroxene, with microcrysts of häuyne and melilite laths (± calcite), forming concentric layers of silicate- and carbonate-rich composition. Olivine microcrysts appear as fragmented, while clinopyroxene and häuyne occur as subhedral to euhedral microcrysts (**Fig. 5.2**).

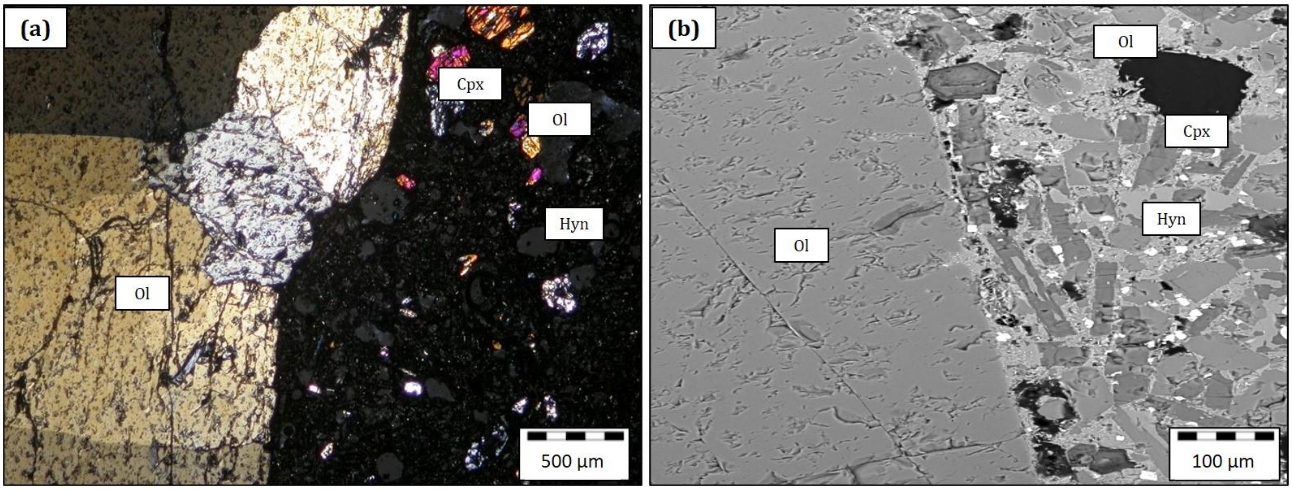

Fig. 5.2: Crossed polars microphotograph (a) and backscattered electrons (BSE) image (b) showing the core (on the left) and the rim (on the right) of pelletal lapilli from Mt. Vulture. Ol-olivine, Cpx-clinopyroxene, Hyn-häuyne.

Samples of mantle xenoliths are rounded, of an average 4-5 cm in diameter, with some rarely samples up to 10 cm. The grain size of the mantle xenoliths is variable, fine- to medium-grained (0.5-1 mm) in the case of the lherzolite (SLP-xen01) and wehrlite (SLP-xen02,04), medium- to coarse-grained (2-5 mm) in the case of the wehrlite (SLP-xen06), ol-clinopyroxenite (SLP-xen03) and dunite (SMC$_{(B)}$-xen01) (**Figs. 5.3** and **5.4**). The texture is usually equigranular and sub-idioblastic, with the exception of dunite xenolith that show an inequigranular texture. All xenoliths show a granoblastic-decussate structure, where the interlocking and randomly oriented grains are variably elongated. Well-defined triple junctions are common. Olivine usually shows undulose extinction and deformation structures such as kink bands, while orthopyroxene and clinopyroxene (emerald green Cr-diopside) occur as subhedral/anhedral with curvilinear boundaries. Spinel is also present as subhedral/anhedral, with colour varying from brown to dark brown. Noteworthy, is the presence in the xenoliths of phlogopite and reaction rim in orthopyroxene replaced by a very fine-grained assemblage of olivine and clinopyroxene microcrysts (**Fig. 5.4**), suggesting that metasomatism processes occurred (more details about carbonatite metasomatism and the process of *wehrlitization* in the Sub-Chapter 5.2).

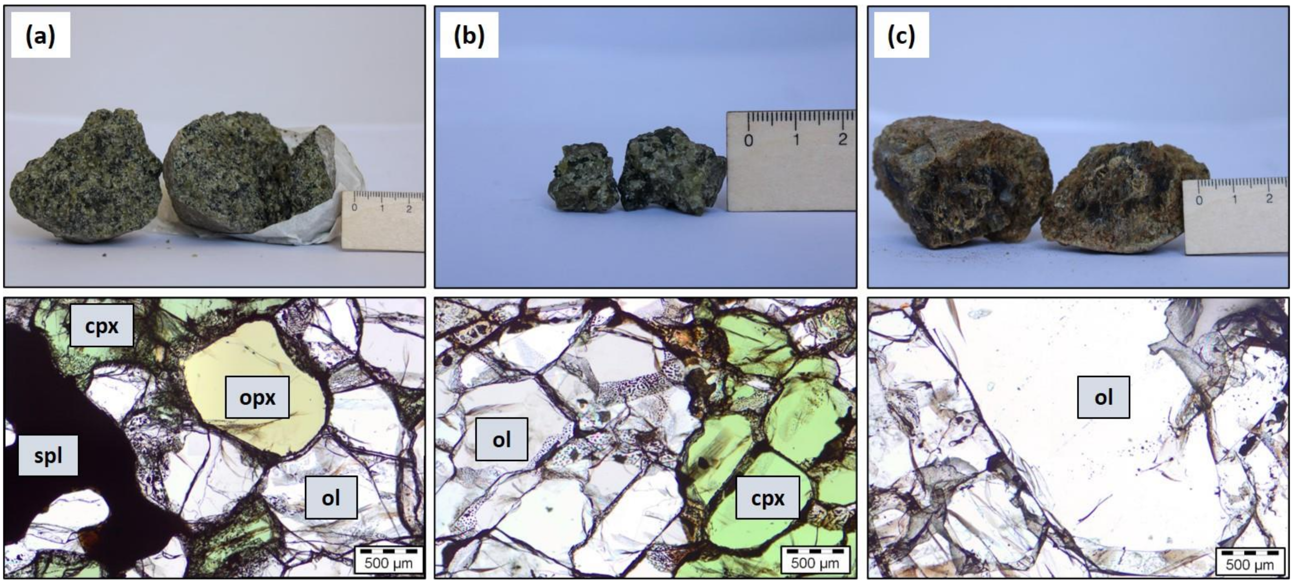

Fig. 5.3: Mantle xenoliths hand specimens and related parallel polars (PPL) photomicrographs of (a) fine-grained lherzolite, (b) medium-grained wehrlite, and (c) coarse-grained dunite, respectively. ol = olivine; opx = orthopyroxene; cpx = clinopyroxene (emerald green Cr-diopside); spl = spinel.

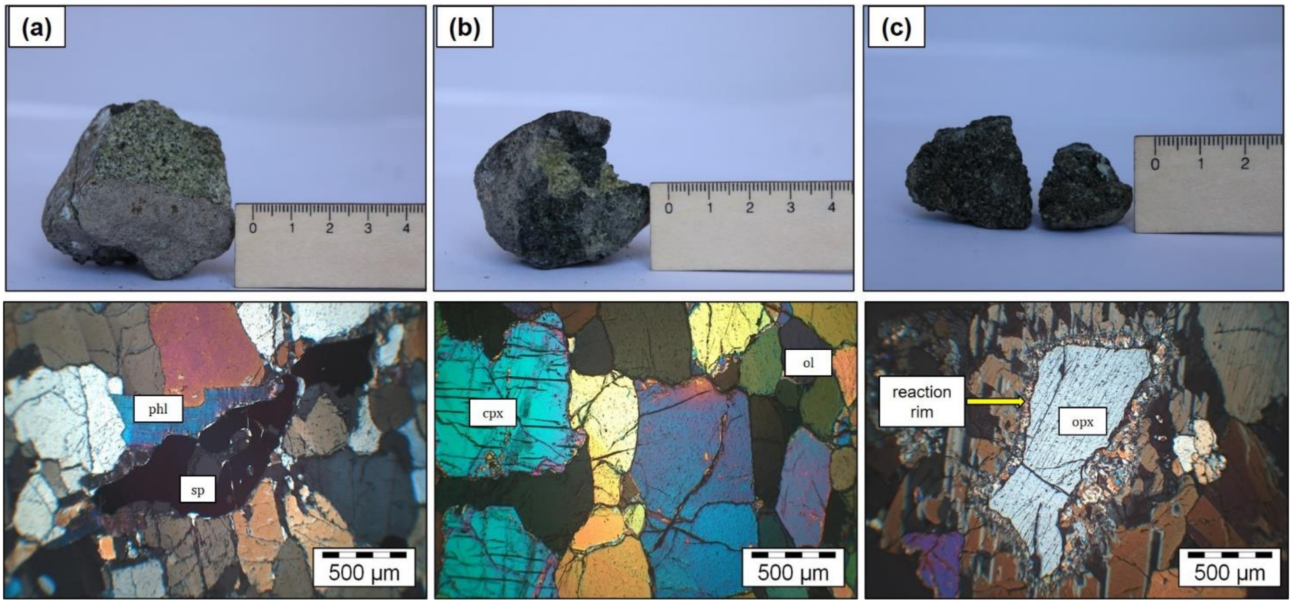

Fig. 5.4: Mantle xenoliths hand specimens and related parallel polars (PPL) photomicrographs of (a) fine-grained wehrlite, (b) medium-grained ol-clinopyroxenite, and (c) medium-grained wehrlite, respectively. ol = olivine; opx = orthopyroxene; cpx = clinopyroxene (emerald green Cr-diopside); spl = spinel.

5.1.2 Mineral and whole-rock chemistry

Loose (disaggregated) mafic minerals in the melilitite-carbonatite matrix generally show primitive composition. Olivine shows Mg-rich composition (Fo_{89-92}), with NiO varying from 0.37 to 0.41 wt. % and FeO_{tot} from 8.11 to 10.35 wt. % (**Table 2**). Clinopyroxene are Cr-rich diopside (Wo_{46-48}, En_{47-48}, Fs_{4-6}) with relatively high Cr_2O_3 (0.4-1.3 wt. %). SiO_2 and CaO content in clinopyroxene xenocrysts ranges from 52.2 to 54.6 wt.%, and from 20.1 to 22.7 wt.%, respectively. TiO_2 and Al_2O_3 content is low and ranges from 0.15 to 0.5 wt.% and from 2 to 5.5 wt.%, respectively (**Table 3**).

The chemical composition of olivine and clinopyroxene minerals within the ultramafic core of pelletal lapilli is similar to those from the loose xenocrysts. Olivine also shows Mg-rich composition (Fo_{90-91}) and relatively high NiO (0.3 to 0.4 wt. %) (**Table 2**), and clinopyroxene are also diopside (Wo_{46-48}, En_{47-48}, Fs_{4-5}) with high Cr_2O_3 (1.3-1.5 wt. %) and high Mg# values (0.90 to 0.92). SiO_2 and CaO content of clinopyroxene from the ultramafic core of pelletal lapilli ranges from 51.7 to 53.1 wt.% and from 22.2 to 22.9 wt.%, respectively. TiO_2 and Al_2O_3 content is also low and ranges from 0.15 to 0.5 wt.% and from 3.6 to 4 wt.%, respectively (**Table 3**).

Table 2. Minero-chemical composition of loose olivine xenocrysts and from the core of pelletal lapilli from Vulture volcano, Monticchio Lakes Synthem.

Sample	ol-xeno1	ol-xeno2	ol-xeno3	ol-xeno4	ol-xeno5	ol-xeno6	ol-xeno7
	xenocryst	xenocryst	xenocryst	xenocryst	xenocryst	xenocryst	xenocryst
SiO_2 (wt. %)	40.50	39.65	40.56	41.50	40.09	41.67	40.97
$FeO_{tot.}$	9.36	10.35	8.11	9.66	9.06	8.49	10.11
MnO	0.14	0.15	0.11	0.13	0.12	0.11	0.14
MgO	49.87	48.97	50.75	50.72	49.83	49.60	50.32
CaO	0.15	0.14	0.19	0.18	0.12	0.18	0.14
Cr_2O_3	0.03	0.02	0.04	0.02	0.04	0.03	0.02
NiO	0.38	0.37	0.41	0.37	0.40	0.39	0.37
Tot.	100.43	99.64	100.16	102.59	99.66	100.48	102.07
Fo	90.48	89.40	91.78	90.35	90.75	91.24	89.87
Fa	9.52	10.60	8.22	9.65	9.25	8.76	10.13

Notes: Each reported analysis is the mean of three spots and core-rim analyses do not show significant zonation.

Table 2. Cont.

Sample	ol-lap1	ol-lap2	ol-lap3	ol-lap4	ol-lap5	ol-lap6	ol-lap7
	core	core	core	core	core	core	core
SiO_2 (wt. %)	41.73	41.70	41.97	42.04	40.76	40.66	40.22
$FeO_{tot.}$	8.97	9.15	9.02	8.97	9.03	10.07	9.00
MnO	0.14	0.14	0.14	0.14	0.13	0.16	0.14
MgO	49.62	49.79	49.66	49.71	50.09	50.80	51.48
CaO	0.09	0.09	0.08	0.09	0.09	0.10	0.09
Cr_2O_3	0.03	0.03	0.03	0.03	0.03	0.03	0.03
NiO	0.38	0.37	0.38	0.37	0.39	0.35	0.37
Tot.	100.95	101.27	101.28	101.35	100.52	102.16	101.33
Mg#	0.91	0.91	0.91	0.91	0.91	0.90	0.91
Fo	90.79	90.65	90.75	90.81	90.82	90.00	91.07
Fa	9.21	9.35	9.25	9.19	9.18	10.00	8.93

Notes: Each reported analysis is the mean of three spots and core-rim analyses do not show significant zonation.

Table 3. Minero-chemical composition of loose clinopyroxene xenocrysts and from the core of pelletal lapilli from Vulture volcano, Monticchio Lakes Synthem.

Sample	Cr-di1	Cr-di2	Cr-di3	Cr-di4	Cr-di5	Cr-di6	Cr-di7
	xenocryst	xenocryst	xenocryst	xenocryst	xenocryst	xenocryst	xenocryst
SiO_2 (wt. %)	54.56	53.09	52.91	52.81	53.13	52.46	52.19
TiO_2	0.16	0.31	0.37	0.38	0.43	0.14	0.48
Al_2O_3	2.09	3.67	3.84	3.80	4.55	5.48	5.19
FeO	3.02	2.90	3.20	2.91	3.33	3.20	3.42
MnO	0.00	0.00	0.00	0.00	0.00	0.00	0.00
MgO	17.42	16.12	16.12	16.52	15.91	16.55	16.25
CaO	21.43	22.41	22.38	22.71	21.91	20.15	21.98
Na_2O	0.73	0.64	0.71	0.61	0.75	1.10	0.79
Cr_2O_3	1.15	1.28	0.92	0.93	0.42	1.25	0.86
Tot.	100.55	100.42	100.45	100.67	100.42	100.33	101.16
Mg#	0.91	0.91	0.90	0.91	0.90	0.90	0.89
Wo	44.62	47.58	47.31	47.34	46.97	44.12	46.51
En	50.47	47.62	47.42	47.93	47.47	50.42	47.84
Fs	4.91	4.80	5.28	4.73	5.56	5.47	5.64

Notes: Mg# = (Mg/Mg + Fe). Each reported analysis is the mean of three spots and core-rim analyses do not show significant zonation.

Table 3. Cont.

Sample	Cr-di lap1	Cr-di lap2	Cr-di lap3	Cr-di lap4
	core	core	core	core
SiO_2 (wt. %)	52.3039	52.9848	53.1418	51.7559
TiO_2	0.33	0.40	0.15	0.48
Al_2O_3	3.63	3.72	3.68	4.02
FeO	2.78	2.59	3.13	3.40
MnO	0.00	0.00	0.00	0.00
MgO	16.20	16.55	16.40	16.44
CaO	22.29	22.90	22.40	22.24
Na_2O	0.62	0.56	0.52	0.49
Cr_2O_3	1.35	1.31	1.47	1.29
Tot.	99.50	101.01	100.89	100.12
Mg#	0.91	0.92	0.90	0.90
Wo	47.42	47.76	46.99	46.57
En	47.96	48.02	47.88	47.88
Fs	4.62	4.22	5.13	5.55

Notes: Mg# = (Mg/Mg + Fe). Each reported analysis is the mean of three spots and core-rim analyses do not show significant zonation.

The chemical composition of olivine, orthopyroxene, and clinopyroxene minerals from the mantle xenoliths is similar to those from the ultramafic core of pelletal lapilli and from the loose xenocrysts within the melilitite-carbonatite matrix, corroborating the hypothesis that loose ultramafic xenocrysts in the melilitite-carbonatite matrix represent fragments of mantle xenoliths. Although olivines show a wider range of composition if compared with those from melilitite-carbonatite matrix and pelletal lapilli, they also show Mg-rich composition (Fo_{87-92}) and relatively high NiO (0.2 to 0.4 wt. %), with some exception in dunite xenolith with low NiO content (0.08 wt. %) (**Table 4**). Orthopyroxenes are consistently present in just one sample (SLP-xen01). They show also high values of Mg (Mg# = 0.89-0.90), and compositionally, the proportion of En (Wo_{2-3}, En_{86-87}, Fs_{10-11}) shows a positive correlation with the Fo content of the coexisting olivine (**Table 5**). Clinopyroxenes also show a wider range of composition if compared with those from melilitite-carbonatite matrix and pelletal lapilli. They are essentially diopside in composition (Wo_{47-51}, En_{44-48}, Fs_{5-7}) with some Na-rich and Ca-poor exceptions, and they generally show high Cr_2O_3 (0.6-1.4 wt. %) and high Mg# values (0.87 to 0.91) (**Table 6**). All chemical compositions of olivine, orthopyroxene, and clinopyroxene from loose xenocrysts, from the ultramafic core of pelletal lapilli, and from the mantle xenoliths are plotted onto the diagram Mg# vs. NiO and Cr_2O_3 (wt. %), respectively for olivine and pyroxenes (**Fig. 5.5**). Chemical composition of mantle xenoliths from the Hyblean Plateau (Scribano et al., 2009; Correale et al., 2012) are also shown for comparison, since, together with the Mt. Vulture xenoliths, they represent one of the rare xenolith occurrences related to diatreme explosive eruptions with high ascent velocity of such CO_2-rich volcanic systems in the European and Mediterranean region.

Table 4. Minero-chemical composition of olivine from mantle xenoliths of Vulture volcano, Monticchio Lakes Synthem.

Sample	SLP-01				SLP-02				SLP-03			
mineral	ol1		ol3		ol1		ol2		ol1		ol2	
	core	rim	core	rim	core	rim	core	rim	core	rim	core	rim
SiO_2 (wt %)	40.49	41.31	41.38	41.80	42.13	41.58	40.91	40.82	41.26	40.20	40.81	40.54
$FeO_{tot.}$	8.69	7.93	8.88	9.14	9.46	9.28	9.73	9.53	11.75	11.50	11.63	12.35
MnO	n.a.	n.a.	n.a.	n.a.	n.a.	n.a.	n.a.	n.a.	n.a.	n.a.	n.a.	n.a.
MgO	49.53	49.61	49.36	48.60	47.43	48.96	48.14	48.24	46.81	46.93	47.04	46.89
CaO	0.16	0.08	0.10	0.19	0.08	0.10	0.11	0.10	0.12	0.12	0.14	0.15
Cr_2O_3	0.06	b.d.l.	0.08	0.02	0.03	0.08	0.07	0.03	0.12	0.02	0.05	b.d.l.
NiO	0.21	0.35	0.31	0.18	0.44	0.30	0.39	0.33	0.31	0.30	0.18	0.31
Tot.	99.14	99.28	100.11	99.93	99.57	100.30	99.35	99.05	100.37	99.07	99.84	100.23
Fo	91.04	91.77	90.83	90.46	89.94	90.39	89.82	90.02	87.66	87.92	87.85	87.17
Fa	8.96	8.23	9.17	9.54	10.06	9.61	10.18	9.98	12.34	12.08	12.15	12.83

Notes: n.a. = not analysed; b.d.l. = below detection limit.

Table 4. Cont.

Sample	SLP-04		SLP-06				SMC-01	
mineral	ol1		ol1		ol2		ol1	
	core	rim	core	rim	core	rim	core	rim
SiO_2 (wt %)	40.48	40.73	40.90	40.76	41.03	41.51	39.87	40.45
$FeO_{tot.}$	10.34	10.26	9.90	10.16	10.12	9.70	10.24	10.16
MnO	n.a.	n.a.	n.a.	n.a.	n.a.	n.a.	n.a.	n.a.
MgO	47.81	48.39	47.77	48.70	48.31	47.07	49.20	48.42
CaO	0.27	0.24	0.17	0.11	0.12	0.16	0.26	0.31
Cr_2O_3	0.04	0.01	0.06	0.07	b.d.l.	0.07	0.04	0.10
NiO	0.25	0.29	0.27	0.22	0.26	0.27	0.08	0.15
Tot.	99.19	99.92	99.07	100.01	99.83	98.77	99.69	99.59
Fo	89.18	89.37	89.57	89.52	89.49	89.64	89.55	89.47
Fa	10.82	10.63	10.43	10.48	10.51	10.36	10.45	10.53

Notes: n.a. = not analysed; b.d.l. = below detection limit.

Table 5. Minero-chemical composition of orthopyroxene from mantle xenoliths of Vulture volcano, Monticchio Lakes Synthem.

Sample	SLP-01					
mineral	opx1		opx2		opx3	
	core	rim	core	rim	core	rim
SiO_2 (wt %)	53.87	54.01	54.56	54.92	54.28	54.65
TiO_2	0.14	0.15	0.13	0.20	0.17	0.37
Al_2O_3	6.13	6.27	6.10	6.15	5.92	6.12
FeO	6.58	6.81	6.88	6.71	6.41	6.61
MnO	n.a.	n.a.	n.a.	n.a.	n.a.	n.a.
MgO	30.71	31.42	30.97	31.39	31.32	31.52
CaO	1.11	1.20	1.17	1.02	1.04	1.24
Na_2O	0.14	0.19	0.20	0.12	0.10	0.30
Cr_2O_3	0.53	0.48	0.48	0.52	0.48	0.68
Tot.	99.21	100.53	100.49	101.03	99.72	101.49
Mg#	0.89	0.89	0.89	0.89	0.90	0.90
Wo	2.26	2.40	2.36	2.04	2.09	2.46
En	87.23	87.04	86.80	87.45	87.80	87.27
Fs	10.51	10.57	10.84	10.52	10.10	10.26

Notes: n.a. = not analysed.

Table 6. Minero-chemical composition of clinopyroxene from mantle xenoliths of Vulture volcano, Monticchio Lakes Synthem.

Sample	SLP-01				SLP-02				SLP-03			
mineral	cpx1		cpx2		cpx1		cpx2		cpx1		cpx2	
	core	rim	core	rim	core	rim	core	rim	core	rim	core	rim
SiO_2 (wt %)	52.32	52.47	51.15	51.86	52.60	52.26	52.40	52.57	52.15	52.86	52.52	52.53
TiO_2	0.45	0.46	0.38	0.53	0.23	0.20	0.18	0.31	0.51	0.36	0.37	0.37
Al_2O_3	7.55	7.75	7.91	8.03	4.98	5.59	4.68	4.75	3.34	3.00	3.53	3.43
FeO	3.77	3.87	3.74	3.70	3.16	2.97	3.21	3.22	3.96	3.92	3.81	3.76
MnO	n.a.	n.a.	n.a.	n.a.	n.a.	n.a.	n.a.	n.a.	n.a.	n.a.	n.a.	n.a.
MgO	15.72	15.84	15.59	15.63	15.98	17.49	15.98	16.10	16.97	16.40	16.58	16.46
CaO	18.74	18.86	18.67	18.56	19.49	19.58	19.65	19.79	20.37	20.36	20.33	20.52
Na_2O	1.31	1.32	1.32	1.29	1.13	1.17	1.09	1.06	0.59	0.64	0.61	0.66
Cr_2O_3	0.81	0.85	0.77	0.79	1.32	1.29	1.53	1.36	1.04	0.89	1.01	1.04
Tot.	100.67	101.42	99.53	100.39	98.88	100.54	98.72	99.16	98.92	98.43	98.77	98.77
Mg#	0.88	0.88	0.88	0.88	0.90	0.91	0.90	0.90	0.88	0.88	0.89	0.89
Wo	43.02	42.93	43.13	42.96	44.09	42.35	44.26	44.26	43.27	44.02	43.83	44.26
En	50.21	50.18	50.12	50.34	50.31	52.64	50.09	50.11	50.17	49.34	49.74	49.40
Fs	6.77	6.89	6.74	6.70	5.60	5.02	5.66	5.63	6.56	6.64	6.43	6.34

Notes: n.a. = not analysed.

Table 6. Cont.

Sample	SLP-04				SLP-06					
mineral	cpx2		cpx3		cpx1		cpx2		cpx3	
	core	rim	core	rim	core	rim	core	rim	core	rim
SiO_2 (wt %)	50.76	47.38	49.24	49.10	52.07	51.80	51.81	51.53	51.67	51.56
TiO_2	0.57	0.99	0.88	0.75	0.43	0.45	0.43	0.52	0.34	0.38
Al_2O_3	5.23	8.02	7.67	7.42	4.57	4.55	4.56	4.69	4.11	4.23
FeO	3.55	3.85	3.97	3.92	2.85	3.11	3.14	3.07	3.00	3.09
MnO	n.a.	n.a.	n.a.	n.a.	n.a.	n.a.	n.a.	n.a.	n.a.	n.a.
MgO	15.61	14.17	14.30	14.21	15.34	15.87	15.66	15.60	16.13	16.23
CaO	23.18	23.50	22.33	22.20	21.47	21.72	21.76	21.97	22.05	22.28
Na_2O	0.41	0.42	0.52	0.49	0.76	0.85	0.82	0.82	0.74	0.84
Cr_2O_3	0.64	1.06	0.98	0.91	1.13	0.85	0.93	1.00	1.08	1.10
Tot.	99.95	99.39	99.89	99.00	98.62	99.20	99.11	99.19	99.12	99.71
Mg#	0.89	0.87	0.87	0.87	0.91	0.90	0.90	0.90	0.91	0.91
Wo	48.64	50.87	49.27	49.34	47.66	46.99	47.30	47.69	47.09	47.14
En	45.58	42.68	43.91	43.95	47.39	47.77	47.37	47.12	47.93	47.79
Fs	5.79	6.44	6.82	6.70	4.96	5.24	5.32	5.19	4.98	5.07

Notes: n.a. = not analysed.

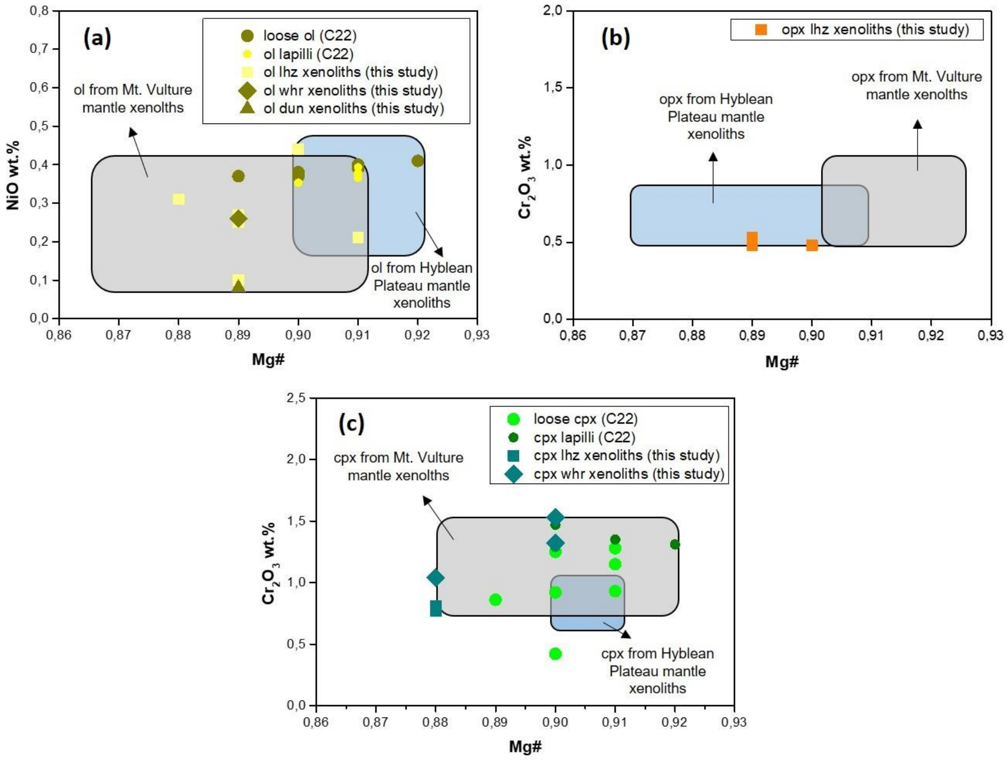

Fig. 5.5: Mg# vs. NiO wt.% in (a) olivine, and Mg# vs. Cr_2O_3 wt.% in (b) orthopyroxene and (c) clinopyroxene in mantle xenoliths from Mt. Vulture. Mt. Vulture xenoliths are from our previous study (Carnevale et al., 2022, C22) and from Jones et al. (2000) (grey and blue fields). Hyblean Plateau xenoliths are from Correale et al. (2012) and Scribano et al. (2009). lhz = lherzolite, whr = wehrlite, dun = dunite.

For the whole rock analysis (major and trace elements), only the external fraction of pelletal lapilli was analysed, since it is considered juvenile component of the studied melilititic-carbonatitic tuff deposit. Indeed, in order to avoid during the analysis the contribution of the ultramafic internal core, this latter was separated by a careful handpicking under the binocular. The whole rock composition for the investigated external fraction of pelletal lapilli, together with a carbonatite rich layer in the melilitite-carbonatite matrix and literature data, is shown in **Table 7**, and depicted in multi-element and REE diagrams (**Fig. 5.6**). Results of whole rock analysis (major elements) show high SiO_2 (39 wt.%) and MgO (16 wt.%) content, with relatively low values of CaO (8 wt.%), MnO (0.2 wt.%), Na_2O (3 wt.%), K_2O (2 wt.%) and LOI (7 wt.%). Concentrations of trace elements are also relatively high, mostly Sr (1250 ppm) and Ba (2430 ppm), with ∑REE up to 526 ppm. The chondrite-normalised REE pattern shows moderate fractionation with (La/Lu)N = 37, and quite flat HREE, with (Ho/Lu)N = 1.5.

Table 7. Whole rock analyses of the external portion of pelletal lapilli and carbonatite layer from Monticchio Lakes Synthem compared with literature data.

Sample	1	2	3	4	5
			whole rock		
SiO_2 (wt. %)	39.10	22.90	39.2-43.8	9.17	11.55
TiO_2	1.34	0.38	1.16-1.66	0.37	0.13
Al_2O_3	10.45	7.76	9.7-12.1	2.81	1.90
$Fe_2O_{3\,tot}$	9.73	3.17	4.35-7.07	1.54	4.04
MnO	0.19	0.07	0.18-0.31	0.03	0.31
MgO	15.75	1.94	12.2-16.1	1.19	1.29
CaO	8.03	33.50	8.34-14.6	45.41	43.80
Na_2O	3.20	0.26	1.1-2.58	0.26	1.50
K_2O	1.93	0.71	0.74-1.51	0.30	0.34
P_2O_5	1.12	0.26	0.73-2.08	0.14	3.01
LOI	6.73	29.80	4.83-6.77	38.12	30.40
Tot.	97.57	100.75		99.34	98.27
Sr (ppm)	1250.0	1190.0	923-1662	443.00	15900.00
Y	251.0	81.0	31-64	5.00	142.50
Zr	200.0	177.0	222-486	52.00	424.00
Nb	75.0	47.1	51-160	10.00	63.70
Rb	38.7	41.8	18-42	12.00	10.40
Ba	2430.0	9550.0	1762-4266	139.00	659.00
La	118.0	92.0	162-369	10.10	607.83
Ce	237.0	148.0	263-672	19.20	1092.91
Pr	26.2	17.9	n.a.	2.08	104.27
Nd	94.6	63.3	n.a.	7.60	355.19
Sm	16.8	11.1	n.a.	1.50	50.47
Eu	4.0	2.9	n.a.	0.41	14.45

Gd	13.0	9.4	n.a.	1.30	39.12
Tb	1.4	1.2	n.a.	0.20	4.46
Dy	7.8	6.7	n.a.	0.90	23.09
Ho	1.1	1.3	n.a.	0.20	4.16
Er	3.1	3.3	n.a.	0.50	10.39
Tm	0.3	0.4	n.a.	0.06	1.26
Yb	2.9	2.7	2.5-4.7	0.40	7.29
Lu	0.3	0.6	n.a.	0.07	1.02
Hf	4.0	3.0	0.2-7.7	1.20	0.01
Ta	0.1	0.1	4.2-6.8	0.60	n.a.
Pb	26.0	40.0	17-65	n.a.	8.00
Th	16.0	16.5	17-28	2.80	33.20
U	5.0	9.4	8-14	1.10	3.70
$(La/Lu)_N$	37.1	16.5		14.9	47.1
∑REE	526.48	360.65		44.52	2315.91

Notes: 1- External portion of pelletal lapilli from Monticchio Lakes Synthem (this study); 2- Carbonatite layer from Monticchio Lakes Synthem (this study), also described as "facies 2" in Stoppa and Principe (1997); 3- Compositional range of pelletal lapilli from Monticchio Lakes Synthem (from Stoppa and Principe, 1997); 4- Sedimentary calcrete-carbonate (from Innocenzi et al., 2021); 5- Fuerteventura oceanic Ca-carbonatites (from Carnevale et al., 2021). n.a. = not analysed.

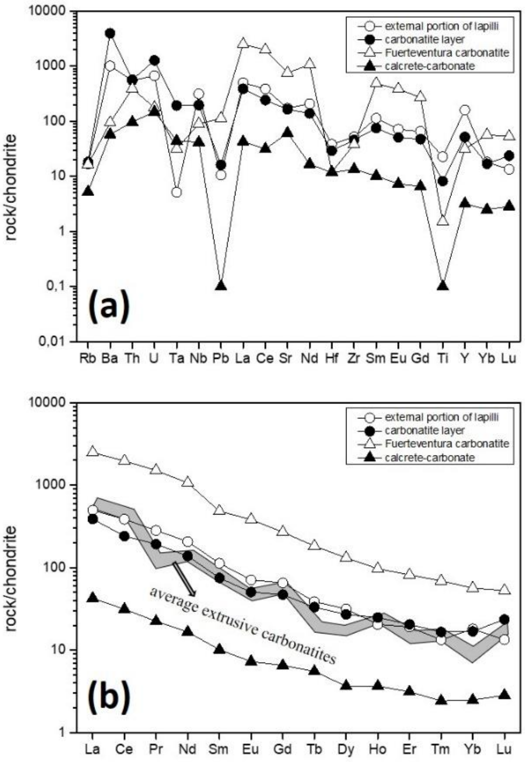

Fig. 5.6: (**a**) Multi-element and (**b**) REE abundance diagram normalized to chondrite (McDonough and Sun, 1995), showing patterns of the external portion of lapilli and the carbonatite layer. Patterns of Fuerteventura oceanic carbonatites (Carnevale et al., 2021) and sedimentary calcrete-carbonate fraction (Innocenzi et al., 2021) are also shown for comparison. Average extrusive carbonatites from Stoppa (2003).

The extreme variability of rock-forming minerals in carbonatites (Christy et al., 2021), together with several processes occurring in the route to the surface or in the source region, make the interpretation of chemical analyses of carbonatite rocks quite difficult. This is particularly verified with major and trace elements concentration. The abundance of major oxides (CaO, MgO, FeO, TiO_2 and P_2O_5) in bulk rock compositions, not only depends on the carbonate minerals that characterised the carbonatite (Chakhmouradian et al., 2016), but also essentially on the forsterite, pyroxene, mica-group minerals, magnetite and apatite content (Kamenetsky et al., 2021), this latter one of the most common accessory minerals in carbonatites (Chakhmouradian et al., 2017). As regards the trace elements concentration, carbonatites contain very high concentration of incompatible trace elements, such as Ba, Sr, REEs, Th, U, Nb, and this is often coupled with negative anomalies of Zr, Hf, and Ti (e.g., Chakhmouradian et al., 2006). In some cases, the concentration of incompatible trace elements is used to distinguish between carbonatite rocks and sedimentary carbonates (e.g., Innocenzi et al., 2021). Moreover, some carbonatite occurrences in central Italy classically interpreted as primary carbonatites (e.g., Stoppa et al., 2005), have been recently classified as pseudocarbonatite or product of interaction between ultrabasic melts and limestones at shallow crustal depths (Lustrino et al., 2019,2020).

Pelletal lapilli are considered the juvenile component of the last Mt. Vulture volcano activity, representing the interface between the erupting silica undersaturated melilititic-carbonatitic magma and the volatile component, this latter considered very important in the evolutionary history of the erupting magma (Lloyd and Stoppa, 2003). Thus, the whole rock chemistry of the external portion of Mt. Vulture pelletal lapilli represents a good tracer to distinguish the literature data of sedimentary calcrete-carbonate portion from the melilitite-carbonatite one. This is particularly verified if we compare trace elements of the sedimentary calcrete-carbonate portion (e.g., Innocenzi et al., 2021) having low concentrations (e.g., Ba = 139 ppm; Sr = 443 ppm; $\sum$REE = 44 ppm), with the average carbonatite concentrations (i.e., Ba = 3044 ppm; Sr = 7272 ppm; $\sum$REE = 3731 ppm) (Wolley and Kempe, 1989; Chakhmouradian 2006). On the contrary, the external portion of pelletal lapilli shows concentrations (e.g., Ba = 2430 ppm; Sr = 1250 ppm; $\sum$REE = 527 ppm) comparable with those of the average values of Ca-carbonatite and plotting onto the average range of extrusive carbonatites (**Fig. 5.6**), suggesting a possible contribution of a carbonatite melt in the trace elements enrichment processes. Our recent study on the same pelletal lapilli, shows several evidences of the role of carbonatite melt in metasomatizing the enclosed mantle xenoliths (Carnevale et al., 2022). The presence of apatite and carbonate within the wehrlite xenoliths (Downes et al., 2002; Jones et al., 2000), and of LREE-apatite and nyerereite (i.e., Na-K-Ca carbonate) inclusions in Mt. Vulture carbonatite (Stoppa et al., 2009), suggest a process of crystallization from a carbonatite melt.

Furthermore, isotope analyses in calcite from a carbonate-dominated matrix in the tuff phreatomagmatic deposit of MLS, show $\delta^{13}C$ values from 4.5 to 5.2 (Stoppa and Principe, 1997), approaching the typical mantle values (Keller and Hoefs, 1995). To resume, (i) the whole rock chemical signature of the external portion of pelletal lapilli, together with evidences of a wehrlitization of the ultramafic core, (ii) the presence of LREE-apatite and Na-K-Ca-rich carbonates inclusions in Vulture carbonatite, and (iii) typical mantle values of $\delta^{13}C$ in calcite minerals, all together suggest a contribution of a primary carbonatite melt in the petrogenesis of Mt. Vulture magmatism.

5.1.3 Micro-thermometry of fluid inclusions

The study of chemical composition together with trapping temperature and pressure of fluid inclusions (FIs) trapped in rock-forming minerals of mantle xenoliths provides insights into the PT history of the mantle and the mineral-melt-fluid interaction processes in the mantle and within the volcano magma storage system. Fluid inclusions (FIs) are present in all studied samples, in both ultramafic cores of pelletal lapilli and in mantle xenoliths. The reduced size (< 1 μm) in dunite prevented the analysis with the micro-thermometric stage and the textural study. FIs are generally rounded (2-10 μm in diameter) with clearly re-equilibration features (**Fig. 5.7**), such as (i) the presence of outer dark halos around the main cavity, and (ii) the presence of stretched FIs in clinopyroxene of wehrlite xenolith. Clinopyroxene represents the main host mineral phase for FIs, especially secondary FIs (classified on the basis of their distribution within the crystals), as evidenced by the presence of abundant intragranular trails in sealed fractures.

In studied xenoliths, FIs are characterized by melting temperatures (Tm) ranging between -56.5 and -57.0 °C (± 0.1 °C), with variable homogenization temperatures of the vapour phase to the liquid phase (ThL). In olivines from lherzolite and wehrlite xenolith, Th_L varies from -26.8 °C to 29.9 °C and from -16.2 °C to 29.1 °C, respectively, corresponding to density ranges (ρ) of 0.62-1.11 g/cm^3 and 0.65-1.06 g/cm^3. In orthopyroxene Th_L varies from -25.6 °C to 29.9 °C (ρ = 0.62-1.10 g/cm^3). In clinopyroxene from lherzolite xenolith, Th_L varies from -25.5 °C to 30.0 °C (ρ = 0.62-1.10 g/cm^3), while from wehrlite xenolith varies from -20.1 °C to 26.8 °C (ρ = 0.71-1.08 g/cm^3). Several polyphase FIs with the presence of different solid phases within the fluid inclusions are also present, but the study of these particular inclusions is beyond the scope of this work. Details about micro-thermometric analyses in ultramafic core of pelletal lapilli are in the Chapter 5.2.

The range of Tm in lherzolite and wehrlite xenoliths (-56.5 − -57.0 °C ± 0.1 °C) is slightly wider if compared with the range of wehrlite cores in pelletal lapilli (-56.6 − -56.8 °C ± 0.1 °C, Carnevale et al., 2022). Our data suggest that the fluid inclusions consist of nearly pure CO_2 (-56.6 °C is the triple point of pure CO_2 at 1 bar), and the slightly wider range may be due to the presence of very low amounts of other volatile species.

The highest corrected densities of FIs in all mineral phases of lherzolite and wehrlite xenoliths are in the range of 1.10-1.11 g/cm^3, corresponding to minimum fluid pressure of 8.5-9.0 kbar (≈ 27-28 km), and they are comparable with values of Hyblean mantle xenoliths for a pure CO_2 system (7.5-9.5 kbar, Sapienza et al., 2005). Equally, FIs show the same low-density peak at 0.6-0.7 g/cm^3, corresponding to minimum fluid pressure between 2.0 and 4.0 kbar (≈ 6-12 km), as also recorded by wehrlitic cores in pelletal lapilli (Carnevale et al., 2022). Re-equilibration pressures and densities were determined at the equilibrium temperature of 1076 °C.

The histograms of densities of FIs in mantle xenoliths (**Fig. 5.8**) show a similar modal distribution if compared with those of mantle xenolith cores of pelletal lapilli (Carnevale et al., 2022). Considering that normally FIs re-equilibrate at important chemical and physical discontinuities such as the crust-mantle boundary (e.g. Zanon et al., 2003; Zanon and Frezzotti, 2013; Zanon, 2015), and only in the case of isochoric ascent they escape re-equilibration (Andersen & Neumann, 2001), re-equilibration processes lowered the pristine FIs density at the time of trapping. Thus, the FIs trapped in lherzolite and wehrlite xenoliths registered magma ponding at different depths within the Mt. Vulture magma system. The first ponding stage corresponds to the local crust-mantle boundary (at about 32 km depth, Kelemework et al., 2021), while the second corresponds to a shallow ponding stage (at about 12-14 km depth), as corroborated by geophysical evidences of solidified magmatic body at the same depth below the Vulture volcano (Improta et al., 2014). To sum up, the micro-thermometric study to different mantle xenoliths further constrains the mantle source beneath Mt. Vulture and depths of magma storage within the volcano plumbing system, according to previous geophysical and petrological data for this volcano (Carnevale et al., 2022; Improta et al., 2014).

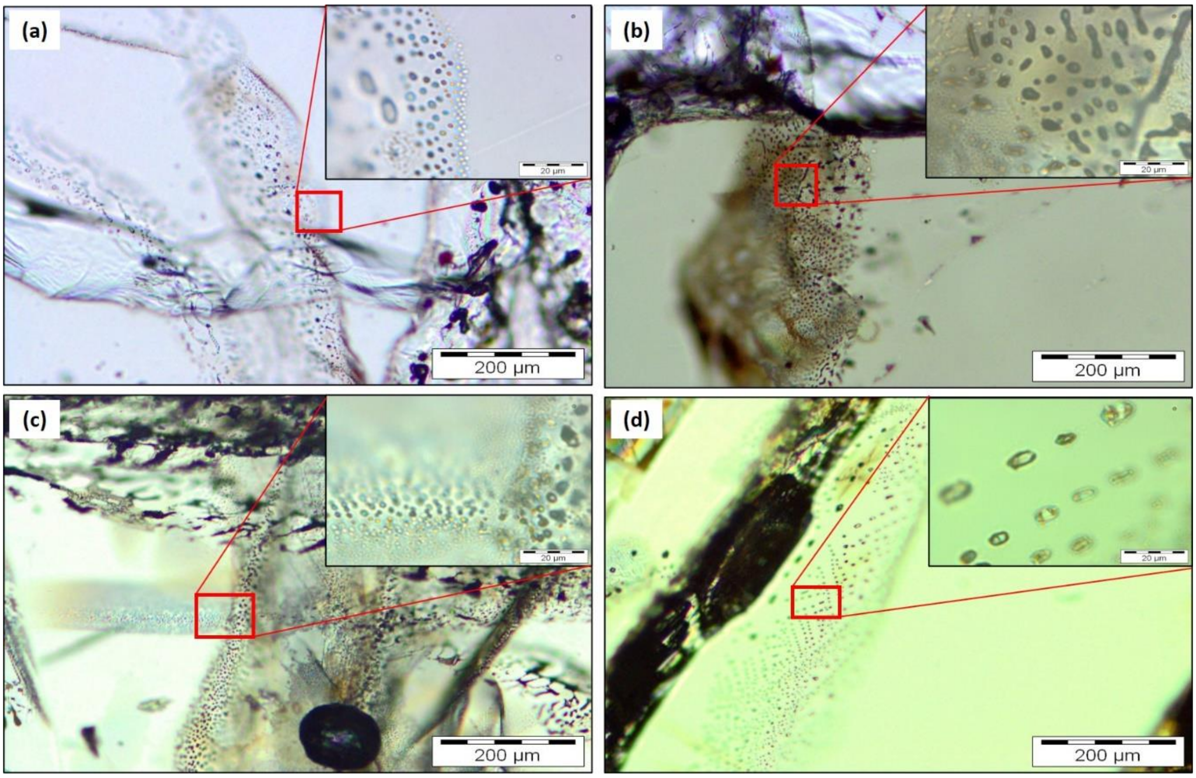

Fig. 5.7: Photomicrographs (parallel polars) of carbonic fluid inclusions and their textures enclosed by (a) olivine, (b) orthopyroxene, (c) clinopyroxene in a lherzolite xenolith, and (d) clinopyroxene in wehrlite xenolith from Mt. Vulture.

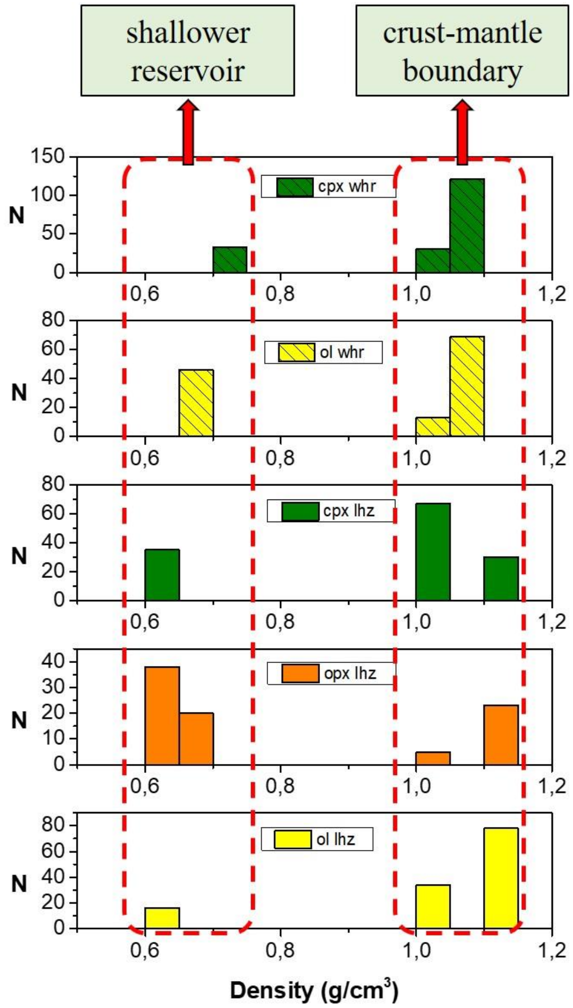

Fig. 5.8: Frequency distribution of densities of fluid inclusions hosted by olivine, orthopyroxene and clinopyroxene in lherzolite (lhz) and wehrlite (whr) xenoliths from Mt. Vulture. N = number of measures.

5.1.4 Geothermobarometry

The mineral assemblage of studied Mt. Vulture xenoliths presents no independent pressure indicators. However, the lack of plagioclase and garnet, with the presence of spinel as accessory mineral phase in lherzolite and wehrlite sample (see Figs. 5.3 and 5.4), allows to constrain the pressure at least between the plagioclase-out boundary at 8-9 kbar (Borghini et al., 2009) and the garnet-spinel phase transition boundary at 15-20 kbar (Su et al., 2010), at the lower part of the spinel peridotite stability field.

The lack of the garnet as accessory mineral phase does not allow to extend the study to several valid geothermometers. However, a variety of geothermometers to estimate the temperature of studied samples applicable to spinel peridotites were used (**Table 8**). They are based on the coexistence of two pyroxene pairs (orthopyroxene and clinopyroxene) (Wells, 1977; Bertrand and Mercier, 1985; Brey and Köhler, 1990), on the Ca content in orthopyroxene (Brey and Köhler, 1990), and on Cr content in olivine (De Hoog et al., 2010). Particularly, temperatures calculated in the lherzolite sample using the coexistence of opx and cpx pairs following Brey and Köhler (1990) and Wells (1977) are 130 °C higher (1158 °C and 1100 °C respectively) than temperature generated using the similar method of Wells (1977) (964 °C). The temperature calculated using the Ca content in orthopyroxene (1084 °C) is comparable with those previously calculated, while the geothermometer based on Cr content in olivine, although applicable, it shows low temperature (842 °C). In the same way, the wehrlite xenoliths show a range of low temperatures (847-944 °C), while the ol-clinopyroxenite and dunite xenoliths show more comparable temperatures (972 °C and 1009 °C respectively). Results are comparable with temperatures calculated by Jones et al. (2000), that reported a temperature range of 1050-1150 °C, with the exception of some sample with too low equilibrium temperatures, clearly affected by the low Cr content in olivine. **Figure 5.9** shows the pressure-temperature region of Mt. Vulture mantle xenoliths along the carbonate-bearing lherzolite solidus in the system CMAS-CO_2 (Dalton and Presnall, 1998), plotted together with Hyblean mantle xenoliths, since both Hyblean and Mt. Vulture xenoliths represent one of the rare occurrences related to diatreme explosive eruptions with high ascent velocity of such CO_2-rich volcanic systems in the Mediterranean region.

Table 8. Temperatures calculated for Mt. Vulture xenoliths.

Sample	Rock type	Temperature (°C)				
		$T(BK_{opx-cpx})$	$T(BK_{Ca-in-opx})$	$T(BM_{opx-cpx})$	$T(W_{opx-cpx})$	$T(DH_{Cr-ol})$
LAP-01	wehrlite					847
LAP-02	wehrlite					847
SLP-xen01	lherzolite	1158	1084	964	1100	842
SLP-xen02	wehrlite					944
SLP-xen03	ol-clinopyroxenite					972
SLP-xen04	wehrlite					847
SLP-xen06	wehrlite					892
$SMC_{(B)}$-xen01	dunite					1009

Notes: T(BK), Brey and Köhler (1990); T(BM), Bertrand and Mercier (1985); T(W), Wells (1977); T(DH), De Hoog et al. (2010).

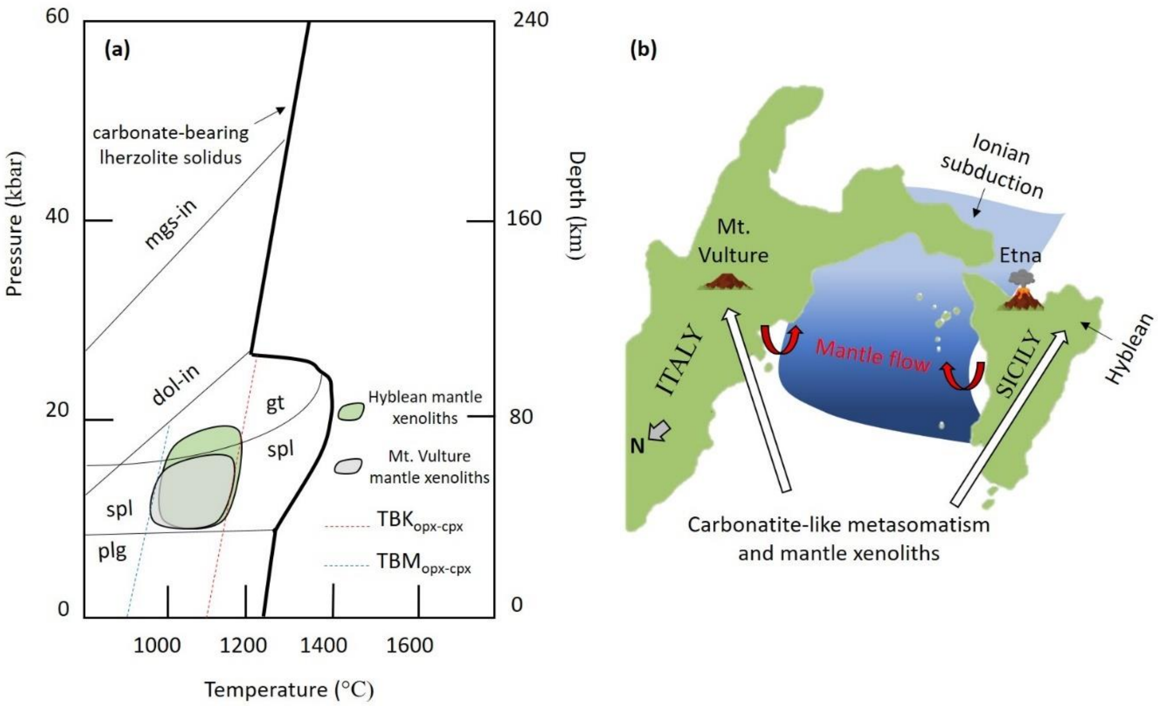

Fig. 5.9: Mt. Vulture mantle xenoliths in the pressure-temperature region of interest along the carbonate-bearing lherzolite solidus in the system CMAS-CO$_2$ (a) (Dalton and Presnall, 1998). Temperature-lines of the lower and higher temperature from the applied geothermometers are depicted (TBM$_{opx-cpx}$ = Bertrand and Mercier, 1985; TBK$_{opx-cpx}$ = Brey and Köhler, 1990) with the plagioclase-out boundary at 8-9 kbar and the spinel-garnet phase transition boundary at 15-20 kbar (Borghini et al., 2010; Su et al., 2010). Hyblean mantle xenoliths are also depicted for comparison (Correale et al., 2012; Scribano et al., 2009). Mt. Vulture within the geodynamic context of the Ionian subduction (b). Red arrows show the asthenospheric mantle flow along the vertical slab windows (Bragagni et al., 2022).

5.1.5 Oxybarometry and redox conditions: Mössbauer spectroscopy on spinel inclusions within mantle xenoliths

All acquired Mössbauer spectra consisted of two doublets for Fe^{2+} and one for Fe^{3+} (**Fig. 5.10**) according to the model proposed by Canil and O’Neill (1996) and Ejima et al. (2018). The quadrupole splitting (QS) and center shift (CS) are depicted in **Fig. 5.11**, all related to mantle peridotites. The contribution of Fe in Be window was taken into account fitting the olivine and spinel spectra with an extra singlet (CS= 0.2991 mm/s), based on background measurements performed before starting of the analytical session. For the olivine, we measured the Fe^{3+}/∑Fe ratio along a transect for a total of 3 points along with two extracted spinel inclusions. Fe^{3+}/∑Fe ratio of olivine ranges between 0.026 and 0.048, while for the extracted spinel inclusions it ranges between 0.38 and 0.40 within 2% of uncertainty.

The $Fe^{3+}/\sum Fe$ ratios measured in the olivine host and spinel inclusions are consistent with those commonly reported by Ejima et al. (2018) and Canil and O'Neill (1996), respectively, in the case of mantle peridotites. Data allow to determine the $D^{Fe3+}_{ol/spl}$ that range between 0.06 and 0.13. $D^{Fe3+}_{ol/spl}$ is not reported by Canil and O'Neill (1996) since Fe^{3+} was not detected in olivines. In addition, the $Fe^{3+}/\sum Fe$ of the included spinel can be compared with values reported by Jones et al. (2000). They reported values ranging from 0.25 to 0.38 but, since Fe^{3+} was obtained by stoichiometric calculations, it can be both over or under estimated. $Fe^{3+}/\sum Fe$ is also consistent with the general trend observed for mantle peridotites and that correlated linearly with the f_{O_2} of the host rock (Stagno 2019).

The knowledge of the $Fe^{3+}/\sum Fe$ of spinel allows to calculate the f_{O_2} of the mantle host rock according to the equation $6Fe^{(2+)}{}_2SiO_4$ (fayalite) + O_2 = $3Fe^{(2+)}{}_2Si_2O_6$ (ferrosilite) + $2Fe^{(2+)}Fe^{(3+)}{}_2O_4$ (magnetite). However, this equilibrium would require the knowledge also of orthopyroxene in order to assess the SiO_2 saturation. The wehrlitic sample used at the aim of this study does not contain visible orthopyroxene as well as spinel disperse in the xenolith, respectively. In any case, the SiO_2 saturation is assumed by similarity of the chemical composition of olivine shown for our sample and with those reported for wehrlite by Jones et al. (2000) where orthopyroxene is also reported, showing low compositional variations. The absence of spinel within the xenolith matrix is overcome by the analogy of the chemical composition of spinel inclusion and spinel from wehrlite reported by Jones et al. (2000). The application of the spinel oxybarometer also requires the knowledge of the P-T conditions. In our case, we can take into consideration a P of 1.6-1.8 GPa and T of 1000-1100 °C proposed by Jones et al. (2000) determined using different models and comparable with temperatures calculated previously. The calculated $\log f_{O_2}$ are 0.76 and 0.81 (±0.6) as normalized to the fayalite-magnetite-quartz (FMQ) buffer adopted as reference (O'Neill, 1987), considering both measured $Fe^{3+}/\sum Fe$ ratios of 0.38 and 0.40, respectively. For comparison, $\log f_{O_2}$ of wehrlite for which Jones et al. (2000) provides the composition of olivine, orthopyroxene and spinel was calculated, and it resulted 0.85 (±0.6; FMQ), consistent with values obtained for our samples. $Fe^{3+}/\sum Fe$ ratios are consistent with the general trend observed for mantle peridotites and that correlated linearly with the f_{O_2} (**Fig. 5.12**). Noteworthy, these values are the highest compared to the f_{O_2} of spinel peridotites (Stagno and Aulbach, 2021) and plot above the water saturation curve determined along a typical geothermal gradient of 44 mW/m^2. Such a result is supported by the presence of H_2O in olivine, although the corresponding high $\log f_{O_2}$ with respect to the average value of -1 to 0 log units would imply (re-)equilibration of olivine with a H_2O-bearing fluid. Such a conclusions based on one single H_2O measurement, obviously, needs of more statistically significant H_2O measurements also extended to coexisting minerals. In any case, the high Fe oxidation state in spinels included in olivine, along with the calculated $\log f_{O_2}$ support the geochemical evidence that these rocks would have formed by interaction with an oxidized metasomatic fluid. In particular, the CO_2-dominant nature of the fluid inclusions analysed in Vulture olivines (Carnevale et al., 2022) highlights the possible presence of a carbonated fluid here supported by the high $f\mathrm{o}_2$. To date, the $f\mathrm{o}_2$ of wehrlitic rocks cannot be calculated because of the lack of representative redox equilibria that can be thermodynamically or experimentally calibrated. The possibility to access the composition of those spinels included in olivine showing a marked mantle affinity represent a valid tool to bypass such issue. In the case of spinel inclusions in olivines from Vulture wehrlites, the $f\mathrm{o}_2$ is that recorded at the time of the first interaction of the (spinel) peridotite with a carbonated oxidized fluid that, eventually, caused re-crystallization of olivine and entrapment of euhedral chromites. Alternatively, the spinel-olivine pairs might have recorded the oxidation event prior to the transport up to shallower conditions by a CO_2-bearing melt. If this was the case, either the olivine-spinel pair experienced very fast ascent by a low viscosity magma, or they re-equilibrated at the lithosphere-asthenosphere boundary (LAB) depths such to retain their mantle affinity. In both cases, no chemical zonation is expected to form that is what is shown for the analysed samples.

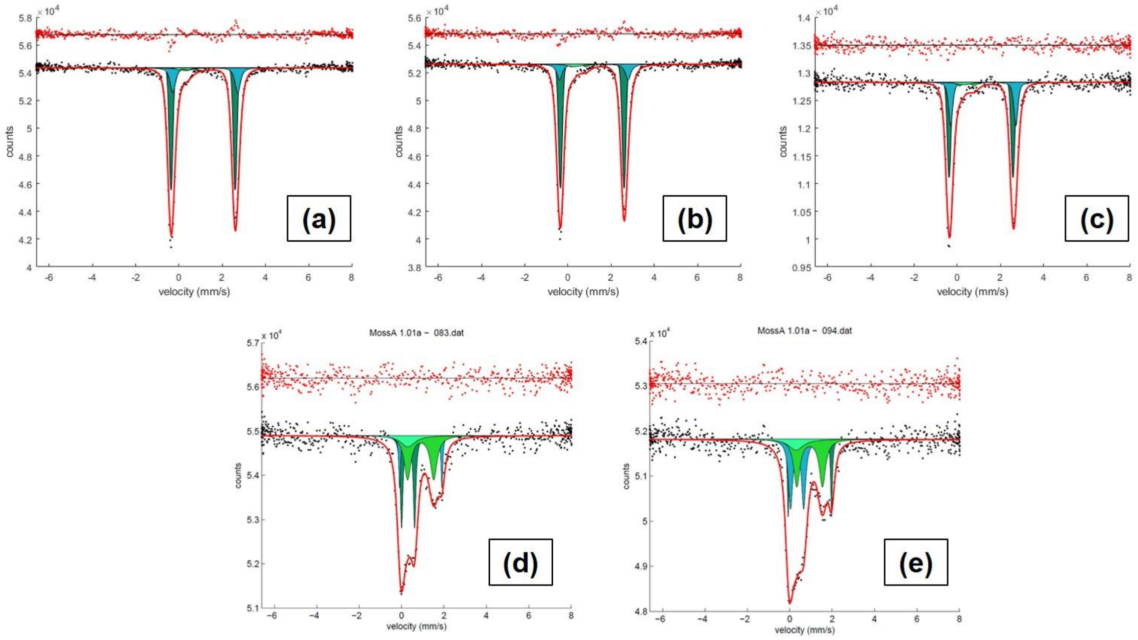

Fig. 5.10: Olivine (a,b,c) and spinel (d,e) Mössbauer spectra with an X-ray beam focused on an area of 8x3 µm^2. Spectra were fitted through a full transmission integral with a normalized Lorentzian-squared source lines shape using MossA software package (Prescher et al., 2012).

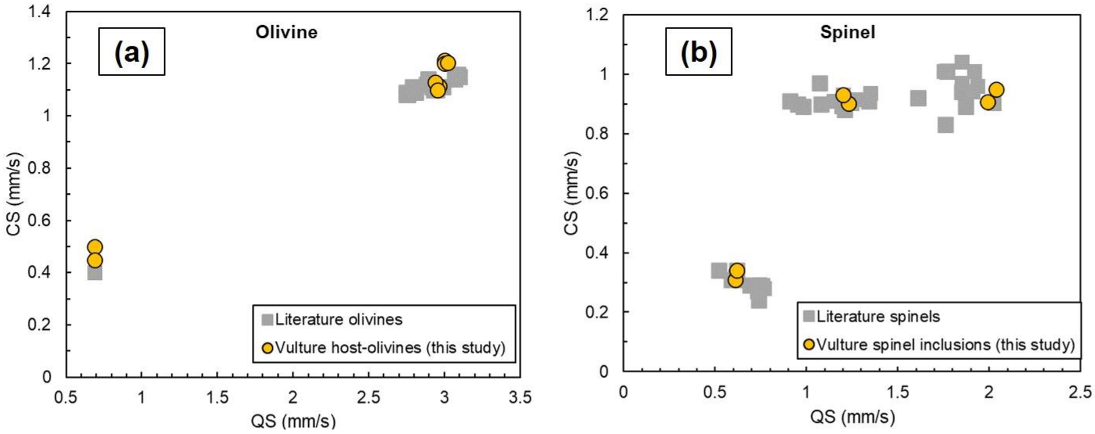

Fig. 5.11: Olivine (a) and spinel (b) hyperfine parameters (CS and QS) of the analysed samples.

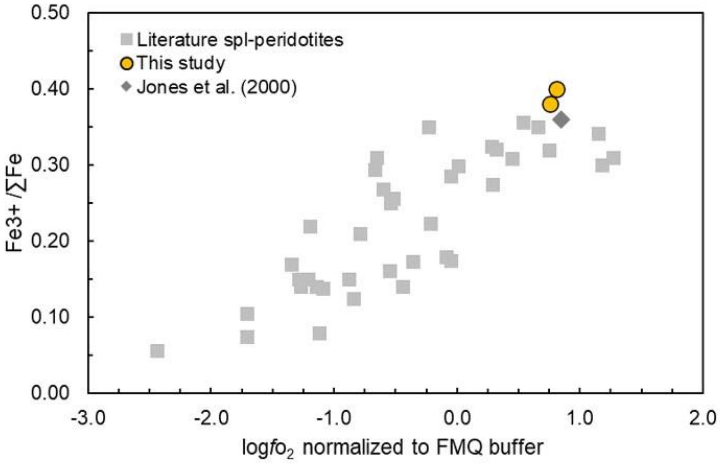

Fig. 5.12: Measured $Fe^{3+}/\sum Fe$ ratio vs log*fo*$_2$ for our samples and literature data (from Stagno, 2019).

5.1.6 Isotope geochemistry: noble gases (He, Ne)

In this study, we measured the He and Ne isotopic compositions in mineral separates of the ultramafic core of pelletal lapilli (olivine) together with loose mafic xenocrysts (olivine and Cr-diopside) embedded in the melilitite-carbonatite matrix of the studied ash-rich tuff deposit. Results are depicted onto the R/Ra vs. $^4He/^{20}Ne$ diagram (**Fig. 5.13**) and shown in **Table 9**.

Olivine separates from the ultramafic core of pelletal lapilli is characterized by ^4He concentrations in the range of 0.1×10^{-13} to 8.6×10^{-13} mol/g. Loose olivine and Cr-diopside xenocrysts show a restricted concentration range, from 0.1×10^{-13} to 0.2×10^{-13} mol/g.

The He isotopic ratios in olivine from pelletal lapilli (R/Ra = 5.96-6.17) are comparable with He isotopic ratios in loose olivine xenocrysts (R/Ra = 6.10-6.11), while loose Cr-diopside xenocrysts show the lowest He isotopic ratios (R/Ra = 5.6). Therefore, $^3He/^4He$ ratios present values slightly lower than typical MORB mantle values (R/Ra = 8 ± 1) (Allègre et al., 1995) and in the range of sub-continental lithospheric mantle values (SCLM, 6.1 Ra ± 0.9 (Gautheron and Moreira, 2002)). The possible contribution of the radiogenic ^{4}He* to decrease the pristine He isotopic signature is here negligible, because of the recent age of the last volcanic activity of the Mt. Vulture. The ^{4}He/^{20}Ne in all the analysed samples are at least two to three orders of magnitude higher than the same ratio in atmosphere (^{4}He/^{20}Ne = 0.318 (Ozima and Podosek, 2002)), indicating that He air component is negligible in all the samples.

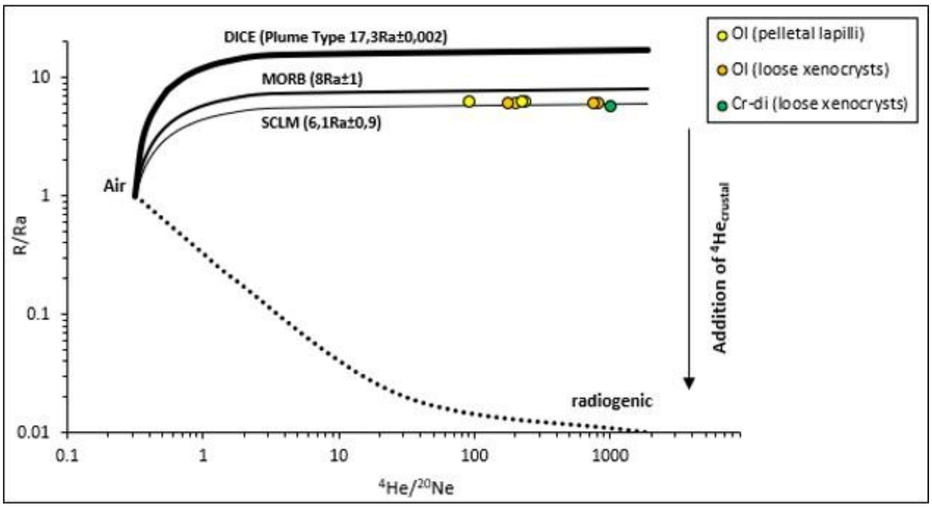

Fig. 5.13: R/Ra ratios vs ^{4}He/^{20}Ne ratios obtained by crushing mineral separates (olivine) of the ultramafic core of pelletal lapilli and loose xenocrysts (olivine and Cr-diopside) from Mt. Vulture.

Table 9. He concentrations (mol/g), He and Ne isotopic ratios on mineral separates of pelletal lapilli and loose xenocrysts from Mt. Vulture.

	^{4}He (10^{-13})	**R/Ra**	**1σ**	**^{4}He/^{20}Ne**
Pelletal lapilli				
Olivine				
Ol-LAP1	0.1	*6.12*	0.06	*240.97*
Ol-LAP2	8.6	*5.96*	0.06	*200.61*
Ol-LAP3	7.4	*6.12*	0.06	*228.23*
Ol-LAP4	7.3	*6.17*	0.07	*92.95*
Loose xenocrysts				
Olivine				
Ol-xeno1	0.1	*6.10*	0.06	*813.18*
Ol-xeno2	0.1	*6.10*	0.06	*759.24*
Ol-xeno3	0.2	*6.11*	0.05	*180.13*
Cr-diopside				
Cr-di1	0.02	*5.6*	0.04	*1021*

5.2 New Inferences on Magma Dynamics in Melilitite-Carbonatite Volcanoes: The Case Study of Mt. Vulture (Southern Italy) (paper published in *Geophysical Research Letters*)

Authors: G. Carnevale[1], A. Caracausi[2], S. G. Rotolo[1,2], M. Paternoster[2,3], and V. Zanon[4]

[1] Dipartimento di Scienze della Terra e del Mare, Università degli Studi di Palermo, Palermo, Italy
[2] Istituto Nazionale di Geofisica e Vulcanologia, Sezione di Palermo, Palermo, Italy
[3] Dipartimento di Scienze, Università degli Studi della Basilicata, Potenza, Italy
[4] Instituto de Vulcanologia e Avaliação de Riscos, Universidade dos Açores, Ponta Delgada, Portugal

Abstract: This study provides the first micro-thermometric data of fluid inclusions in mafic loose (disaggregated) xenocrysts and ultramafic xenoliths in explosive products of the melilitite-carbonatite Mt. Vulture volcano (southern Italy). Pure CO_2 late-stage fluid inclusions hosted in rock-forming minerals of wehrlite xenoliths and clinopyroxene xenocrysts were trapped at the local crust-mantle boundary (32 km). In contrast, trapping pressures within the loose olivine xenocrysts are from 3.2 to 4.5 kbar (8-13 km). Considering the ongoing degassing of mantle-derived CO_2 rich gases, together with seismic evidences of the presence of low amount of melts at depth, and the tectonic control of the past volcanic activity, our study opens new perspective about the hazardous nature of the "quiescent" melilitite-carbonatite volcanoes.

Plain Language Summary: The study of fluid inclusions (small amount of fluid trapped within minerals) provides important information on variable environments and magmatological processes in which the host minerals were formed. Investigation of the fluid inclusions with respect to their composition, trapping pressure and temperature, allow us to constrain magma ascent history. To understand the last explosive volcanic activity of Mt. Vulture volcano (southern Italy), we investigated fluid inclusions in mafic minerals and mantle fragments brought to the surface by a melilitite-carbonatite magma. Our results show the presence of CO_2-rich fluid inclusions with trapping pressure corresponding to a depth of 32 km in mantle fragments, and a shallower depth (8-13 km) in mafic mineral. Estimates on magma ascent rate show rapid ascent dynamics to the surface. Our study emphasizes the importance of a multidisciplinary approach that combine geochemistry and petrology to investigate a volcanic system even if the volcano is considered "quiescent", as is the case of Mt. Vulture volcano, where mantle degassing is still ongoing.

Introduction

Carbonatite magmatism is mainly associated with intraplate continental tectonic settings characterized by significant extension and even rifting, with a temporal distribution from Archean to the present (e.g., Jones et al., 2013; Woolley & Kjarsgaard, 2008; Yaxley et al., 2022), and currently, Oldoinyo Lengai (Tanzania) represents the only active carbonatite volcano, characterized by a natrocarbonatitic affinity (e.g., Berkesi et al., 2020). The growing number of carbonatite occurrences from unconventional tectonic settings, such as oceanic contexts (e.g., Carnevale et al., 2021; Day, 2022; Doucelance et al., 2010; Mata et al., 2010; Schmidt & Weidendorfer, 2018) or subduction zones (e.g., D'Orazio et al., 2007; Li et al., 2018; Lustrino et al., 2019, 2020), received considerable attention during last two decades, given their importance as source of rare elements such as La, Ce, Pr, and Nd (Anenburg et al., 2021; Verplanck et al., 2016), and, most importantly, because they provide meaningful information on the geochemical cycle of carbon and mantle metasomatism as well (e.g., Bouabdellah et al., 2010; Horton, 2021).

Mt. Vulture (southern Italy) is an isolated volcano located between the Apulia foreland and the eastern side of the Apennine orogenic belt, in correspondence of the geodynamic context of the Apennine subduction zone (D'Orazio et al., 2007; Peccerillo, 2017). This volcano is located along the deep NE-SW lithospheric faults that represent a local vertical tear of the slab (e.g., Rosenbaum et al., 2008), a potential pathway for the ascent of melts (Caracausi, Martelli, et al., 2013; D'Orazio et al., 2007).

The Vulture volcano is a small volcanic complex, with several eccentric eruptive vents, covering an area of approximately 70 km^2. Its eruptive activity started about 739 ± 12 ka (Villa & Buettner, 2009) and it continued until to 141 ± 11 ka (Villa & Buettner, 2009), with long inter-eruptive quiescence (>105 years, Buettner et al., 2006). The last volcanic event was a maar-forming eruption (Stoppa & Principe, 1997). Water of the two resulting crater lakes (Monticchio Lakes) dissolves CO_2-rich mantle-derived volatiles (Caracausi, Nicolosi, et al., 2013; Caracausi et al., 2009; Paternoster et al., 2016), supporting the active degassing at this volcano (Caracausi et al., 2009, 2015). The last volcanic activity (identified as Monticchio Lakes Formation, Stoppa & Principe, 1997), fed by a melilitite-carbonatite magma, brought to the surface some pelletal lapilli (enclosing abundant ultramafic mantle xenoliths and xenocrysts) considered to be juvenile component, because they represent the interface between the erupting magma and the volatile component (Lloyd & Stoppa, 2003). These products are particularly useful to characterize the mantle source beneath Vulture volcano, providing important information about the melilitite-carbonatite magma ascent path and its mantle source.

To this aim, micro-thermometric data of fluid inclusions (FIs), hosted in the ultramafic xenolith cores of pelletal lapilli and in loose olivine and clinopyroxene xenocrysts, have been used together with mineral chemistry in order to describe the way in which these very particular magmas are transported to the surface and the possible implications in terms of volcanic hazard.

Sample Description

Samples were collected from the Lago Piccolo Subsynthem (Giannandrea et al., 2006) (Figure S1 in Supporting Information S1). Twenty-nine pelletal lapilli were sampled from a compact fine-grained carbonate-dominated matrix in an ash-tuff phreatomagmatic deposit. The ultramafic xenoliths (dominantly wehrlitic in modal composition) constitute the core of pelletal lapilli and are surrounded by a 3–10 mm thick rim of micro-phenocrysts (Figures 1a and 1b). We also selected approximately 200 olivine and 100 clinopyroxene (Cr-diopside) xenocrysts (Figures 1c and 1d) from the fine-grained carbonate-rich matrix, where xenocrysts of blackish clinopyroxene, amphibole, mica (phlogopite) and spinel, were also present. To compare the FIs within the xenocrysts with those trapped in the ultramafic xenolith cores of pelletal lapilli, we selected two wehrlite cores, three olivine and two clinopyroxene xenocrysts. We analysed 171 FIs in olivine xenocrysts, 107 in clinopyroxene xenocrysts, and 184 FIs in the ultramafic cores of studied lapilli, all being <10 μm in size and most of them in the range of 1–5 μm.

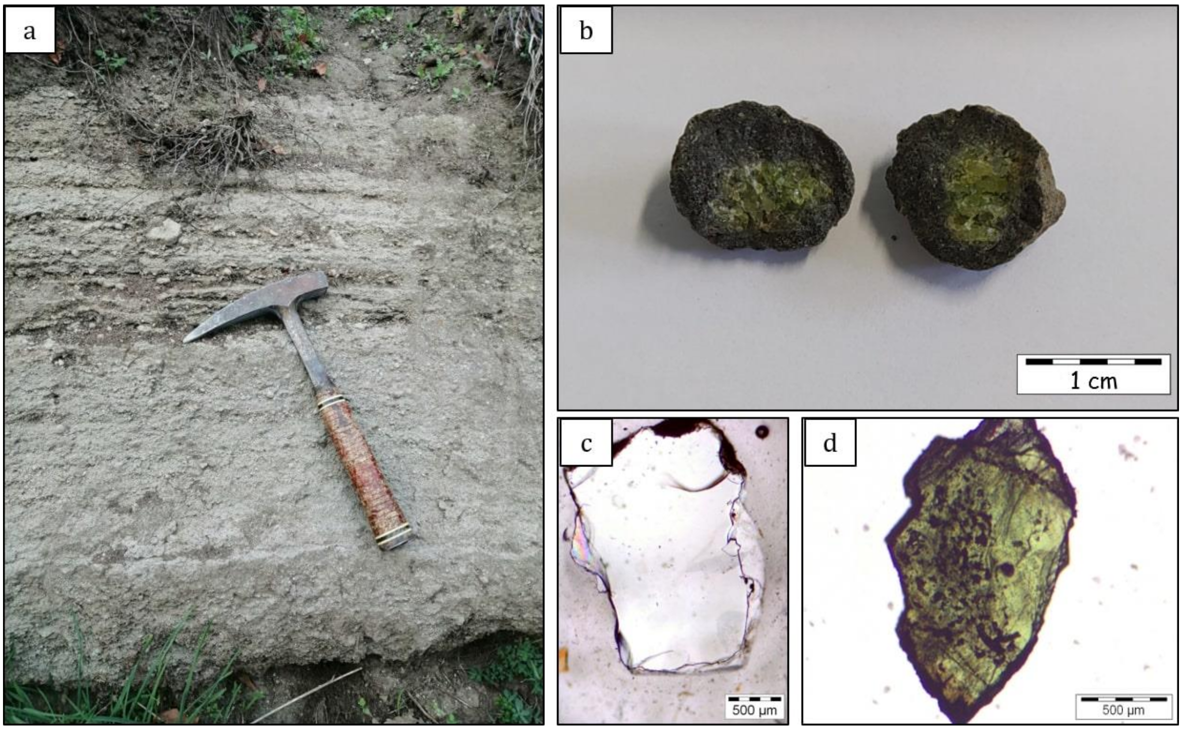

Figure 1. Photomicrographs of the sampling site together with pelletal lapilli and loose crystals. a) Ash-rich tuff surge deposit of Lago Piccolo Sub-Synthem. b) Pelletal lapilli with ultramafic xenolith cores. c) Olivine xenocryst from the fine-grained matrix (parallel polars). d) Clinopyroxene (Cr-diopside) xenocryst from the fine-grained matrix (parallel polars).

Results: Petrography, Mineral Chemistry and Fluid Inclusions

The ultramafic xenolith cores of pelletal lapilli (the diameter of enclaves vary from 6 to 17 mm) are characterized by the presence of Mg-rich olivine (Fo_{90-91}, NiO varying from 0.35 to 0.38 wt. %, Table S1 in Supporting Information S1) and diopside (Wo_{46-48}, En_{47-48}, and Fs_{4-5}) with relatively high Cr_2O_3 content (1.3–1.5 wt. %, Table S2 in Supporting Information S1). The Mg# values of olivine and clinopyroxene in the ultramafic xenolith cores are uniform (0.90–0.92). The grain size of the ultramafic xenolith cores is fine-to medium-grained (300–600 μm) with granoblastic texture, interlocking with randomly oriented olivine and elongated clinopyroxene (Figure S2 in Supporting Information S1). The thick rim of fine-grained material surrounding the xenoliths, is composed essentially of häuyne micro-phenocrysts, with xenocrystic debris of olivine and clinopyroxene (Figure S3 in Supporting Information S1).

Olivine xenocrysts show very similar composition ($Fo_{89–92}$, NiO = 0.37–0.41 wt. %, Table S1 in Supporting Information S1) compared to olivine from the ultramafic xenolith cores of pelletal lapilli. Similarly, almost all clinopyroxene xenocrysts show akin composition ($Wo_{46–48}$, $En_{47–48}$, $Fs_{4–6}$, Cr_2O_3 = 0.4–1.3 wt. %) with respect to clinopyroxene from the ultramafic xenolith cores of pelletal lapilli (Table S2 in Supporting Information S1). The Mg# values in olivine and clinopyroxene xenocrysts are also uniform (0.89–0.92) (Figure S4 in Supporting Information S1).

In all studied samples FIs are usually rounded and slightly stretched (Figures 2a–2d), and some of them form trails of variable length (0.1–1 mm), lined in sealed fractures (Figure 2c). Re-equilibration features in FIs are present (i.e., stretching and/or decrepitation process), as evidenced by the occurring of an outer dark halo around the FIs (Figure 2d). In the xenocrysts, secondary FIs (distinguished on the basis of their textural characteristics and distribution within the crystals, such as the presence of trails in sealed fractures) are more abundant than primary FIs and tend to be smaller than the primary ones. On the contrary, in olivine and clinopyroxene in the ultramafic cores of pelletal lapilli, early stage FIs are more abundant than late stage FIs. The studied FIs are characterized by pure CO_2, with melting temperatures (Tm) ranging in a very narrow interval between −56.6 (i.e., the triple point of pure CO_2 at 1 bar) and −56.8°C ± 0.1°C. All FIs homogenized to a liquid phase with temperatures of homogenization (ThL) ranging from 11.5°C to 30.2°C and from −20.0°C to 13.2°C, respectively for olivine and clinopyroxene xenocrysts, and corresponding to density range (ρ) of 0.58–0.85 and 0.84–1.03 g/cm^3. In FIs hosted in ultramafic xenoliths, ThL range from −27.3°C to −8.5°C (ρ = 0.98–1.06 g/cm^3) in clinopyroxene crystals, and from −27.7°C to −6.0°C (ρ = 0.96–1.07 g/cm^3) in olivine crystals. Values of Th_L, densities, corrected densities and number of measures are reported in Table S3 in Supporting Information S1. Further details, also about analytical methods, are reported in Supporting Information S1.

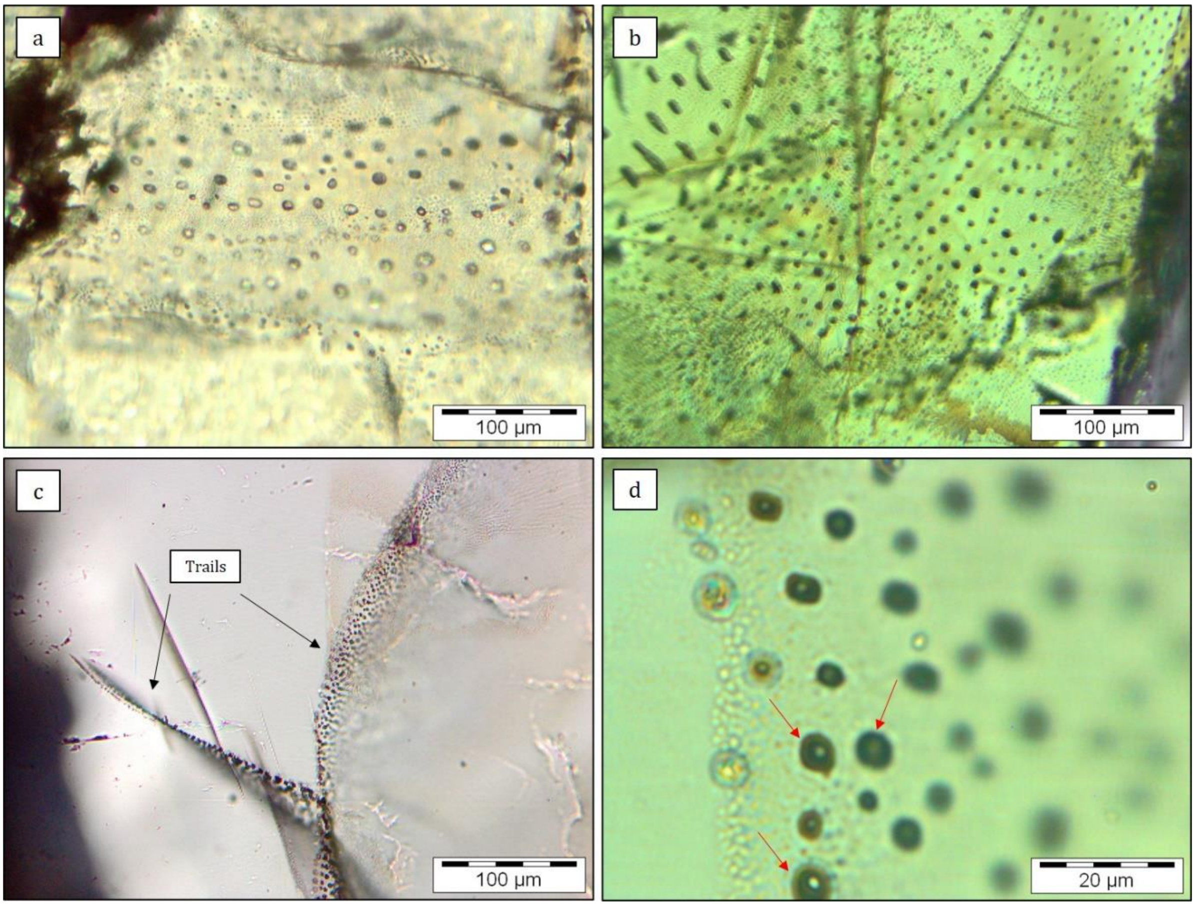

Figure 2. Photomicrographs (parallel polars) of fluid inclusions (FIs) and their textural position. FIs enclosed by (a) olivine and (b) clinopyroxene xenocrysts. (c) Intragranular trails (black arrows) of FIs in olivine xenocryst. (d) FIs with decrepitation features (red arrows) in clinopyroxene from the ultramafic core of a pelletal lapillus.

Significance of Fluid Inclusions Data

Histograms of homogenization temperatures (Figure 3a) and densities (Figure 3b) show polymodal skewed distributions. These distributions are due to fluid trapping episodes and re-equilibration that occur at different depth of the volcanic system. The highest corrected density values of FIs are in the ultramafic xenoliths (1.10–1.11 g/cm^3), corresponding to minimum fluid pressure between 8.5 and 9.0 kbar (≈27–28 km). In the clinopyroxene xenocrysts FIs recorded fluid pressure of 8.2–8.7 (≈26–27 km) and 6.7–7.2 kbar (≈21–22 km). FIs in olivine xenocrysts show fluid pressures of 2.8–3.1 (≈8–9 km) and 4.1–4.5 kbar (≈12–13 km). The low-density peak (ρ = 0.63 g/cm^3) is also present in ultramafic xenoliths. Trapping pressures and densities were estimated at the equilibrium temperature of 1100°C, that is, an intermediate value of the temperature in the range 1050°C–1150°C previously inferred by Jones et al. (2000) on pyroxenes from mantle xenoliths. All FIs show stretching and, most importantly, partial decrepitation process (Figure 2d), which is evidence of volumetric re-equilibration at high strain rates associated with a short-time scale event (e.g., Bodnar, 2003), and this is supported also by the skewed distribution of histograms. The pristine density of trapped fluid was therefore lowered during crustal ascent. Magma ascending through the lithosphere halted at important discontinuities marked by changes in chemical and physical properties of country rocks (Menand, 2011), the most important being the crust-mantle boundary. This is the case of the common depth registered by FIs in ultramafic xenoliths and clinopyroxene xenocrysts. Olivine composition (Fo% > 0.90, NiO > 0.35 wt.%), clinopyroxene Cr content (Cr_2O_3 > 1.3 wt. %) and spinel Cr# (Cr/Cr + Al) (>0.38), strongly suggest that the studied wehrlitic cores are of mantle origin and are not cumulates produced by fractional crystallization in shallow level magma ponding stages (Beccaluva et al., 2002), although cumulates can be also formed by underplating in the vicinity of Moho (e.g., Kovács et al., 2004). Furthermore, the xenoliths have no cumulative or poikilitic textures, they lack plagioclase that often occurs in cumulates, and the chemical composition overlaps well with other xenoliths from previous studies (Figure S4 in Supporting Information S1). Coherently with the crust-mantle boundary inferred beneath the Vulture area with geophysical methods (magnetism and gravimetry) at a depth of about 32 km (Kelemework et al., 2021), the re-equilibration processes lowered by about 15% the fluid density at the time of trapping. Thus, the xenoliths probably represent the shallowest upper mantle, and the FIs in the rock-forming minerals of these xenoliths suggest a minimum trapping pressure of 9–10 kbar, which is around the local Moho. FIs in loose clinopyroxene xenocrysts suggest a minimum trapping pressure of 7–9 kbar. Therefore, if we consider these clinopyroxenes as fragments of the xenoliths (as also witnessed by their similar chemical composition) it is likely that they crystallized nearby the Moho. The crystallization of loose olivine xenocrysts may have taken place at shallower, crustal depths, with FIs suggesting a minimum trapping pressure of 3–4 kbar.

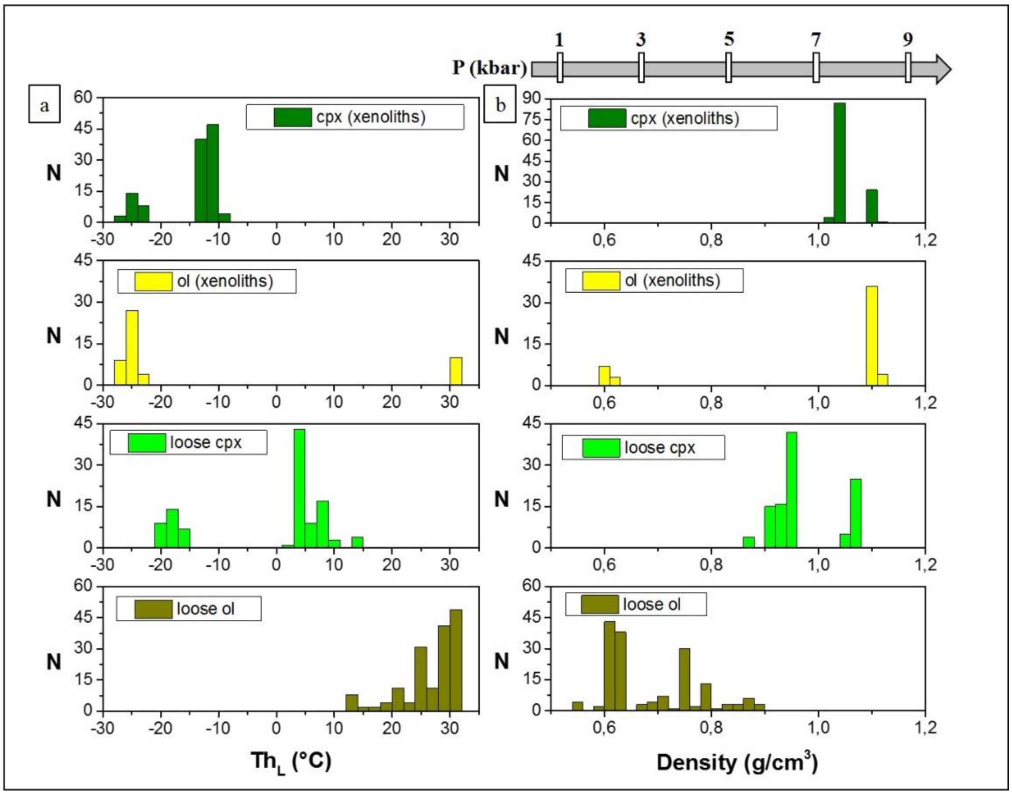

Figure 3. Frequency distribution of a) homogenization temperatures (Th$_L$) and (b) densities of FIs hosted in olivine and clinopyroxene xenocrysts and in ultramafic cores of pelletal lapilli from Mt. Vulture. The number of the total measurements (N) is reported to the left of each graph.

It is worthy of note that the shallowest trapping event in olivine xenocrysts occurring at depth of 8–13 km overlaps the depth (6–15 km) of a mafic body, probably a dense crystal mush, within the Vulture volcano magma system. Petrological investigation located a shallow magma reservoir down to 6 km (Beccaluva et al., 2002). To resume, the micro-thermometric data here presented and obtained from the crystal content from a single eruption, show a very good agreement with both geophysical and petrological data for this volcano. Figure 4 shows a simplified schematic profile view of Vulture volcano with our considerations.

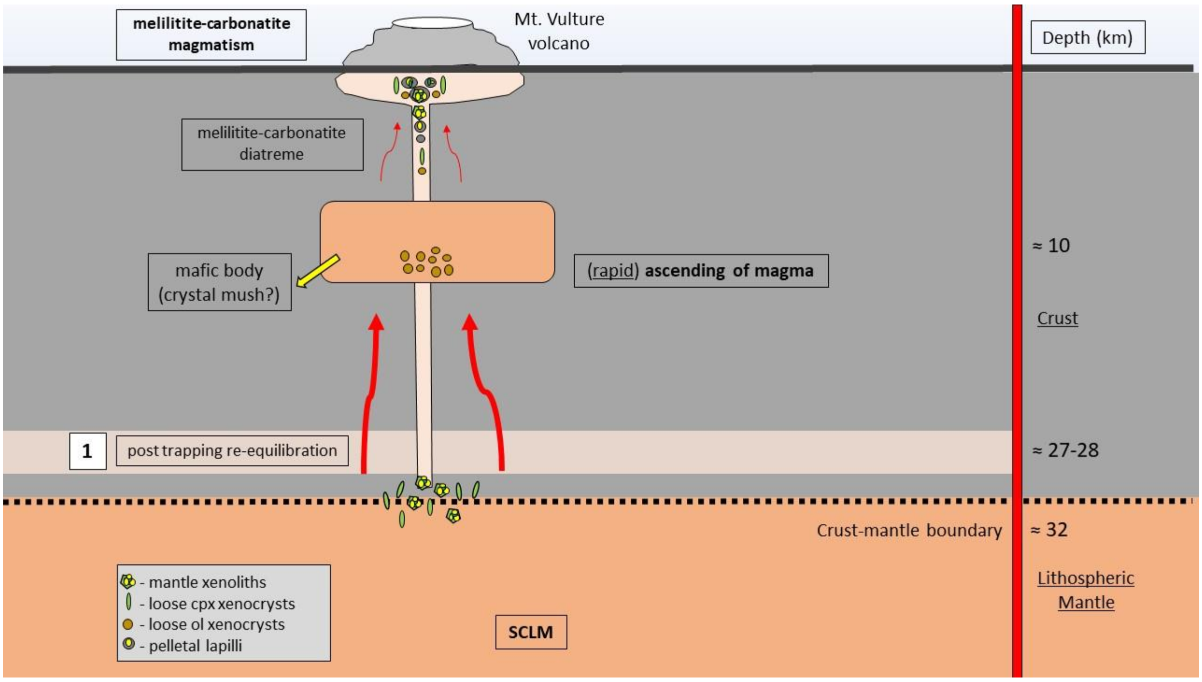

Figure 4. Simplified cross section of Vulture volcano ponding stages. Olivine and clinopyroxene of wehrlite cores of pelletal lapilli, together with clinopyroxene xenocrysts register the same fluid trapping event at the local crust-mantle boundary. Olivine xenocrysts show a shallower signature of fluid entrapment, overlapping the depth of the mafic body within the Mt. Vulture plumbing system (Improta et al., 2014). The involvement of a carbon-rich subcontinental lithospheric mantle (SCLM) beneath Vulture volcano is from Bragagni et al. (2022).

Carbonatite Metasomatism and Magma Ascent Dynamics

The study of mantle xenoliths represents a great tool to understand the composition and possible modification of a mantle source influenced by metasomatic fluids. In this framework, the increase of modal clinopyroxene at the expense of orthopyroxene has been interpreted as a result of the interaction between ultramafic material and carbonate melts, and carbonatite metasomatism is accompanied by the formation of secondary clinopyroxene formed during the reaction of carbonatite melts with orthopyroxene (Dalton & Wood, 1993; Russell et al., 2012). Although interaction between peridotite wall rock and alkaline mafic melts normally lead to clinopyroxene enrichment in the mantle, with the consequent formation of wehrlites (e.g., Patkó et al., 2020), in our case study, the process of "*wehrlitization*" in the lithospheric mantle is primary due to carbonate melts instead of mafic silicate melts.

Among the Mt. Vulture mantle products, the presence of wehrlite xenoliths is widely recognized (e.g., Beccaluva et al., 2002; Downes et al., 2002; Jones et al., 2000) and is corroborated by our findings where pelletal lapilli cores are largely wehrlitic. According to Zong and Liu (2018), specific crystallochemical patterns in clinopyroxenes (e.g., Mg# vs. Ca/Al; and Ca/Al vs. $^{87}Sr/^{86}Sr$) fall into the mantle-related carbonate metasomatism field (Figure S5 in Supporting Information S1), and $(La/Yb)_N$ ratios (>3–4), further suggest carbonatite metasomatism (Coltorti et al., 1999). Furthermore, the presence of carbonates and apatites in some wehrlites of the Mt. Vulture (Downes et al., 2002; Jones et al., 2000), reinforce the role of carbonatite melts instead of silicate melts in metasomatizing the wehrlite xenoliths. Rosatelli et al. (2007) also propose carbonatite melts as the main metasomatism agent of Mt. Vulture mantle source region, emphasizing the role of silicate-carbonatite magma immiscibility during the magma evolution at shallower depths (Solovova et al., 2005), supported by a number of experimental constrains underlying melilititic magma (the last erupted at Vulture volcano) as the best candidate to exsolve an immiscible carbonatite melt (Brooker & Kjarsgaard, 2011). Further evidence of metasomatism by carbonatite melts is given by the presence of interstitial calcite associated with Fe-Ni-sulphides between olivine grains in a mantle xenolith from Mt. Vulture (Blanks et al., 2020).

Despite the last eruptive event of Mt. Vulture dates back to 141 ± 11 ka (Villa & Buettner, 2009), geochemical evidences support that active degassing of mantle-derived volatiles is still ongoing in Mt. Vulture area (Caracausi, Martelli, et al., 2013; Caracausi et al., 2009), showing how the relationship between the deep CO_2 release and the time of its last eruption could be an important tool for evaluating the state of current activity (Caracausi et al., 2015). Moreover, recent studies show how the source of CO_2 degassing in Mt. Vulture area is related to the presence of a subcontinental lithospheric mantle (SCLM), that sequesters large amounts of CO_2 due to the infiltration of fluids and melts during carbonatite-like metasomatism (Bragagni et al., 2022). In this scenario the He isotopic signature in FIs of the Vulture mantle xenoliths (<6.1Ra; Ra is the He isotopic signature in air) overlap the range of the SCLM He end member (6.1 ± 0.9; Gautheron & Moreira, 2002).

Considering, (a) the degassing of mantle-derived fluids in Mt. Vulture area (Caracausi, Martelli, et al., 2013; Caracausi, Nicolosi, et al., 2013; Caracausi et al., 2009, 2015), (b) the explosive behavior associated with a maar-diatreme system of the Monticchio Lakes Synthem (Solovova et al., 2005; Stoppa & Principe, 1997), (c) the occurrence of small amounts of magma at the crust-mantle boundary depth (<1.6%, Tumanian et al., 2012), in absence of mantle upwelling or extensional tectonics that could favour decompression melting (Peccerillo & Frezzotti, 2015), (d) the role of tectonics in the transfer of the mantle-derived magma and volatiles and its control of the Vulture volcanism and outgassing (e.g., Caracausi, Martelli, et al., 2013; D’Orazio et al., 2007; Rosenbaum et al., 2008), (e) the long inter-eruptive periods (>140 ka, Buettner et al., 2006), and (f) the recognized occurring of volatiles rich magmas at the crust-mantle boundary (Section 4, Significance of Fluid Inclusions Data), we computed by using a simplified model the possible melilitite-carbonatite magma ascent rate to figure out fast versus slow uprise of these magmas from the crust-mantle boundary, furnishing new elements to the knowledge of Mt. Vulture activity. In order to constrain the ascent velocity of the melilitite-carbonatite magma, we used the equation from Lister and Kerr (1991) and applied by Sparks et al. (2006) in their physical model, with the same approach also proposed by Moussallam et al. (2016).

Taking into consideration (a) a closed system during the magma ascent with a constant dike width of 1 m, (b) a magma density of 2,500 kg/m^3, (c) a constant viscosity of 0.6 Pa s, and (d) a mean density of the crust of 2,600 kg/m^3, we obtain ascent rate of about 17 m/s (Equation 8 from Sparks et al. (2006)), assuming that the buoyancy is the main driving force. As there are no previous works that can help to fix the dike width in our case study, we assumed the unity (1 m) as a conservative dimension value, with the awareness of the non-linear correlation between the dike width and magma ascent rate, and the effect of different variables on dike propagation (e.g., uneven stress distribution within the crust). Magma viscosity value is taken from experimental studies of a representative melilitite synthetic melt (Stagno et al., 2020). Magma density is calculated using the model of Ochs and Lange (1999) at 1,100°C and 10 kbar, assuming a bulk composition from Stoppa and Principe (1997) with SiO_2 = 37 wt. %, and a mean CO_2 value of 7.5 wt. %, obtained from the H_2O-CO_2 solubility model proposed by Moussallam et al. (2016). Indeed, if we consider their model for a low SiO_2- and H_2O-free melts (our FIs study indicates the presence of pure CO_2 as the main volatile phase), at about 30 km depth, we obtain bulk CO_2 concentration between 5 and 10 wt. %. The model of Moussallam et al. (2016) is applied to a kimberlite magmatism (and to basalt magmatism) with 25 wt. % $\leq SiO_2 \leq$ 32 wt. %, and it is comparable to the melilitite-carbonatite magmatism of Monticchio Lakes Syntheme with $SiO_2 <$ 40 wt. % (Stoppa & Principe, 1997).

Our result of the ascent rate of the melilitite-carbonatite magma is in the same order of the ascent rates of kimberlite magmatism (e.g., Kelley & Wartho, 2000; Moussallam et al., 2016) and more than two times faster if compared with ascent rate calculated from other volcanic complexes where CO_2-rich FIs in metasomatized upper mantle xenoliths occur (e.g., 5 m/s, Szabó & Bodnar, 1996). In our simplified modelling the melilitite-carbonatite magmas could reach the surface from the depth of 30 km in less than an hour, considering, however, a single fast event without taking into account possible ponding level at crustal depth. If we consider also recent studies showing how volcanic systems where activity has remained dormant for protracted periods (>100 ka) still have the potential for reactivation (e.g., Giordano & Caricchi, 2022; Harangi et al., 2015; Molnár et al., 2018, 2019), and in Mt. Vulture there is a possible link between the development of tear faults, magmatism and related magma ascent along these tectonic pathways (Peccerillo, 2017; Rosenbaum et al., 2008), our study highlight that the volcanological community should pose great attention to volcanic hazard in melilitite-carbonatite volcanoes, and it should be carefully evaluated even after long time of quiescence.

Conclusion

We analysed FIs hosted in rock-forming minerals of the wehrlitic cores of pelletal lapilli and in xenocrysts of olivine and clinopyroxene brought to the surface by a melilitite-carbonatite magma from the last eruption of Vulture volcano (Monticchio Lakes Synthem, Lago Piccolo Subsynthem). We found pure CO_2 FIs with different trapping pressures (from 3.2 to 10.3 kbar) that correspond to magma storage at different depths within the volcano plumbing system. The deepest ponding stage is represented by the crust-mantle boundary (at a 32 km depth), while the shallower corresponds to a solidified magmatic body (former crystal mush) imaged by geophysical investigations (Improta et al., 2014). Modelling magma ascent rate results in quite high velocity (≈20 m/s) for melilitite-carbonatite magma from the crust-mantle boundary to the surface, and it is comparable with ascent rate of kimberlite magmatism (e.g., ≈45 m/s, Moussallam et al., 2016). These evidences, coupled to (a) the outgassing of magmatic volatiles at Mt. Vulture, which isotopic signature correspond to those in the FIs of the last activity of the volcano (Caracausi, Martelli, et al., 2013; Caracausi et al., 2009), and to (b) the presence of small amounts of melt (<1.6%) at the crust-mantle boundary depth, add constraints for magma production and ascent pathways. Therefore, this study confirms that the scientific community must pay attention also to the inactive volcanoes, because they could be still hazardous systems notwithstanding the last volcanic activity occurred hundreds/thousands of years ago.

Supporting Information

Text S1.

Geological Background

Mount Vulture is one of the major Quaternary volcanoes of the central Italian peninsula, located within Apulian foreland (Figure S1) with a consistent east offset with respect to the peri-thyrrenian Campanian-Latium-Tuscany volcanic alignment. The Moho beneath the Mt. Vulture is around 32 km with a lithospheric thickness approaching 100 km (Kelemework et al., 2021; Peccerillo, 2017).

The erupted silicate magmas are all silica undersaturated, ranging from foidites (leucitites, haünites, nephelinites), tephrites and basanites to phonolites (Peccerillo, 2017). The presence of intrusive calciocarbonatite ejecta (sövite), carbonatitic tephra in the pyroclastic products and carbonatite lava flows, witness the role of carbonatite magmatism beneath Mt. Vulture area (D’Orazio et al., 2007; Rosatelli et al., 2000; Stoppa & Principe, 1997), although the primary origin of the carbonate fraction is yet to be univocally accepted (D’Orazio et al., 2007, 2008; Stoppa et al., 2008).

The Monticchio Lakes Synthem (MLS) represents the most recent activity of Vulture volcano and includes five Subsynthems characterised by the presence of abundant lapilli and ultramafic mantle xenoliths (Giannandrea et al., 2006). They consist essentially of fresh spinel-lherzolite, harzburgites, dunites, wehrlite and clinopyroxenites (Downes et al., 2002; Jones et al., 2000). Geothermobarometric studies (En-Sp and Di-Sp thermo-barometers) constrained pressures and temperatures for upper mantle xenoliths in the range of 1.4-2.2 GPa and 1050-1150 °C respectively (Jones et al., 2000).

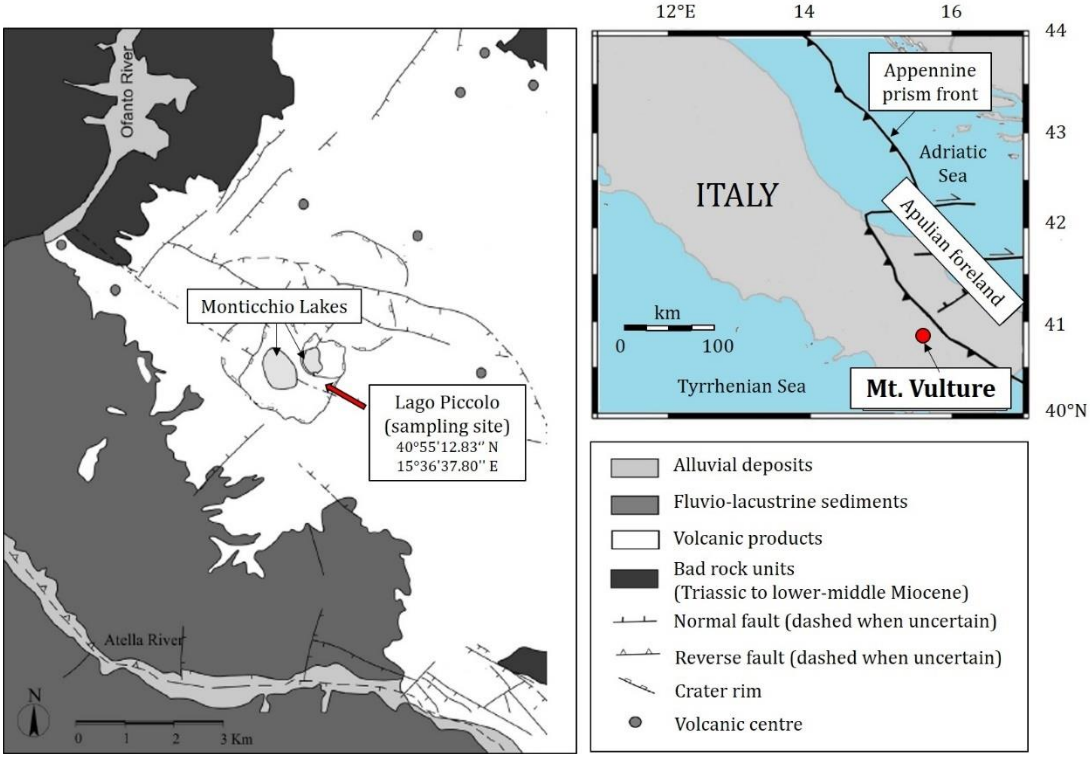

Figure S1. Simplified geological sketch map of the Mt. Vulture volcano within the central-southern italian peninsula and the front of Apennine prism (D'Orazio et al., 2007). Sampling site with GPS coordinates is also depicted.

Petrography and Mineral Chemistry

The ultramafic cores of studied pelletal lapilli consist essentially of olivine and clinopyroxene phenocrysts with very rare orthopyroxene (wherlites), while few samples (≈ 10 %) are characterised only by olivine megacrysts (dunites). Our study is focused in these wehrlites.

Olivine from the ultramafic cores of pelletal lapilli usually shows irregular elongated shape with curvilinear boundaries and also undulose extinction and intracrystalline deformation structures (Figure S2). Inclusions of spinel within the olivine phenocrysts are also present. Clinopyroxene occurs as a distinctive emerald green coloured Cr-diopside and it occurs in all of the samples subhedral/anhedral with strongly curvilinear boundaries, apparently with no deformation structures.

Cr_2O_3 content of olivine from the ultramafic cores of pelletal lapilli and of loose olivine xenocrysts varies in a very narrow range from 0.02 to 0.04 wt.% (Table S1).

The SiO_2 and CaO content of clinopyroxene from the ultramafic core of pelletal lapilli ranges from 51.7 to 53.1 wt.% and from 22.2 to 22.9 wt.% respectively. Both the SiO_2 and CaO content in clinopyroxene xenocrysts ranges from 52.2 to 54.6 wt.% and from 20.1 to 22.7 wt.% respectively, overlapping the range of values of the clinopyroxene from the ultramafic core of pelletal lapilli. The TiO_2 and Al_2O_3 content of clinopyroxene is low and ranges from 0.15 to 0.5 wt.% (in both ultramafic cores and xenocrysts) and from 3.6 to 4 wt.% (in ultramafic cores) and 2 to 5.5 wt.% (in xenocrysts), respectively (Table S2). The rim of ultramafic core of pelletal lapilli is composed of fine-grained micro-phenocrysts of häuyne, with xenocrystic debris of olivine and clinopyroxene (Figure S3). Olivine and clinopyroxene minerals from the ultramafic xenoliths and xenocrysts show almost the same chemical composition. Indeed, it is evident in the diagram Mg# vs. NiO wt. % (olivine) and Cr_2O_3 wt. % (clinopyroxene) (Figure S4).

In the Ca/Al vs Mg# and $^{87}Sr/^{86}Sr$ vs Ca/Al diagrams, clinopyroxenes present as xenocrysts and in the Mt. Vulture xenoliths both fall within the field of the mantle-related carbonate metasomatism field (Figure S5). Indeed, clinopyroxenes from Mt. Vulture show restricted range of every ratio ($5 \leq Ca/Al \leq 14$; $0.88 \leq Mg\# \leq 0.91$; $0.70424 \leq {}^{87}Sr/^{86}Sr \leq 0.70585$) (data are from Downes et al., 2002; Jones et al., 2000), in accordance with type 2 mantle-related carbonate metasomatism described by Zong and Liu (2018).

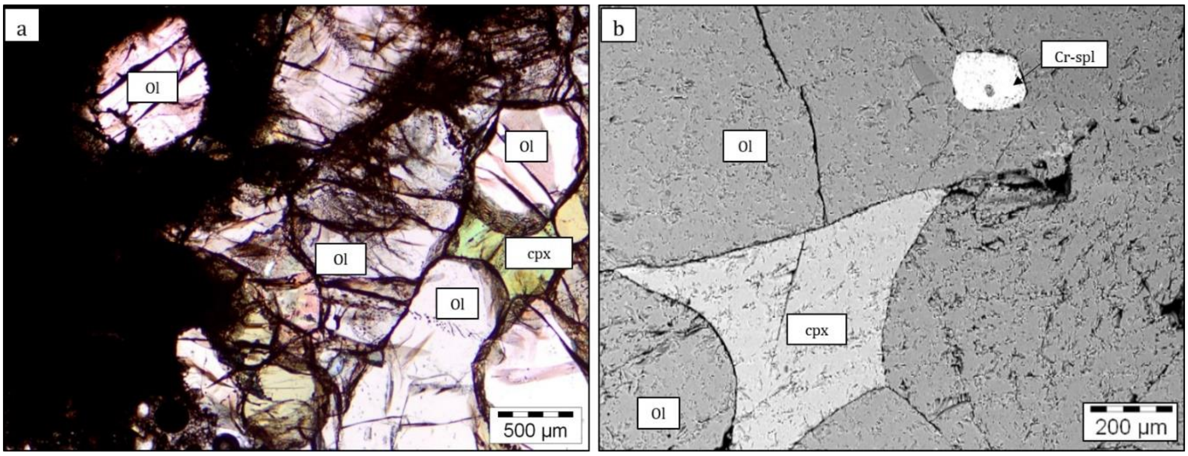

Figure S2. Photomicrographs of the ultramafic core of pelletal lapilli from Vulture volcano. a) Granoblastic texture with clinopyroxene (emerald green Cr-diopside) and elongated olivine crystal with intracrystalline deformations (parallel polars). b) Backscattered electrons (BSE) image showing clinopyroxene and olivine crystal with Cr-spinel inclusion.

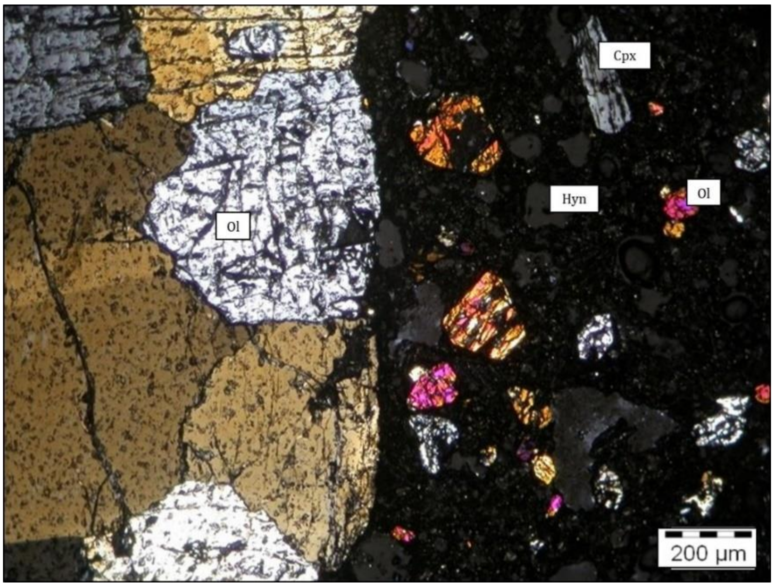

Figure S3. Crossed polars microphotograph showing the olivine micro-phenocrysts of the wehrlitic core of pelletal lapilli (on the left) and the rim of pelletal lapillus composed of fine-grained micro-phenocrysts of häuyne and xenocrystic debris of olivine and clinopyroxene (on the right), Monticchio Lake Synthem, Mt. Vulture volcano. Ol-olivine, Cpx-clinopyroxene, Hyn-häuyne.

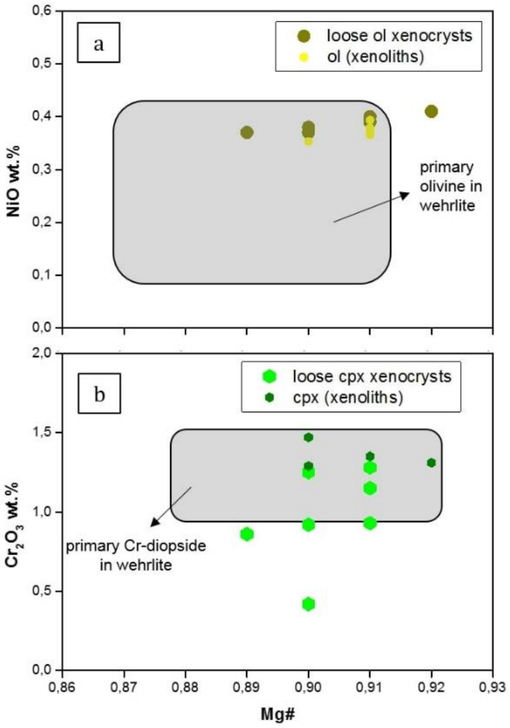

Figure S4. Chemical composition of olivine and clinopyroxene (Cr-diopside) from the ultramafic xenoliths and olivine and clinopyroxene xenocrysts from Mt. Vulture volcano. a) Mg# vs. NiO wt. % in olivine crystals. b) Mg# vs. Cr_2O_3 wt. % in clinopyroxene crystals. The field of the primary olivine and Cr-diopside in wehrlite Mt. Vulture xenoliths are from Jones et al. (2000).

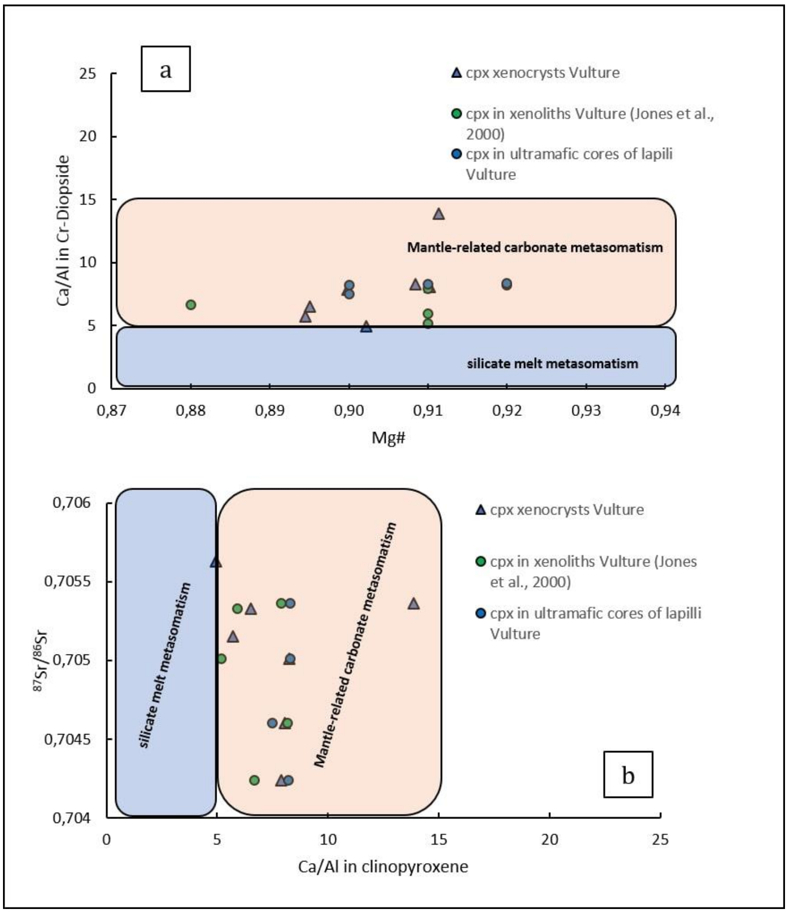

Figure S5. Ca/Al ratio vs. a) Mg# and b) ^{87}Sr/^{86}Sr ratio of clinopyroxene from Mt. Vulture. Sr isotopic ratios are from Downes et al. (2002). Fields of carbonate vs. silicate melts metasomatism are taken from Zong and Liu (2018).

Table S1. Minerochemical composition of olivine (in wt. %) from the core of pelletal lapilli and olivine xenocrysts from Vulture volcano, Monticchio Lakes Synthem.

Sample	ol1-lap	ol2-lap	ol3-lap	ol4-lap	ol5-lap	ol6-lap	ol7-lap
	core	core	core	core	core	core	core
	n=3	n=3	n=3	n=3	n=3	n=3	n=3
SiO_2	41.73	41.70	41.97	42.04	40.76	40.66	40.22
$FeO_{tot.}$	8.97	9.15	9.02	8.97	9.03	10.07	9.00
MnO	0.14	0.14	0.14	0.14	0.13	0.16	0.14
MgO	49.62	49.79	49.66	49.71	50.09	50.80	51.48
CaO	0.09	0.09	0.08	0.09	0.09	0.10	0.09
Cr_2O_3	0.03	0.03	0.03	0.03	0.03	0.03	0.03
NiO	0.38	0.37	0.38	0.37	0.39	0.35	0.37
Tot.	100.95	101.27	101.28	101.35	100.52	102.16	101.33
Fo	90.79	90.65	90.75	90.81	90.82	90.00	91.07
Fa	9.21	9.35	9.25	9.19	9.18	10.00	8.93

Notes: n= number of analyses. Core-rim analyses do not show significant zonation.

Table S1. Cont.

Sample	ol-1	ol-2	ol-3	ol-4	ol-5	ol-6	ol-7
	xenocryst	xenocryst	xenocryst	xenocryst	xenocryst	xenocryst	xenocryst
	n=3	n=3	n=3	n=3	n=3	n=3	n=3
SiO_2	40.50	39.65	40.56	41.50	40.09	41.67	40.97
$FeO_{tot.}$	9.36	10.35	8.11	9.66	9.06	8.49	10.11
MnO	0.14	0.15	0.11	0.13	0.12	0.11	0.14
MgO	49.87	48.97	50.75	50.72	49.83	49.60	50.32
CaO	0.15	0.14	0.19	0.18	0.12	0.18	0.14
Cr_2O_3	0.03	0.02	0.04	0.02	0.04	0.03	0.02
NiO	0.38	0.37	0.41	0.37	0.40	0.39	0.37
Tot.	100.43	99.64	100.16	102.59	99.66	100.48	102.07
Fo	90.48	89.40	91.78	90.35	90.75	91.24	89.87
Fa	9.52	10.60	8.22	9.65	9.25	8.76	10.13

Notes: n= number of analyses. Core-rim analyses do not show significant zonation.

Table S2. Minerochemical composition of clinopyroxene (in wt. %) from the core of pelletal lapilli and clinopyroxene xenocrysts from Vulture volcano, Monticchio Lakes Synthem.

Sample	cpx1-lap	cpx2-lap	cpx3-lap	cpx4-lap
	core	core	core	core
	n=3	n=3	n=3	n=3
SiO_2	52.30	52.98	53.14	51.75
TiO_2	0.33	0.40	0.15	0.48
Al_2O_3	3.63	3.72	3.68	4.02
FeO	2.78	2.59	3.13	3.40
MnO	b.d.l	b.d.l	b.d.l	b.d.l
MgO	16.20	16.55	16.40	16.44
CaO	22.29	22.90	22.40	22.24
Na_2O	0.62	0.56	0.52	0.49
Cr_2O_3	1.35	1.31	1.47	1.29
Tot.	99.50	101.01	100.89	100.12
Mg#	0.91	0.92	0.90	0.90
Wo	47.42	47.76	46.99	46.57
En	47.96	48.02	47.88	47.88
Fs	4.62	4.22	5.13	5.55

Notes: Mg# = (Mg/Mg + Fe). n= number of analyses. b.d.l= below detection limit. Core-rim analyses do not show significant zonation.

Table S2. Cont.

Sample	cpx-1	cpx-2	cpx-3	cpx-4	cpx-5	cpx-6	cpx-7
	xenocryst	xenocryst	xenocryst	xenocryst	xenocryst	xenocryst	xenocryst
	n=3	n=3	n=3	n=3	n=3	n=3	n=3
SiO_2	54.56	53.09	52.91	52.81	53.13	52.46	52.19
TiO_2	0.16	0.31	0.37	0.38	0.43	0.14	0.48
Al_2O_3	2.09	3.67	3.84	3.80	4.55	5.48	5.19
FeO	3.02	2.90	3.20	2.91	3.33	3.20	3.42
MnO	b.d.l	b.d.l	b.d.l	b.d.l	b.d.l	b.d.l	b.d.l
MgO	17.42	16.12	16.12	16.52	15.91	16.55	16.25
CaO	21.43	22.41	22.38	22.71	21.91	20.15	21.98
Na_2O	0.73	0.64	0.71	0.61	0.75	1.10	0.79
Cr_2O_3	1.15	1.28	0.92	0.93	0.42	1.25	0.86
Tot.	100.55	100.42	100.45	100.67	100.42	100.33	101.16
Mg#	0.91	0.91	0.90	0.91	0.90	0.90	0.89
Wo	44.62	47.58	47.31	47.34	46.97	44.12	46.51
En	50.47	47.62	47.42	47.93	47.47	50.42	47.84
Fs	4.91	4.80	5.28	4.73	5.56	5.47	5.64

Notes: Mg# = (Mg/Mg + Fe). n= number of analyses. b.d.l= below detection limit. Core-rim analyses do not show significant zonation.

Analytical Methods

Mineral composition of analysed samples was determined by a CAMECA SX100 electron microprobe at Observatoire des Sciences de l’Univers (UPMC-INSU) (Paris, France), operating at 15 kV accelerating voltage and a 20nA beam current.

Fluid Inclusions were studied in doubly-polished wafers and single mineral grains by a Linkam THMSG 600 microscopic heating/cooling stage, at the Instituto de Vulcanologia e Avaliação de Riscos (IVAR) (Ponta Delgada, Portugal). Olivine and clinopyroxene xenocrysts were embedded in epoxy resin and doubly polished until a thickness of 100-80 µm. The stage was cooled with liquid nitrogen and calibrated using a single standard crystal of quartz with pure H_2O and CO_2 inclusions. Cooling and heating rates varied during the analysis. Indeed, in order to minimize the effect of metastable transformations during cooling, very common in fluid inclusions, melting and homogenization temperatures were determined during heating at the minimum rate (1 °C/min). For CO_2-rich inclusions (H_2O:CO_2 ratio = 1:10) densities were firstly calculated on the basis of the equation provided in Sterner and Bodnar (1991) and finally corrected according to Hansteen and Klügel (2008), while isochore trajectories/curves were calculated using the software "Fluids" (Bakker, 2003).

In order to convert barometric data into depths, we made some assumptions on crustal density of along the inferred magma pathway, using the stratigraphy presented in the CROP-4 deep seismic profile beneath the Mt. Vulture area (Scrocca et al., 2007). Considering (i) the average value of 2600 kg/m^3 of the shallow crust lithologies, (ii) an average value of 3300 kg/m^3 of the shallow mantle lithologies, and (iii) the probable presence of a mafic body beneath Mt. Vulture (Improta et al., 2014 and references therein), a single representative average value of 3000 kg/m^3 was considered. Micro-thermometric data of studied samples are reported in Table S3.

Table S3. Micro-thermometric data of studied samples.

Sample	Mineral analysed	N° measures	Th_L (°C)	ρ (g/cm^3)	ρ (g/cm^3)$_{corrected}$
Ol-I	olivine	46	Th_L 11.5 – 30.2	0.58 – 0.85	0.61 – 0.89
Ol-II	olivine	12	Th_L 13.0 – 20.9	0.76 – 0.84	0.80 – 0.88
Ol-III	olivine	113	Th_L 23.3 – 30.9	0.52 – 0.73	0.54 – 0.77
Cr-cpx I	clinopyroxene	77	Th_L 2.7 – 13.2	0.84 – 0.91	0.88 – 0.95
Cr-cpx II	clinopyroxene	30	Th_L -20.0 – -15.1	1.01 – 1.03	1.05 – 1.08
LAP-1	olivine (1)	40	Th_L -27.7 – -23.4	1.05 – 1.07	1.10 – 1.11
	clinopyroxene (2)	36	Th_L -27.3 – -8.5	0.98 – 1.06	1.02 – 1.11
LAP-2	olivine (1)	28	Th_L -9.0 – 30.3	0.58 – 0.98	0.60 – 1.02
	clinopyroxene (1)	80	Th_L -13.5 – -11.5	0.99 – 1.00	1.04 – 1.05

Notes: in brackets the number of analysed minerals; Th_L= homogenization temperature; ρ = density

5.2.1 The role of the gas expansion in the melilitite-carbonatite magma

In order to calculate all aspect ratio-related parameters of pelletal lapilli from Mt. Vulture (i.e. major and minor axis, perimeter, cross-sectional area of rim and core and circularity values), individual samples were selected, digitised and processed in the image-analysis software package ImageJ, following the method of Gernon et al. (2012). The main geometric measurements of studied pelletal lapilli are reported in **Table 10**.

Table 10. Calculated geometric parameters of studied pelletal lapilli from Vulture volcano, Monticchio Lakes Synthem.

Sample	**ax$_{min}$** (mm)	**ax$_{max}$**	**ax core$_{min}$**	**ax core$_{max}$**	**P** (mm)	**P core**	**A** (mm^2)	**A core**	**A rim**	**circularity**
LAP-1W	14.0	15.0	7.5	10.0	47.1	31.4	153.9	78.5	75.4	0.9
LAP-2W	13.0	15.8	6.7	9.0	49.6	28.3	132.7	63.6	69.1	0.7
LAP-3W	11.4	14.7	7.9	8.0	46.2	25.1	102.0	50.2	51.8	0.6
LAP-4W	8.7	9.7	3.7	6.0	30.5	18.8	59.4	28.3	31.2	0.8
LAP-5W	7.1	8.2	4.1	5.5	25.7	17.3	39.6	23.7	15.8	0.7
LAP-6W	9.7	11.9	7.0	7.5	37.4	23.6	73.9	44.2	29.7	0.7
LAP-7W	9.8	12.5	3.8	6.4	39.3	20.1	75.4	32.2	43.2	0.6
LAP-8W	12.2	14.9	4.0	8.2	46.8	25.7	116.8	52.8	64.1	0.7
LAP-9W	12.5	14.0	6.0	8.5	44.0	26.7	122.7	56.7	65.9	0.8
LAP-10W	11.0	16.1	2.5	6.8	50.6	21.4	95.0	36.3	58.7	0.5
LAP-11ol	9.3	10.3	6.6	7.0	32.3	22.0	67.9	38.5	29.4	0.8
LAP-12ol	12.8	14.5	8.8	9.1	45.5	28.6	128.6	65.0	63.6	0.8
LAP-13D	12.3	12.4	5.0	9.0	38.9	28.3	118.8	63.6	55.2	1.0
LAP-14ol	9.0	10.6	6.5	6.9	33.3	21.7	63.6	37.4	26.2	0.7
LAP-15D	11.3	11.4	5.9	7.2	35.8	22.6	100.2	40.7	59.5	1.0
LAP-16ol	8.9	10.0	4.1	7.0	31.4	22.0	62.2	38.5	23.7	0.8
LAP-17W	9.6	9.7	6.8	7.0	30.5	22.0	72.3	38.5	33.9	1.0
LAP-18W	6.8	7.5	3.9	5.0	23.6	15.7	36.3	19.6	16.7	0.8
LAP-19W	7.7	8.8	5.8	6.1	27.6	19.2	46.5	29.2	17.3	0.8
LAP-20D	6.9	10.5	5.7	6.0	33.0	18.8	37.4	28.3	9.1	0.4
LAP-21W	6.8	7.3	4.5	5.0	22.9	15.7	36.3	19.6	16.7	0.9
LAP-22D	7.6	10.0	4.7	4.8	31.4	15.1	45.3	18.1	27.3	0.6
LAP-23D	8.4	11.0	4.6	5.9	34.5	18.5	55.4	27.3	28.1	0.6
LAP-24W	6.4	6.9	5.0	5.1	21.7	16.0	32.2	20.4	11.7	0.9
LAP-25W	8.4	9.2	6.8	6.9	28.9	21.7	55.4	37.4	18.0	0.8
LAP-26W	9.9	10.7	6.8	7.5	33.6	23.6	76.9	44.2	32.8	0.9
LAP-27D	11.7	12.8	7.0	8.1	40.2	25.4	107.5	51.5	56.0	0.8
LAP-28W	7.5	10.6	5.3	5.5	33.3	17.3	44.2	23.7	20.4	0.5
LAP-29W	10.4	11.3	5.5	6.7	35.5	21.0	84.9	35.2	49.7	0.8

Notes: W = wehrlite; D = dunite; ol = olivine; ax = axis; P = perimeter; A = area.

The minimum axis of the entire pelletal lapilli sample data set range from 6.4 to 14 mm, while the maximum axis ranges from 6.9 to 16.1 mm. As regards the ultramafic cores of lapilli, the minimum axis ranges from 2.5 to 8.8 mm and the maximum axis ranges from 4.8 to 10 mm. The calculated cross-sectional areas of rims of pelletal lapilli show a good correlation with cross-sectional areas of cores (**Fig. 5.14**), with a correlation coefficient r = 0.84. The circularity (defined as 4π x area/perimeter^2) varies from 0.4 to 1.0 (i.e., 1.0 indicates a perfect circle), although the percentage frequency distribution shows that the most frequent value is 0.8.

Pelletal lapilli associated with diatreme-maar systems present similar physical and geometrical characteristics to specific particles formed during an industrial process known as ‘fluidised spray granulation’, widely used in industrial engineering and applied in geological contexts in the case of the genesis of some southern African pelletal lapilli in deposits produced by some kimberlite eruptions (Gernon et al., 2012), and partially applied also in the genesis of pelletal lapilli from Cabezo Segura volcano, in south central Spain (Carracedo Sánchez et al., 2015). The observed geometrical characteristics of Mt. Vulture pelletal lapilli are similar to those of southern African associated with volcaniclastic kimberlite of Venetia and Letšeng (Gernon et al., 2012). Indeed, considering the evaluation of the aspect ratio and internal structure of both pelletal lapilli occurrences, they show moderate to strong positive correlation between the cross-sectional areas of rims and cores, with high circularity values, suggesting a uniform process of coating. Furthermore, the presence of concentric accretionary rims suggests a multi-stage layering process of early nucleation and accretion, as exhibited by Mt. Vulture lapilli (Lloyd and Stoppa, 2003).

The role of gas-fluidisation in the formation of pelletal lapilli and in their transport to the surface, as a process involving a bed of particles in an upward moving elutriated gas-dominated medium, is widely recognized (e.g., Wilson, 1984). When the gas flow velocity is sufficiently high to support the weight of particles, these latter are fluidised, without being carried out of the system. In this way, a minimum gas fluidisation velocity (i.e., *Umf*, to fluidised the particles) and a terminal velocity (i.e., *Ut*, to entrained and transport out of the system the particles) can be defined (Sparks, 1976). Computing the Ergun equation for estimation of minimum gas fluidisation velocity in a turbulent flow, we calculated and plotted the variation of minimum fluidisation velocity of studied pelletal lapilli (**Fig. 5.15**). To fluidise a pelletal lapillus of 1 cm in diameter (a representative diameter value of studied sample), with a density of 3300 kg/m^3 (to represent the dense ultramafic core), a porosity of 0.5, a sphericity of 0.8 (the value with the highest measured percentage frequency), a gas dynamic viscosity of 4.62 x 10^{-6} Pa s, and a gas density of 1100 kg/m^3 (i.e., the highest calculated CO_2 density from FIs in our previous work, Carnevale et al., 2022), gas velocity must have reached at least 11 m/s, while to entrain and transport it out of the system, a higher gas terminal velocity (i.e., exit velocity) is needed. Our results are in the range of minimum gas fluidisation velocities calculated in Venetia and Letšeng pelletal lapilli (Gernon et al., 2012), and comparable with gas terminal velocities previously calculated in Mt. Vulture lapilli (Stoppa et al., 2011). In our previous magma ascent rate calculations in the last melilitite-carbonatite activity of the Mt. Vulture volcano (≈ 20 m/s, Carnevale et al., 2022) we did not take account of the exsolution and expansion of CO_2, considered the main accelerating gas agent during the melilitite-carbonatite magma evolution, as evidenced by the presence of pure CO_2 primary fluid inclusions within the rock-forming minerals of wehrlite xenoliths (Carnevale et al., 2022). However, exsolution and expansion of volatiles during magma ascent are expected to exert a major role on melilitite-carbonatite eruptive processes. Although at high pressure CO_2 does not behave ideally, most of the gas exsolution, expansion and cooling take place at low pressure where is reasonable to assume a behaviour close to ideal (Spera, 1984). Sparks et al. (2006) shows the volumetric fraction of exsolved gas as a function of pressure expressed as a depth equivalent assuming lithostatic pressure conditions. Thus, the role of gas exsolution and bubble expansion is crucial, contributing to accelerate the magma ascent towards the surface, and for this reason it should be evaluated in any similar study.

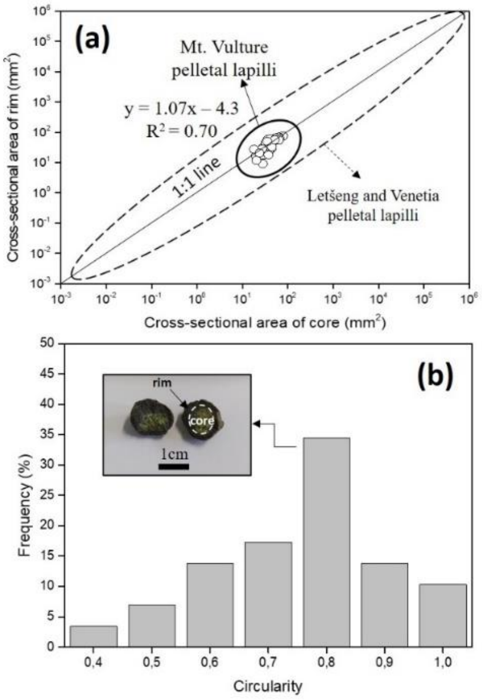

Fig. 5.14: Diagrams of the main geometric characteristics of pelletal lapilli from Mt. Vulture. a) Cross-sectional area of core vs. cross-sectional area of rim (data of pelletal lapilli from Letšeng and Venetia are also plotted for comparison; Gernon et al., 2012). b) Histograms showing circularity values of pelletal lapilli.

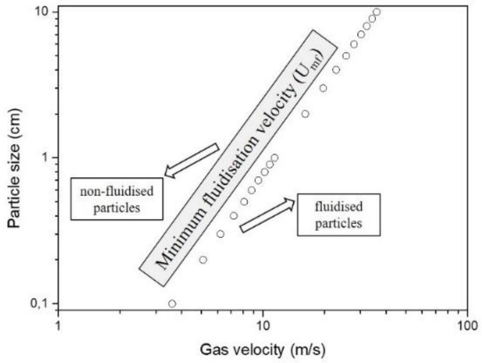

Fig. 5.15: Variation of minimum fluidisation velocity (Umf, equation (2) from Wilson, 1984) and terminal velocity (Ut, equation (4) from Sparks, 1976) for studied Mt. Vulture lapilli, fluidised by CO_2 at 1100 °C.

Chapter 6: Oceanic vs continental carbonatites: petrogenetic model and future perspectives

As described in the Sub-Chapter 2.4, carbonatite magmatism is essentially related to intraplate continental tectonic settings, with only two occurrences in oceanic tectonic setting: Cape Verde and Canary (Fuerteventura) Archipelago. Several studies were proposed trying to explain why oceanic carbonatites are so rare and are not found in all HIMU-OIB-like archipelagos (e.g., Hoernle et al., 2002; Doucelance et al., 2010; Schmidt and Weidendorfer, 2018; Carnevale et al., 2021), but currently there is no petrogenetic model that can constrain the issue in detail. Although it is a simple model, here is presented a carbonatite petrogenetic model in oceanic environment (**Fig. 6.1**) based essentially on the most important geochemical and experimental petrology studies and on the main results of this thesis (see Chapter 4). Since the pioneering studies of experimental petrology about carbonatite petrogenesis (see Sub-Chapter 2.2 for more details) it is clear that all petrogenetic processes are related to the formation of a primary carbonate melt derived from a carbonated mantle, with processes of metasomatism with carbonatitic melts, notwithstanding the oceanic or intracontinental context. Hammouda and Keshav (2015) show how the region located in the depth range of 90 to 150 km deep is where carbonatitic melts can most likely be produced and impregnate the surrounding mantle through metasomatism, and the upper bound of this region is called the *carbonate ledge*. This latter represents the shallowest depth at which carbonate melt is stable before degassing, and in the carbonated peridotite system is located between 20 and 30 kbar (Hammouda and Keshav, 2015). Therefore, the presence of the carbonate ledge prevents carbonatite magmas to reach the surface, and only very fast ascent rates can prevent primary carbonatites from degassing by reaction at the ledge through the ascent to the surface. However, Hammouda et al. (2014) experimentally demonstrated that in hot thermal environments the ledge could be avoided, reacting with an harzburgitic mantle and becoming more calcic upon ascent. Moreover, according to them, Shmidt and Weidendorfer (2018) proposed that oceanic carbonatites develop in hotspots where primitive silicate melts have the lowest SiO_2 and highest total alkalis, characteristics that originate from deep and low-degree melting, and this would be responsible for more abundant carbonatites in continental hotspots, where the lithosphere is a priori thicker than below oceanic crust. Thus, in oceanic tectonic settings it is fundamental the thickness of the lithosphere, and this is perfectly in agreement with the thickness of the lithosphere under Fuerteventura and Cape Verde archipelago, with an anomalously high transitional oceanic to continental crust (Lodge and Helffrich, 2006; Martinez-Arevalo et al., 2013). Indeed, as highlighted in both Fuerteventura and Cape Verde carbonatite occurrences, the contribution of a SCLM in their petrogenesis is fundamental. To resume, according also with Doucelance et al. (2010), here it is proposed a petrogenetic model that can be described as the “**PluMeTh**” condition: 1) there must be a mantle **Plu**me to preserve the required hot environment and acting as a trigger for low-degree partial melting at the base of the oceanic lithosphere; 2) processes of mantle **Me**tasomatism by carbonatitic melts in a carbonated mantle with the involvement of a SCLM are needed; 3) the oceanic lithosphere must be **Th**ick in order to favor plume-induced partial melting at the base, with the production of primitive silicate melts with the lowest SiO_2 and highest total alkalis and the subsequent processes that drive evolving melts into the carbonatite–silicate miscibility gap.

Although during the last decade many important contributions from petrology, experimental petrology, and geochemistry dealing with carbonatite systems are available (Yaxley et al., 2022 and references therein), some open questions still require future researches:

- What are the main processes that concentrate the critical metals to economic interest in carbonatite systems?
- Is the involvement of a SCLM in oceanic carbonatite petrogenesis a *conditio sine qua non* or there are other important conditions? Moreover, how can we unequivocally distinguish carbonatite derived directly from partial melting of the upper mantle from parental melts formed by secondary processes?
- What is the role of the carbonatite mantle metasomatism (and related processes such as *wehrlitization*) in those areas with CO_2 mantle degassing and volcanic systems related to diatreme explosive eruptions? Since the correlation between CO_2 degassing and active seismicity areas is recognized, detailed studies of those areas where carbonatite-like metasomatism with the involvement of SCLM and dissolved CO_2 partial pressure anomalies occur and several mantle xenoliths are available (to evaluate wehrlitization processes), could be crucial for future considerations?

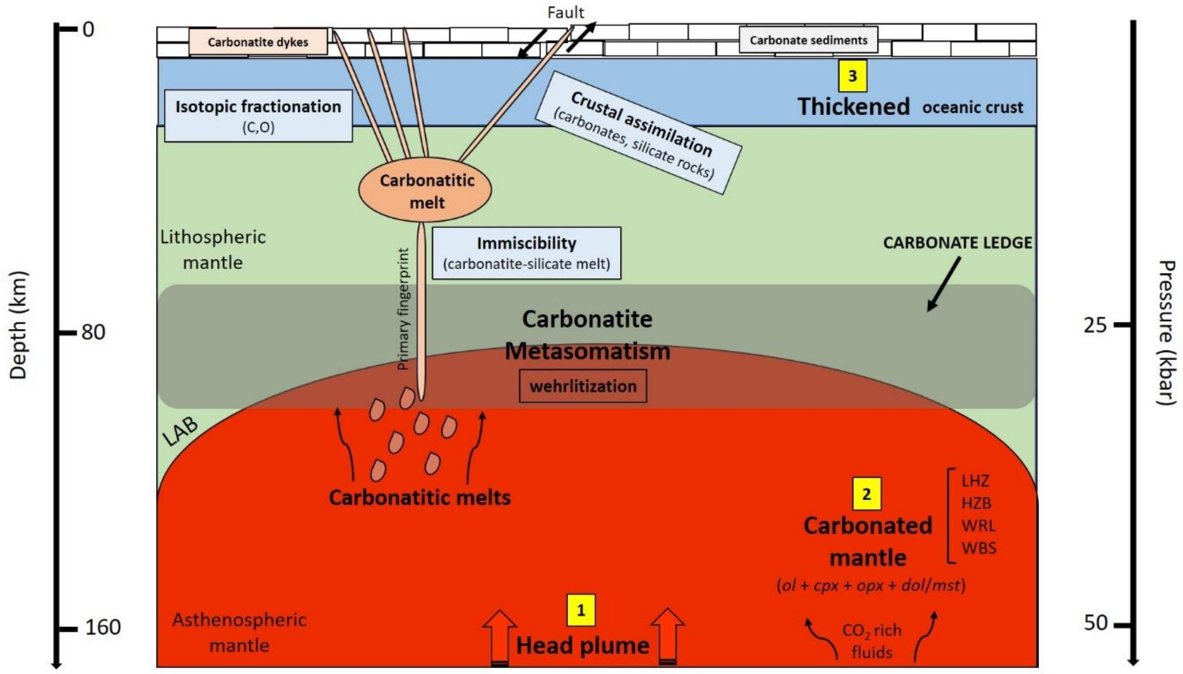

Fig. 6.1: Proposed simple petrogenetic model for oceanic carbonatites with the PluMeTh condition.

Chapter 7: Final remarks

The multidisciplinary approach of this thesis on petrology and geochemistry of carbonatites permitted characterize the source of carbonatite magmatism in different geodynamic settings, identifying the role of the infiltrating fluids in the transport and concentration of Rare Earth Elements (REEs), and the role of the carbonatite primary melts in metasomatizing the mantle source.

Petrographic and micro-thermometric analyses of Fuerteventura intrusive Ca-carbonatites show the presence of REEs-rich filled microfractures in accessory minerals with primary low temperature and low salinity fluids, proving how REEs can be mobilised and concentrated on the local scale by low-temperature hydrothermal fluids (< 300 °C) with a process known as autometasomatism. First geochemical isotope analyses (noble gases and Fe isotopes) on the same Fuerteventura oceanic Ca-carbonatites show how in the rare context of oceanic lithosphere a contribute of a sub-continental lithospheric mantle (SCLM) in their petrogenesis is needed, and among the differentiation processes, liquid immiscibility with the silicate melt counterpart is the most important.

Petrographic and chemical analyses of the melilitite-carbonatite matrix, carbonatite-rich layer, and enclosed pelletal lapilli in the ash-rich tuff deposit of the last melilitite-carbonatite explosive activity of the Mt. Vulture volcano, show compositions comparable with those of the average values of extrusive carbonatite, suggesting a contribution of a carbonatite melt in the trace elements enrichment processes. Furthermore, the presence of several wehrlite xenoliths, together with petrographic evidences such as reaction coronas in orthopyroxenes or the presence of hydrous phases (phlogopite), suggest that processes of *wehrlitization* and mantle metasomatism beneath Mt. Vulture area occurred, with carbonatite melt representing the main metasomatic agent. Calculated values of oxygen fugacity support the evidence that Mt. Vulture xenoliths would have formed by interaction with an oxidized CO_2-rich metasomatic fluid. Accordingly, micro-thermometric studies on mantle xenoliths-forming minerals show the presence of high density (1.10-1.11 g/cm^3) pure CO_2 fluid inclusions, and histograms of densities and homogenization temperatures of fluid inclusions permitted to identify two different magma ponding stages at a minimum trapping pressure coinciding with the local crust-mantle boundary (≈ 30 km depth) and at a shallower crustal level, where a solidified magmatic body was identified. Modelling magma ascent rate results in quite high velocity (≈ 20 m/s) for melilitite-carbonatite magma. Moreover, modelling of geometric data, together with inferences regarding the role of a pure CO_2 gas phase as principal propellent in an upward moving elutriated gas-dominated medium, resulted in gas minimum fluidisation velocities of about 10 m/s, allowing to reconstruct a possible scenario where the role of pure CO_2 bubbles expansion and the fluidised spray granulation process are important during the volcanic conduit dynamics in explosive carbonatite eruptions.

To resume,

(i) as regards the case study of Fuerteventura, this thesis contributes to further constrain the petrogenesis of oceanic carbonatites, particularly:

(1) isotope geochemistry (noble gases and Fe isotopes) gives an important contribution to the oceanic carbonatite petrogenesis emphasizing the role of SCLM in the rare context of oceanic carbonatites and the role of liquid immiscibility as the main differentiation processes;

(2) combining our results with the most important geochemical and experimental petrology studies a general petrogenetic model for oceanic carbonatites is proposed, where a mantle plume, a metasomatized mantle (with the involvement of a SCLM), and a thick oceanic lithosphere are considered fundamental conditions for oceanic carbonatites petrogenesis;

(3) petrography, mineral and whole-rock chemistry show not only a primary nature of the carbonatite melts but also how the low temperature fluids play an important role in the transport and REEs concentration processes in carbonatites after the magmatic stage, with direct implications of economic interest;

(ii) as regards the case study of Mt. Vulture, this thesis contributes to further constrain the petrogenesis of intra-continental carbonatites and related mantle processes, particularly:

(4) fluid inclusions micro-thermometry shows the presence of CO_2-rich fluids in mantle xenoliths, and two different magma storage at different depth in Mt. Vulture volcanic system;

(5) modelling magma ascent rate results in quite high velocity (≈ 20 m/s) for melilitite-carbonatite magmas, while modelling gas expansion results in comparable minimum gas fluidisation velocities (≈ 10 m/s);

(6) detailed petrographic studies show evidences of wehrlitization processes as a consequence of carbonatite metasomatism in lithospheric mantle, emphasizing the role of primary carbonatite melts in metasomatizing the mantle source with related CO_2 degassing;

(7) high redox conditions support an interaction with an oxidized carbonated metasomatic fluid;

(8) the evidences of carbonatite-like metasomatism and mantle degassing, and the presence of mantle xenoliths in volcanic systems related to diatreme explosive eruptions with long quiescence period and high velocity magma ascent rate, are considered important in the evaluation of volcanic hazard.

Acknowledgments

The moment of writing the acknowledgments is extremely intense, because all emotions are transformed into words, and this is certainly not an easy work. To say that these last 3 years have been difficult would be banal, but surely starting a PhD course in the middle of a global pandemic is not something that often happens. The real added value of my PhD are the different people that accompanied me on this fascinating “journey”, with their role they contributed to making it even easier, and for this reason, I want to thank them individually.

Firstly, i would like to thank my tutor Professor S.G. Rotolo. With him it is a relationship that began in 2015 with the Bachelor’s thesis and continued with the Master's one, up to the drafting of this Doctoral thesis. Professors that our department will rarely have again. A scientific guide and a mentor for me, and for this reason I will never stop thanking him.

One of the most beautiful "discoveries" that has positively changed my career is certainly my co-tutor Antonio Caracausi. I learned many qualities from him, such as the scientific rigor, teamwork, passion for everything, and he really puts a lot of it into all his works. Not only a tutor for me, but also a friend, an older brother, who always knows how to advise you on the best. Most of my acknowledgments go to him.

I thank Vittorio Zanon, who kindly hosted me in his laboratory and allowed me to learn a new analysis technique. I would also like to thank Xabier Arroyo Rey, Vincenzo Stagno, Michele Paternoster, and all the people with whom I collaborated, and I hope to be able to do it also in the future. I am grateful also to Vincenzo Stagno and Francesco Stoppa for reviewing this thesis.

During my PhD I met many people and colleagues, but few of them really left their mark on myself. Filippo Zummo (Zù Fulì), a friend, a colleague and an adventure partner. With him I shared various experiences, including sampling campaigns, sausage sandwiches and nights in the car. Francesco Maria Lo Forte (Pisci Spata), with him I shared one of the best experiences, in one of the most beautiful places I know, the Azores. I share a lot with him, ideas, passions, football role (i am better than him), but above all the philosophy of life. A very good friend for me. Alessandra Cinquegrani (5G), the only person able to understand some aspects related to my PhD and how this can sometimes be destabilizing. Epic night spent together in Paris. Partner of interesting discussions, although most of them were monologues, since it is hard to find her in silence for a long time.

My thanks also go to my family. Mom, Dad, my brother, my sister-in-law and the little Federico, who gave so much love to our entire family. No one can ever replace the strength and wisdom of a father, the love of a mother, the support and advice of an older brother. This is why they represent an important part of my PhD.

Finally, I would like to thank the most important part, my life partner and future wife Bea. She had (and will have throughout her life) the hard task of supporting me in times of difficulty. Her strength has been fundamental during these years and it is important every single day of my life. Precisely for this reason, I decided to share my life with her and I can assure that preparing a Doctoral thesis and a wedding at the same time is not easy at all.

References

Abouchami, W., Galer, S.J.G., Hofmann, A.W. (2000). High precision lead isotope systematics of lavas from the Hawaiian Scientific Drilling Project. *Chemical Geology, 169*, 187–209. https://doi.org/10.1016/S0009-2541(00)00328-4.

Ahijado, A., Casillas, R., Nagy, G., Fernández, C. (2005). Sr-rich minerals in a carbonatite skarn, Fuerteventura, Canary Islands (Spain). *Mineralogy and Petrology*, *84*, 107–127. https://doi.org/10.1007/s00710-005-0074-8.

Allègre, C.J. (1987). Isotope geodynamics. *Earth and Planetary Science Letters*, *86*, 175–203. https://doi.org/10.1016/0012-821X(87)90220-2.

Allègre, C.J., Moreira, M., Staudacher, T. (1995). ^{4}He/^{3}He dispersion and mantle convection. *Geophysical Research Letters*, 22, 2325–2328. https://doi.org/10.1029/95GL02307.

Amsellem, E., Moynier, F., Moynier, F., Bertrand, H., Bouyon, A., Mata, J., Tappe, S., Day, J.M.D. (2020). Calcium isotopic evidence for the mantle sources of carbonatites. *Science Advances, 6*, 1–6. https://doi.org/10.1126/sciadv.aba3269.

Ancochea, E., Brändle, J.L., Cubas, C.R., Hernán, F., Huertas, M.J. (1996). Volcanic complexes in the eastern ridge of the Canary Islands: The Miocene activity of the island of Fuerteventura. *Journal of Volcanology and Geothermal Research*, *70*, 183–204. https://doi.org/10.1016/0377-0273(95)00051-8.

Ancochea, E., Huertas, M.J., Hernán, F., Brändle, J.L. (2010). Volcanic evolution of São Vicente, Cape Verde Islands: The Praia Grande landslide. *Journal of Volcanology and Geothermal Research*, *198*, 143–157. https://doi.org/10.1016/j.jvolgeores.2010.08.016.

Anenburg, M., Broom-Fendley, S., Chen, W. (2021). Formation of Rare Earth Deposits in Carbonatites. *Elements*, *17*(5), 327–332. https://doi.org/10.2138/gselements.17.5.327.

Bakker, R. J. (2003). Package FLUIDS 1. Computer programs for analysis of fluid inclusion data and for modelling bulk fluid properties. *Chemical Geology*, *194*(1–3), 3–23. https://doi.org/10.1016/S0009-2541(02)00268-1.

Balogh, K., Ahijado, A., Casillas, R., Fernández, C. (1999). Contributions to the chronology of the Basal Complex of Fuerteventura, Canary Islands. *Journal of Volcanology and Geothermal Research*, *90*, 81–102. https://doi.org/10.1016/S0377-0273(99)00008-6.

Beard, B.L., Johnson, C.M., Skulan, J.L., Nealson, K.H., Cox, L., Sun, H. (2003). Application of Fe isotopes to tracing the geochemical and biological cycling of Fe. *Chemical Geology*, *195*(1–4), 87–117.

Beccaluva, L., Coltorti, M., Di Girolamo, P., Melluso, L., Milani, L., Morra, V., Siena, F. (2002). Petrogenesis and evolution of Mt. Vulture alkaline volcanism (Southern Italy). *Mineralogy and Petrology*, *74*(2–4), 277–297. https://doi.org/10.1007/s007100200007.

Bell, K., Tilton, G.R. (2001). Nd, Pb and Sr isotopic compositions of East African carbonatites: evidence for mantle mixing and plume inhomogeneity. Journal of Petrology, 42:19 27–45.

Bell, K., Tilton, G.R. (2002). Probing the mantle: the story from carbonatites. Eos Trans. AGU 83:273–77.

Berkesi, M., Bali, E., Bodnar, R. J., Szabó, Á., Guzmics, T. (2020). Carbonatite and highly peralkaline nephelinite melts from Oldoinyo Lengai Volcano, Tanzania: The role of natrite-normative fluid degassing. *Gondwana Research*, *85*, 76-83. https://doi.org/10.1016/j.gr.2020.03.013.

Bertrand P. and Mercier J-C. C. (1985). The mutual solubility of coexisting ortho- and clinopyroxene: toward an absolute geothermometer for the natural system?. *Earth and Planetary Science Letters, 76*(1-2), 109-122. https://doi.org/10.1016/0012-821X(85)90152-9.

Bizzarro, M., Simonetti, A., Stevenson, R.K., David, J. (2002). Hf isotope evidence for a hidden mantle reservoir. *Geology, 30*, 771-774.

Blanks, D. E., Holwell, D. A., Fiorentini, M. L., Moroni, M., Giuliani, A., Tassara, S., et al. (2020). Fluxing of mantle carbon as a physical agent for metallogenic fertilization of the crust. *Nature Communications*, *11*(1). https://doi.org/10.1038/s41467-020-18157-6.

Bodnar, R.J. (1993). Revised equation and table for determining the freezing point depression of H_2O-NaCl solutions. *Geochimica et Cosmochimica Acta*, *57,* 683-684.

Bodnar, R.J., Vityk, M.O (1994). In: Fluid Inclusions in Minerals: Methods and Applications (B.De Vivo and M.L.Frezzotti, Eds.). Blacksburg, VA, 117-130.

Bodnar, R.J. (2003). In: Fluid Inclusions: Analysis and Interpretation (I.Samson, A.Anderson and D.Marshall, Eds.). Mineralogical Association of Canada, Short-Course series 32, 213-230.

Bonadiman, C., Beccaluva, L., Coltorti, M., Siena, F. (2005). Kimberlite-like metasomatism and “garnet signature” in spinel-peridotite xenoliths from Sal, Cape Verde Archipelago: Relics of a subcontinental mantle domain within the Atlantic oceanic lithosphere? *Journal of Petrology*, *46*, 2465–2493. https://doi.org/10.1093/petrology/egi061.

Borghini, G., Fumagalli, P., Rampone, E. (2010): The stability of plagioclase in the upper mantle: subsolidus experiments on fertile and depleted lherzolite. *Journal of Petrology, 51*, 229–254. https://doi.org/10.1093/petrology/egp079

Bouabdellah, M., Hoernle, K., Kchit, A., Duggen, S., Hauff, F., Klügel, A., et al. (2010). Petrogenesis of the Eocene Tamazert continental carbonatites (Central High Atlas, Morocco): Implications for a common source for the Tamazert and Canary and Cape Verde Island carbonatites. *Journal of Petrology, 51*, 1655–1686. https://doi.org/10.1093/petrology/egq033.

Bragagni, A., Mastroianni, F., Münker, C., Conticelli, S., Avanzinelli, R. (2022). A carbon-rich lithospheric mantle as a source for the large CO_2 emissions of Etna volcano (Italy). *Geology, 50*(4), 486–490. https://doi.org/10.1130/g49510.1.

Brey, G.P., Köhler, T. (1990). Geothermobarometry in four-phase lherzolites II. New thermobarometers, and practical assessment of existing thermobarometers. *Journal of Petrology, 31*, 1353–1378. https://doi.org/10.1093/petrology/31.6.1353

Broadley, M.W., Barry, P.H., Bekaert, D. V., Byrne, D.J., Caracausi, A., Ballentine, C.J., Marty, B. (2020). Identification of chondritic krypton and xenon in Yellowstone gases and the timing of terrestrial volatile accretion. Proc. Natl. Acad. Sci. U. S. A. 117, 13997−14004. https://doi.org/10.1073/pnas.2003907117.

Brooker, R.A. (1998). The effect of CO_2 saturation on immiscibility between silicate and carbonate liquids: An experimental study. *Journal of Petrology, 39*, 1905–1915. https://doi.org/10.1093/petroj/39.11-12.1905.

Brooker, R. A., Kjarsgaard, B. A. (2011). Silicate-carbonate liquid immiscibility and phase relations in the system SiO_2-Na_2O-Al_2O_3-CaO-CO_2 at 0·1-2·5 GPa with applications to carbonatite genesis. *Journal of Petrology, 52*, 1281−1305. https://doi.org/10.1093/petrology/egq081.

Bryce, J.G., DePaolo, D.J., Lassiter, J.C. (2005). Geochemical structure of the Hawaiian plume: Sr, Nd, and Os isotopes in the 2.8 km HSDP-2 section of Mauna Kea volcano. *Geochemistry, Geophysics, Geosystems*, *6*, 1–36. https://doi.org/10.1029/2004GC000809.

Buettner, A., Principe, C., Villa, I. M., Bocchini, D. (2006). Geocronologia 39Ar-40Ar del Monte Vulture. In C. Principe (Ed.), La Geologia del Monte Vulture (pp. 73–86). Lavello.

Canil, D., O'Neill, H.S.C. (1996). Distribution of ferric iron in some upper-mantle assemblages. *Journal of Petrology, 37*(3), 609-635.

Caracausi, A., Nuccio, P. M., Favara, R., Nicolosi, M., Paternoster, M. (2009). Gas hazard assessment at the Monticchio crater lakes of Mt. Vulture, a volcano in Southern Italy. *Terra Nova*, *21*(2), 83–87. https://doi.org/10.1111/j.1365-3121.2008.00858.x.

Caracausi, A., Martelli, M., Nuccio, P. M., Paternoster, M., Stuart, F. M. (2013). Active degassing of mantle-derived fluid: A geochemical study along the Vulture line, southern Apennines (Italy). *Journal of Volcanology and Geothermal Research, 253,* 65–74. https://doi.org/10.1016/j.jvolgeores.2012.12.005.

Caracausi, A., Nicolosi, M., Nuccio, P. M., Favara, R., Paternoster, M., Rosciglione, A. (2013). Geochemical insight into differences in the physical structures and dynamics of two adjacent maar lakes at Mt. Vulture volcano (southern Italy). *Geochemistry, Geophysics, Geosystems, 14*(5), 1411–1434. https://doi.org/10.1002/ggge.20111.

Caracausi, A., Paternoster, M., Nuccio, P. M. (2015). Mantle CO_2 degassing at Mt. Vulture volcano (Italy): Relationship between CO_2 outgassing of volcanoes and the time of their last eruption. *Earth and Planetary Science Letters, 411*, 268–280. https://doi.org/10.1016/j.epsl.2014.11.049.

Carnevale, G., Arroyo Rey, X., Correale, A., Rotolo, S.G. (2020). Procesos hidrotermales con enriquecimiento en REE en las carbonatitas de Fuerteventura: evidencias en minerales accesorios. *Geogaceta*, *69*, 23-26.

Carnevale, G., Caracausi, A., Correale, A., Italiano, L., Rotolo, S.G. (2021). An Overview of the Geochemical Characteristics of Oceanic Carbonatites: New Insights from Fuerteventura Carbonatites (Canary Islands). *Minerals 11* (2), 203.

Carnevale, G., Caracausi, A., Rotolo, S. G., Paternoster, M., & Zanon, V. (2022). New Inferences on Magma Dynamics in Melilitite-Carbonatite Volcanoes: The Case Study of Mt. Vulture (Southern Italy). *Geophysical Research Letters*, *49*, e2022GL099075. https://doi.org/10.1029/2022GL099075

Carracedo Sánchez, M., Sarrionandia, F., Arostegui, J., Jil Ibarguchi, J.I. (2015). Silicate glass micro and nanospherules generated in explosive eruptions of ultrabasic magmas: Implications for the origin of pelletal lapilli. *Journal of Volcanology and Geothermal Research, 293,* 13–24. https://doi.org/10.1016/j.jvolgeores.2014.12.010.

Casillas, R., Demény, A., Nagy, G., Ahijado, A., Fernández, C. (2011). Metacarbonatites in the Basal Complex of Fuerteventura (Canary Islands). The role of fluid/rock interactions during contact metamorphism and anatexis. *Lithos*, *125*, 503–520. https://doi.org/10.1016/j.lithos.2011.03.007.

Chakhmouradian, A.R., Zaitsev, A.N. (2012). Rare earth mineralization in igneous rocks: Sources and processes. *Elements, 8*, 347–353. https://doi.org/10.2113/gselements.8.5.347.

Chakhmouradian, A.R., Reguir, E.P., Zaitsev, A.N., Couëslan, C., Xu, C., Kynický, J., Mumin, A.H., Yang, P. (2017). Apatite in carbonatitic rocks: Compositional variation, zoning, element partitioning and petrogenetic significance. *Lithos, 274–275,* 188–213. https://doi.org/10.1016/j.lithos.2016.12.037.

Chi, G., Diamond, L.W., Lu, H., Lai, J. Chu, H. (2021). Common Problems and Pitfalls in Fluid Inclusion Study: A Review and Discussion. *Minerals, 11* (1), 7.

Christensen, B.P., Holm, P.M., Jambon, A., Wilson, J.R. (2001). Helium, argon and lead isotopic composition of volcanics from Santo Antão and Fogo, Cape Verde Islands. *Chemical Geology*, *178,* 127–142. https://doi.org/10.1016/S0009-2541(01)00261-3.

Coello, J., Cantagrel, J.M., Hernán, F., Fúster, J.M., Ibarrola, E., Ancochea, E., Casquet, C., Jamond, C., Díaz de Téran, J.R., Cendrero, A. (1992). Evolution of the eastern volcanic ridge of the Canary Islands based on new KAr data. *Journal of Volcanology and Geothermal Research*, *53*, 251–274. https://doi.org/10.1016/0377-0273(92)90085-R.

Coltorti, M., Bonadiman, C., Hinton, R. W., Siena, F., Upton, B. G. J. (1999). Carbonatite Metasomatism of the Oceanic Upper Mantle: Evidence from Clinopyroxenes and Glasses in Ultramafic Xenoliths of Grande Comore, Indian Ocean. *Journal of Petrology*, *40*(1), 133–165. https://doi.org/10.1093/petroj/40.1.133.

Correale, A., Martelli, M., Paonita, A., Rizzo, A., Brusca, L., & Scribano, V. (2012). New evidence of mantle heterogeneity beneath the Hyblean Plateau (southeast Sicily, Italy) as inferred from noble gases and geochemistry of ultramafic xenoliths. *Lithos*, *132–133*, 70–81. https://doi.org/10.1016/j.lithos.2011.11.007

D'Orazio, M., Innocenti, F., Tonarini, S., Doglioni, C. (2007). Carbonatites in a subduction system: The Pleistocene alvikites from Mt. Vulture (southern Italy). *Lithos*, *98*(1–4), 313–334. https://doi.org/10.1016/j.lithos.2007.05.004.

D'Orazio, M., Innocenti, F., Tonarini, S., Doglioni, C. (2008). Reply to the discussion of: "Carbonatites in a subduction system: The Pleistocene alvikites from Mt. Vulture (Southern Italy)" by M. D'Orazio, F. Innocenti, S. Tonarini, C. Doglioni (Lithos 98, 313-334) by F. Stoppa, C. Principe and P. Giannandrea. *Lithos*, *103*(3–4), 557–561. https://doi.org/10.1016/j.lithos.2007.10.010.

Dalton, J. A., Wood, B. J. (1993). The compositions of primary carbonate melts and their evolution through wallrock reaction in the mantle. *Earth and Planetary Science Letters*, *119*, 511–525. https://doi.org/10.1016/0012-821X(93)90059-I.

Dalton, J.D., Presnall, D.C. (1998). Carbonatitic melts along the solidus of model lherzolite in the system CaO–MgO–Al_2O_3–SiO_2–CO_2 from 3 to 7 GPa. *Contributions to Mineralogy and Petrology, 131*, 123–135.

Dalton, J.D., Presnall, D.C. (1998). The continuum of primary carbonatitic–kimberlitic melt compositions in equilibrium with lherzolite: data from the system CaO–MgO–Al_2O_3–SiO_2–CO_2 at 6 GPa. *Journal of Petrology, 39*, 1953–1964.

Dasgupta, R., Hirschmann, M.M., Withers, A.C. (2004). Deep global cycling of carbon constrained by the solidus of anhydrous, carbonated eclogite under upper mantle conditions. *Earth and Planetary Science Letters*, *227,* 73–85. https://doi.org/10.1016/j.epsl.2004.08.004.

Dasgupta, R., Hirschmann, M.M., McDonough, W.F., Spiegelman, M., Withers, A.C. (2009). Trace element partitioning between garnet lherzolite and carbonatite at 6.6 and 8.6 GPa with applications to the geochemistry of the mantle and of mantle-derived melts. *Chemical Geology*, *262*, 57–77. https://doi.org/10.1016/j.chemgeo.2009.02.004.

Day, J.M.D., Hilton, D.R. (2011). Origin of ^{3}He/^{4}He ratios in HIMU-type basalts constrained from Canary Island lavas. *Earth and Planetary Science Letters*, *305*, 226–234. https://doi.org/10.1016/j.epsl.2011.03.006

Day, J.M.D., Hilton, D.R. (2020). Heterogeneous mantle-derived helium isotopes in the Canary Islands and other ocean islands. *Geology*, *49*. https://doi.org/10.1130/g47676.1.

Day, J. M. D. (2022). Noble gas isotope systematics in the Canary Islands and implications for refractory mantle components. *Geochimica et Cosmochimica Acta*, *331*, 35–47. https://doi.org/10.1016/j.gca.2022.06.002.

De Hoog, J.C.M., Gall, L., Cornell, D.H. (2010). Trace-element geochemistry of mantle olivine and application to mantle petrogenesis and geothermobarometry. *Chemical Geology*, *270*, 196-215.

de Ignacio, C., Muñoz, M., Sagredo, J., Fernández-Santín, S., Johansson, Å. (2006). Isotope geochemistry and FOZO mantle component of the alkaline-carbonatitic association of Fuerteventura, Canary Islands, Spain. *Chemical Geology*, *232*, 99–113. https://doi.org/10.1016/j.chemgeo.2006.02.009.

de Ignacio, C., Muñoz, M., Sagredo, J. (2012). Carbonatites and associated nephelinites from São Vicente, Cape Verde Islands. *Mineralogical Magazine*, *76*, 311–355. https://doi.org/10.1180/minmag.2012.076.2.05.

Deines, P. (1989). Stable isotope variations in carbonatites, in: Genesis and Evolution (Ed. K. Bell). Unwin Hyman Ltd., London, UK, pp. 301–359.

Demény, A., Ahijado, A., Casillas, R., Vennemann, T.W. (1998). Crustal contamination and fluid/rock interaction in the carbonatites of Fuerteventura (Canary Islands, Spain): A C, O, H isotope study. *Lithos*, *44*, 101–115. https://doi.org/10.1016/S0024-4937(98)00050-4.

Doucelance, R., Escrig, S., Moreira, M., Gariépy, C., Kurz, M.D. (2003). Pb-Sr-He isotope and trace element geochemistry of the Cape Verde Archipelago. *Geochimica et Cosmochimica Acta*, *67*, 3717–3733. https://doi.org/10.1016/S0016-7037(03)00161-3.

Doucelance, R., Hammouda, T., Moreira, M., Martins, J. C. (2010). Geochemical constraints on depth of origin of oceanic carbonatites: The Cape Verde case. *Geochimica et Cosmochimica Acta*, *74*, 7261–7282. https://doi.org/10.1016/j.gca.2010.09.024.

Doucelance, R., Bellot, N., Boyet, M., Hammouda, T., Bosq, C. (2014). What coupled cerium and neodymium isotopes tell us about the deep source of oceanic carbonatites. *Earth and Planetary Science Letters*, *407*, 175–186. https://doi.org/10.1016/j.epsl.2014.09.042.

Downes, H., Kostoula, T., Jones, A. P., Beard, A. D., Thirlwall, M. F., Bodinier, J. L. (2002). Geochemistry and Sr-Nd isotopic compositions of mantle xenoliths from the Monte Vulture carbonatite-melilitite volcano, central southern Italy. *Contributions to Mineralogy and Petrology, 144*(1), 78–92. https://doi.org/10.1007/s00410-002-0383-4.

Duggen, S., Hoernle, K.A., Hauff, F., Klügel, A., Bouabdellah, M., Thirlwall, M.F. (2009). Flow of Canary mantle plume material through a subcontinental lithospheric corridor beneath Africa to the Mediterranean. *Geology*, *37*, 283–286. https://doi.org/10.1130/G25426A.1.

Duprat, H.I., Friis, J., Holm, P.M., Grandvuinet, T., Sørensen, R.V. (2007). The volcanic and geochemical development of São Nicolau, Cape Verde Islands: Constraints from field and ^{40}Ar/^{39}Ar evidence. *Journal of Volcanology and Geothermal Research, 162,* 1–19. https://doi.org/10.1016/j.jvolgeores.2007.01.001

Ejima, T., Osanai, Y., Akasaka, M., Adachi, T., Nakano, N., Kon, Y., Ohfuji, H., Sereenen, J. (2018). Oxidation states of Fe in constituent minerals of a spinel lherzolite xenolith from the Tariat Depression, Mongolia: the significance of Fe^{3+} in olivine. *Minerals*, *8*(5), 204.

Fernández, C., Casillas, R., García-Navarro, E., Gutiérrez, M., Camacho, M.A., Ahijado, A. (2006). Miocene rifting of Fuerteventura (Canary Islands). *Tectonics, 5,* 127–140. https://doi.org/10.1029/2005TC001941.

Ferrero S, Wunder B, Ziemann MA, Wälle M, O’Brien PJ. (2016). Carbonatitic and granitic melts produced under conditions of primary immiscibility during anataxis in the lower crust. *Earth and Planetary Science Letters*, *454*, 121–131.

Fúster, J.M., Cendrero, A., Gastesi, P., Ibarrola, E., Lopez Ruiz, J. (1968). Geología y Volcanología de las Islas Canarias- Fuerteventura. Consejo Superior de Investigaciones Científicas, Madrid, Instituto “Lucas Mallada”.

Gautheron, C., Moreira, M. (2002). Helium signature of the subcontinental lithospheric mantle. *Earth and Planetary Science Letters*, *199*, 39–47. https://doi.org/10.1016/S0012-821X(02)00563-0.

Gerlach, D.C., Cliff, R.A., Davies, G.R., Norry, M., Hodgson, N. (1988). Magma sources of the Cape Verdes archipelago: Isotopic and trace element constraints. *Geochimica et Cosmochimica Acta*, *52*, 2979–2992. https://doi.org/10.1016/0016-7037(88)90162-7.

Gernon, T.M., Brown, R.J., Tait, M.A., Hincks, T.K. (2012). The origin of pelletal lapilli in explosive kimberlite eruptions. *Nature Communications*, *3*, 832–837. https://doi.org/10.1038/ncomms1842.

Giannandrea, P., La Volpe, L., Principe, C., Schiattarella, M. (2006). Unità stratigrafiche a limiti inconformi e storia evolutiva del vulcano medio-pleistocenico di Monte Vulture (Appennino meridionale, Italia). *Bollettino Della Societa Geologica Italiana*, *125*(1), 67–92.

Giebel, R. J., Gauert, C. D. K., Marks, M. A. W., Costin, G., Markl, G. (2017). Multi-stage formation of REE minerals in the Palabora Carbonatite Complex, South Africa. *American Mineralogist, 102,* 1218-1233. doi: 10.2138/am-2017-6004.

Giordano, G., & Caricchi, L. (2022). Determining the state of activity of Transcrustal magmatic systems and their volcanoes. *Annual Review of Earth and Planetary Sciences*, *50*(1), 231–259. https://doi.org/10.1146/annurev-earth-032320-084733.

Grachev, A.F. (2012). MORB-like mantle beneath Lanzarote Island, Canary Islands. *Russian Journal of Earth Science*, *12*, 1–7. https://doi.org/10.2205/2012es000515.

Gudfinnsson, G.H., & Presnall, D.C. (2005). Continuous Gradations among Primary Carbonatitic, Kimberlitic, Melilititic, Basaltic, Picritic, and Komatiitic Melts in Equilibrium with Garnet Lherzolite at 3–8 GPa. *Journal of Petrology*, *46*(8), 1645–1659. https://doi.org/10.1093/petrology/egi029.

Gurenko, A.A., Hoernle, K.A., Hauff, F., Schmincke, H.U., Han, D., Miura, Y.N., Kaneoka, I. (2006). Major, trace element and Nd-Sr-Pb-O-He-Ar isotope signatures of shield stage lavas from the central and western Canary Islands: Insights into mantle and crustal processes. *Chemical Geology*, *233*, 75–112. https://doi.org/10.1016/j.chemgeo.2006.02.016.

Gurenko, A.A., Hoernle, K.A., Sobolev, A. V., Hauff, F., Schmincke, H.U. (2010). Source components of the Gran Canaria (Canary Islands) shield stage magmas: Evidence from olivine composition and Sr-Nd-Pb isotopes. *Contributions to Mineralogy and Petrology*, *159*, 689–702. https://doi.org/10.1007/s00410-009-0448-8.

Gutiérrez, M. (2000). Estudio petrológico, geoquímico y estructural de la serie volcánica submarina del Complejo Basal de Fuerteventura (Islas Canarias): caracterización del crecimiento submarino y de la emersión de la Isla. Universidad de La Laguna, Spain.

Gutiérrez, M., Casillas, R., Fernández, C., Balogh, K., Ahijado, A., Castillo, C., Colmenero, J.R., García-Navarro, E. (2006). The submarine volcanic succession of the basal complex of Fuerteventura, Canary Islands: A model of submarine growth and emergence of tectonic volcanic islands. *Geological Society of America Bulletin*, *118*, 785–804. https://doi.org/10.1130/B25821.1.

Halama, R., McDonough, W.F., Rudnick, R.L., Bell, K. (2008) Tracking the lithium isotopic evolution of the mantle using carbonatites. *Earth and Planetary Science Letters*, *265*, 726–742. https://doi.org/10.1016/j.epsl.2007.11.007.

Hammouda, T. (2003). High-pressure melting of carbonated eclogite and experimental constraints on carbon recycling and storage in the mantle. *Earth and Planetary Science Letters*, *214*, 357–368. https://doi.org/10.1016/S0012-821X(03)00361-3.

Hammouda, T., Chantel, J., Manthilake, G., Guignard, J., Crichton, W. (2014). Hot mantle geotherms stabilize calcic carbonatite magmas up to the surface. *Geology*, *42*, 911–914. https://doi.org/10.1130/G35778.1.

Hammouda, T., Keshav, S. (2015). Melting in the mantle in the presence of carbon: Review of experiments and discussion on the origin of carbonatites. *Chemical Geology, 418,* 171–188. https://doi.org/10.1016/j.chemgeo.2015.05.018.

Hansteen, T. H., & Klügel, A. (2008). Fluid inclusion thermobarometry as a tracer for magmatic processes. *Reviews in Mineralogy and Geochemistry, 69*(Roedder 1984), 143–177. https://doi.org/10.2138/rmg.2008.69.5.

Harangi, S., Lukács, R., Schmitt, A. K., Dunkl, I., Molnár, K., Kiss, B., et al. (2015). Constraints on the timing of Quaternary volcanism and duration of magma residence at Ciomadul volcano, east-central Europe, from combined U-Th/He and U-Th zircon geochronology. *Journal of Volcanology and Geothermal Research, 301,* 66–80. https://doi.org/10.1016/j.jvolgeores.2015.05.002.

Harrison, L.N., Weis, D. (2018). The Size and Emergence of Geochemical Heterogeneities in the Hawaiian Mantle Plume Constrained by Sr-Nd-Hf Isotopic Variation Over ~47 Million Years. *Geochemistry, Geophysics, Geosystems, 19,* 2823–2842. https://doi.org/10.1029/2017GC007389

Hart, S.R. (1984). A large-scale isotope anomaly in the Southern Hemisphere mantle. *Nature, 309,* 753–757. https://doi.org/10.1038/309753a0.

Hart, S.R. (1988). Heterogeneous mantle domains: signatures, genesis and mixing chronologies. *Earth and Planetary Science Letters, 90,* 273–296. https://doi.org/10.1016/0012-821X(88)90131-8.

Hart, S.R., Hauri, E.H., Oschmann, L.A., Whitehead, J.A. (1992). Mantle plumes and entrainment: Isotopic evidence. *Science, 256*(80), 517–520. https://doi.org/10.1126/science.256.5056.517.

Hauri, E.H., Whitehead, J.A., Hart, S.R. (1994). Fluid dynamic and geochemical aspects of entrainment in mantle plumes. *Journal of Geophysical Research, 99,* 24275–24300. https://doi.org/10.1029/94jb01257.

Hilton, D.R., Hammerschmidt, K., Teufel, S., Friedrichsen, H. (1993). Helium isotope characteristics of Andean geothermal fluids and lavas. *Earth and Planetary Science Letters, 120,* 265–282. https://doi.org/10.1016/0012-821X(93)90244-4.

Hilton, D.R., Fischer, T.P., Marry, B. (2002). Noble gases and volatile recycling at subduction zones. *Reviews in Mineralogy and Geochemistry, 47,* 319–370. https://doi.org/10.2138/rmg.2002.47.9.

Hobson, A., Bussy, F., Hernandez, J. (1998). Shallow-level migmatization of gabbros in a metamorphic contact aureole, Fuerteventura basal complex, Canary Islands. *Journal of Petrology, 39,* 125–137. https://doi.org/10.1093/petroj/39.5.1025.

Hoefs, J. (1987). Stable isotope geochemistry, 3rd ed. Springer, Berlin, Heidelberg.

Hoernle, K., Tilton, G., Schmincke, H.U. (1991). Sr-Nd-Pb isotopic evolution of Gran Canaria: Evidence for shallow enriched mantle beneath the Canary Islands. *Earth and Planetary Science Letters, 106,* 44–63. https://doi.org/10.1016/0012-821X(91)90062-M.

Hoernle, K.A., Tilton, G.R. (1991). Sr–Nd–Pb isotope data for Fuerteventura (Canary Islands). Schweizerische Mineral. und Petrogr. Mitteilungen 71, 3–18.

Hoernle, K. (1998). Geochemistry of Jurassic oceanic crust beneath Gran Canaria (Canary Islands): implications for crustal recycling and assimilation. *Journal of Petrology*, 39, 859–880. https://doi.org/10.1093/petroj/39.5.859.

Hoernle, K., Tilton, G., Le Bas, M.J., Duggen, S., Garbe-Schönberg, D. (2002). Geochemistry of oceanic carbonatites compared with continental carbonatites: Mantle recycling of oceanic crustal carbonate. *Contributions to Mineralogy and Petrology*, 142, 520–542. https://doi.org/10.1007/s004100100308.

Holm, P.M., Wilson, J.R., Christensen, B.P., Hansen, L., Hansen, S.L., Hein, K.M., Mortensen, A.K., Pedersen, R., Plesner, S., Runge, M.K. (2006). Sampling the Cape Verde Mantle Plume: Evolution of melt compositions on Santo Antão, Cape Verde Islands. *Journal of Petrology*, *47*, 145–189. https://doi.org/10.1093/petrology/egi071.

Holm, P.M., Grandvuinet, T., Friis, J., Wilson, J.R., Barker, A.K., Plesner, S. (2008). An ^{40}Ar-^{39}Ar study of the Cape Verde hot spot: Temporal evolution in a semistationary plate environment. *Journal of Geophysical Research: Solid Earth*, *113*, 1–22. https://doi.org/10.1029/2007JB005339.

Horton, F. (2021). Rapid recycling of subducted sedimentary carbon revealed by Afghanistan carbonatite volcano. *Nature Geoscience*, *14*(7), 508–512. https://doi.org/10.1038/s41561-021-00764-7.

Huertas, M.J., Hernán, F., Ancochea, E., Brändle, J.L. (2006). El Edificio Antiguo de la isla de San Vicente (Cabo Verde): características del sector occidental. *Geogaceta*, *40*, 95–98.

Improta, L., De Gori, P., Chiarabba, C. (2014). New insights into crustal structure, Cenozoic magmatism, CO_2 degassing, and seismogenesis in the southern Apennines and Irpinia region from local earthquake tomography. *Journal of Geophysical Research: Solid Earth*, *119*(11), 8283–8311. https://doi.org/10.1002/2013JB010890.

Jackson, M.G., Kurz, M.D., Hart, S.R., Workman, R.K. (2007). New Samoan lavas from Ofu Island reveal a hemispherically heterogeneous high ^{3}He/^{4}He mantle. *Earth Planetary Science Letters*, *264*, 360–374. https://doi.org/10.1016/j.epsl.2007.09.023.

Johnson, C.M., Bell, K., Beard, B.L., Shultis, A.I. (2010). Iron isotope compositions of carbonatites record melt generation, crystallization, and late-stage volatile-transport processes. *Mineralogy and Petrology*, *98*, 91–110. https://doi.org/10.1007/s00710-009-0055-4.

Jones, A. P., Kostoula, T., Stoppa, F., Woolley, A. R. (2000). Petrography and mineral chemistry of mantle xenoliths in a carbonate-rich melilititic tuff from Mt. Vulture volcano, southern Italy. *Mineralogical Magazine*, *64*(4), 593–613. https://doi.org/10.1180/002646100549634.

Jones, A.P., Genge, M., Carmody, L. (2013). Carbonate melts and carbonatites. *Reviews in Mineralogy and Geochemistry, 75*, 289–322. https://doi.org/10.2138/rmg.2013.75.10.

Kamenetsky, V.S., Doroshkevich, A.G., Elliot, H.A.L., Zaitsev, A.N. (2021). Carbonatites: Contrasting, Complex, and Controversial. *Elements,* 17, 307–314.

Kelemework, Y., Milano, M., La Manna, M., de Alteriis, G., Iorio, M., Fedi, M. (2021). Crustal structure in the Campanian region (Southern Apennines, Italy) from potential field modelling. *Scientific Reports*, *11*(1), 1–18. https://doi.org/10.1038/s41598-021-93945-8.

Keller, J., Hoefs, J. (1995). Stable Isotope Characteristics of Recent Natrocarbonatites from Oldoinyo Lengai, in: Carbonatite Volcanism: Oldoinyo Lengai and the Petrogenesis of Natrocarbonatites (K. Bell & J. Keller, Eds.). Springer-Verlag, Berlin, Heidelberg, pp. 113–123. https://doi.org/10.1007/978-3-642-79182-6_9.

Kelley, S. P., Wartho, J. A. (2000). Rapid kimberlite ascent and the significance of Ar-Ar ages in xenolith phlogopites. *Science, 289*(5479), 609-611. https://doi.org/10.1126/science.289.5479.609.

Klitgord, K.D., Schouten, H. (1986). Plate kinematics of the central Atlantic, in: Vogt, P.R., Tucholke, B.E. (Eds.), The Western North Atlantic Region. Geological Society of America, pp. 351–378. https://doi.org/10.1130/dnag-gna-m.351.

Kogarko, L.N. (1993). Geochemical characteristics of oceanic carbonatites from the Cape Verde Islands. *South African Journal of Geology*, *96*, 119–125.

Kono, Y., Kenney-Benson, C., Hummer, D., Ohfuji, H., Park, C., Shen, G., Wang, Y., Kavner, A., Manning, C.E. (2014). Ultralow viscosity of carbonate melts at high pressures. *Nature Communications*, 5, 1–8. https://doi.org/10.1038/ncomms6091.

Kovács, I., Zajacz, Z., Szabó, C. (2004). Type-II xenoliths and related metasomatism from the Nógrád-Gömör Volcanic Field, Carpathian-Pannonian region (northern Hungary–southern Slovakia). *Tectonophysics*, *393*(1-4), 139-161. https://doi.org/10.1016/j.tecto.2004.07.032.

Le Bas, M.J., Rex, D.C., Stillman, C.J. (1986). The early magmatic chronology of Fuerteventura, Canary Islands. *Geological Magazine*, *123*, 287–298. https://doi.org/10.1017/S0016756800034762.

Le Maitre, R.., Streckeisen, A., Zanettin, B., Le Bas, M.J., Bonin, B., Bateman, P. (2002). Igneous Rocks: A Classification and Glossary of Terms (Recommendations of the IUGS Subcommission on the Systematics of Igneous Rocks), 2nd ed. Cambridge University Press.

Lee, W.J., Wyllie, P.J. (1994). Experimental data bearing on liquid immiscibility, crystal fractionation, and the origin of calciocarbonatites and natrocarbonatites. *International Geological Review*, *36*, 797–819. https://doi.org/10.1080/00206819409465489.

Lee, J.Y., Marti, K., Severinghaus, J.P., Kawamura, K., Yoo, H.S., Lee, J.B., Kim, J.S. (2006). A redetermination of the isotopic abundances of atmospheric Ar. *Geochimica et Cosmochimica Acta*, *70*, 4507–4512. https://doi.org/10.1016/j.gca.2006.06.1563.

Li, Y., Zhang, J., Mostofa, K. M. G., Wang, Y., Yu, S., Cai, Z., et al. (2018). Petrogenesis of carbonatites in the Luliangshan region, North Qaidam, northern Tibet, China: Evidence for recycling of sedimentary carbonate and mantle metasomatism within a subduction zone. *Lithos*, *322*, 148–165. https://doi.org/10.1016/j.lithos.2018.10.010.

Lister, J. R., Kerr, R. C. (1991). Fluid-mechanical models of crack propagation and their application to magma transport in dykes. *Journal of Geophysical Research*, *96*(B6), 49–77. https://doi.org/10.1029/91jb00600.

Lloyd, F. E., Stoppa, F. (2003). Pelletal Lapilli in Diatremes – Some Inspiration from the Old Masters. *GeoLines*, *15*, 65–71.

Lodge, A., Helffrich, G. (2006). Depleted swell root beneath the Cape Verde Islands. *Geology*, *34*, 449–452. https://doi.org/10.1130/G22030.1.

Lustrino, M., Luciani, N., Stagno, V. (2019). Fuzzy petrology in the origin of carbonatitic/pseudocarbonatitic Ca-rich ultrabasic magma at Polino (central Italy). *Scientific Reports*, *9*, 9212. https://doi.org/10.1038/s41598-019-45471-x.

Lustrino, M., Ronca, S., Caracausi, A., Ventura-Bordenca, C., Agostini, S., Faraone, D. B. (2020). Strongly SiO_2-undersaturated, CaO-rich kamafugitic Pleistocene magmatism in Central Italy (San Venanzo volcanic complex) and the role of shallow depth limestone assimilation. *Earth Science Reviews*, *208*, 103256. https://doi.org/10.1016/j.earscirev.2020.103256.

Mangas, J., Pérez Torrado, F.J., Martín, A. Reguilón, R. (1996). Minerales de tierras raras en las carbonatitas del Complejo Basal de Fuerteventura (Islas Canarias). *Geogaceta*, *20*, 1511-1513.

Martinez-Arevalo, C., Mancilla, F. de L., Helffrich, G., Garcia, A. (2013). Seismic evidence of a regional sublithospheric low velocity layer beneath the Canary Islands. *Tectonophysics*, 608, 586–599. https://doi.org/10.1016/j.tecto.2013.08.021.

Martins, S., Mata, J., Munhá, J., Mendes, M.H., Maerschalk, C., Caldeira, R., Mattielli, N. (2010). Chemical and mineralogical evidence of the occurrence of mantle metasomatism by carbonate-rich melts in an oceanic environment (Santiago Island, Cape Verde). *Mineralogy and Petrology*, *99*, 43–65. https://doi.org/10.1007/s00710-009-0078-x.

Marty, B., Alexander, C.M.O.D., Raymond, S.N. (2013). Primordial origins of earth's carbon. *Reviews in Mineralogy and Geochemistry*, 75, 149–181. https://doi.org/10.2138/rmg.2013.75.6.

Mata, J., Moreira, M., Doucelance, R., Ader, M., Silva, L. C. (2010). Noble gas and carbon isotopic signatures of Cape Verde oceanic carbonatites: Implications for carbon provenance. *Earth and Planetary Science Letters, 291*, 70–83. https://doi.org/10.1016/j.epsl.2009.12.052.

Mata, J., Martins, S., Mattielli, N., Madeira, J., Faria, B., Ramalho, R.S., Silva, P., Moreira, M., Caldeira, R., Moreira, M., Rodrigues, J., Martins, L. (2017). The 2014–15 eruption and the short-term geochemical evolution of the Fogo volcano (Cape Verde): Evidence for small-scale mantle heterogeneity. *Lithos*, *288–289*, 91–107. https://doi.org/10.1016/j.lithos.2017.07.001.

McDonough, W.F., Sun, S. s. (1995). The composition of the Earth. *Chemical Geology, 120*, 223–253. https://doi.org/10.1016/0009-2541(94)00140-4.

Menand, T. (2011). Physical controls and depth of emplacement of igneous bodies: A review. *Tectonophysics, 500*(1-4), 11-19. https://doi.org/10.1016/j.tecto.2009.10.016.

Mikhail, S., Shahar, A., Hunt, S.A., Verchovsky, A.B., Jones, A.P. (2011). An experimental investigation of the pressure effect on stable isotope fractionation at high temperature: Implications for mantle processes and core formation in celestial bodies, in: Lunar and Planetary Science Conference. Texas, USA.

Mikhailenko, D.S., Stagno, V., Korsakov, A.V., Andreozzi, G.B., Marras, G., Cerantola, V., Malygina, E.V. (2020). Redox state determination of eclogite xenoliths from Udachnaya kimberlite pipe (Siberian craton), with some implications for the graphite/diamond formation. *Contributions to Mineralogy and Petrology*, *175*(11), 1-17.

Millet, M.A., Doucelance, R., Schiano, P., David, K., Bosq, C. (2008). Mantle plume heterogeneity versus shallow-level interactions: A case study, the São Nicolau Island, Cape Verde archipelago. *Journal of Volcanology and Geothermal Research*, *176*, 265–276. https://doi.org/10.1016/j.jvolgeores.2008.04.003.

Mitchell, J.G., Le Bas, M.J., Zielonka, J., Furnes, H. (1983). On dating the magmatism of Maio, Cape Verde Islands. *Earth and Planetary Science Letters*, *64*, 61–76. https://doi.org/10.1016/0012-821X(83)90053-5.

Mitchell R.H. (2005). Carbonatites and carbonatites and carbonatites. *Canadian Mineralogist*, *43*, 2049–2068.

Mitchell R.H., Gittings J. (2022). Carbonatites and carbothermalites: A revised classification. *Lithos*, 430-431, 106861. https://doi.org/10.1016/j.lithos.2022.106861.

Molnár, K., Harangi, S., Lukács, R., Dunkl, I., Schmitt, A. K., Kiss, B., et al. (2018). The onset of the volcanism in the Ciomadul Volcanic Dome Complex (Eastern Carpathians): Eruption chronology and magma type variation. *Journal of Volcanology and Geothermal Research*, *354*, 39–56. https://doi.org/10.1016/j.jvolgeores.2018.01.025.

Molnár, K., Lukács, R., Dunkl, I., Schmitt, A. K., Kiss, B., Seghedi, I., et al. (2019). Episodes of dormancy and eruption of the Late Pleistocene Ciomadul volcanic complex (Eastern Carpathians, Romania) constrained by zircon geochronology. *Journal of Volcanology and Geothermal Research*, *373*, 133–147. https://doi.org/10.1016/j.jvolgeores.2019.01.025.

Montelli, R., Nolet, G., Dahlen, F.A., Masters, G. (2006). A catalogue of deep mantle plumes: New results from finite frequency tomography. *Geochemistry, Geophysics, Geosystems*, *7*, 1–69. https://doi.org/10.1029/2006GC001248.

Moore, D.M., Reynolds, R.C. (1997). X-Ray Diffraction and the Identification and Analysis of Clay Minerals. Cambridge University Press, 378 p.

Moore, K.R., Wood, B.J. (1998). The transition from carbonate to silicate melts in the system CaO–MgO SiO_2–CO_2. *Journal of Petrology*, *39*, 1943–1951.

Mourão, C., Mata, J., Doucelance, R., Madeira, J., Silveira, A.B. da, Silva, L.C., Moreira, M. (2010). Quaternary extrusive calcio-carbonatite volcanism on Brava Island (Cape Verde): A nephelinite-carbonatite immiscibility product. *Journal of African Earth Science*, 56, 59–74. https://doi.org/10.1016/j.jafrearsci.2009.06.003.

Mourão, C., Mata, J., Doucelance, R., Madeira, J., Millet, M.A., Moreira, M. (2012). Geochemical temporal evolution of Brava Island magmatism: Constraints on the variability of Cape Verde mantle sources and on carbonatite-silicate magma link. *Chemical Geology*, *334*, 44–61. https://doi.org/10.1016/j.chemgeo.2012.09.031.

Moussallam, Y., Morizet, Y., Gaillard, F. (2016). H_2O–CO_2 solubility in low SiO_2-melts and the unique mode of kimberlite degassing and emplacement. *Earth and Planetary Science Letters*, *447*, 151–160. https://doi.org/10.1016/j.epsl.2016.04.037.

Muñoz, M., Sagredo, J., de Ignacio, C., Fernández-Suárez, J., Jeffries, T.E. (2005). New data (U-Pb, K-Ar) on the geochronology of the alkaline-carbonatitic association of Fuerteventura, Canary Islands, Spain. *Lithos*, *85*, 140–153. https://doi.org/10.1016/j.lithos.2005.03.024.

Nasir, S., Al-Khirbash, Rollinson H., Al-Harthy A., Al-Sayigh, A., Al-Lazki, A., Theye, T., Massonne, H. J., Belousova, E. (2011). Petrogenesis of early cretaceous carbonatite and ultramafic lamprophyres in a diatreme I the Batain Nappes, Eastern Oman continental margin. *Contributions to Mineralogy and Petrology*, *161*, 47-74.

Nasraoui, M., Bilal, E. y Gibert, R. (1999). Fresh and weathered pyrochlore studies by Fourier transform infrared spectroscopy coupled with thermal analysis. *Mineralogical Magazine*, *63*, 567-578.

Norton, G., Pinkerton, H. (1997). Rheological properties of natrocarbonatite lavas from Lengai, Tanzania. *European Journal of Mineralogy*, *9*, 351−364.

Ochs, F. A., Lange, R. A. (1999). The density of hydrous magmatic liquids. *Science, 283*(5406), 1314–1317. https://doi.org/10.1126/science.283.5406.1314.

Ozima, M., Podosek, F.A. (2002). Noble Gas Geochemistry, 2nd ed, Noble Gas Geochemistry. Cambridge University Press.

Paternoster, M., Mongelli, G., Caracausi, A., Favara, R. (2016). Depth influence on the distribution of chemical elements and saturation index of mineral phases in twins maar lakes: The case of the Monticchio lakes (southern Italy). *Journal of Geochemical Exploration*, *163*, 10–18. https://doi.org/10.1016/j.gexplo.2016.01.001.

Peccerillo, A., Frezzotti, M. L. (2015). Magmatism, mantle evolution and geodynamics at the converging plate margins of Italy. *Journal of the Geological Society*, *172*(4), 407–427. https://doi.org/10.1144/jgs2014-085.

Peccerillo, A. (2017). The Apulian Province (Mount Vulture). *Advances in Volcanology*, 203–216. https://doi.org/10.1007/978-3-319-42491-0_8.

Peslier, A.H., Woodland, A.B., Bell, D.R., Lazarov, M. (2010). Olivine water contents in the continental lithosphere and the longevity of cratons. *Nature*, *467*, 78–81.

Pim, J., Peirce, C., Watts, A.B., Grevemeyer, I., Krabbenhoeft, A. (2008). Crustal structure and origin of the Cape Verde Rise. *Earth and Planetary Science Letters*, *272*, 422–428. https://doi.org/10.1016/j.epsl.2008.05.012.

Plesner, S., Holm, P.M., Wilson, J.R. (2003). ^{40}-^{39}Ar geochronology of Santo Antão, Cape Verde Islands. *Journal of Volcanology and Geothermal Research*, *120*, 103–121. https://doi.org/10.1016/S0377-0273(02)00367-0.

Porcelli, D., Wasserburg, G.J. (1995). Mass transfer of helium, neon, argon, and xenon through a steady-state upper mantle. *Geochimica et Cosmochimica Acta, 59*, 4921–4937. https://doi.org/10.1016/0016-7037(95)00336-3.

Randive, K.R., Hari, K.R., Dora, M.L., Malpe, D.B., Bhondwe, A.A. (2014). Study of Fluid Inclusions: Methods, Techniques and Applications. *Gondwana Geological Magazine*, *29*(1-2), 19-28.

Rizzo, A.L., Pelorosso, B., Coltorti, M., Ntaflos, T., Bonadiman, C., Matusiak-Małek, M., Italiano, F., Bergonzoni, G. (2018). Geochemistry of noble gases and CO_2 in fluid inclusions from lithospheric mantle beneath wilcza góra (Lower silesia, southwest Poland). Frontiers in Earth Science, *6*:215. https://doi.org/10.3389/feart.2018.00215.

Rizzo, A.L., Uysal, I.T., Mutlu, H., Ünal-İmer, E., Dirik, K., Yüce, G., Caracausi, A., Italiano, F., Misseri, M., Temel, A., Bayarı, S., Özyurt, N., Zhao, J. xin, Deniz, K. (2019). Geochemistry of Fluid Inclusions in Travertines From Western and Northern Turkey: Inferences on the Role of Active Faults in Fluids Circulation. *Geochemistry, Geophysics, Geosystems, 20*, 5473–5498. https://doi.org/10.1029/2019GC008453.

Roeser, H.A. (1982). Magnetic anomalies in the magnetic quiet zone off Morocco., in: von Rad, U., Hinz, K., Sarnthein, M., Seibold, E. (Eds.), Geology of the Northwest African Continental Margin. Springer, Berlin, Heidelberg. https://doi.org/10.1007/978-3-642-68409-8_4.

Roest, W.R., Dañobeitia, J.J., Verhoef, J., Collette, B.J. (1992). Magnetic anomalies in the canary basin and the Mesozoic evolution of the central North Atlantic. *Marine Geophysical Research*, *14*, 1–24. https://doi.org/10.1007/BF01674063.

Rosatelli, G., Wall, F., Stoppa, F. (2007). Calcio-carbonatite melts and metasomatism in the mantle beneath Mt. Vulture (Southern Italy). *Lithos*, *99*(3–4), 229–248. https://doi.org/10.1016/j.lithos.2007.05.011.

Rosenbaum, G., Gasparon, M., Lucente, F. P., Peccerillo, A., Miller, M. S. (2008). Kinematics of slab tear faults during subduction segmentation and implications for Italian magmatism. *Tectonics, 27*(2), 1–16. https://doi.org/10.1029/2007TC002143.

Russell, J. K., Porritt, L. A., Lavallé, Y., Dingwell, D. B. (2012). Kimberlite ascent by assimilation-fuelled buoyancy. *Nature*, *481*(7381), 352–356. https://doi.org/10.1038/nature10740.

Sagan, M., Heaman, L.M., Pearson, D.G., Luo, Y., Stern, R.A. (2020). Removal of continental lithosphere beneath the Canary archipelago revealed from a U—Pb Age and Hf/O isotope study of modern sand detrital zircons. *Lithos, 362–363*, 1–18. https://doi.org/10.1016/j.lithos.2020.105448.

Santos, R. V., Clayton, R.N. (1995). Variations of oxygen and carbon isotopes in carbonatites: A study of Brazilian alkaline complexes. *Geochimica et Cosmochimica Acta*, *59*, 1339–1352. https://doi.org/10.1016/0016-7037(95)00048-5.

Sapienza, G., Hilton, D. R., & Scribano, V. (2005). Helium isotopes in peridotite mineral phases from Hyblean Plateau xenoliths (south-eastern Sicily, Italy). *Chemical Geology*, *219*(1-4), 115–129. https://doi.org/10.1016/j.chemgeo.2005.02.012

Schmidt, M. W., Weidendorfer, D. (2018). Carbonatites in oceanic hotspots. *Geology*, *46*, 435–438. https://doi.org/10.1130/G39621.1.

Scribano, V., Viccaro, M., Cristofolini, R., & Ottolini, L. (2009). Metasomatic events recorded in ultramafic xenoliths from the Hyblean area (Southeastern Sicily, Italy). *Mineralogy and Petrology*, *95*, 235–250. https://doi.org/10.1007/s00710-008-0031-4

Scrocca, D., Sciamanna, S., Di Luzio, E., Tozzi, M., Nicolai, C., Gambini, R. (2007). Structural setting along the CROP-04 deep seismic profile (Southern Apennines - Italy). *Bollettino Della Società Geologica Italiana*, Supplemento, *7*, 283–296.

Sharygin, V.V., Stoppa, F., Kolesov, B.A. (1996). Zr-Ti disilicates from the Pian di Celle Volcano, Umbria, Italy. *European Journal of Mineralogy, 8*, 1199–1212.

Sheppard, S.M.F., Dawson, J.B. (1973). C^{13}/C^{12} and D/H isotope variations in “Primary Igneous Carbonatites.” *Fortschr. Miner. 50*, 128–129.

Shirey, S.B., Cartigny, P., Frost, D.J., Keshav, S., Nestola, F., Nimis, P., Pearson, D.G., Sobolev, N. V., Walter, M.J. (2013). Diamonds and the geology of mantle carbon. *Reviews in Mineralogy and Geochemistry*, *75*, 355–421. https://doi.org/10.2138/rmg.2013.75.12.

Schmidt, M. W., & Weidendorfer, D. (2018). Carbonatites in oceanic hotspots. *Geology*, *46*(5), 435–438. https://doi.org/10.1130/G39621.1.

Shu, X., Liu, Y. (2019). Fluid inclusion constraints on the hydrothermal evolution of the Dalucao Carbonatite-related REE deposit, Sichuan Province, China. *Ore Geology Reviews*, *107*, 41–57. https://doi.org/10.1016/j.oregeorev.2019.02.014.

Smith MP, Campbell LS, Kynicky J. (2015). A review of the genesis of the world class Bayan Obo Fe REE-Nb deposits, Inner Mongolia, China: multistage processes and outstanding questions. *Ore Geology Reviews, 64,* 459–476.

Solovova, I. P., Girnis, A. V., Kogarko, L. N., Kononkova, N. N., Stoppa, F., Rosatelli, G. (2005). Compositions of magmas and carbonate-silicate liquid immiscibility in the Vulture alkaline igneous complex, Italy. *Lithos*, *85*(1-4 SPEC. ISS.), 113–128. https://doi.org/10.1016/j.lithos.2005.03.022.

Song W, Xu C, Chakhmouradian AR, Kynicky J, Huang K, Zhang Z. (2017). Carbonatites of Tarim (NW China): first evidence of crustal contribution in carbonatites from a large igneous province. *Lithos*, *282,* 1–9.

Sparks, R. S. J. (1976). Grain size variations in ignimbrites and implications for the transport of pyroclastic flows. *Sedimentology*, *23*(2), 147–188. https://doi.org/10.1111/j.1365-3091.1976.tb00045.x.

Sparks, R. S. J., Baker, L., Brown, R. J., Field, M., Schumacher, J., Stripp, G., Walters, A. (2006). Dynamical constraints on kimberlite volcanism. *Journal of Volcanology and Geothermal Research*, *155*(1–2), 18–48. https://doi.org/10.1016/j.jvolgeores.2006.02.010.

Spera, F.J. (1984). Carbon dioxide in igneous petrogenesis III: role of volatiles in the ascent of alkaline magma with special reference to xenolith-bearing mafic lavas. *Contributions to Mineralogy and Petrology, 88*, 217–232.

Stagno, V., Stopponi, V., Kono, Y., Manning, C.E., Irifune, T. (2018). Experimental determination of the viscosity of Na_2CO_3 melt between 1.7 and 4.6 GPa at 1200–1700 °C: Implications for the rheology of carbonatite magmas in the Earth’s upper mantle. *Chemical Geology, 501,* 19–25. https://doi.org/10.1016/j.chemgeo.2018.09.036.

Stagno, V. (2019). Carbon, carbides, carbonates and carbonatitic melts in the Earth's interior. *Journal of the Geological Society, 176*(2), 375-387.

Stagno, V., Stopponi, V., Kono, Y., D’arco, A., Lupi, S., Romano, C., et al. (2020). The viscosity and atomic structure of volatile-bearing melilititic melts at high pressure and temperature and the transport of deep carbon. *Minerals, 10*(3), 1–13. https://doi.org/10.3390/min10030267.

Stagno, V., Aulbach, S. (2021) Redox processes before, during and after Earth’s accretion affecting the deep carbon cycle. In: AGU monographs (editors: Moretti R., Neuville D.R.).

Steiner, C., Hobson, A., Favre, P., Stampfli, G.M., Hernandez, J. (1998). Mesozoic sequence of Fuerteventura (Canary Islands): Witness of early Jurassic sea-floor spreading in the central Atlantic. *Geological Society of America Bulletin, 110,* 1304–1317. https://doi.org/10.1130/0016-7606(1998)110<1304:MSOFCI>2.3.CO;2.

Sterner, S. M., Bodnar, R. J. (1991). Synthetic fluid inclusions. X: Experimental determination of P-V-T-X properties in the CO_2-H_2O system to 6 kb and 700 °C. *American Journal of Science*, *291*, 1–54. https://doi.org/https://doi.org/10.2475/ajs.291.1.1.

Stillman, C.J., Bennell-baker, M.J., Smewing, J.D., Fúster, J.M., Muñoz, M., Sagredo, J. (1975). Basal complex of Fuerteventura (Canary Islands) is an oceanic intrusive complex with rift-system affinities. *Nature, 257*, 469–471. https://doi.org/10.1038/257469a0.

Stoppa, F., Principe, C. (1997). Eruption style and petrology of a new carbonatitic suite from the Mt. Vulture Southern Italy /: The Monticchio Lakes Formation. *Journal of Volcanology and Geothermal Research*, *78*(3–4), 251–265. https://doi.org/10.1016/S0377-0273(97)00004-8.

Stoppa, F., Principe, C., Giannandrea, P. (2008). Comments on: Carbonatites in a subduction system: The Pleistocene alvikites from Mt. Vulture (southern Italy) by D’Orazio et al., (2007). *Lithos*, *103*(3–4), 550–556. https://doi.org/10.1016/j.lithos.2007.10.012.

Stracke, A., Hofmann, A.W., Hart, S.R. (2005). FOZO, HIMU, and the rest of the mantle zoo. *Geochemistry, Geophysics, Geosystems*, *6*, 1–20. https://doi.org/10.1029/2004GC000824.

Streckeisen A. (1980). Classification and Nomenclature of Volcanic Rocks, Lamprophyres, Carbonatites and Melilitic Rocks. IUGS Subcommission on the Systematics of the Igneous Rocks. *Geology*, *7*, 331-335.

Su, B., Zhang, H., Asamoah, S. P., Qin, K., Tang, Y., Ying, J., Xiao, Y. (2010). Garnet-spinel transition in the upper mantle: Review and interpretation. *Journal of Earth Science, 21,* 635–640. https://doi.org/10.1007/s12583-010-0117-x

Sun, S.S., McDonough, W.F. (1989). Chemical and isotopic systematics of oceanic basalts: Implications for mantle composition and processes, in: Saunders, A.D., Norry, M.J. (Eds.), Magmatism in the

Ocean Basins. *Geological Society*, London, pp. 313–345. https://doi.org/10.1144/GSL.SP.1989.042.01.19.

Sun, J., Zhu, X.K, Belshaw, N.S, Chen, W., Doroshkevich, A.G., Luo, W.-J., Song, W.-L., Chen, B.-B., Cheng, Z.-G., Li, Z.-H., Wang, Y., Kynicky, J., Henderson, J.M. (2021). Ca isotope systematics of carbonatites: insights into carbonatite source and evolution. *Geochemical Perspective Letters*, *17*, 11–15.

Szabó, C., Bodnar, R. J. (1996). Changing magma ascent rates in the Nograd-Gomor volcanic field northern Hungary southern Slovakia: evidence from CO_2-rich fluid inclusions in metasomatized upper mantle xenoliths. *Petrology*, *4*(3), 240-249.

Taylor, H.P., Frechen, J., Degens, E.T. (1967). Oxygen and carbon isotope studies of carbonatites from the Laacher See District, West Germany and the Alnö District, Sweden. *Geochimica et Cosmochimica Acta*, *31*, 407–430. https://doi.org/10.1016/0016-7037(67)90051-8.

Thirlwall, M.F. (1997). Pb isotopic and elemental evidence for OIB derivation from young HIMU mantle. *Chemical Geology*, *139*, 51–74. https://doi.org/10.1016/S0009-2541(97)00033-8.

Torres, P., Silva, L.C., Munhá, J., Caldeira, R., Mata, J., Tassinari, C. (2010). Petrology and geochemistry of lavas from Sal Island: Implications for the variability of the Cape Verde magmatism. *Comunicacoes Geologicas*, *97*, 35–62.

Tumanian, M., Frezzotti, M. L., Peccerillo, A., Brandmayr, E., Panza, G. F. (2012). Thermal structure of the shallow upper mantle beneath Italy and neighbouring areas: Correlation with magmatic activity and geodynamic significance. *Earth-Science Reviews*, *114*(3–4), 369–385. https://doi.org/10.1016/j.earscirev.2012.07.002.

Tumiati, S., Fumagalli, P., Tiraboschi, C., Poli, S. (2013). An Experimental Study on COH-bearing Peridotite up to 3·2 GPa and Implications for Crust–Mantle Recycling. *Journal of Petrology*, *54*(3), 453–479. https://doi.org/10.1093/petrology/egs074.

Veksler, I. V., Nielsen, T.F.D., Sokolov, S. V. (1998). Mineralogy of crystallized melt inclusions from Gardiner and Kovdor ultramafic alkaline complexes: Implications for carbonatite genesis. *Journal of Petrology*, *39*, 2015–2031. https://doi.org/10.1093/petroj/39.11-12.2015.

Verplanck, P. L., Mariano, A. N., Mariano, A. (2016). Rare Earth Element Ore Geology of Carbonatites. Rare Earth and Critical Elements in Ore Deposits. *Reviews in Economic Geology*, 5–32. https://doi.org/10.5382/rev.18.01.

Villa, I. M., Buettner, A. (2009). Chronostratigraphy of Monte Vulture volcano (southern Italy): Secondary mineral microtextures and ^{39}Ar-^{40}Ar systematics. *Bulletin of Volcanology*, *71*(10), 1195–1208. https://doi.org/10.1007/s00445-009-0294-6.

Wallace, M.E., Green, D.H. (1988). An experimental determination of primary carbonatite magma composition. *Nature, 335,* 343–346. https://doi.org/10.1038/335343a0.

Walter, B.F., Steele-MacInnis, M., Giebel, R.J., Marks, M.A.W., Markl, G. (2020). Complex carbonate-sulfate brines in fluid inclusions from carbonatites: Estimating compositions in the system H_2O-Na-K-CO_3-SO_4-Cl. *Geochimica et Cosmochimica Acta*, *277*, 224-242.

Wells, P.R.A. (1977). Pyroxene thermometry in simple and complex systems. Contributions to *Mineralogy and Petrology*, *62*, 129-139. https://doi.org/10.1007/BF00372872.

Williams, C.A., Hill, A., Young, R., White, R.S. (1990). Fracture zones across the Cape Verde Rise, NE Atlantic. *Journal of Geological Society*, London, *147*, 851–857. https://doi.org/10.1144/gsjgs.147.5.0851.

Wilson, C. J. N. (1984). The role of fluidization in the emplacement of pyroclastic flows, 2: Experimental results and their interpretation. *Journal of Volcanology and Geothermal Research*, *20*(1–2), 55–84. https://doi.org/10.1016/0377-0273(84)90066-0.

Wood, B.J., Li, J., Shahar, A. (2013). Carbon in the core: Its influence on the properties of core and mantle. *Reviews in Mineralogy and Geochemistry, 75,* 231–250. https://doi.org/10.2138/rmg.2013.75.8.

Woolley, A.R, Kempe, D.R.C. (1989). Carbonatites: Nomenclature, average chemical compositions and element distribution. In Carbonatites: Genesis and Evolution. Bell K (ed) Unwin Hyman, London, p 1-14.

Woolley, A. R., Kjarsgaard, B. A. (2008). Carbonatite occurrences of the world: map and database. *Geological Survey of Canada*, *5796*, 1–28. https://doi.org/https://doi.org/10.4095/225115.

Wyllie, P.J., Huang, W.L. (1975). Peridotite, kimberlite, and carbonatite explained in the system CaO-MgO-SiO_2-CO_2. *Geology, 3,* 621–624. https://doi.org/10.1130/0091-7613(1975)3<621:PKACEI>2.0.CO;2.

Wyllie, P.J., Lee, W.J. (1998). Model system controls on conditions for formation of magnesiocarbonatite and calciocarbonatite magmas from the mantle. *Journal of Petrology*, *39*, 1885–1893. https://doi.org/10.1093/petroj/39.11-12.1885.

Yaxley, G.M., Brey, G.P. (2004). Phase relations of carbonate-bearing eclogite assemblages from 2.5 to 5.5 GPa: Implications for petrogenesis of carbonatites. *Contributions to Mineralogy and Petrology, 146*, 606–619. https://doi.org/10.1007/s00410-003-0517-3.

Yaxley, G.M., Kjarsgaard, B.A., Lynton Jaques, A. (2021). Evolution of Carbonatite Magmas in the Upper Mantle and Crust. *Elements, 17,* 315–320.

Yaxley, G. M., Anenburg, M., Tappe, S., Decree, S., Guzmics, T. (2022). Carbonatites: Classification, Sources, Evolution, and Emplacement. *Annual Review of Earth and Planetary Sciences*, *50*. https://doi.org/10.1146/annurev-earth-032320-104243.

Zaitsev, A.N, Demény, A., Sindern, S, Wall, F. (2002). Burbankite group minerals and their alteration in rare earth carbonatites source of elements and fluids (evidence from C–O and Sr–Nd isotopic data). *Lithos*, *62*, 15-33. doi: 10.1016/S0024-4937(02)00084-1.

Zanon, V., (2015). Conditions for mafic magma storage beneath fissure zones at oceanic islands. The case of São Miguel Island (Azores archipelago). In Caricchi L and Blundy J.D. (eds). Chemical, physical and temporal evolution of magmatic systems. *Geological Society of London*, special publication, *442*, 85-104. https://doi.org/10.1144/SP422.4

Zanon, V., Frezzotti, M. L. (2013). Magma storage and ascent conditions beneath Pico and Faial islands (Azores archipelago): A study on fluid inclusions. *Geochemistry, Geophysics, Geosystems*, *14*(9), 3494-3514. https://doi.org/10.1002/ggge.20221

Zanon, V., Frezzotti, M. L., Peccerillo, A. (2003). Magmatic feeding system and crustal magma accumulation beneath Vulcano Island (Italy): Evidence from fluid inclusions in quartz xenoliths. *Journal of Geophysical Research*, *108*(B6), 2298. https://doi.org/10.1029/2002JB002140

Zazo, C., Goy, J.L., Hillaire-Marcel, C., Gillot, P.Y., Soler, V., González, J.Á., Dabrio, C.J., Ghaleb, B. (2002). Raised marine sequences of Lanzarote and Fuerteventura revisited - A reappraisal of relative sea-level changes and vertical movements in the eastern Canary Islands during the Quaternary. *Quaternary Science Reviews*, *21*, 2019–2046. https://doi.org/10.1016/S0277-3791(02)00009-4.

Zhao, D. (2007). Seismic images under 60 hotspots: Search for mantle plumes. *Gondwana Research*, *12*, 335–355. https://doi.org/10.1016/j.gr.2007.03.001.

Zindler, A., Hart, S. (1986). Chemical geodynamics. *Annual Review of Earth and Planetary Sciences*, *14*, 493–571. https://doi.org/10.1146/annurev.ea.14.050186.002425.

Zong, K., Liu, Y. (2018). Carbonate metasomatism in the lithospheric mantle: Implications for cratonic destruction in North China. *China Earth Sciences*, *61*(6), 711–729. https://doi.org/10.1007/s11430-017-9185-2.